

University of Nottingham

UK | CHINA | MALAYSIA

Elucidating the Molecular Architecture of the Skin and Plant Leaves, Novel Insights into the *in-situ* Permeation of Formulations

Mohammed Haroon Khan

Submitted to the University of Nottingham for the award of Doctorate in Philosophy

February 2024

Abstract

It is estimated, approximately $5.6 billion dollars is invested globally in agrochemicals to enhance crop yields and improve crop quality. This is achieved by controlling invasive species from competing with or damaging the desired crop. While this is has led to financial benefits to farmers, there is a significant gap in the knowledge surrounding the molecular compositions of skin and leaves. This significantly impacts the fundamental understanding and development of optimised foliar delivery of agrochemical products including mandatory risk assessments for exposure to agricultural workers.

To understand the dermal absorption of compounds, a comprehensive understanding of the molecular architecture of the skin, particularly the primary barrier, the *stratum corneum*, is necessary. The research detailed in this thesis employs the OrbiSIMS in conjunction with an Ar_{3000}^+ gas cluster ion beam (GCIB) to initially investigate the molecular chemistry of the *stratum corneum*. This exploration entails studying the non-homogeneity of the barrier layer in terms of depth and lateral distributions. Through *in situ depth* profiling and SIMS-MFP filtering of the dataset, the identification of over 140 species across five compound classes (amino acids, fatty acids, ceramides, phospholipids, and triglycerides) was achieved. Additionally, the chemical gradients of pivotal components involved in the cholesterol sulfate cycle, including the major fatty acid palmitic acid, were unveiled. Ultimately, the study demonstrated the permeation of an anti-aging peptide, Pal-GHK, through human skin at relatively low concentrations (100 ppm).

To address the limitations of conventional techniques used in evaluating agrochemical permeation into skin tissue, the OrbiSIMS was utilised to map the depth distribution of model agrochemical formulation, CCZ EC, simultaneously at application rates relevant to real-life conditions. The localisation of the active ingredient, cyproconazole, along with the co-formulants of the formulation, was illustrated as a function of depth at varying exposure levels within the layers of the skin.

Similar to the skin, there is limited knowledge available concerning the chemical composition of leaves, specifically the barrier layer known as, cutin. The limited understanding significantly affects the comprehension of product function and the development of optimized pesticide delivery systems. A thorough understanding of the molecular composition of leaves would also contribute to the formulation of more targeted pesticides with fewer adverse human health effects. Employing the recently developed OrbiSIMS profiling method, this study identified the *in situ* precise localisations of over 90 individual species across seven compound classes (amino acids, fatty acids, aldehydes, vitamins, flavones, nucleic acids, and phospholipids) within wheat leaves. Key fatty acids and aldehydes related to cutin and epicuticular waxes were identified, including flavones and vitamins relevant to the underlying epidermis. Subsequently, the CCZ EC model formulation was applied at a 1 % v/v dilution, representative of what is typically applied to crops, for various exposure times. The entirety of the formulation was successfully depicted in a label-free manner at a relatively low concentration, revealing intricate differences in permeation characteristics at different time points.

The Franz cell method has a relatively low throughput, to address this issue the dermal absorption of a model agrochemical formulation containing the three active ingredients mefenoxam, isopyrazam, and cyproconazole was effectively demonstrated. Highlighting varied levels of permeation attributed to their distinct physicochemical properties. Similarly, the limitations of the Franz cell methodology become apparent when the test compound remains undetectable within the skin tissue post-procedure, leading to inefficiencies and cost-ineffectiveness. Therefore, 20 active ingredients spanning the pharmaceutical, cosmetic, and agrochemical sectors were screened using the OrbiSIMS to evaluate the method's sensitivity across a range of different chemistries.

The insights gained from this work holds substantial implications for attaining more precision and optimisation in pesticide delivery into plant systems. Simultaneously, the research can aid in the generation of a refined understanding of exposure risks for agricultural workers. Comprehensive knowledge of the molecular architecture of the skin has the potential to enhance drug delivery and diagnostics. Similarly, insights into the molecular composition of leaves can contribute to the advancement of pesticide development, fostering more effective and targeted formulations.

Declaration

I, Mohammed Haroon Khan, hereby declare that this Ph.D. thesis is my own work and that, to the best of my knowledge and belief, it contains no material previously published or written by another person, except where explicitly stated in the acknowledgments or references.

I further declare that the work presented in this thesis has not been submitted for the award of any other degree or professional qualification.

I acknowledge that appropriate citations and references have been provided for all sources and materials used in this thesis. Any contributions from collaborators or assistance received from others have been duly acknowledged.

This thesis represents the culmination of my research work conducted at The University of Nottingham under the guidance of my supervisors:

David J. Scurr: School of Pharmacy, University of Nottingham, University Park, Nottingham, NG7 2RD, UK

Tim Powell: Syngenta, Bracknell, Berkshire RG42 6EY, UK

Conor Whitehouse: Syngenta, Bracknell, Berkshire RG42 6EY, UK

Clive J. Roberts: School of Pharmacy, University of Nottingham, University Park, Nottingham, NG7 2RD, UK

and I have adhered to the ethical standards and guidelines set forth by the institution. Date: February 2024

This work was funded by the following funding bodies: EPSRC and Syngenta UK

Acknowledgements

Completing this PhD has been a profound and transformative journey, and I owe my deepest gratitude to those whose unwavering support and guidance have made it possible.

First and foremost, my deepest thanks to my supervisor and mentor, David. The invaluable support and profound insights have not only shaped the trajectories of this PhD but have also been a source of encouragement during challenging moments. I am particularly grateful for the 'quick calls' that were always a beacon of reassurance and effortlessly resolving any issues or concerns.

I am equally indebted to my co-supervisors, Clive, Conor and Tim, your expertise and constructive criticism have been instrumental in refining the conceptual framework and methodology of this PhD. The commitment to excellence has left an indelible mark on my academic journey.

My special thanks to my fellow Nottingham colleagues Akmal, Marion, Anna K, Nichola, Julie, Max and Steffi for their friendship, encouragement, and creating a supportive academic community that has been a source of inspiration and motivation. A heartfelt thanks to Anna T, for making my life hard and easy at the same time. The memories we created together in the 'Orbi' and 'ToF' labs are etched in the fabric of this experience.

A wholehearted thanks to Meedi, Faddy, Baaj, Rux, Ingy, and Moon—your unwavering presence has been the anchor. Each step of this long and arduous journey has been accompanied by your invaluable companionship, shaping me into

the person I am today. Gratitude flows for enduring my highs and lows with unparalleled patience, providing a source of strength and firm belief. This is not just my accomplishment; it's a celebration shared with each of you.

Covid Statement

The completion of this PhD has taken place against the backdrop of the global COVID-19 pandemic, which has profoundly impacted individuals, communities, and academic pursuits worldwide. The challenges posed by the pandemic have been significant, requiring adjustments to the usual research methodologies, timelines, and modes of collaboration.

In adherence to public health guidelines and institutional protocols, certain aspects of this research, including data collection and experimental work, were inevitably affected. The University of Nottingham closed barely 3 months (March) after my commencement of the PhD program. The closure of laboratories and other facilities imposed by the pandemic necessitated innovative approaches to maintain the integrity of the research process while prioritizing the safety and well-being of all involved. As a result, initial work involved collaborating with peers on existing projects to gain an understanding of key concepts and building experience. The university re-opened in August in a phased approach, with limited access to facilities and a semblance of normalcy ensued in my second year of study.

I extend my sincere gratitude to all individuals, institutions, and colleagues who have demonstrated flexibility and support throughout this unprecedented period. The spirit of collaboration and understanding has been instrumental in navigating the complexities imposed by the pandemic.

Publications associated with this thesis

1. Elucidating the molecular landscape of the stratum corneum. Nichola J Starr 1, Mohammed H Khan, Max K Edney, Gustavo F Trindade, Stefanie Kern, Alexander Pirkl, Matthias Kleine-Boymann, Christopher Elms, Mark M O'Mahony, Mike Bell, Morgan R Alexander, David J Scurr. https://doi.org:10.1073/pnas.2114380119

Conferences associated with this thesis

1. Syngenta Collaborative Research Conference 2023
    a. Winner of best poster presentation
2. UK Surface Analysis Forum
    a. Crossley Award- Best Industrial Related Presentation
3. SIMS Europe 2023

Contents

Abstract 2
Declaration 5
Acknowledgements 6
Chapter 1. Literature Review 21
1.1 Introduction 21
1.2 Skin 24
1.2.1 Epidermis 25
1.2.2 *Stratum Corneum* 27
1.2.3 *Stratum Lucidum* 27
1.2.4 *Stratum Granulosum* 28
1.2.5 *Stratum Spinosum* 28
1.2.6 *Stratum Basale* 29
1.2.7 Current Insights into Skin Chemistry 29
1.3 Plant Leaves 30
1.3.1 The Cuticle 31
1.3.2 Upper Epidermis 32
1.3.3 Palisade Mesophyll 32
1.3.4 Spongy Mesophyll 33
1.3.5 Lower Epidermis 33
1.3.6 Current Insights into Leaf Chemistry 33
1.4 Agricultural Chemicals 34
1.4.1 Toxicity Associated with Agricultural Chemicals 36
1.4.2 Types of Exposure 37
1.4.3 Pesticide Classification 37
1.4.3.1 Organochlorine Pesticides 38
1.4.3.2 Organophosphorus Pesticides 39
1.4.3.3 Carbamate Pesticides 39
1.5 Characterising Skin Permeation 41
1.5.1 Factors Affecting Skin Permeation of Agrochemicals 41
1.6 Methods to Assess Skin Permeation 44
1.6.1 *In Vivo* Analysis 45
1.6.2 Traditional *in Vivo* Method 45
1.6.3 Tape Stripping 46
1.6.4 *In Vitro* Analysis 47

1.6.5 Static-diffusion Cells 47
1.6.6 Flow-Through Systems 48
1.7 Methods for Assessing Foliar Permeation 49
1.7.1 Assessment of *In Vivo* Foliar Permeation 49
1.7.2 Analytical Methods for Assessing Foliar Permeation 51
1.8 Analytical Methods for Assessing Skin Permeation 52
1.8.1 Chromatographic Techniques 52
1.8.2 Spectrophotometry Imaging Techniques 53
1.9 Mass Spectrometry Imaging Techniques 56
1.9.1 Time-of-Flight Secondary Ion Mass Spectrometry (ToF-SIMS) 56
1.9.1.1 Applications of the ToF-SIMS 57
1.9.2 OrbiSIMS 62
1.9.3 Applications of OrbiSIMS 63
Chapter 2. Elucidating the molecular landscape of the *stratum corneum* 68
2.1 Abstract 68
2.2 Introduction 70
2.3 Materials and Methods 74
2.3.1 Skin Acquisition 74
2.3.2 3D OrbiSIMS Single Beam Depth Profile Analysis of *ex vivo* Skin 75
2.3.3 3D OrbiSIMS Analysis of Individual Corneocyte Layers Permeation analysis. 76
2.3.4 SIMS-MFP software 77
2.4 Results and Discussion 78
2.4.1 Identifying the importance of cryogenic sample fixation for skin analysis. 78
2.4.2 Elucidating *stratum corneum* molecular gradients. 79
2.4.3 Exogenous Species within native tissue. 89
2.4.4 Lateral distribution of *stratum corneum* compounds. 90
2.4.5 Peptide delivery through the *stratum corneum*. 92
2.5 Conclusions 95
Chapter 3. OrbiSIMS Profiling for Elucidating the Surface Chemistry of Wheat Leaves and Assessing Agrochemical Permeation 96
3.1 Abstract 96
3.2 Introduction 97
3.3 Materials and Methods 101
3.3.1 Reagents 101
3.3.2 OrbiSIMS Depth Profile Analysis of Wheat Leaves 102
3.3.3 Leaf *in vivo* Permeation Study 102

3.3.4 Agrochemical Reference Preparation 102
3.3.5 Porcine Skin Preparation 102
3.3.6 Franz Cell Permeation Set-Up 103
3.3.7 OrbiSIMS Depth Profile Analysis of Skin and Leaves 103
3.3.8 Liquid Chromatography with Tandem Mass Spectrometry (LC-MS/MS) Analysis 104
3.4 Results & Discussion 105
3.4.1 Determining the molecular composition of wheat leaves 105
3.4.2 Agrochemical formulation delivery through wheat leaves 110
3.4.3 Assessing the dermal absorption of an agrochemical formulation 113
3.5 Conclusions 120
Chapter 4. OrbiSIMS Screening of Active Ingredients spanning Agrochemical, Pharmaceutical and Cosmetic Industries 122
4.1 Abstract 122
4.2 Introduction 123
4.3 Materials and Methods 125
4.3.1 Reagents 125
4.3.2 Porcine Skin Preparation 126
4.3.3 Franz Cell Permeation Set-Up for Multi-AI Formulation 127
4.3.4 Preparation of Porcine Skin Homogenates for AI Screening 127
4.3.5 OrbiSIMS Analysis of Skin with Multi-AI Formulation and AI Screening 128
4.4 Results 128
4.4.1 Multiple-AI Agrochemical Formulation Delivery Through Skin 128
4.4.2 Evaluation of the Sensitivity of the OrbiSIMS for Active Ingredients 137
4.4.3 Ion Intensity Comparison of the Active Ingredients 148
4.4.4 Assessment of the Linearity of OrbiSIMS Intensity with Concentration 157
4.5 Conclusion 158
5. Concluding Remarks and Future Perspectives 160
5.1 Conclusions 160
5.2 Future Perspectives 163
6. Supporting Information 165
6.1 Chapter 2 Supporting Information 165
6.2 Chapter 3 Supporting Information 189
..... 189
..... 193
..... 194
7. References 211

Abbreviations

µG	Micrograms
µM	Micrometers
$[M+H]^+$	Molecular ion in positive ion mode
$[M+H]^-$	Molecular ion in negative ion mode
AA	Amino Acid
AI	Active Ingredient
ALD	Aldehyde
CER	Ceramide
CCZ	Cyproconazole
CCZ EC	Cyproconazole Emulsifiable Concentrate
CS	Cholesterol Sulfate
EC	Emulsifiable Concentrate
FA	Fatty Acid
FLA	Flavones
GCIB	Gas Cluster Ion Beam
HPLC	High Performance Liquid Chromatography
IZM	Isopyrazam
LC-MS	Liquid Chromatography-Mass Spectrometry
LMSD	Lipid Maps Structural Database
LOGP	Partition Coefficient
M/Z	Mass to Charge Ratio
MFX	Mefenoxam
MW	Molecular Weight
NMF	Natural Moisturising Factor
NUC	Nucleic Acid
PL	Phospholipid
PPM	Parts Per Million
SC	Stratum Corneum
SD	Standard Deviation
TG	Triglyceride
SEM	Standard Error of Mean

SIMS	**Secondary Ion Mass Spectrometry**
TOF-SIMS	**Time Of Flight- Secondary Ion Mass Spectrometry**
VIT	**Vitamin**
WP	**Wettable Powder**

Table of Figures

Figure 1.1: Schematic diagram of skin in cross-sectional view illustrating the anatomy (Taken from Voegeli et al[34]). 25

Figure 1.2: Cross-section of a typical leaf depicting the anatomy (Taken from Levin and Nackley[65]). 31

Figure 1.3: Structures of Dichlorodiphenyltrichloroethane (a), glyphosate (b) carbofuran (c) (Adapted from Pubchem[97,121,122]. 40

Figure 1.4: Diagram of a Franz -type static diffusion cell. 48

Figure 1.5: Schematic of the flow-through diffusion cell (Taken from SES[154]). 49

Figure 1.6: Diagram of two-photon microscopy for imaging skin samples. OBJ, Objective lens; SPF, single band pass filter; DBS, dichroic beam splitter; BPF, band pass filter; PMT, photomultiplier tube. (Taken from Ahn et al[187]). 55

Figure 1.6: Schematic representation of the ToF-SIMS apparatus and generation of secondary ions. (Taken from Mazel et al and Aoki et al[196,197]). 57

Figure 1.7: ToF-SIMS imaging data highlighting the distribution of various compounds within skin. (a) ToF-SIMS images illustrating the distribution of imiquimod in human skin. (b) Negative ion ToF-SIMS data of the dermis showing the distribution of lipids within the skin layers. (c) Secondary ion images of chlorohexidine and PAMAM dendrimers within porcine skin. (d) ToF-

SIMS analyses of ceramides from cross sections of the epidermis. Adapted from:[17,56,19,205] 61

Figure 1.8: Schematic diagram of the OrbiSIMS spectrometer (Taken from Aoki et al[197]). 63

Figure 1.9: OrbiSIMS images of rat alveolar macrophage cell at 400 nm depth incubated with amiodarone (Taken from Passarelli et al[30]). 64

Figure 1.9.1: OrbiSIMS images of the perialgal vacuole of C. variabilis containing various metabolites including: chlorophyll (green), phosphocholine (red) and peptide markers (grey). (Taken from Aoyagi et al 207). 64

Figure 1.9.2: OrbiSIMS images of P. aeruginosa biofilm deducing the spatial distribution of adenine, PE lipids and 2-nonyl-4-hydroxyquinoline (NHQ). (Taken from Zhang et al[208]). 65

Figure 2.1. OrbiSIMS depth profile analysis of frozen hydrated ex vivo human skin tissue. (a) A schematic illustrating the process. (b) An example negative polarity spectrum. The spectrum presents the total ion intensity for the 250 x 250 µm area summed across the whole depth profile (total applied ion dose is 2.88×10^{13}). Using the SIMS-MFP software we were able to putatively assign over 140 different species across 5 compound classes (amino acids, fatty acids, ceramides, phospholipids and triglycerides). The mass regions for these classes are highlighted on the spectrum and an example compound is labelled for each class, detailing the molecular assignment, chemical formula and the observed mass (*m/z*) and deviation. 81

Figure 2.2. OrbiSIMS negative polarity depth profile data showing the ion intensity variation as function of ion dose/skin depth for various putatively assigned

compounds. The primary ion beam was Ar_{3000}^+. The ion intensities have been normalized to the total ion count and the profiles have been compressed using a running average method (using a 100 data point average). The *stratum corneum* – epidermal boundary, approximated with a dotted vertical line, has been determined based on the ion intensity variation of the phospholipid species (Fig. S2). (a) Example ions from each identified compound class: PL – phospholipids ($C_{41}H_{77}NPO_8^-$), TG – triglycerides ($C_{55}H_{101}O_6^-$), Cer – ceramides ($C_{44}H_{86}NO_5^-$), FA1 and FA2 – fatty acids ($C_{27}H_{47}O_2^-$ and $C_{16}H_{31}O_2^-$), AA – amino acids ($C_5H_{11}N_2O_2^-$) and CS – cholesterol sulfate ($C_{27}H_{45}SO_4^-$). The normalized intensity for the phospholipid ion has been multiplied by a factor of 50. (b) Cholesterol sulfate molecular ion ($C_{27}H_{45}SO_4^-$). (c) Fatty acids, palmitic acid ($C_{16}H_{31}O_2^-$) and lignoceric acid ($C_{24}H_{47}O_2^-$). (d) NMF compounds, the amino acid arginine ($C_6H_{13}N_4O_2^-$) and amino acid derivatives PCA ($C_5H_6NO_3^-$) and ornithine ($C_5H_{11}N_2O_2^-$). The normalized intensity for the arginine ion has been multiplied by a factor of 10. 83

Figure 2.3. OrbiSIMS high resolution negative polarity ion images, produced from the analysis of an individual human corneocyte skin layer, collected *in vivo* using a tape stripping method. The primary ion beam was Ar_{1700}^+. The data shown is from tape strip 7, which represents the middle of the *stratum corneum*. The ion images illustrate the 2D spatial distribution for the following molecular ions (a) Cholesterol sulfate ($C_{27}H_{45}SO_4^-$) (b) Lignoceric acid ($C_{24}H_{47}O_2^-$) (c) Pyrrolidone carboxylic acid ($C_5H_6NO_3^-$) (d) Sodium lauryl sulfate ($C_{12}H_{25}SO_4^-$). All ion images have been normalized to the total ion image and their relative intensity scales set to 50 % of the maximum. 92

Figure 2.4. 3D OrbiSIMS data showing the ion intensity variation as function of skin depth for various different compounds, highlighting the subtle changes in skin chemistry that can be detected using this method. The primary ion beam was Ar_{3000}^+.The ion intensities have been normalized to the total ion count. (a) Data demonstrating the permeation of an exogenous compound, the palmitoyl oligopeptide Pal-GHK ($C_{30}H_{55}N_6O_5^+$), into the *stratum corneum* layer of *ex vivo* human skin tissue. The *stratum corneum* – epidermal boundary has been determined, and approximated with a dotted vertical line, based on the ion intensity variation of the intrinsic phosphocholine molecular ion ($C_5H_{15}NO_4P^+$). The profiles have been compressed using a running average method (100 data points) and the skin depth is represented by total ion dose. (b) Data showing the normalized intensity for the Pal-GHK molecular ion ($C_{30}H_{55}N_6O_5^+$) as a function of tape strip number, produced from OrbiSIMS analysis of human tape strips collected *in vivo* following application of a commercially relevant formulation. The graph contains data from 15 sequential tape strips collected from both treated and untreated sites and is represented as the average and standard error of three different volunteers (n=3). 94

Figure 3.1. OrbiSIMS for label free imaging of *in situ* wheat leaf with mass resolving power of >240,000 and mass accuracy of <1 ppm. (a) A mass spectrum of negative polarity highlighting the molecular speciation of seven distinct compound classes (fatty acids, aldehydes, amino acids, nucleic acids, phospholipids, vitamins and flavonoids) employing the SIMS-MFP technique. (b) Overall localisation trends of example ions including: FA- Fatty acids (FA 18:1) ($C_{18}H_{33}O_2^-$) Ald- Aldehydes (2,4-Nonanedione) ($C_9H_{15}O_2^-$), AA- Amino acids

(Histidine) ($C_6H_8N_3O_2^-$), Fla- Flavones (Kaempferol) ($C_{15}H_9O_6^-$), Vit- Vitamins (Niacin) ($C_6H_4NO_2^-$) and Nuc- Nucleic acids (Uracil) ($C_4H_3N_2O_2^-$). (c) Chemical structures of the key ions explored and localisation within the leaf structure. 106

Figure 3.2. OrbiSIMS depth profile analysis of the fungicide, CCZ EC, through *in vivo* wheat leaf. (a) Localisation trends for the active ingredient CCZ- cyproconazole ($ClC_6H_4CH_2^+$) at 2, 4 and 6 hr exposure intervals. (b) Depth distributions of five co-formulants (Emulsogen EL 360- non ionic emulsifier, Hallcomid M-8-10 AI carrier solvent, Synperonic™ L11 non-ionic emulsifier, Atlox™ 4838B- anionic emulsifier, Solvesso™ 200 ND- water immiscible solvent) through *in vivo* treated wheat leaves including ionic/anionic emulsifying agents and carrier solvents. 113

Figure 3.3. (a) Static Franz cell permeation study conducted under infinite dosing, assessing the dermal absorption of SAN 619 (EC) at 10%, 50% and 100% v/v dilutions. (b) OrbiSIMS mass spectra depicting the chlorobenzyl molecular ion for the overall depth profile at varying concentrations within *ex vivo* skin. (c) Data demonstrating the determination of the *stratum corneum*-epidermal boundary depicted by the phosphocholine biomarker ($C_5H_{15}NO_4P^+$). (d) *In situ* profiling of cyproconazole within porcine skin at 10%, 50% and 100% v/v dilution post 4 -hour exposure time. 116

Figure 3.4. OrbiSIMS depth analysis of the fungicide, CCZ EC, through *ex vivo* porcine skin. (ai) LC-MS/MS analytical standard calibrations.) (aii) Total recovery of cyproconazole in the tape strips and remaining skin post-Franz cell permeation after 4, 7 and 24 -hour exposure intervals. (b) Depth distributions

of cyproconazole ($ClC_6H_4CH_2^+$) in *ex vivo* porcine skin at 4, 7, and 24 hours. (c) Distribution trends for the CCZ EC formulation excipients in *ex vivo* porcine skin after 4, 7 and 24 -hour exposure intervals. 120

Figure 4.1. OrbiSIMS mass spectra showing the molecular ions identified for the active ingredients within the multi-AI formulation spiked into skin, including two endogenous chemical constituent examples of the skin, specifically (a) cyproconazole ([ClC6H4CH2+]) (b) phosphocholine fragment, [$C_5H_{15}NO_4P^+$], (c) palmitic acid, [$C_{18}H_{33}O_2^+$], (d) mefenoxam [$C_{15}H_{22}NO_4^+$] and (e) isopyrazam in spiked skin, [$C_{20}H_{24}F_2N_3O^+$]. 130

Figure 4.2. OrbiSIMS depth profiles of a multi-AI agrochemical formulation through *ex vivo* porcine skin showing (a) isopyrazam ($C_{20}H_{24}F_2N_3O^+$), mefenoxam ($C_{15}H_{22}NO_4^+$) and ($ClC_6H_4CH_2^+$) and (b) six co-formulants (Emulsogen EL 360- non-ionic emulsifier, Hallcomid M-8-10 AI carrier solvent, Synperonic™ L11 non-ionic emulsifier, Atlox™ 4838B- anionic emulsifier, Solvesso™ 200 ND- water immiscible solvent, Dowanol™ DPM water miscible solvent) through *ex vivo* treated porcine skin, including the replicate depth profiles. 132

Figure 4.3. OrbiSIMS depth profiling mass spectra of the agrochemical active ingredients spiked in skin homogenates, illustrating the molecular ions and fragments detected within the spiked skin homogenates and their absence in the control skin homogenates. 142

Figure 4.4. OrbiSIMS mass spectra of the pharmaceutical active ingredients spiked in skin homogenates, showing the molecular ions and fragments detected within the spiked skin homogenates. 144

Figure 4.5. OrbiSIMS mass spectra ranging from 100 to 600 *m/z* of the cosmetic active ingredients spiked in skin homogenates. 148

Figure 4.6. The highest ion intensities of the 8 agrochemicals detected in the skin homogenate samples, ordered from high to low, with '+' and '–' denoting the polarity in which the ion or fragment was observed. (a) The unadjusted scale for the normalised intensity. (b) A split y- axis bar chart illustrating the large range of values. 150

152

Figure 4.7. The highest ion intensities of the 5 pharmaceutical drugs detected in the skin homogenate samples, ordered from high to low, with '+' and '–' denoting the polarity in which the ion or fragment was observed. (a) The unadjusted scale for the normalised intensity. (b) A split y- axis bar chart illustrating the large range of values. 152

Figure 4.8. The highest ion intensities of the 7 cosmetic actives detected in the skin homogenate samples, ordered from high to low, with '+' and '–' denoting the polarity in which the ion or fragment was observed. (a) The unadjusted scale for the normalised intensity. (b) A split y- axis bar chart illustrating the large range of values. 154

Figure 4.9. The impact of the LogP of an active ingredient on the ion intensity obtained by the OrbiSIMS in dosed skin homogenates. 156

Figure 4.9.1. Assessment of the linearity of the OrbiSIMS approach for three actives ingredients; cyproconazole, Pal-GHK and lidocaine. (a) The principle of the skin homogenate analysis, utilising the Ar_{3000}^{+} primary ion beam for depth profiling.

(b) Calibration curves for three active ingredients; cyproconazole, Pal-GHK and lidocaine, displaying a linear relationship. 158

List of Tables

Table 1.1 The prevalent types of pesticides and their respective functions. 35

Table 3.1: The composition of the CCZ EC formulation. 101

Table 4.1: The composition of the multi-AI formulation. 126

Table 4.3. A breakdown of the active ingredients investigated in this study, encompassing their respective structures, structural formulas, molecular weights and molecular ions/fragments identified using the OrbiSIMS. 138

Chapter 1. Literature Review

1.1 Introduction

Gaining an understanding of the molecular architecture of the skin particularly, the *stratum corneum,* is essential for enhanced diagnostics and tailored delivery of topical formulations in pharmaceutics and cosmetics. Presently, our comprehension of the barrier layer largely relies on the extraction of key compounds inherent to this layer, followed by quantification using liquid chromatography mass spectrometry[1,2,3,4,5]. While this approach provides precise identification, crucial information regarding the distribution of key species within the *stratum corneum*, both laterally and as a function of depth, is lost. A comprehensive understanding of the *in situ* distribution patterns of endogenous species would be immensely valuable for understanding the regulatory processes of bioactive compounds, particularly lipid species[6].

An improvement in the fundamental understanding of the skin's structure would contribute to a more profound comprehension of the dermal absorption mechanisms of compounds. The topical delivery of pharmaceutics and cosmetics is highly attractive, as it bypasses the first pass metabolism, thereby significantly reducing the systemic side effects[7]. Transdermal delivery of peptides is currently of great interest[8] due to the reduction in degradation and improved patient compliance. The ability to monitor the permeation characteristics of these

compounds within the skin including the distribution patterns would be a valuable tool.

Since 1989, the utilisation of agricultural chemicals has surged nearly five-fold, with a remarkable 1169 % increase in the past two decades, primarily driven for the sustenance of the ever-growing popullation[9]. While pesticides contribute significantly to crop intensification and enhanced productivity, it is imperative to acknowledge potential health risks, particularly for agricultural users consistently exposed to formulations during application. Notably, crops treated with pesticides are deemed safe for consumption, given the judicious use of these chemicals. Furthermore, residues of agrochemicals undergo processes of physical, chemical, and biological degradation. Risk assessments are routinely carried out to monitor potential adverse effects of human exposure to pesticides which can encompass respiratory issues[10,11], endocrine disruption[12,13], and reproductive hinderance[14,15]. Dermal penetration emerges as the most common route of exposure [16], often occurring during mixing, application, or cleanup operations, highlighting the critical need for comprehensive understanding and mitigation measures.

While skin permeation kinetics have been extensively explored for various compounds, including pharmaceuticals[17,18] and cosmetics[19,20] using a combination of Franz diffusion cells and time-of-flight secondary ion mass spectrometry (ToF-SIMS), there remains a significant gap in understanding the skin permeation and distribution of agrochemicals. Previous studies have employed static diffusion cells coupled with high-performance liquid chromatography (HPLC)[21,22] or liquid chromatography-mass spectrometry (LC-MS)[23]. However, HPLC methodologies exhibit relatively poor sensitivity due to UV-vis based detection systems. The

effective detection of analytes depends upon the presence of the chromophore thus the method is not suitable for all types of samples. This knowledge void underscores the need for comprehensive investigations into the skin's response to agrochemicals, a critical aspect that has not been adequately addressed in existing research.

Recent studies[24] have emphasized, agricultural productivity has plateaued in recent years, experiencing a global annual increase of 1 %, which is lower than the population growth rate. Addressing the requirement to sustain the ever-growing population necessitates innovative approaches to enhance both crop yields and quality. Enhancing our comprehension of the seemingly simple structure of plant leaves would enable the development of optimised, targeted and efficient agrochemicals for the production of high-quality, high-yield crops.

The cuticle, serving as the barrier layer, has emerged as a highly intricate and dynamic system[25, 26]. Despite this recognition, there exists a significant gap in our understanding of the inherent chemical composition of this structure. The molecular composition and functionality of plant leaves have been shown to have significant implications on the efficacy of agrochemical formulations[27,28,29]. Consequently, it is crucial not only to comprehend the intrinsic chemical composition of leaves but also to delineate the foliar permeation kinetics of pesticides into the tissues.

This research project seeks to evaluate the efficacy of the OrbiSIMS [30] as a tool for label-free imaging and depth profiling of skin and plant leaf tissues, aiming to elucidate the inherent diverse chemistries. Additionally, the study aims to

investigate the percutaneous uptake of a model agrochemical formulation at concentrations relevant to real-life conditions and explore the impact of exposure time on the uptake process. The investigation extends to assessing the foliar uptake of a model agrochemical formulation and understanding the permeation kinetics of the entire pesticide at concentrations applied in crop systems. The anticipated outcomes of this research promise to contribute valuable insights into both skin and leaf structure. The elucidation of tissue architecture and absorption characteristics, when combined, may offer essential insights that can aid in the development of pesticide delivery systems tailored to target specific areas, thereby mitigating risks for agricultural workers.

1.2 Skin

With an approximate surface area of 2 m^2 in healthy adults, the skin stands as the largest organ within the human body. Given its perpetual interaction with the external environment, the skin assumes a crucial immunological function, serving as a robust barrier that shields against pathogens[31] and offers protection from fluctuations in temperature, pressure, radiation, and chemical exposures[32].

The epidermis, dermis and the subcutaneous tissue (hypodermis) illustrated in **Figure 1.1** are the main three layers, comprising the structure of the largest organ. The outermost layer, the epidermis, functions to provide protection by acting as a barrier against pathogens but also offers waterproofing and prevents water loss[33,34]. The dermis is the middle layer of the skin, a fibrous structure consisting of collagen and other extracellular components for example nerves, vasculature, hair

follicles and glands. The dermis aids in homeostasis, by regulating internal temperature, producing sweat and distributing blood[35]. The hypodermis, or subcutaneous tissue, represents the innermost layer of the skin, encompassing adipose tissue, significant blood vessels, connective tissue, and glands. This layer assumes multifaceted roles, including fat storage, protective functions, and the connection of the epidermis and dermis to underlying tissues, such as cartilage and bones, thereby providing additional structural support[36].

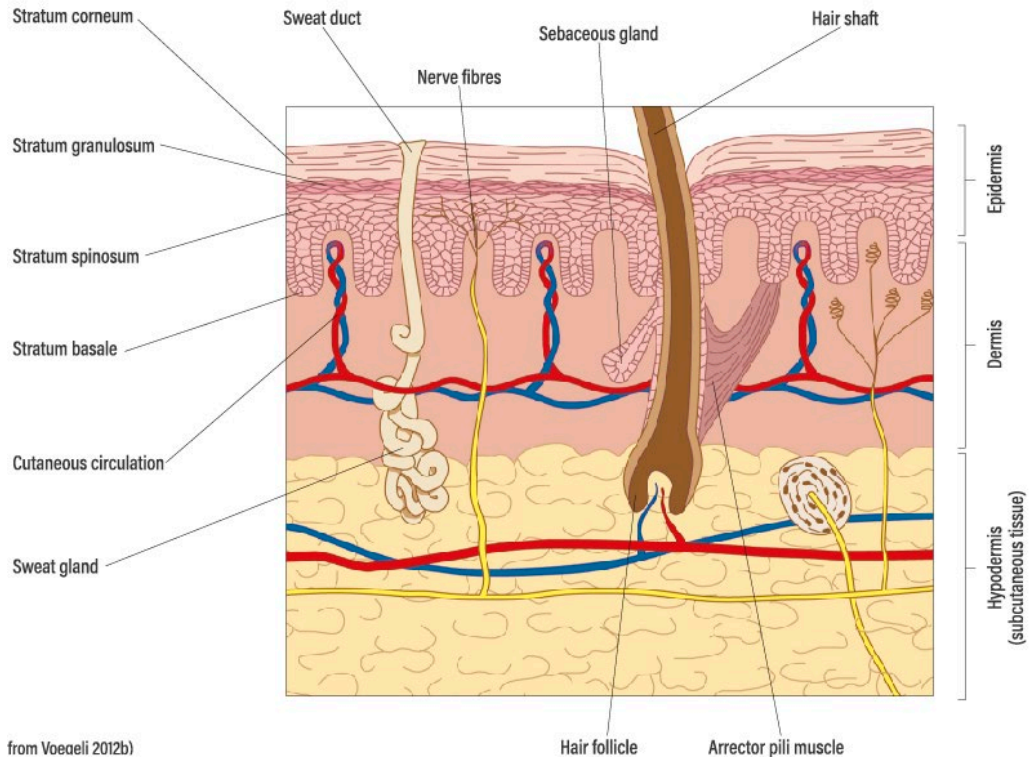


Figure 1.1: Schematic diagram of skin in cross-sectional view illustrating the anatomy (Taken from Voegeli et al[34]).

1.2.1 Epidermis

The epidermis is approximately 0.05 - 1 mm in thickness dependent upon the body region, with variations such as increased thickness on the palm compared to the

armpit. Keratinocytes, melanocytes and Langerhans cells are the three main types of cells composing the epidermis layer[37]. Comprising the epidermal layer are three primary cell types: keratinocytes, melanocytes, and Langerhans cells. Keratinocytes, deriving from stratified epithelium, constitute approximately 85 % of the total cell population in the epidermis. Keratinocytes establish tight junctions with skin nerves, maintaining the position of Langerhans cells and lymphocytes, and contribute significantly to immunological defense by forming a barrier against pathogens. Keratinocytes also play a crucial role in immune modulation, triggering inflammation by activating Langerhans cells post-injury[38]. Melanocytes, responsible for melanin production, fulfil an immunological role by serving as UV radical scavengers. Beyond shielding against skin cancer induced by UV radiation, melanocytes possess phagocytic properties, acting as antigen-presenting cells to T-cells and produce cytokines[39]. Meanwhile, Langerhans cells contribute to immune homeostasis by absorbing microbial antigens and transforming into antigen-presenting cells. Additionally, Langerhans cells can transition into dendritic-like cells, relocating to lymph nodes for interaction with T-cells[40].

Additionally, the epidermis is continually regenerated, with an estimated renewal time of approximately 2 months. It consists of five layers: the *stratum corneum*, *stratum lucidum*, *stratum granulosum*, *stratum spinosum*, and *stratum germinativum*[41].

1.2.2 *Stratum Corneum*

The *stratum corneum,* also known as the cornified layer, is the outermost layer of the epidermis comprising of 10 - 30 layers of cells called corneocytes with an approximate thickness of 10 - 40 μm[42]. Corneocytes are terminally differentiated keratinocytes without nuclei or cytoplasmic organelles, formed *via* a process known as cornification. Keratinocytes proliferate within the *stratum basale* of the epidermis through cell division and migrate to the surface of the skin[43]. As these cells migrate, they undergo multiple stages of differentiation and transform into corneocytes in the *stratum corneum*. The physiological function of the *stratum corneum* is to offer impact resistance and withhold against mechanical shear. The *stratum corneum* provides an immunological barrier, not only impeding the entry of pathogens but also, owing to the non-living nature of corneocytes, resisting viral attacks and preventing DNA damage induced by UV radiation[44,45,46].

1.2.3 *Stratum Lucidum*

The *stratum lucidum* also referred to as the 'clear layer', due to its translucent appearance, is a thin transitional layer located between the *stratum corneum* and *stratum granulosum*. The clear layer is exclusively found in thicker regions of skin for example the palms of hands or the soles of feet where it is composed of dead keratinocytes approximately three to six layers thick. The function of the *stratum lucidum* is to provide the skin with the capability to stretch and also lower friction particularly in the soles of feet and palms of hands. In addition, keratinocytes contain the protein eleidin and other various oily components improving skin waterproofing[47].

1.2.4 *Stratum Granulosum*

The *stratum* granulosum or granular layer is composed of granular cells made from keratinocytes migrating from the underlying *stratum spinosum*. The granular cells contain keratohyalin granules responsible for aggregating keratin filaments in the cytoplasm with the aid of cysteine and histidine rich proteins[48]. Moreover, these cells secrete lipid-rich lamellar bodies into the extracellular space between the *stratum granulosum* and *stratum corneum*, forming a hydrophobic region which gives rise to the skins barrier properties and prevents excessive water loss[49]. Moreover, it is evident granular cells also possess the ability to lose their nuclei and cytoplasmic organelles to transform into corneocytes that can migrate to the *stratum corneum*[43].

1.2.5 *Stratum Spinosum*

The stratum spinosum also known as the prickle cell layer is found between the *stratum granulosm* and *stratum basale* with an approximate thickness of 8 - 10 layers of keratinocytes[50]. Similarly, this structure contains desmosomes which interlock with one another to provide additional strength. Langerhans cells, interspersed among keratinocytes, function as dendritic cells with macrophage-like properties, engulfing foreign materials such as pathogens. Keratin synthesis commences in the *stratum spinosum* contributing to waterproofing of the skin by releasing hydrophobic glycolipids. As keratinocytes are produced in the *stratum basale*, those within the *stratum spinosum* are progress toward the *stratum granulosum*[28].

1.2.6 *Stratum Basale*

The *stratum basale* also called the *stratum germinativum* is the deepest layer of the epidermis composed of cuboidal shaped stem cells called basal cells which rest on the basement membrane zone separating the epidermis from the dermis. These basal cells continually undergo mitosis and the existing cells are driven superficially away from the *stratum basale*[29]. Among the keratinocytes exist Merkel cells, responsible for stimulating nerve cells for sensory input. Within the basale layer exist melanocytes responsible for the production of melanin which not only provides hair and skin with colour but also provides protection against UV radiation[30].

1.2.7 Current Insights into Skin Chemistry

Numerous studies have investigated the composition of the *stratum corneum*, continually updating the exact composition of the lipid matrix. Currently, 17 subclasses of ceramides have been identified in the human *stratum corneum*[51], including the identification of 1,000 various ceramide molecules from human and porcine *stratum corneum*[52].

Saturated and unsaturated free fatty acids comprise a diverse group, encompassing 30 different species identified, featuring chain lengths spanning 14 to 34 carbon atoms. Among these, lignoceric and hexacosanoic acid (C 24:0 and C 26:0) have been identified as the most abundant[53,3]. Beyond this intricate mixture, the *stratum corneum* hosts compounds associated with surface sebum and a blend of hygroscopic species collectively termed natural moisturizing factor (NMF). These compounds play a pivotal role in skin hydration[54,55]. The molecular speciation of the

skin consists of LC-MS[3,56,57] and HPLC[58,59] based quantification, necessitating the bulk analysis via laborious and complex solvent-based extraction. Consequently, all information regarding the localisation of compounds is lost both laterally and as a function of depth.

Sjovall *et al*[60] employed the ToF-SIMS for the most comprehensive analysis of the 2D spatial distribution of skin lipids in human skin. The localisation of ceramides and saturated long-chain fatty acids in the *stratum corneum* was demonstrated including the abundance of cholesterol sulfate in the upper regions of the epidermis. However, due to the limitations in sensitivity and resolution (discussed in later sections) of the ToF-SIMS instrumentation, the presence of subtle chemical gradients specifically in the various layers of the skin were not detected.

1.3 Plant Leaves

Plant leaves consist of a layered structure (**Figure 1.2)**, each layer performing distinct roles in safeguarding and supporting the plant's well-being. These are identified as the cuticle, upper epidermis, palisade mesophyll, spongy mesophyll and lower epidermis[61]. Collectively, the various layers contribute to several essential functions including facilitating photosynthesis for plant growth[62,63], enabling the gaseous exchange of CO_2 and O_2[64,65], regulating water balance through transpiration[66,67] and maintaining temperature[68].

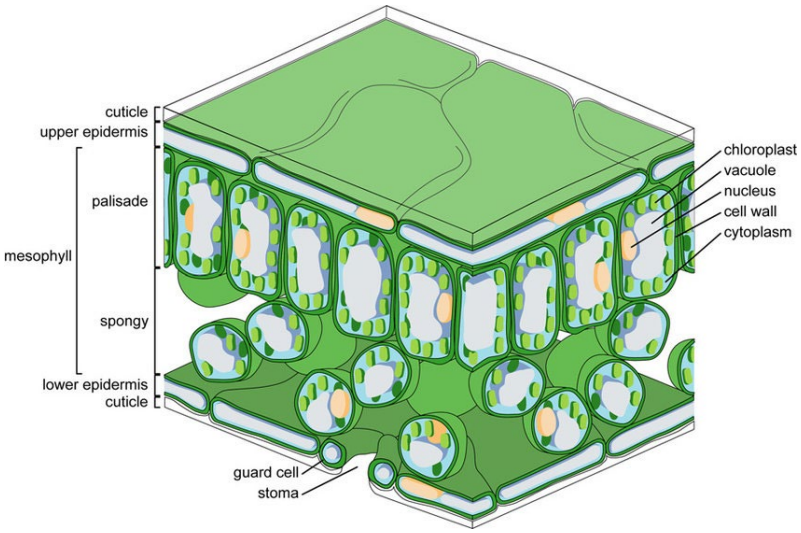


Figure 1.2: Cross-section of a typical leaf depicting the anatomy (Taken from Levin and Nackley[69]).

1.3.1 The Cuticle

The outermost layer, known as the cuticle, is a relatively thin (1 – 10 µm) hydrophobic polymeric structure that serves as a primary defence barrier against environmental elements, for example biotics and xenobiotics[70]. It offers regulation of water and heat loss[71], providing a selective filter for absorption of UV[72] and permits resistance to mechanical stress.

Multiple studies[73,74,75] have confirmed, the composition of the cuticle, comprising of two primary components. The first component is cutin, a polyester formed from hydroxylated C_{16} and C_{18} fatty acids and glycerol, integrated into the epicuticular waxes. The waxes, in turn, constitute a complex mixture of aliphatic hydrocarbons, alkanes, alcohols, ketones and aldehydes[76,77,78,79]. Recent studies have highlighted the intricate roles of specific molecular species involved in various metabolic. Notably, these pathways include the regulation of epidermal cell division through fatty acids[80] and the involvement of cuticular polymeric signalling molecules in cell adhesion[76].

The cuticle exhibits a comparative thinness in comparison to the *stratum corneum* found in skin tissue. A notable similarity between the structures is discernible, predominately in the fatty acid composition. The notable enrichment at the surface of both structures is known to contribute significantly to the primary barrier function against biotic and abiotic environmental stresses[81,82]. However, the resemblance between the two ceases here, as the stratum corneum displays a far more intricate composition including ceramides, amino acids triglycerides and cholesterol which serve additional functions such as moisturisation, regulation of water loss and cell signalling. In contrast the cuticle is primarily comprised of waxy components, aimed at the safeguarding of the plant surface.

1.3.2 Upper Epidermis

The upper epidermis is a single layer of transparent cells permitting the penetration of light through to the underlying chloroplasts for photosynthesis[83] as well as providing an extra layer of protection to the leaf structure. Housing guard cells, the upper epidermis plays a pivotal role in the stomatal exchange of CO_2 for O_2 as well as regulating water levels. Additionally, the upper epidermis contributed to sensory function, aiding in the orientation of leaves towards light[84].

1.3.3 Palisade Mesophyll

The palisade layer is composed of densely packed columnar-shaped cells abundant in chloroplasts, in addition to, housing nuclei and cytoplasm for photosynthetic purposes[85]. The primary function of this layer is to carry out photosynthesis whilst maintaining the continuous exchange of CO_2 and O_2 including regulating water content.

1.3.4 Spongy Mesophyll

The spongy mesophyll is a complex, porous layer consisting of 'gaps' allowing the exchange of gases necessary for photosynthesis[86]. Additionally, the mesophyll layer is responsible for the storage of carbohydrates and glucose to serve as a source of energy for the plant[86].

1.3.5 Lower Epidermis

Similar to the upper epidermis, this layer is also a single layer thick providing protection to the leaf structure. The cells of this the lower epidermis are squarer in shape, containing guard cells and stomata for the regulation of gas exchange and water retention. In addition, some plants contain trichomes in this layer for additional protection against herbivores[86].

1.3.6 Current Insights into Leaf Chemistry

The molecular speciation of the cuticle consists of LC-MS quantification[87,88] resulting in the loss of spatial resolution due to extraction procedures. It is widely acknowledged that the cuticle matrix is predominately (<80 %) composed of C_{16} and C_{18} fatty acids at approximately 1000 µg/cm^{-2}, [81] however, localisation of these individual species and others is not known. Waxes are a vital constituent of the leaf cuticle, serving a pivotal role in mitigating water loss and safeguarding against environmental stressors. Jefree *et al.*[89] demonstrated the homogenous dispersion of the epicuticular wax throughout the entire depth of the cuticle with a degree of embedding into the cutin layer, nevertheless, the precise composition, structure, and biosynthetic pathways governing leaf waxes have not been elucidated. Currently, there is limited knowledge regarding the exact distributions of wax

constituents, including alkanes, aldehydes, alcohols, and esters. In addition to cuticular compounds, there are various species that are localised in the underlying epidermal layers of leaves. Flavonoids are diverse secondary metabolites in leaves, synthesised via the phenylpropanoid pathway[90]. Kaempferol and vitexin are two of the abundant flavonoids functioning as antioxidants, protect against oxidative stress, influence plant-microbe interactions, and are regulated by environmental and physiological factors. Huang *et al.*[91] successfully quantified the presence of flavonoids within the leaf however, due to solvent-based extraction procedures spatially resolved data was not acquired. Additional compounds associated with the deeper palisade and mesophyll layers encompass nucleic acids, vitamins, sugars and phospholipids, the depth distributions of which remain largely unexplored. As stated by Kerstiens[92], *in situ* analysis without prerequisite extraction would be crucial in understanding surface specific molecular information. Further research is required to unravel the complex and dynamic nature of leaf waxes and their contribution to the overall functionality of the leaf cuticle. As the fatty acids and waxy esters primarily compose the barrier cuticle layer, the interaction between the two could provide vital insights into the absorption characteristics into the leaf. A comprehensive understanding of the molecular architecture of the leaf can contribute to refining the optimisation of pesticide development with improved delivery and efficacy.

1.4 Agricultural Chemicals

Chemical compounds or combinations thereof employed to manage pests, encompassing insects, fungi, rodents, and weeds, fall under the category of

pesticides. Additionally, public health systems utilize these substances to prevent vector-borne diseases by eradicating vectors, such as mosquitoes and other organisms.

Agricultural chemicals possess a variety of advantages particularly increasing crop yields and improving crop quality by controlling invasive species from competing or damaging the desired crop. A study conducted by Pimentel et al[93] concluded an average of $10 billion dollars is spent yearly on pesticides resulting in $40 billion worth of savings in crops portraying the great monetary gain for farmers. Pesticides have also been linked to reducing malaria by controlling the population of mosquitoes however, certain vectors have gained resistance in particular, DDT resistance in *Aedes* and pyrethroid resistance in C. *quinquefasciatus*[94]. Various classes of pesticides exist, categorised based on the type of pest they aim to control. **Table 1.1** illustrates the diverse classes of pesticides and the mechanisms of action they employ.

Table 1.1 The prevalent types of pesticides and their respective functions.

CATEGORY	PURPOSE	EXAMPLES
INSECTICIDES	Controls the population of insects, mites and ticks. Also effective against insect eggs and larvae.	Organochlorides- DDT Carbamates- Carbofuran Neonicotinoids- Acetamiprid
HERBICIDES	Substances used to control unwanted plants and weed species whilst unharming the desired crop.	Atrazine Simazine 2,4-dichlorophenoxyacetic acid
FUNGICIDES	Biocidal pesticide used to kill unwanted parasitic fungi and spores.	Sulfur Captan Mancozeb
RODENTICIDES	Non-specific pesticides used to kill rodents for example mice, beavers and gophers.	Warfarin Bromadiolone Difenacoum
DISINFECTANTS	Also known as antimicrobials these are designed to reduce the populations of bacteria, viruses and in some cases fungi.	Oxytetracycline Ammonia Bleach

1.4.1 Toxicity Associated with Agricultural Chemicals

The toxicity in terms of agricultural chemical safety refers to the poisonous ability of a compound to cause injury or illness (hazard). The acute toxicity of a compound is expressed in terms of lethal dose (LD_{50}) or lethal concentration (LC_{50}), the dose or concentration at which a compound will kill 50 % of an organism[95].

The potential for adverse effects on humans (risk) depends upon a range of factors including concentration/dosage of the pesticide, exposure time and route of entry into the body. Agricultural chemicals, such as glyphosate and carbofuran, can pose a threat through poisoning (systemic effects), potentially causing harmful effects on biological reactions, molecules, or organs within the body, resulting in severe injury or fatality. Conversely, pesticides that are external irritants (local effects) for instance, pyrethroid insecticides can also cause injuries for example burns or rashes[16].

As reported by the World Health Organisation[96], agrochemical poisoning is responsible for approximately 200,000 deaths per year with 99 % occurring in the developing world. The cases for acute pesticide poisoning accounts for significant mortality for occupational and non-occupational exposure however, due to the lack of understanding of the uptake of agrochemicals through and into the skin, preventative measures are not greatly effective[96]. Personal protective equipment (PPE), such as gloves, masks, and coveralls, faces limited availability in third-world countries and poses financial challenges for economically disadvantaged nations due to their relatively high costs. Furthermore, occlusion effects can exacerbate the dermal absorption of substances if they manage to infiltrate the PPE.

Percutaneous uptake is particularly relevant to agricultural workers that manually apply these pesticides to crops and come into treated crops and surfaces. By understanding the mechanisms of delivery and the distribution characteristics of these compounds in the various layers of skin, formulations can be produced to prevent the exposure and reduce pesticide poisoning.

1.4.2 Types of Exposure

The toxicity linked to exposure to agricultural chemicals can be categorised based on the correlation between the promptness of symptom development and the duration of exposure[97].

Acute toxicity refers to a single incident of exposure also known as short-term exposure. From the acute toxicity profile, it can be deduced how poisonous a pesticide is to an organism after a single incident and helps describe toxic effects appearing immediately (within 24 hours)[16]. Generally, insecticides exhibit the highest acute toxicity[98], such as carbofuran, due to their neurotoxic properties. Sub-chronic toxicity is the exposure to pesticides from repeated incidents which can span over several weeks or months but not exceeding 10 % of the lifespan of the organism[99]. Dichlorodiphenyltrichloroethane[100] is an example of a sub-chronic pesticide, causing adverse effects on the liver, kidney and immune system. Lastly, chronic toxicity is repeated exposure for several months or years, lasting for the entire lifespan of the organism. Chlorpropham[101] can cause detrimental chronic effects lasting for the organism's lifespan including retarded growth, congestion of the spleen and increased organ weights.

1.4.3 Pesticide Classification

1.4.3.1 Organochlorine Pesticides

Dichlorodiphenyltrichloroethane (DDT) (**Figure 1.3a**)[102] is an organochlorine pesticide first synthesised in 1874 gaining popularity in WWII for combat against disease including typhus, malaria and the bubonic plague[103]. Due to the potency of this organochlorine, cost effectiveness and relatively large half-life of 10 years[104], over the years it was adopted as a pesticide. DDT is one of the most commonly used pesticides worldwide and is applied to various crops to improve yields by fighting against insects and pests. By facilitating the opening of sodium ion channels in neurons, DDT causes repeated depolarisation leading to spasms and the eventual death[105] of the pests. Although DDT is effective in terminating pests its action is not limited to them, and in mammals similar effects for instance tremors and seizures may occur.

DDT has proven to be advantageous in the past for improving crop quality and increasing yields by conserving the environment and preventing insect transmitted disease[106], however, human exposure to this chemical has proven to be detrimental to health.

The US Environmental Protection Agency (EPA) has categorised DDT as a B2 carcinogen due to its ability to promote the growth of malignant cells specifically breast cancer in women[107]. It has been proven DDT accumulates within tissue specifically adipose stores and the metabolism of this chemical can cause liver and kidney toxicity[108]. A number of studies[109,110] have suggested DDT can act as an endocrine disruptor, by inhibiting the androgen receptor and interacting with other endocrine disruptive pollutants the risk of mammary cancer increases. Excessive

exposure to DDT has been linked to cause lung tumours, liver tumours and lymphomas[111,112,113].

1.4.3.2 Organophosphorus Pesticides

The most common organophosphorus pesticide is the 'weed-killer', glyphosate (**Figure 1.3b**) used to kill broadleaf weeds and grass which compete with crops. The herbicide is responsible for impeding the shikimate pathway therefore, preventing the biosynthesis of vital aromatic amino acids essential for plant growth[114]. Glyphosate disrupts plant growth shortly after application by efficiently translocating through roots and leaves, making it highly advantageous.

However, similar to organochlorine compounds, glyphosate and other organophosphorus chemicals have been associated with endocrine disruptors in human cell lines, having been linked to the promotion of carcinogenicity, birth defects, cognitive and developmental brain disorders[115]. Furthermore, it has been noted by Jaga and Dharmani[116], organophosphorus compounds effect the function of the enzyme cholinesterase, responsible for the lysis of choline-based esters specifically, the neurotransmitter acetylcholine[117]. The inhibition of cholinesterase by glyphosate has been linked with a decrease in insulin secretion[118], oxidative stress due to the disruption of oxidative phosphorylation in mitochondria[119] and other nervous system related diseases.

1.4.3.3 Carbamate Pesticides

Carbofuran (**Figure 1.3c**) is a broad-spectrum carbamate pesticide used for a variety of crops including potatoes, soya beans and corn to prevent insect, mites and nematode attack. Carbofuran is classed as a systemic pesticide whereby it is

absorbed through the roots of the plant and circulates within plant tissue and organs killing insects that feed on them[120]. Carbofuran induces acute toxicity within pests by reversibly inhibiting acetylcholinesterase, an enzyme responsible for the hydrolysis of the neurotransmitter acetylcholine. The inhibition of acetylcholinesterase results in the accumulation of acetylcholine at neuromuscular junctions causing overstimulation of nerves and eventual death of the insect[121].

In addition to the advantages carbofuran possesses, it is also recognised as one of the most toxic agricultural chemicals, with a LD_{50} of 8-14 mg/kg in rats and since been banned in Canada and the European Union[122]. In addition to its reported endocrine-disruption and potential impact on reproductive conditions[123] carbofuran is documented to suppress cytokine production, leading to apoptosis and necrosis of T-lymphocytes[124]. Moreover, carbamates have been associated with amplifying neurobehavioral disorders for example Alzheimer's and Parkinson's disease[125].

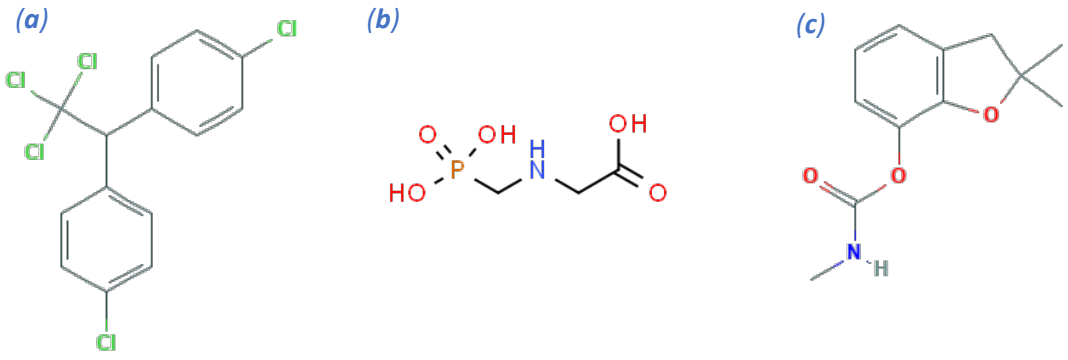


Figure 1.3: Structures of Dichlorodiphenyltrichloroethane **(a)**, glyphosate **(b)** carbofuran **(c)** (Adapted from Pubchem[102,126,127].

1.5 Characterising Skin Permeation

Since dermal penetration is the most common route of exposure[16] to agrochemicals occurring during splashes or spills, whilst mixing, loading or disposing it is a key area of interest. The skin permeation of pesticides can potentially be more detrimental to health compared to ingestion due to eliminating first pass metabolism and entering directly into the bloodstream for distribution[128]. While percutaneous uptake of agrochemicals represents the primary route of exposure, there remains a significant gap in our understanding of the specific routes of permeation, the underlying mechanisms of delivery, and the precise localisation of these substances within the skin. This knowledge gap is critical for developing products with minimized risks of exposure for users.

Pesticides can interact with the skin in three distinct ways firstly, the chemical may penetrate the skin and contribute to the systemic load. Secondly, local effects may be induced ranging from irritation to degradation of tissue. Lastly, by affecting the immune system agrochemicals can trigger allergic reactions at the point of contact or even across the entire body. Respiratory sensitisation has also been linked to excessive exposure to pesticides *via* the dermal route causing hypersensitivity of the airways and the development of allergies[129].

1.5.1 Factors Affecting Skin Permeation of Agrochemicals

The physicochemical properties of a pesticide play a pivotal role in skin permeation including sufficient aqueous solubility in order to partition into the epidermis *via* the aqueous pores. Moreover, the hydrophilicity and lipophilicity of the molecule must be balanced in order for the molecules to partition between the polar and

non-polar environments of the body. Studies [130] have indicated that substances with a molecular size below 500 Da experience an elevated rate of absorption through the skin, a factor that holds relevance in the context of agrochemical skin permeation. Chen *et al*[131] investigated the permeation of pesticides through nanofiltration membranes mimicking human skin. It was established, the length of the pesticide had a greater effect on pesticide permeation rejection in comparison to pesticide width. As noted by the researchers, the molecular sizes of pesticides typically do not surpass 500 Da, suggesting that agrochemicals can be readily transported into the skin. The impact of pesticide molecular size and weight on percutaneous absorption in human skin has not been extensively investigated, creating a knowledge gap that warrants further exploration.

Numerous biological factors influence the skin permeation of pesticides, with one critical determinant being the specific anatomical site of exposure. The thickness of the skin varies from as little as 0.5 - 4 mm depending on the body part due to the presence hair follicles, glands and other morphological differences[49]. Where the skin is relatively thin, for instance the armpits, molecules can be absorbed relatively easily and at faster rates compared to thicker sections. Research conducted by Feldman and Maibach[132] on human males proved the skin permeation of pesticides parathion and malathion increased 50-fold when applied to the genital areas compared to the leg where the skin is thicker due to the presence of hair follicles and glands. Moreover, the structural integrity of the *stratum corneum* is pivotal since any open wounds, abrasions or dermal diseases may increase skin permeation significantly. Akomeah *et al*[133] conducted research into the effects of abrasions on dermal penetration of caffeine, acyclovir and angiotensin II and it was

noted epidermal permeation increased up to a 100-fold when skin was damaged. With respect to agrochemicals, the same increased percutaneous absorption may be present, especially with farmers who are more likely to cut or bruise their skin. The use of gloves is a common practice to mitigate this issue; however, occlusion may still occur when pesticides infiltrate beneath clothing, leading to increased skin permeation[134].

It has been noted skin penetration of pesticides is more effective and faster with an increase in temperature. A study presented by Thredgold *et al*[135] deduced by increasing the temperature of the insecticide, dichlorvos from 25 to 37 °C there was an approximate 13-fold increase in skin permeation over an 8-hr period. The rise in temperature is attributed to the increased flexibility and fluidity of the *stratum corneum*, making it more susceptible to permeants. Regions with warmer climates may require additional skin protection to prevent the absorption of agrochemicals. However, in many developing countries, providing such protection to users is often challenging due to cost constraints.

The hydration of the skin is an important factor when considering dermal penetration since, a balanced level of hydration acts as a barrier against permeants. However, if the water content of the skin increases above the optimal levels, permeability also increases. A study conducted by Zhai *et al*[136] concluded the absorption of nicotinate significantly increased following hyper-hydration of the *stratum corneum*.

Pesticide users administering skin permeation enhancers which promote the absorption of a substance through the skin for example dimethylsulphoxide

(DMSO) or pyrrolidones are at elevated risked of dermal exposure of agrochemicals. These penetration enhancers have various modes of action including; disruption of the packing motifs within intercellular lipid matrices, may act as a solvent for the permeant therefore increasing partitioning into the tissue or alter the metabolic activity within the skin[137]. A study conducted by Brand[138] conveyed sunscreen led to a significant enhancement of the dermal exposure to the herbicide 2,4-dichlorophenoxyacetic acid compared to non-sunscreen users. Agricultural workers are advised to use sunscreen to prevent skin melanomas, however, additional precautions are necessary to avoid unintended chemical exposures.

It is evident that the growing use of agrochemicals poses an escalating risk of excessive and harmful exposure to farmers. As dermal penetration is the most common route of exposure to pesticides, it becomes crucial to conduct further research in this area to delineate absorption and distribution characteristics. Investigating how pesticides impact skin chemistry and understanding the permeation characteristics of agrochemicals is imperative for formulating products that exhibit high efficacy with minimal risk to users and consumers.

1.6 Methods to Assess Skin Permeation

Numerous methods have been devised for the assessment of percutaneous permeation of molecules, aiming to evaluate dermal and transdermal delivery systems. The standardisation and validation of models including, *in vitro* and *in vivo*

methods have been of great interest during the last decade, each of which possessing unique advantages and disadvantages.

1.6.1 *In Vivo* Analysis

In vivo techniques are generally studies performed on animals or humans where the biological system is metabolically and physiologically integral. Initially, *in vivo* studies involved the use of rodents specifically rats due to availability, simple handling and structural similarities to human skin. However, several studies comparing skin permeation between the two organisms proved rat skin was more permeable and resulted in the overestimation of penetration in human skin[139,140]. Conversely, porcine skin is generally accepted as a suitable surrogate to human skin due to many histological similarities between the two. A study conducted by Barbero and Frasch[141] proposed porcine and human skin exhibited similar permeation profiles for many compounds including caffeine, benzoic acid and testosterone. There was also a positive correlation between the two organisms and the slopes were close to unity.

1.6.2 Traditional *in Vivo* Method

The traditional *in vivo* method involves applying the test compound to the skin of humans or animals and after a certain time period the amount of the compound present in blood, urine or faeces can be measured thus, providing an indication of penetration. Hueber-Becker[142] performed a study examining the human systemic exposure of an oxidative dye ([^{14}C]-*para*-phenylenediamine), achieving a comprehensive measurement of the compound in blood, urine, and faeces compared to *in vitro* studies. The traditional *in vivo* approach is advantageous because it takes into account the condition of the body for example metabolism

however, this method falls short when the compound being tested has unknown characteristics giving rise to ethical and moral concerns.

1.6.3 Tape Stripping

The skin permeation of topically applied formulations can be quantified by entirely stripping the *stratum corneum* using an adhesive tape. The test compound is allowed to penetrate the skin for a predetermined time after which the microscopic layers of the *stratum corneum* are removed by repeated application and removal of adhesive films (up to 100 times)[143]. The removed layers of the *stratum corneum* can be analysed using analytical methods for example HPLC and LC-MS. Tape stripping is commonly used for the assessment of the quality and efficacy of drugs. Research involving tape stripping includes assessing the bioavailability of topical formulations like eutectic mixture of local anaesthetics (EMLA)[144] in the stratum corneum and profiling dermal exposure to methacrylates found in cosmetics[145].

Tape stripping is an advantageous technique due to its simplicity, minimal invasion, cost-effectiveness and specific layers of the skin can be easily analysed[145]. However, the drawback of this method is the difficulty in reproducing results due to variation in models. The amount and thickness of layers removed depends upon the type of adhesion film also the location of the tape strip on the skin can also give varying results[146].

1.6.4 *In Vitro* Analysis

In vitro methods are conducted externally to the organism and typically involve isolated tissues, organs, or cells. The primary *in vitro* techniques employed in skin permeation research encompass flow-through systems and static diffusion cells.

1.6.5 Static-diffusion Cells

The static diffusion cell method (**Figure 1.4**) is considered as the 'gold standard' for skin permeation studies due to its simple design and cost effectiveness. A section of excised skin is positioned between an upper (donor) chamber and a lower receptor (acceptor) chamber and the extent of permeation through the tissue is quantifed[146]. The skin, whether full or split thickness, remains in continuous contact with the receptor fluid. The Franz cell is the placed within a water bath at 37^{o}C maintaining the skin temperature at 32^{o}C. The receptor fluid remains constant throughout the experiment and can be sampled at regular intervals.

Franz cell experiments are widely used to assess the permeation characteristics of various types of compounds including agrochemicals[147,148], cosmetics[149,19] and pharmaceutics[150,151]. Studies using the Franz cell approach include investigating skin permeation of methotrexate for the treatment of psoriasis[152] and transdermal delivery of galantamine for the treatment of Alzheimer's[153].

The primary advantage of Franz-type static diffusion cells lies in their relatively simple design and cost-effectiveness. Additionally, these cells offer a larger absorption area compared to other flow systems, leading to improved absorption indicators[154]. Since this method can be automated all technical difficulties can be eliminated.

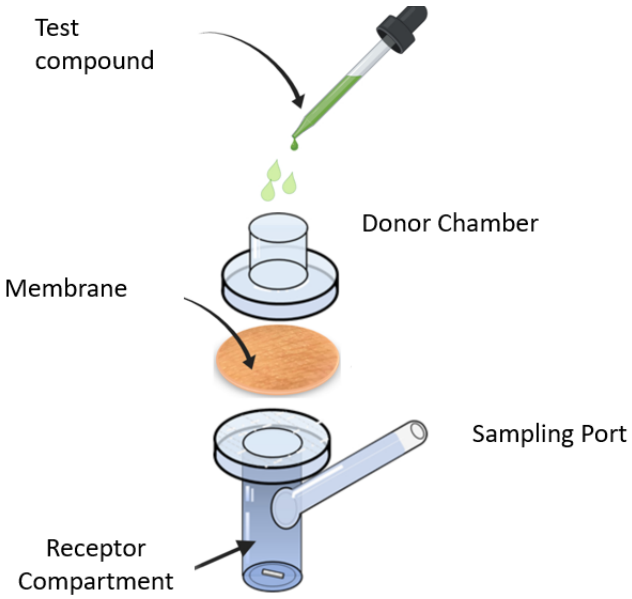


Figure 1.4: Diagram of a Franz -type static diffusion cell.

1.6.6 Flow-Through Systems

The flow-through system developed by Bronaugh and Stewart in 1985[155] (**Figure 1.5**) shares similarities with the static diffusion cell presented by Franz[156]. Where the static cell has a fixed receptor fluid system, the flow-through system continually replaces the receptor fluid and may be collected at regular intervals[157]. A key advantage of the flow-through system is its ability to mimic physiological conditions, specifically the blood circulation. This system also addresses solubility issues of compounds within the receptor fluid and maximises sink conditions[158]. However, compared to static diffusion cells, the flow-through systems are more expensive and require greater technical expertise whereas, static diffusion cells are relatively inexpensive and are simpler to operate[154].

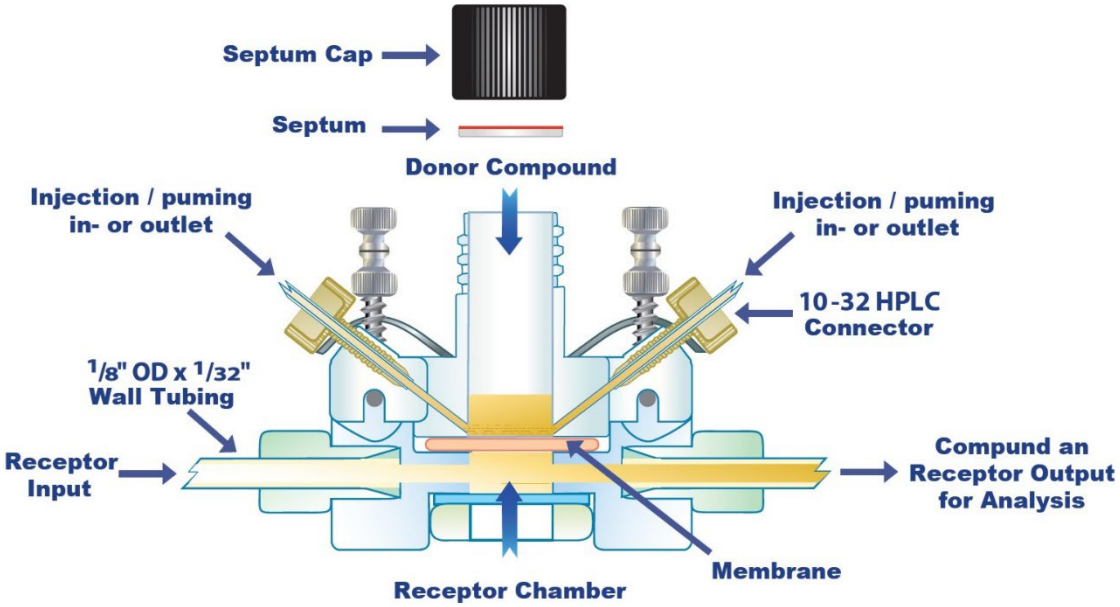


Figure 1.5: Schematic of the flow-through diffusion cell (Taken from SES[159]).

1.7 Methods for Assessing Foliar Permeation

Several techniques have been devised for evaluating the permeation of compounds through plant leaves. This short review focuses on the standard *in vivo* methods used to quantify the uptake of substances into the various layers of the leaf.

1.7.1 Assessment of *In Vivo* Foliar Permeation

Conventional methodologies for evaluating the absorption of pesticides by plant leaves primarily involve direct application onto the leaf surface via spraying methods. These approaches are considered optimal as they replicate real-world application conditions, thereby offering accurate insights into permeation characteristics. Yao *et al*[160] investigated the leaf uptake of epoxiconazole through direct spraying of the formulation. The study successfully identified the partitioning into the leaf tissue, including its retention. However, the authors observed uneven

permeation across the leaf, attributed to the deposition of the pesticide at the leaf tips influenced by aerodynamics and leaf microstructure.

Numerous studies[161,162,163] have employed leaf disc assays for the evaluation of the absorption for various compounds into the leaf. Leaf discs are extracted from plant leaves and placed on a solution containing the test substance. The solution is periodically sampled, and the concentration of the substance is subsequently analysed over time[164]. This method is advantageous due to its cost-effectiveness and simplicity, enabling high-throughput screening of various treatments or conditions. However, the leaf disc environment may not accurately replicate real-life conditions resulting in the unreliable permeation characteristics. Additionally, the cutting of the plant leaves may induce undesired wounding stress which may not faithfully reflect the plant's response to a specific treatment.

The static diffusion cell method (**Figure 1.4**) can also be adapted for foliar permeation studies due to its simple design and cost effectiveness. A section of plant leaf can be placed between a donor and receptor chambers and the extent of permeation through the tissue is quantifed[156]. The receptor fluid remains constant throughout the experiment and can be sampled at regular intervals.

The agrochemical industry heavily utilises this methodology[165,166,28] for pesticide absorption into leaf tissues owing to the many benefits it possesses. The primary advantage of Franz-type static diffusion cells lies in their relatively simple design and cost-effectiveness. Furthermore, these cells provide a larger absorption area compared to other flow systems, resulting in enhanced absorption indicators [154]. Automation of this method helps eliminate reduce technical difficulties.

1.7.2 Analytical Methods for Assessing Foliar Permeation

Current methodologies for the evaluation of the uptake of pesticides through plant leaves necessitate laborious and time-consuming organic solvent extraction or mechanical stripping prior to analysis. The extracted material is typically analysed using chromatographic mass spectrometry analytical techniques[28,167,168], providing excellent identification and quantification, however, all information regarding the distribution of key species both laterally and as a function of depth is lost. A combination of FTIR[169,170,171] and Raman spectroscopy[172,173,174] is a staple for non-destructive and relatively quick chemical and structural analysis unfortunately, FTIR techniques are limited to the identification of functional groups with limited information regarding chemical structures. Similarly, Raman spectroscopy can be significantly affected by fluorescence naturally emitted by biological samples. Here the weak Raman scattering signal can be overwhelmed by the strong fluorescence as a result, significantly reducing sensitivity and reliability of measurements[175].

Liquid scintillation[176] is a popular method employed in the agricultural sector for the evaluation of the uptake of foliar permeation of agrochemicals. The underlying principle involves the measurement of low-energy radioisotopes, predominantly alpha and beta emitting isotopes. The methodology enables automation, rapid qualitative analysis with high sensitivity[177]. Nevertheless, challenges associated with this technique include the requirement of radiolabelling[178], influencing permeation characteristics. Additionally, the sample preparation is time consuming and quenching effects can affect the accuracy of the data[179].

Currently, there exists a deficit in analytical methodologies for assessing the foliar absorption of compounds, particularly those offering label-free, *in situ* permeation analysis without the reliance on radiolabelling or complex sample preparation such as solvent extraction.

1.8 Analytical Methods for Assessing Skin Permeation

Numerous analytical techniques can be paired with skin permeation studies for further quantification of compounds. Conventional chromatographic techniques for example high performance liquid chromatography (HPLC) and more recently, LC-MS methods have been employed for testing various compounds. The selection of a specific technique depends heavily on the nature of the compound under investigation and the type of data required.

1.8.1 Chromatographic Techniques

Liquid chromatography coupled with UV-Visible (UV-Vis) spectroscopy is widely employed for investigating skin permeation. HPLC stands out as a valuable method, delivering fast quantitative results with relative ease and inexpensively. Its application in skin permeation studies facilitates the determination of absolute concentrations in receptor fluids. However, since the analyte is required to be within solution, extraction or full recovery is required for samples like tape strips. The extraction of analytes presents drawbacks involving additional steps, contamination and the loss of spatial resolution of the analyte within the skin layers[146].

In order to obtain the necessary sensitivity, and precise determination of analytes, a strong chromophore is essential. This is a region within the molecule that absorbs

light strongly in the UV-vis region, allowing accurate detection/identification using a UV detector. Alternatively, molecules may need isotopic labelling or fluorescent tagging. It is also important to note the addition of a fluorescent tag may modify the physiochemical properties of the test compound and have a direct effect on permeation characteristics[146].

The UV detection system can also be replaced with a mass spectrometer (MS) to provide quantitative results however in contrast to HPLC, LC-MS isolates analytes by physical separation of the target compound in combination of their mass-based detection. In addition, the structural determination of a molecule can be deduced using the combination of fragmentation patterns and molecular ions (m/z).

Extensive skin permeation research in pharmaceutics[180,181,182] cosmetics[183,184], anti-microbials[185,186] and agrochemicals[148,187] has been conducted using HPLC as the analytical technique. Nielsen *et al*[188] effectively examined the impact of molecular weight and solubility of the percutaneous permeation of five pesticides using a combination of Franz cells and HPLC. However, limitations were observed in the HPLC method when attempting depth profiling, and spatial distributions were unattainable due to the constraints of the extraction procedure employed.

1.8.2 Spectrophotometry Imaging Techniques

In contrast to chromatographic methods, imaging techniques have the potential to offer crucial insights into the spatial distribution of compounds, such as agrochemicals, within the different layers of the skin. These methods can provide valuable information about the mechanisms of penetration and distribution within the tissues.

Two-photon microscopy (illustrated schematically in **Figure 1.6**) is a relatively 'young' fluorescence imaging technique in skin permeation research, operating *via* the two-photon absorption concept. In this model, two photons are used to excite electrons from a ground state to an excited state[186]. This technique has been employed over the years for various types of research including imaging the *stratum corneum* pH gradient and investigating the permeation characteristics and impact of xylitol on lipid dynamics within the skin[189,190]. Two-photon microscopy is a valuable technique since it is non-destructive as skin samples can be studied without cryofixation and cutting. Additionally, the possibility of photo-bleaching and photo-damage is decreased, since the two-photon excitation occurs at small focal volumes on the fluorophores[146]. However, this technique is limited to molecules with a strong fluorophore otherwise, fluorescent tagging may be required. Tagging with fluorescent dyes can change the physicochemical properties of compounds and affect permeation characteristics. Regarding agrochemicals, the compounds generally do not exhibit strong fluorescence therefore, detection within skin compounds may be hindered. DiScenza *et al*.[191] addressed this challenge in their study by employing cyclodextrin tags. However, it is important to note that this approach may impact skin permeation characteristics. Consequently, the use of alternative analytical techniques might be necessary to ensure accurate assessments.

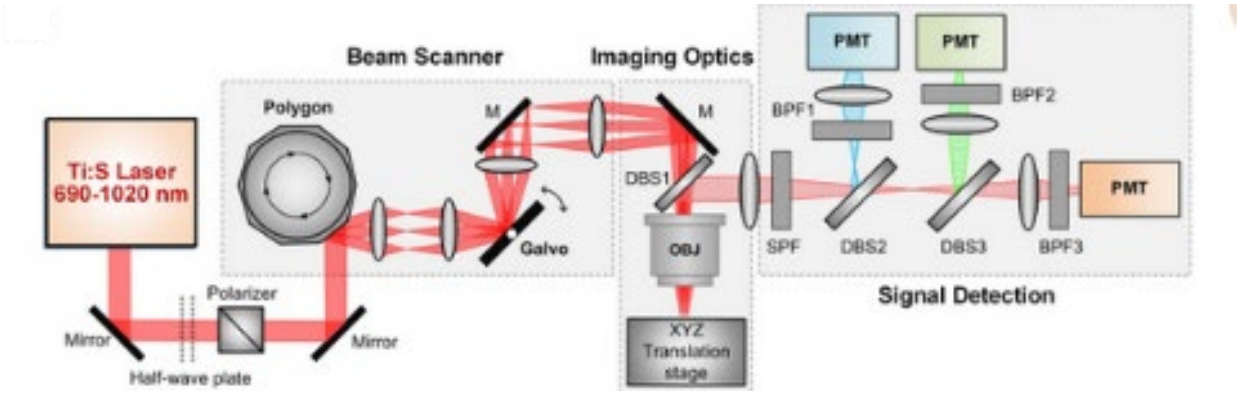


Figure 1.6: Diagram of two-photon microscopy for imaging skin samples. OBJ, Objective lens; SPF, single band pass filter; DBS, dichroic beam splitter; BPF, band pass filter; PMT, photomultiplier tube. (Taken from Ahn et al[192]).

Raman scattering microscopy is a label-free imaging tool with the ability to provide three-dimensional images of biological samples with high resolution, fast acquisition rates and in a non-destructive manner. Although this analytical method has not been employed for the study of agrochemical skin penetration, it has been utilised to visualise the penetration of drug molecules[193] and cosmetics[194]. A study conducted by Saar *et al*[195] was able to directly visualise the distinct penetration pathways of ketoprofen and ibuprofen with the deduction of differences in the kinetic behaviours between the two routes. Moreover, Tippavajhala[196] was able to characterise the percutaneous penetration of sunscreens in the *stratum corneum*, up to 10 µm in depth and conveyed the distribution characteristics of the compound in real time. Raman spectroscopy is an advantageous technique due to its non-destructive characteristics however, since Raman signal is generally weak it can be masked by fluorescence emitted by biological tissue. Therefore, it is vital the molecule of interest is of enough concentration to allow accurate visualisation[197].

1.9 Mass Spectrometry Imaging Techniques

Mass spectrometry imaging (MSI) techniques have been used extensively for the evaluation of skin permeation of various compounds including drugs[17,198,199] and cosmetics[20,126]. These techniques offer significant advantages over chromatographic and spectroscopic methods. Enabling the visualization of spatial distribution of molecules by scanning molecular masses without requiring fluorescent labelling. This allows for the mapping of molecules within different layers of the skin with high selectivity and specificity.

1.9.1 Time-of-Flight Secondary Ion Mass Spectrometry (ToF-SIMS)

Time-of-Flight Secondary Ion Mass Spectrometry (ToF-SIMS) stands out as a highly sensitive (detection threshold below 0.1 μm) and provides exceptional spatial resolution (less than 1 μm). This vacuum-based surface analytical technique has been effectively employed for the analysis of diverse biological compounds[127].

ToF-SIMS employs a pulsed primary ion beam typically Cs or Ga, bombarding the surface of a sample inducing a fragmentation cascade. This collision cascade results in the production of 'sputtered material' which are neutral ions that are desorbed and not analysed[127]. Whereas the ionised species are accelerated *via* a flight tube to the detector portrayed in **Figure 1.7**. The mass of the ionised species is determined by measuring the time at which they reach the detector. The ToF-SIMS apparatus can map the ions in 2D and 3D, if the incident beam is focussed across the entire surface of the sample a chemical (ion) map can be obtained[200].

a **b**

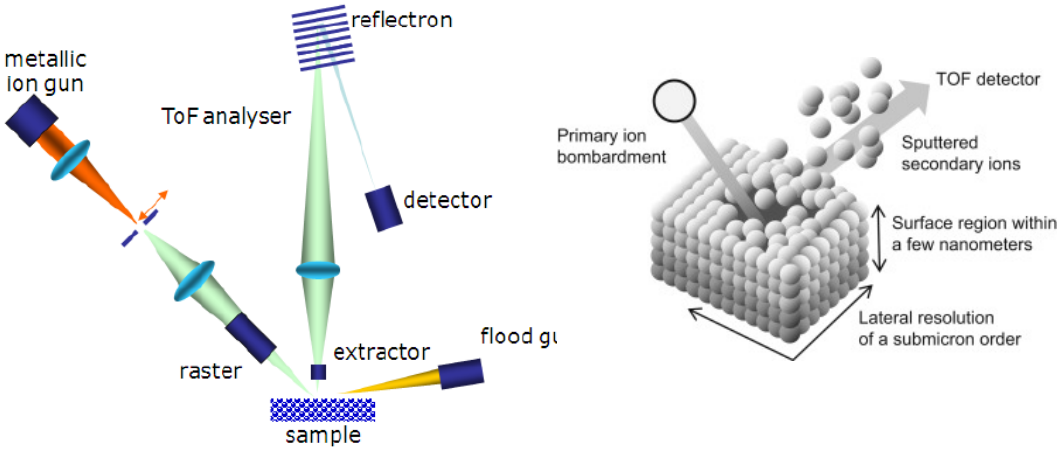


Figure 1.7: Schematic representation of the ToF-SIMS **(a)** apparatus and generation of secondary ions **(b)** (Taken from Mazel et al and Aoki et al[201,202]).

1.9.1.1 Applications of the ToF-SIMS

The utilisation of ToF-SIMS on skin samples aims to visualise the spatial distribution of both exogenous and endogenous skin compounds with high spatial resolution and chemical specificity. An early attempt to map an active substance in skin was undertaken by Judd et al[203], focusing on the distribution of chlorohexidine within the skin. The approach demonstrated the delivery of chlorhexidine into the upper layers of the *stratum corneum* with very limited to no permeation into the underlying epidermis. However, the investigation focussed on a small fragment ($C_7H_4N_2Cl^-$) of the compound rather than the molecular ion due to sensitivity issues inherent to the ToF-SIMS and the increased fragmentation caused by the liquid metal ion gun (LMIG). The inability to detect the molecular ion within the skin represents a significant limitation, as this can significantly reduce the sensitivity of the analysis and, consequently, offer restricted insight into permeation behaviour.

ToF-SIMS has also been applied to evaluate the chemical structure of skin[204,205]. A notable publication from Starr *et al*[206] delved into the metabolomics of the *stratum*

corneum, exploring the lipid composition and age-related changes to the architecture. Key components of the *stratum corneum* were identified including the relatively abundant fatty acids, lignoceric acid (C24:0) and hexacosanoic acid (C26:0). Starr *et al* were able to confirm the increase in intensity of these compounds in post-menopausal women suggesting, an increase in overall fatty content with intrinsic aging. Additionally, the authors were able to reveal the chemical maps of the major epidermal component, cholesterol sulfate. The secondary ion maps revealed the non-uniform distribution of the compound showcasing, the non-homogenous increases with photoaging. The significant limitation of the study was the extensive fragmentation caused by the Bi_3^+ LMIG, leading to the generation of smaller fragmented ions that were challenging to unequivocally identify. The Bi_3^+ ion beam lacked the sufficient mass resolving power (ability to differentiate between to adjacent peaks) to distinguish between the many structurally similar *stratum corneum* lipids.

In terms of the agrochemical field, ToF-SIMS is a relatively unexplored technique however recent research conducted by Converso[207] successfully profiled a number of biocidal active ingredients (44 compounds) including herbicides, insecticides and fungicides. Only 15 out of the 44 compounds could be identified as molecular ions, while the remaining compounds were observable as solely fragments, posing a significant challenge for confident assignment. In addition, many compounds produced negligible signal at the concentration (1000 to 0.1 pg nL^{-1}) they were tested. Once again, the Bi_3^+ LMIG induced excessive fragmentation leading to heightened sensitivity and resolution issues.

Moreover, Cliff et al[208] attempted to detect chlorinated pesticides, lindane on the surface of fungi. Although, there has been various research conducted for the direct analysis of agrochemicals and evaluation of pesticide penetration into leaf cuticles[209] using ToF-SIMS, there is insufficient data for skin permeation. Thus, this technique could be utilised for evaluating the permeation characteristics and spatial distribution of agrochemicals within skin.

As displayed by **Figure 1.8**, it is evident ToF-SIMS has been applied to evaluate the percutaneous penetration of various topical formulations. A notable study from Al-Mayahy *et al*[17] studied the penetration of imiquimod, highlighting the skin depth and lateral distribution of the compound within the layers of skin. **Figure 1.8(a)** depicts ToF-SIMS analysis of tape strips of imiquimod treated skin, as witnessed the authors were able to distinguish the localisation of the drug within the *stratum corneum* and observe lateral permeation. In terms of agrochemical skin permeation, there have been no notable publications investigating the skin and lateral depth distributions of formulations however, the utilisation of ToF-SIMS can aid in defining the mechanisms of skin penetration.

Sjovall *et al*[60] examined the distribution of skin lipids and the effect of topically applied compounds on their physicochemical properties. As portrayed by **Figure 1.8(b)** the authors successfully imaged a variety of molecular species from the *stratum corneum* to the dermis. The authors highlighted the distribution of ceramides and fatty acids within the *stratum corneum* and cholesterol sulfate in the epidermis. Furthermore, the authors were able to provide details on the effects of topically applied carvacrol to the endogenous compounds in skin. The ability to

assess the spatial distribution of compounds within skin in addition to the effects of the permeation of compounds on the exogenous species within skin is beneficial to understand the toxicities and mechanisms of delivery of pesticide formulations.

Other publications (presented in **Figure 1.8 (c)(d)**) have also successfully obtained 3D skin permeation profiles of compounds within the skin layers including, chlorohexidine[210] and pseudo-ceramides[19]. As Holmes *et al*[210] has demonstrated the ability to evaluate permeation enhancers is highly advantageous for the assessment of the uptake of agrochemicals since, the effects of co-formulants including solvents and emulsifiers on active ingredients can be reviewed.

Although the ToF-SIMS proves to be a viable tool for the *in situ*, label-free imaging with relatively high sensitivity and exceptional resolution, the approach possesses significant drawbacks. The employment of liquid metal ion guns induces excessive fragmentation leading to the non-detection of molecular ions and large biomolecules. Furthermore, the small high energy ion beams are adept at deciphering the lateral distribution of *in situ* key compounds but less suitable for depth profiling. The high energy ion beams are susceptible to channelling effects, causing significant sub-surface damage. The insufficient mass resolving power (>12000) of the technique poses a challenge, making it difficult to distinguish between similar ions.

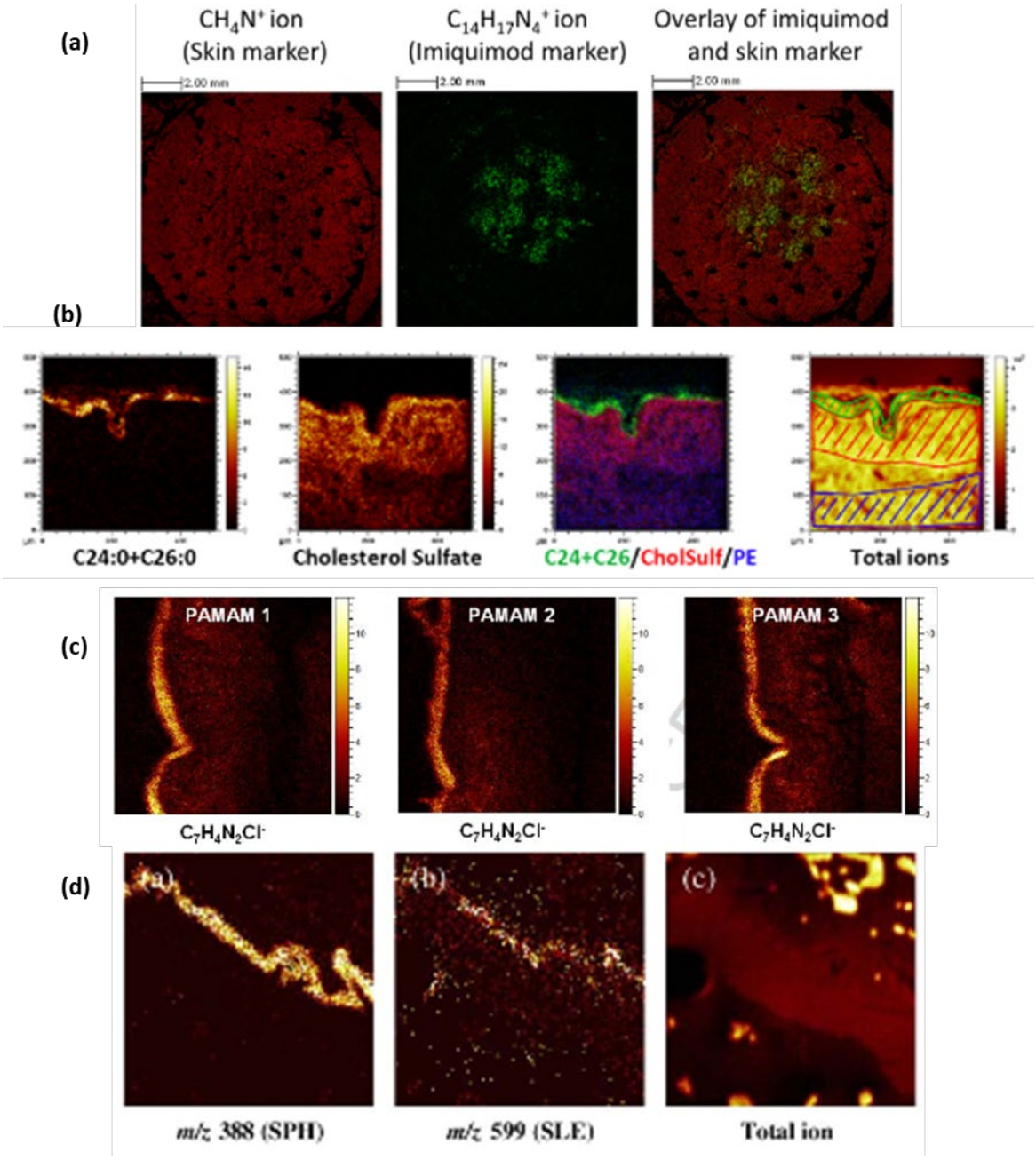


Figure 1.8: ToF-SIMS imaging data highlighting the distribution of various compounds within skin. **(a)** ToF-SIMS images illustrating the distribution of imiquimod in human skin. **(b)** Negative ion ToF-SIMS data of the dermis showing the distribution of lipids within the skin layers. **(c)** Secondary ion images of chlorohexidine and PAMAM dendrimers within porcine skin. **(d)** ToF-SIMS analyses of ceramides from cross sections of the epidermis. Adapted from:[17,60,19,210]

1.9.2 OrbiSIMS

The OrbiSIMS technique[30] is the next development in the area of secondary ion mass spectrometry (SIMS), based on the ToF-SIMS platform however, hybridised with an Orbitrap™ mass analyser. This detection system operates by employing electrodynamic confinement to capture ions, subsequently inducing their oscillation around a central electrode. The frequency of these oscillations correlates directly with the mass-to-charge ratio of the ions. Utilising Fourier-transform techniques, the resultant frequencies are converted into mass spectra. This label free mass spectrometry imaging technique combines the high spatial resolution of SIMS with the high mass resolving power of an Orbitrap™, allowing the visualisation of exogenous and endogenous compounds at a subcellular resolution.

As depicted by the schematic presented in **Figure 1.9**, the OrbiSIMS is based on the ToF-SIMS platform which is hybridised with an Orbitrap™ mass analyser. The hybridisation offers higher mass accuracy (1 - 2 ppm), high sensitivity (10^5 for ratio of total ion counts to noise) and high mass resolving power (up to 480,000 at m/z 200)[30]. A primary ion beam consisting of gas clusters (GCIB) is used to remove monolayers of cells with precision in the Z-direction. Moreover, the ion source can also be equipped with bismuth metal liquid ion gun giving the ability to achieve resolutions as low as 200 nm. An electrostatic deflector placed at 90^o allows switching between time of flight and Orbitrap mass analyser[211]. The time of flight mass analyser allows for fast scans at relatively low mass resolving power. Conversly, the Orbitrap™ analyser allows for high resolution scans albeit at lower acquisition rates.

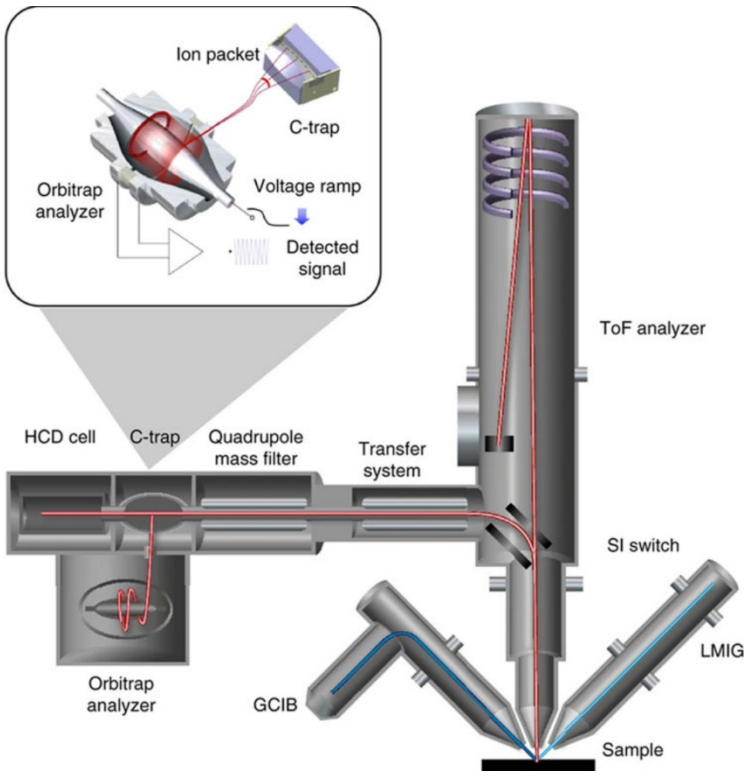


Figure 1.9: Schematic diagram of the OrbiSIMS spectrometer (Taken from Aoki et al[202]).

1.9.3 Applications of OrbiSIMS

Passarelli *et al*[30] demonstrated the advantages and adaptability of OrbiSIMS by visualising and mapping the subcellular localisation of sulfoglycosphingolipids and glycerophospholipids in mice hippocampus with a spatial resolution of under 2 µm. Moreover, by single cell metabolomic profiling of mice macrophage cells shown in **Figure 1.9.1**, the visualisation of the upregulation of amiodarone was possible with great confidence. The high spatial resolution is advantageous for the analysis of pesticide formulations as this can help in the differentiation between the chemically similar constituents of the formulations.

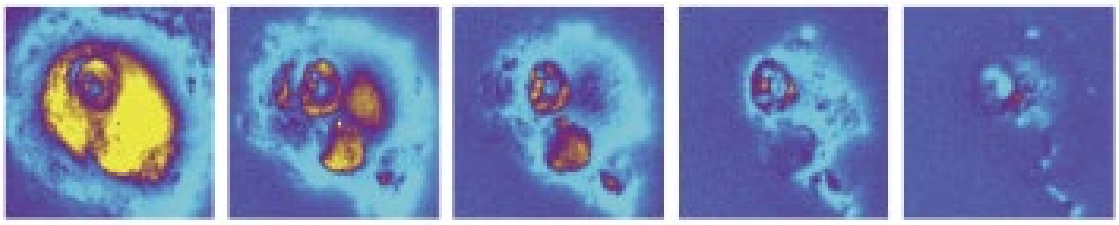


Figure 1.9.1: OrbiSIMS images of rat alveolar macrophage cell at 400 nm depth incubated with amiodarone (Taken from Passarelli et al[30]).

Aoyagi *et al*[212] employed OrbiSIMS to study the compartmentalisation and distribution of endosymbionts including biomolecular interactions within *C. variabilis.* Using conventional methods, studying molecular composition within *C. variabilis* was difficult due to the fragile nature of the membrane however, the utilisation of OrbiSIMS allowed the analysis without any damage to the sample. As depicted by **Figure 1.9.2**, sputtering with an argon gas cluster ion beam, Aoyagi was able to deduce the identity and distribution within the perialgal vacuole of *C. variabilis* without damaging the sample.

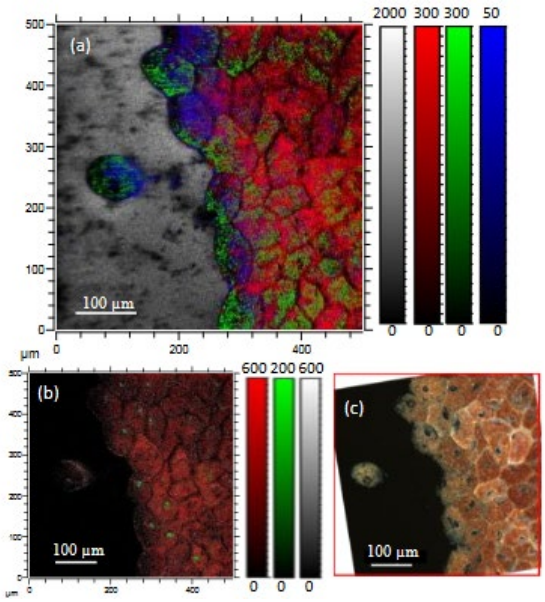


Figure 1.9.2: OrbiSIMS images of the perialgal vacuole of C. variabilis containing various metabolites including: chlorophyll (green), phosphocholine (red) and peptide markers (grey). (Taken from Aoyagi et al [212]).

A study presented by Zhang *et al*[213] employed OrbiSIMS to visualise the spatial distribution of signalling molecules, nucleobases and bacterial membrane molecules in *P. aeruginosa* biofilm. As depicted in **Figure 1.9.3**, 97 different compounds were identified including lipids and nucleobases with high spatial-resolution and high mass-resolution. By using cryo-OrbiSIMS the problem of water condensation on the sample surface was averted allowing better resolution and specificity. The cryo-OrbiSIMS technique would be advantageous in pesticide analysis featuring higher spatial and mass resolution. Additionally, this technique prevents the chemical redistribution of lipids and other artifacts, while reducing the risk of cell membrane rupture and tissue damage through the formulation of water crystals, ultimately enhancing the precision of analyses.

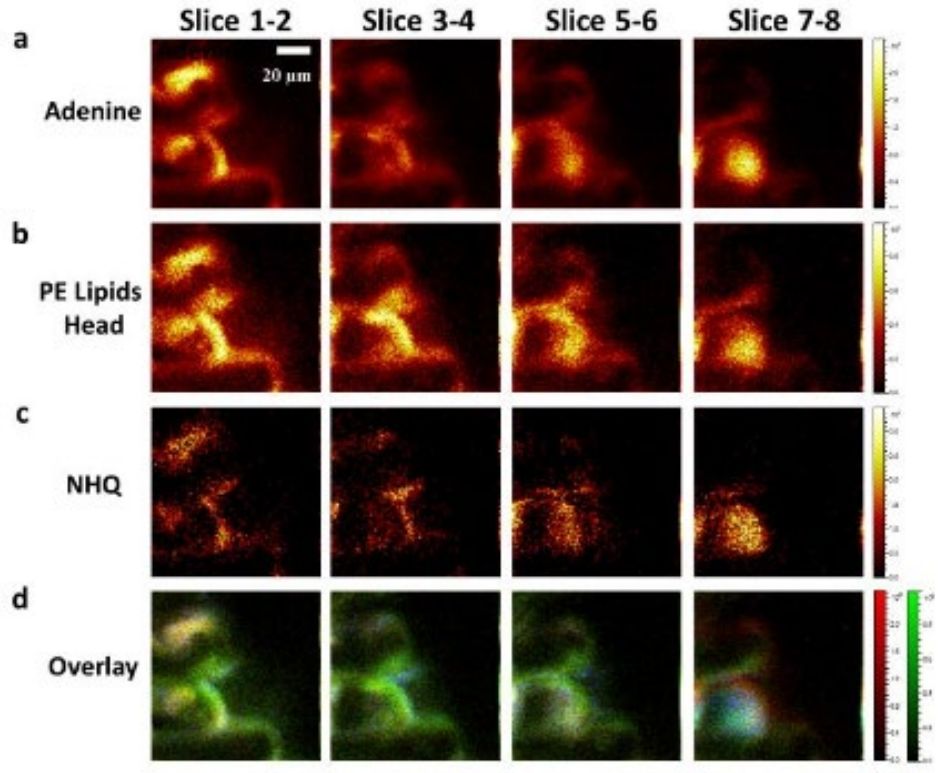


Figure 1.9.3: OrbiSIMS images of P. aeruginosa biofilm deducing the spatial distribution of adenine, PE lipids and 2-nonyl-4-hydroxyquinoline (NHQ). (Taken from Zhang et al[213]).

The utilisation of large GCIBs opens up the opportunity for conducting depth profiling of samples, offering insights into the *in situ* depth distributions of compounds within the sample. Kotowska *et al*[214] facilitated the *in situ* imaging and depth profiling of peptides in human skin samples, showing the depth distributions of keratin, collagen and corneodesmosin (**Figure 1.9.3**). The ToF-SIMS Bi_3^+ approach was flawed, yielding single amino acid secondary ions while the Ar_{3000}^+ ion beam generated larger peptide fragments. The application of the GCIB minimised the sub-surface damage to the sample, enabling the detection of the localisation of these peptides in the various layers of the skin. It was revealed corneodesmosin, keratin and collagen were situated in the *stratum corneum*, epidermis and dermis, respectively.

OrbiSIMS can prove to be a vital tool, with the ability to not only provide information about the spatial distribution of molecules inside the skin layers but also deduce the mechanisms of penetration. ToF-SIMS shows great promise for the assessment of the *in situ* and label-free skin permeation of compounds however falls shorts with inherent issues highlighted in previous studies[206, 207, 60] including, excessive fragmentation by the Bi_3^+ ion beam, insufficient mass resolving power and difficulties to depth profile due to sub-surface damage.

The OrbiSIMS hold the potential to address the limitations of the ToF-SIMS, boasting a higher mass-resolving power of >240,000 at m/z 200 and mass accuracy of <1 ppm. Prior investigations[212, 215, 214] highlight, this approach overcomes numerous drawbacks associated with alternative methods including, the necessity for solvent-based extraction procedures required for HPLC/LC-MS approaches, the

elimination of isotopic labelling necessary for spectrophotometry and the excessive fragmentation and mass resolving power associated with ToF-SIMS.

The OrbiSIMS, as a relatively recent analytical method, has not been employed extensively for generating permeation profiles of compounds. The dermal absorption of agrochemicals is a relatively unexplored domain, and the utilisation of OrbiSIMS to deduce the spatial distribution of pesticides represents uncharted territory.

The employment of the OrbiSIMS has the potential to build on our existing understanding of the chemical architecture of skin and leaves. With the utilisation of the Ar_{3000}^{+}, larger biomolecules can be preserved, and the enhanced mass resolving power may facilitate the differentiation of compounds with similar structure. Similarly, the OrbiSIMS holds promise in providing crucial insights into the dermal absorption of agrochemical formulations, thereby contributing to improved pesticide development with minimised exposure risks to agricultural workers.

Chapter 2. Elucidating the molecular landscape of the *stratum corneum*

Disclaimer: The contents of this work reflect a collaborative effort involving multiple contributors. Each contributor has played a distinct role in the conception, execution, and refinement of the presented work. My contributions are demonstrated in the native skin analysis and molecular assignment for the key endogenous species. Additionally, my involvement extends to the dermal peptide delivery including Franz cell and OrbiSIMS analysis.

2.1 Abstract

Characterization of the molecular structure of skin, especially the barrier layer, the stratum corneum, is a key research priority to generate understanding to improve diagnostics, aid pharmaceutical delivery and prevent environmental damage. Our study uses the recently developed 3D OrbiSIMS technique to conduct in situ analysis of ex vivo human skin tissue and reveals the molecular chemistry of skin in unprecedented detail, as a result of the step change in high mass resolving power compared to previous studies. This characterization exposes the non-homogeneity of the stratum corneum, both laterally and as a function of depth. Chemical variations relating to fundamental biological processes, such as the epidermal cholesterol sulfate cycle, are visualized using in situ analysis for the first time. We are able to resolve the debate around the chemical gradients present within the epidermis, for example, whether palmitic acid is of sebaceous origin or a true component of the stratum corneum. Through in situ depth analysis of cryogenically

preserved samples, we are able to propose that it is actually a component of both surface sebum and the intrinsic lipid matrix. This approach also confirms a high degree of similarity between the epidermis compounds found in human and porcine skin as a function of depth. Since porcine skin is a widely used model for testing within the pharmaceutical sector, this result has significant clinical relevance. In addition to endogenous species, we have also used this technique to demonstrate the permeation of a commercially important anti-aging peptide into human stratum corneum. Due to its chemical similarity to native skin components and exceptionally low effective concentration, this information was previously unattainable.

Significance Statement

Skin is recognized as an intricate assembly of molecular components, which facilitate cell signaling, metabolism and protein synthesis mechanisms in order to offer protection, regulation and sensation to the body. Our study takes significant steps to characterize in more detail the complex chemistry of the skin, in particular generating a better understanding of the uppermost layer, the stratum corneum. Using a state-of-the-art 3D OrbiSIMS technique we were able to observe the depth distribution, in situ, for a wide range of molecular species. This unprecedented molecular characterization of skin provides understanding that has the potential to benefit research into fundamental processes, such as those associated with skin aging and disease, and the development and delivery of effective topical formulations.

2.2 Introduction

The skin is described using its three distinct layers, the hypodermis, dermis and epidermis. The outermost layer, the epidermis, is chemically complex and contains five sub-layers, defined by the differentiation stage of keratinocyte cells. The uppermost sub-layer, the *stratum corneum* (*SC*), is the body's primary defense against the environment, despite an average thickness of only 20 cell-layers[216]. This protective role includes the regulation of water and heat loss, resistance against mechanical stress, the prevention of xenobiotic permeation and protection against UV exposure. Once thought to act as a physical barrier of 'dead' corneocyte cells, it is now recognized that the surrounding lipid matrix acts as a sophisticated 'biosensor', regulating metabolic activity in response to external stimuli[42,43,6]. This lipid matrix is unique among biological membranes, both in terms of composition and organization, and it is known that these lipids act as bioactive compounds in numerous cellular processes. However, the mechanisms behind these regulatory processes and the involvement of individual lipid species are still not fully understood[6]. Improving the molecular characterization of the *SC* is therefore at the forefront of current skin research, to provide the basis to enable better diagnostics, improve pharmaceutical delivery and enable strategies to reduce environmental damage.

It is widely acknowledged that the main lipid classes present in the *SC* matrix are ceramides, free fatty acids and cholesterol, cholesterol sulfate and cholesterol esters[216]. Unlike the underlying epidermal layers, the *SC* contains almost no

phospholipids, as their depletion accompanies the differentiation of the keratinocyte cells, known as cornification, which creates the skin's physical barrier. Although the main components are known, the exact composition of this lipid matrix is continually being updated through ongoing research. To date, 17 subclasses of ceramide have been recognized in human *SC*[217], with Laffet *et al*. recently demonstrating the identification of 1000 different ceramide molecules from human and porcine *SC*[52]. Free fatty acids exist as both saturated and unsaturated compounds, with 30 different species currently detected with chain lengths ranging from 14 to 34 carbon atoms. Of these, lignoceric and hexacosanoic acid (C24:0 and C26:0) have been demonstrated to be the most abundant[53,51]. In addition to this complex mixture, the *SC* is also populated with compounds relating to both surface sebum and a mix of hygroscopic species termed natural moisturizing factor (NMF). These compounds play a key role in the hydration of the skin[218,55]. Sebum, secreted onto the surface through sebaceous glands, is known to contain triglycerides, wax esters, free fatty acids and squalene, with smaller quantities of cholesterol and cholesterol esters also present[219,220]. Enzymatic degradation of the binding protein filaggrin results in *SC* localization of free amino acids, notably histidine, glutamine, arginine, and their derivatives, urocanic acid, pyroglutamic acid or 2-pyrrolidone-5-carboxylic acid (PCA) and urea/ornithine respectively[55,221].

Given the complex nature of the *SC* it is unsurprising that imbalances within this chemical matrix have been associated with numerous biological changes, including aging[206,222,223], UV damage[206,222,224,225], and multiple skin disorders[43,226,51,227] (3, 20-

23). Different analytical techniques have been employed to investigate the *SC*, most notably chromatographic mass spectrometry[51,228]. However, although this technique enables accurate identification and quantification of biological molecules, it relies on the physical separation of individual skin layers, followed by successful extraction of the compounds of interest. This is not only time consuming, but much information regarding the distribution of key species within the *SC*, both laterally and as a function a depth, is lost. This means that, for most analytical studies, the chemical composition of the *SC* is assumed to be homogenous. The use of tape stripping as a sampling method, removing individual corneocyte layers for analysis, can be used to circumvent this issue. Yet, this method of sampling can be subject to large variabilities and requires the strict control of multiple parameters[143]. Limited instrument sensitivity can also dictate that strips need to be pooled for analysis, causing a loss of depth resolution.

Time-of-flight secondary ion mass spectrometry (ToF-SIMS) offers an advantage over other techniques as it can provide *in situ* analysis with minimal sample preparation, whilst still offering high chemical sensitivity and specificity. Another unique feature of this technique is its ability to probe compound distribution both laterally and as a function of sample depth, through either surface or depth profile analysis modes down to a microscopic scale for molecular characterization. It is therefore becomingly increasingly popular for skin tissue analysis, with numerous groups demonstrating the effectiveness of this technique to analyze both native

and exogenously altered skin samples, including analysis of tape stripped SC, cross sections and *ex vivo* full thickness skin[206,20,229,60,230,17,231,203].

A small number of analytical studies, using various instrumentation, have demonstrated a change in lipid composition with epidermal depth[206,229,232,233,234,] (15, 27, 33-35), suggesting that the assumption that the lipid matrix is homogeneous is an oversimplification. However, all of these suffer from limited depth resolution or lipid specificity. The most comprehensive analysis carried out using ToF-SIMS was by Sjövall *et al.* in 2018[60], imaging a cross sectioned skin sample to reveal the 2D spatial distribution of a variety of molecular species and highlight their localization within the main skin layers. However, due to limitations with the time of flight SIMS instrumentation, the presence of subtle chemical gradients, in particular within individual skin layers, remains unexplored.

In order to address the lack of insight into the 3D molecular landscape of the SC, we have exploited the improved capabilities of the recently developed 3D OrbiSIMS profiling technique using a Hybrid SIMS instrument (IONTOF GmbH)[30]. This instrument combines traditional ToF-SIMS with Orbitrap™ mass spectrometry and as a result can offer significant analytical advancements for biological analysis compared to previous ToF-SIMS instruments. The exceptional mass resolution (>240,000) and mass accuracy (< 1 ppm) enables unique biological molecule identification of large diagnostic molecular fragments, generated by a low-energy argon gas cluster primary ion beam. In addition, the ability to conduct this analysis on samples maintained in a cryogenic state is hugely important, to preserve the

native state and improve the detection of biomolecules[235,213]. The *in situ* analysis employed in SIMS, combined with gas cluster etching to generate depth profile analysis, is ideally suited to 3D characterization of skin and has allowed us to delineate the chemical composition of human *SC,* revealing previously unreported trends in the chemistry of this important sensory skin barrier.

2.3 Materials and Methods

2.3.1 Skin Acquisition

In our study *ex vivo* porcine skin refers to full thickness skin taken from the posterior ear tissue of 6 month old pigs (full method in SI) and *ex vivo* human skin refers to full thickness skin tissue that was purchased from Tissue Solutions (www.tissue-solutions.com). Skin tissue was obtained from three different Caucasian female donors, between 35 - 70 years old, all non-smokers, removed during cosmetic surgery. The specific details of each donor can be found in the supplementary information (**Table S9**). The tissue was frozen immediately post-surgery, shipped and stored at – 20 °C prior to use. It is to be noted, the human skin was obtained with all ethical considerations and the approval of the Human Tissue Authority.

Skin samples were also collected *ex vivo* from the flexor forearms of one healthy volunteer, who participated after providing consent and confirming they were free from skin conditions and medication. In order to remove individual layers of the *SC*, tape stripping experiments were performed using D-Squame skin sampling discs (CuDerm, Dallas, TX, U.S.A.). The circular discs had a diameter of 22 mm and used a

fully cured medical grade synthetic polyacrylate ester adhesive. The disc was applied to the skin, a constant pressure was applied using a pressure disc applicator (CuDerm), and the disc was removed in one fluent motion. Consecutive tape strips were taken to remove individual corneocyte layers, with strip 1 specified as the uppermost layer of the *SC*. Samples were stored at −20 °C prior to analysis.

2.3.2 3D OrbiSIMS Single Beam Depth Profile Analysis of *ex vivo* Skin

For the analysis of frozen hydrated skin samples, the skin samples were first introduced into the airlock on the cryo stage of the instrument. This was flooded with Argon gas and the cooling process initiated. Once the stage had reached - 80 °C, the vacuum pump was initiated, which accelerated the cooling process and brought the stage, and consequently skin, temperature down to -170 °C. During both the vacuum transfer and the analysis, the sample was maintained at this temperature using a novel closed-loop liquid nitrogen pumping system (IONTOF GmbH), which allowed stable cryo operation for more than 24 h, with a single dewar filling. The depth profiling settings were as follows: An Ar_{3000}^{+} analysis beam with an energy of 20 keV and diameter of 20 µm was used as the primary ion beam. The duty cycle of the beam was set to 4.4 % and the GCIB current was 250 pA. The depth profile was run on an area of 200 × 200 µm using a sawtooth raster mode with crater size 280 × 280 µm. The cycle time was set to 200 µs. Optimal target potential varied for different samples, averaging at approximately +/- 384.5 V. Depth profiles were collected in both positive and negative polarity, in the mass range 75 – 1125 *m/z* and the injection time was set to 500 ms. Mass-resolving power was set to 240,000 at 200 *m/z*.

All data analysis was carried out using Surface Lab 7.1 (IONTOF GmbH). Using the software, some depth profiles have been compressed using a running average method (100 data points), where the individual data points represent the secondary ion intensities for a selected mass peak at subsequent depths of the sample. Where this has been done it has been confirmed in the figure caption.

2.3.3 3D OrbiSIMS Analysis of Individual Corneocyte Layers Permeation analysis.

For permeation analysis, consecutive tape strips from healthy volunteers were used. 3D OrbiSIMS analysis was performed on a hybrid instrument (IONTOF GmbH) instrument. For the acquisition of 3D OrbiSIMS permeation analysis, a 20 KeV Ar_{3000}^{+} analysis beam with a diameter of 20 µm was used as primary ion source. Samples were analyzed at room temperature across a 400 × 400 µm area in positive polarity with sawtooth raster mode and a crater size of 486 × 486 µm. Ar_{3000}^{+} primary ions were used with a target current of 230 pA with charge compensation performed using a low energy (20 eV) electron flood gun. Duty cycle was set to 4.4 % and cycle time to 200 µs. Argon gas flooding was in operation to aid with charge compensation, which led to a pressure of 9.0 × 10−7 bar in the main chamber. Optimal target potential was at approximately +130 V at average. Mass spectra were recorded at a resolution of 240 000 at m/z 200 in the mass range of 75 – 1125 m/z. The AGC target was off with the maximum injection time set at 500 ms. 30 scans were conducted for each tape strip as well as 3 areas per tape strip as technical replicates. Both data acquisition and the subsequent data processing were performed using SurfaceLab 7 software (IONTOF GmbH). Orbitrap™ data was

acquired using a Thermo Fisher Orbitrap HF mass spectrometer. Assignments were determined by accurate mass within 3 ppm error of the calculated mass.

High Resolution Imaging. The images were acquired using a 20 keV Ar_{1700}^+ cluster ion beam with a primary ion current of 9 pA. The beam size was around 2 µm in diameter, but the final pixel size was set to 4 µm to reduce image acquisition time. The primary ion dose was distributed equally across each pixel area by rastering the beam in a 10 × 10 pixel micro raster. Four imaging scans were acquired from a field of view area of 500 x 500 µm² leading to a total primary ion dose density of 3.53×10^{14} ions/cm². Charge compensation was performed by flooding the sample using 20 eV electrons. The mass resolution was set to 240,000 (at *m/z* 200) and a fixed injection time of 500 ms was used.

2.3.4 SIMS-MFP software

To help perform a more comprehensive search on classes of compounds present in the data, SIMS-MFP software was used. This software is optimized for SIMS data and is based on molecular formula matching, first described by Kind *et al.*[236]. This was used to perform molecular formula prediction over the negative ion depth profile 3D OrbiSIMS dataset acquired from frozen hydrated human skin. After performing a peak search using the SurfaceLab software (IONTOF, GmbH) (minimum count = 70,000) we created a dataset containing 11,000 discrete ion signals. We searched for compounds containing $C_nH_nO_2^-$ (fatty acids), $C_nH_nO_6^-$ (triglycerides), $C_nH_nO_nN_1^-$ (ceramides), $C_nH_nO_nS_1^-$ (sulfates), $C_{<6}H_{<20}N_{<4}O_{<3}^-$ (amino acids) and $C_nH_nO_nN_nP_1^-$ (phospholipids) where n = any integer value and

assignments were made from the output data tables. All assignments were made with < 2 ppm mass deviation. The assignments were then verified by comparing against the LIPID MAPS® Structure[237] and/or previous literature.

2.4 Results and Discussion

2.4.1 Identifying the importance of cryogenic sample fixation for skin analysis.

Ex vivo full thickness human skin tissue samples were primarily used for this study and a single gas cluster ion beam was employed to both sputter through the skin and generate secondary ions, which were analyzed using an Orbitrap™ analyzer to generate a depth profile (**Figure 2.1a**). As part of the initial method development, *ex vivo* full thickness porcine skin samples were analyzed in either a dehydrated state at room temperature (RT) or frozen (-170 °C) to maintain the native hydration state of the sample (termed "frozen hydrated"). There was a significant intensity reduction for the majority of ions generated from the dehydrated sample, especially the higher mass species (**SI Figure. S1a**), with some ions absent from the spectra altogether (examples in **SI Figure. S1b**). This is consistent with previous studies that postulate an ionization enhancement due to the presence of water[235,213,238,239]. Cryo-fixation of samples for SIMS analysis also has the advantage

of preventing lipid migration and maintaining native structure. The frozen hydrated sample preparation method is therefore used subsequently.

2.4.2 Elucidating *stratum corneum* molecular gradients.

Depth profiling was conducted on frozen hydrated *ex vivo* human skin samples in both negative and positive polarity with more than 8,000 ions detected with an intensity above 1×10^5 in the former and more than 1,000 ions in the latter. Secondary ion mass spectra consist of both ionized molecular species with very little modification, such as gain or loss of a proton, or more fragmented ions. An example negative polarity 3D OrbiSIMS spectrum is shown in **Figure 2.1b**. In order to assign structures to the large number of detected ions and delineate the chemical complexity of this tissue, the recently developed chemical filtering (SIMS-MFP) method was used[240]. This predicts the molecular formula of species in a 3D OrbiSIMS data-set based on accurate mass determination of an elemental formula and categorizes the species based on their double bond equivalents. This enables targeted searches to be carried out for different compound classes based on unique functional groups contained within. For the purpose of our study we focus on the negative polarity data, due to the large number of species present. This data is taken from one analysis area, yet it was repeatable across the four different areas analyzed. The following molecular compositions were used to focus the software search, in order to focus on species known to be present within the *SC* and underlying epidermis: $C_nH_nO_2$ (fatty acids, wax esters, cholesterol esters); $C_nH_nO_6$ (triglycerides); $C_nH_nO_nN_1$ (ceramides, amino acids and derivatives);

$C_nH_nO_nN_nP_1$ (phospholipids); $C_nH_nS_1O_n$ (sulfate-based lipids). The assignments were then verified by comparing against the LIPID MAPS® Structure Database[237] and/or previous literature, allowing us to putatively annotate over 140 molecular species across 5 different compound classes (**Figure 2.1b**).

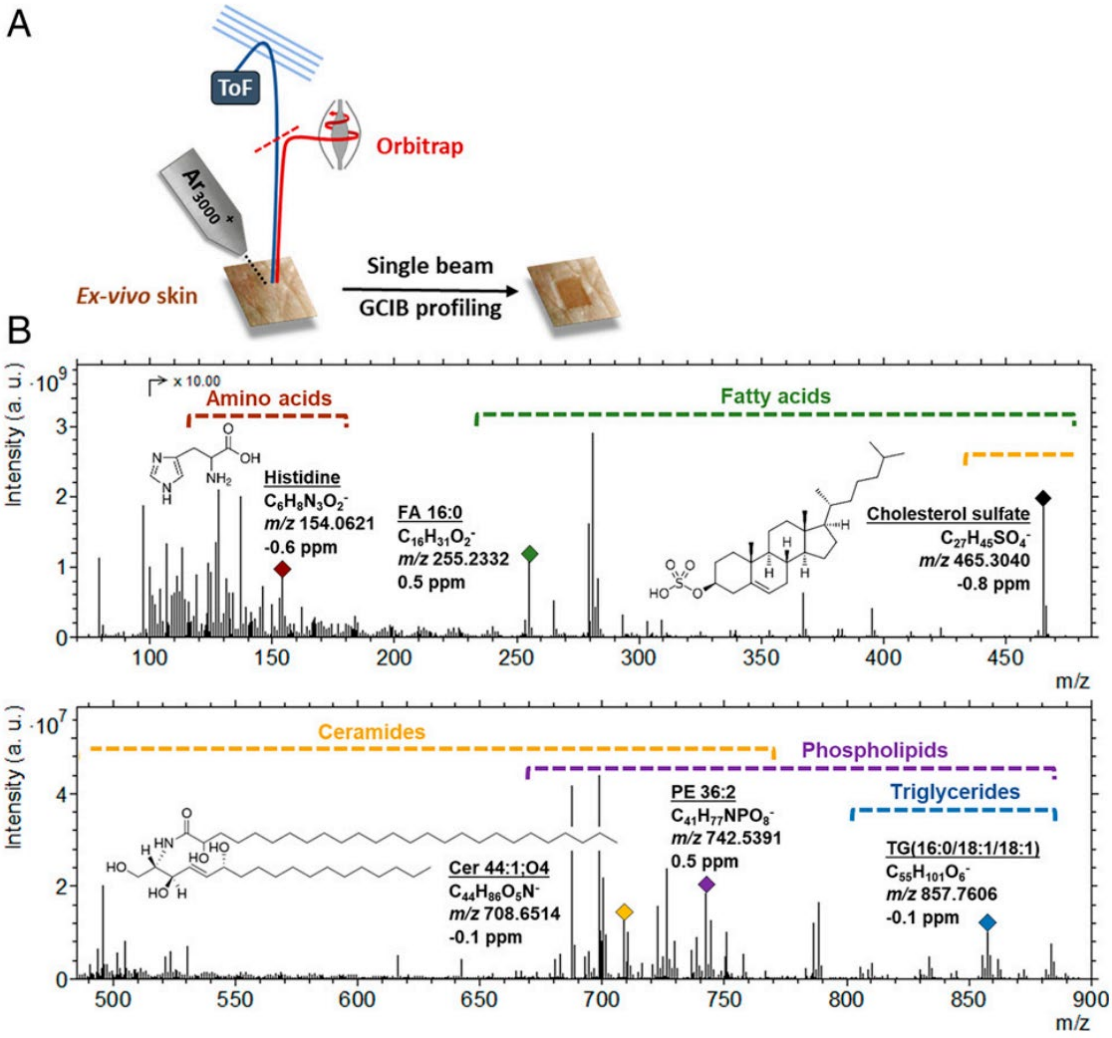


Figure 2.1. OrbiSIMS depth profile analysis of frozen hydrated ex vivo human skin tissue. **(a)** A schematic illustrating the process. **(b)** An example negative polarity spectrum. The spectrum presents the total ion intensity for the 250 x 250 µm area summed across the whole depth profile (total applied ion dose is 2.88 x 10^{13}). Using the SIMS-MFP software we were able to putatively assign over 140 different species across 5 compound classes (amino acids, fatty acids, ceramides, phospholipids and triglycerides). The mass regions for these classes are highlighted on the spectrum and an example compound is labelled for each class, detailing the molecular assignment, chemical formula and the observed mass (*m/z*) and deviation.

Examining the depth profiles for these assignments revealed that these different compound classes exhibited different trends with depth away from the surface of the skin, with some classes even showing a variation between individual species. The negative polarity depth profile data for an example ion from each detected compound class, specifically, triglycerides, ceramides, fatty acids, phospholipids and amino acids and their derivatives and sulfated compounds is shown in **Figure 2.2a**. The full list of identified species and their respective depth profiles, separated by class, can be found in the supplementary information, **Tables S2.1-S2.5** and **Figures S2.1-S2.6** respectively. The ion intensity, representing the relevant concentration of a molecule, is plotted as a function of total ion dose, which equates to the depth below the surface of the skin. Due to the non-homogeneity of the *SC* thickness across the 250 × 250 μm area analysed, distinct ion intensity changes are not expected, and gradual molecular gradients are observed in comparison to a sample with a flat interface. However, our study demonstrates that different molecular species demonstrate different sloped gradients, which suggests that these are “real” molecular variations with depth and not artefacts of a heterogeneous SC layer.

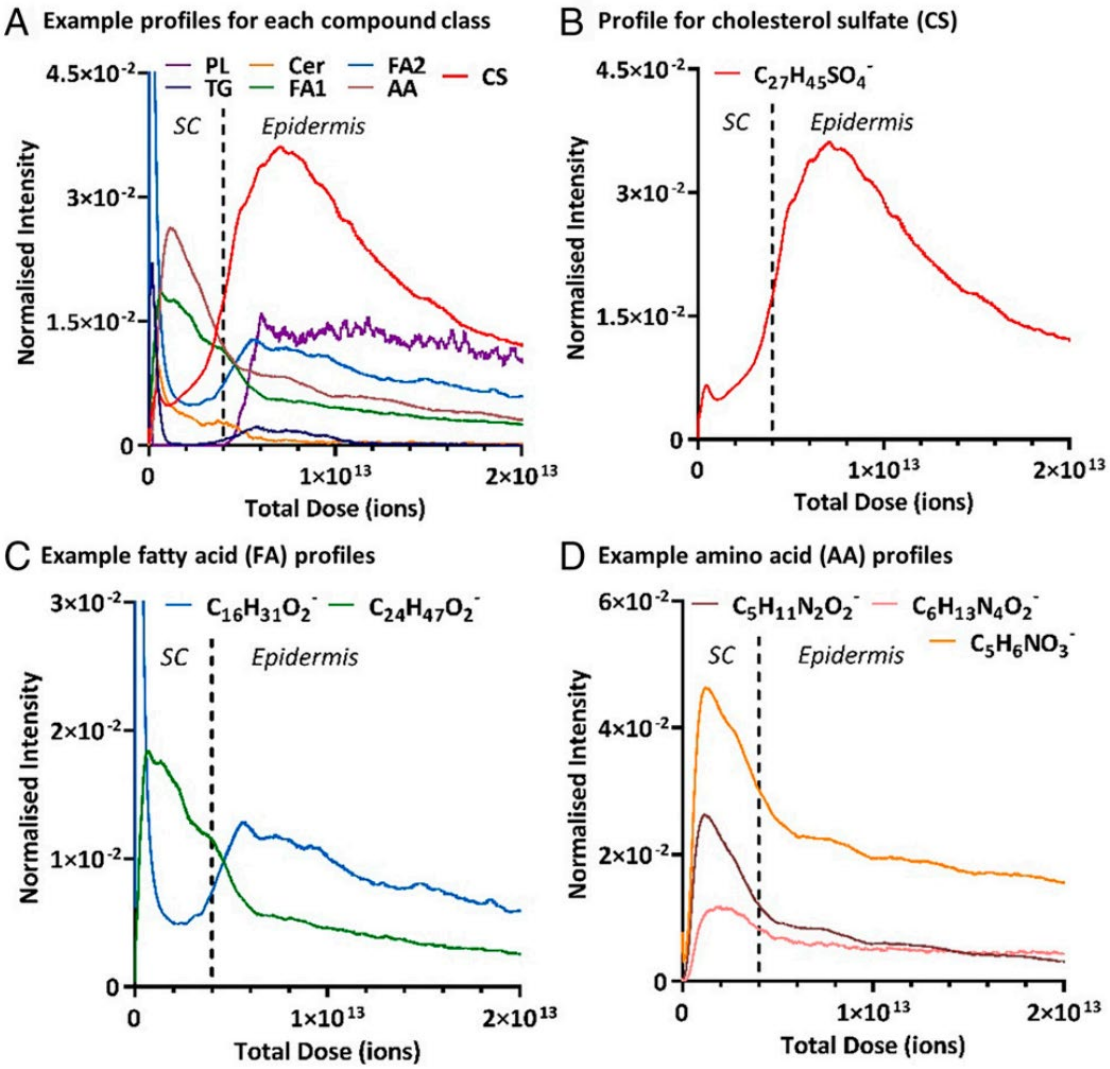


Figure 2.2. OrbiSIMS negative polarity depth profile data showing the ion intensity variation as function of ion dose/skin depth for various putatively assigned compounds. The primary ion beam was Ar_{3000}^+. The ion intensities have been normalized to the total ion count and the profiles have been compressed using a running average method (using a 100 data point average). The *stratum corneum* – epidermal boundary, approximated with a dotted vertical line, has been determined based on the ion intensity variation of the phospholipid species (Fig. S2). **(a)** Example ions from each identified compound class: PL – phospholipids ($C_{41}H_{77}NPO_8^-$), TG – triglycerides ($C_{55}H_{101}O_6^-$), Cer – ceramides ($C_{44}H_{86}NO_5^-$), FA1 and FA2 – fatty acids ($C_{27}H_{47}O_2^-$ and $C_{16}H_{31}O_2^-$), AA – amino acids ($C_5H_{11}N_2O_2^-$) and CS – cholesterol sulfate ($C_{27}H_{45}SO_4^-$). The normalized intensity for the phospholipid ion has been multiplied by a factor of 50. **(b)** Cholesterol sulfate molecular ion ($C_{27}H_{45}SO_4^-$). **(c)** Fatty acids, palmitic acid ($C_{16}H_{31}O_2^-$) and lignoceric acid ($C_{24}H_{47}O_2^-$). **(d)** NMF compounds, the amino acid arginine ($C_6H_{13}N_4O_2^-$) and amino acid derivatives PCA ($C_5H_6NO_3^-$) and ornithine ($C_5H_{11}N_2O_2^-$). The normalized intensity for the arginine ion has been multiplied by a factor of 10.

This heterogeneity, plus the impracticalities of physically measuring the *SC* depth for every individual analysis area, resulted in a method to intrinsically monitor the location within the *SC in situ* while profiling[20]. Specifically, the intensity of a phospholipid ion was monitored throughout the profile, as **phospholipids** are at a minimal level within the *SC* until the transition into the underlying epidermis. This intensity increase is clearly observed in all the phospholipid species that we identified (**SI Figure S2.1**), enabling the *SC* – epidermal boundary to be easily identified as a function of skin depth. In contrast, both triglycerides and ceramides were shown to be present within the *SC*, but exhibited different trends to each other. **Triglyceride** species showed a high ion intensity at the surface of the skin which rapidly decreased to a baseline level in the latter part of the *SC*, which agrees with their known skin sebum origins. However, the depth profiles (**SI Figure S2.3**) highlight that these species are also present, to a much lesser extent, in the upper part of the epidermis. **Ceramides** on the other hand are solely localised to the *SC*, as previously believed, reaching a baseline level once the *SC* – epidermal boundary has been passed. Yet the profiles for these species (**SI Figure S2.4**) highlight that this localisation is not uniform across the *SC* layer, with the ion intensity decreasing initially from the skin surface before reaching a maximum in the upper-central part of the *SC*. These observed molecular gradients exemplify the usefulness of this *in situ* depth profiling approach. Although it is currently understood that ceramides are only found within the *SC*, demonstrating their localisation to the central portion has not previously been achievable.

Although **cholesterol sulfate** is a minor component of the *SC* lipid matrix in terms of concentration, it plays an essential key role in desquamation and skin regeneration,

with increased levels linked to both ageing and skin disorders[206,42,241]. The 'epidermal cholesterol sulfate cycle' was first hypothesized in 1984 by Epstein *et al.*[242] and describes fluctuating levels of this molecule throughout the epidermis, increasing from the basal layer to reach a peak in the *stratum granulosum*, before decreasing once the *SC* is reached. Quantification of cholesterol sulfate levels in extracted skin layers has been achieved through chromatographic mass spectrometry[42], but to date this concentration fluctuation has not been visualized *in situ*. Recent work by Sjövall *et al.* used ToF-SIMS analysis of *ex vivo* human skin cross sections to illustrate a decrease in cholesterol sulfate intensity in the *SC* region compared to the underlying epidermis[60]. The depth profile for the cholesterol sulfate molecular ion ($C_{27}H_{45}SO_4^-$) observed in this study (**Figure 2.2b**) not only confirms this trend but also offers a more detailed insight into the distribution gradient of this molecule within individual layers. It is apparent that cholesterol sulfate steadily increases throughout the *SC* but then reaches a maximum concentration in the upper portion of the underlying epidermis, which based on its location is assumed to correlate to the *stratum granulosum*, before then starting to decline. This agrees with the proposed relative levels of cholesterol sulfate and the mechanisms behind the epidermal cholesterol sulfate cycle, which has previously only been shown through a layer vs. layer comparison. This trend is shown repeatedly for the three different human donor samples analyzed (**Si Figure S2.7**). The use of the *in situ* 3D OrbiSIMS profiling method has enabled the subtlety of this continuous cholesterol sulfate gradient to be observed as a function of skin depth.

Free fatty acids are a major lipid class within the *SC*. Not only is the 3D OrbiSIMS method able to uniquely identify individual fatty acid species with mass deviations

< 0.9 ppm, it also revealed differing depth distributions within the skin for individual species within this class (**SI Figure S2.5**). The intensity profiles for two example fatty acids, palmitic and lignoceric acid, are shown in **Figure 2.2c**. Palmitic acid (C16:0) exhibits an initial rapid decrease in molecular ion ($C_{16}H_{31}O_2^-$) intensity, reaching a baseline level in the upper part of the *SC*. However, towards the deeper part of the *SC* the intensity for this molecule starts to increase again, achieving a local maximum intensity as the underlying epidermis is reached. This fatty acid has previously been shown to be present within the *SC*, but there is debate over whether it is sebum-related or originates from the intrinsic lipid matrix[82]. The results seen here suggest that palmitic acid comes from both sources. It appears to be present on the very surface of the skin before its rapid decrease in intensity, behavior which would be expected from sebum components, but is also present to a lesser extent within the lipid matrix of the lower part of the *SC*. In contrast to palmitic acid, the molecular ion ($C_{24}H_{47}O_2^-$) intensity of lignoceric acid (C24:0) experiences an initial increase once the surface of the skin has been passed. This is followed by a gradual decline in intensity, reaching a baseline level upon entering the underlying epidermis. This trend is consistent with previous studies highlighting its localization solely within the *SC* layer, as one of the most abundant fatty acids present in the lipid matrix[53,51]. However, the profiling method used here suggests that, although localized to the *SC*, lignoceric acid is not uniform across this layer. It is almost devoid at the skin surface and then present to a greater extent within the upper layers compared to the lower layers (**Figure 2.2c**). These trends are reproduced in the three human donor samples analyzed with a reduced relative intensity of lignoceric acid observed in donor 2 (**SI Figure S2.7b**). It is known that

fatty acids are present within the *SC* as free species, but also as components of larger species, such as ceramides. Without more comprehensive analysis we cannot say conclusively that the ions we are observing originate from the free form of this species. However, as the fatty acids present a different depth profile trend compared to the larger lipid species, it suggests that they are likely to be free fatty acid molecules rather than fragment ions.

In addition to the major lipid components, the *SC* also contains natural moisturizing factor (NMF), a mix of hygroscopic molecules including **amino acids** and their derivatives, some of which we were able to identify and show their *SC* localization (**SI Table S2.5** and **SI Figure S2.6**). These compounds are a product of the enzymatic breakdown of filaggrin and although previously demonstrated to be present within the *SC*, little information is known about their depth distribution. A recent paper by Kubo *et al.*[229] focused on the localization of one of these amino acids, arginine, through ToF-SIMS ion image analysis of cross-sectioned mouse tail. Their findings suggested that the *SC* was made up of three distinct layers, with arginine present to a greater extent in the upper and central portions of the *SC*. Our study was able to accurately identify secondary ions relating to not only arginine but also the other main NMF components. The molecular ion intensity profiles of three of these compounds, arginine ($C_6H_{13}N_4O_2^-$), its derivative ornithine ($C_5H_{11}N_2O_2^-$) and the most abundant NMF molecule PCA ($C_5H_6NO_3^-$)[55,221] are highlighted in **Figure 2.2d**. It is apparent that they are all localized within the *SC*, as expected (shown for the three donor samples analyzed in **SI Figure S2.7**, and all follow the same intensity trend with depth. Specifically, an absence at the immediate surface, before reaching a maximum intensity within the upper portion of the *SC*, followed by a

constant decrease in intensity as the underlying epidermis is approached. This result confirms the outcome published by Kubo *et al.*[229], with greater levels of these molecules present in the upper and central part of the *SC*. However, this profiling method provides the ability to assess the relative quantities of these molecules as a constantly changing gradient throughout the *SC*, rather than the three distinct layers portrayed in the ion images presented by Kubo *et al.*[229].

It is important to note that in addition to the epidermal lipids we were also able to detect and observe trends as a function of skin depth for peptide sequences characteristic to three key skin proteins, corneodesmosin, keratin and collagen. Protein analysis of skin using cryo-OrbiSIMS has been previously demonstrated by Kotowska *et al.*[214], but a detailed investigation into these trends is outside the scope of this current study.

Overall, the 3D OrbiSIMS profiling method, coupled with the SIMS-MFP analytical approach, has enabled an extensive analysis of the chemical species present within the upper layers of the skin, revealing previously unexplored gradients with skin depth for various compound classes. This has been achieved by successfully combining the chemical specificity usually associated with traditional mass spectrometry techniques with the localization information produced from *in situ* SIMS analysis. Positive polarity data was also assessed and showed a similar series of trends and behaviors denoting the same species as observed in the negative data-set within different layers of the skin. As with the negative polarity data within similar chemical species both similar and dissimilar trends were observed (**SI Figure**

S2.8). A more comprehensive list of ceramides, fatty acids and amino acid secondary ions observed in the positive data-sets are shown in **Table S2.6-S2.8**.

The general trends discussed in skin chemistry from human samples were also observed within porcine skin tissue analyzed with a comparison of the data shown in **SI Figure S2.9**. Porcine skin is routinely used as an alternative to human skin for pharmaceutical and clinical testing, as it has been demonstrated to be similar in both structure and chemical composition to human skin[141,243]. Our data would also suggest that there is a significant similarity extending to the subtle chemical gradients we can now identify using the 3D OrbiSIMS method.

2.4.3 Exogenous Species within native tissue.

From the native *ex vivo* human skin analysis we also detected the exogenous species, **sodium lauryl sulfate (SLS),** a popular anionic surfactant used in many hygiene products. The depth profile for this compound, identified from the $[M\text{-}Na]^-$ ion ($C_{12}H_{25}SO_4^-$) (**SI Figure S2.1.1**) also highlights a localization to the *SC*. However, it is apparent that this molecule did not decrease to zero intensity once the skin surface has been passed, as was observed with sebum-related native species like palmitic acid (**Figure 2.2c**). Instead it shows an initial increase in the upper layers of the *SC*, before declining rapidly and then at a lower rate. This suggests that this exogenous compound, not designed to intentionally penetrate the skin, is not

solely present on the surface but has actually permeated into the *SC* as a result of exposure to SLS containing products.

2.4.4 Lateral distribution of *stratum corneum* compounds.

Although the 3D OrbiSIMS single beam profiling method applied used here can provide useful insights into the chemistry of the *SC* as a function of depth, it is not able to offer information regarding lateral composition. A combination of *in vivo* tape stripping sampling method with 3D OrbiSIMS imaging was therefore used to investigate the lateral distribution of *SC* compounds within an individual corneocyte layer. Molecular ion images for four example compounds found in the *SC*, specifically cholesterol sulfate, lignoceric acid, 2-pyrrolidone-5-carboxylic acid (PCA) and the exogenous SLS, are displayed in **Figure 2.3**, following analysis of a tape strip sample proposed to represent the middle of the *SC* layer (tape strip number 7). These compounds displayed divergent depth distributions and from these ion images it is clearly apparent that they also present different lateral distributions within a single *SC* layer. This further confirms that the *SC* is not a homogenous layer, as regularly portrayed, but in fact a complex mixture of compounds that vary in concentration both within and between layers. Although cholesterol sulfate (**Figure 2.3a**), lignoceric acid (**Figure 2.3b**) and PCA (**Figure 2.3c**) all display a similar level of coverage across the imaged area, there are clear areas of localization that differ between the compounds. We were even able to demonstrate that the lateral localization varied between different NMF compounds (**SI Figure S2.1.2**), indicating that the breakdown of these amino acids into their derivatives is not a uniform process within a layer. The depth profile for sodium lauryl sulfate (**SI Figure S2.9**),

highlighted the permeation of this molecule into the *SC*, which is confirmed by a clear presence of this molecule within this sampled corneocyte layer (**Figure 2.3b**). However, it appears that this permeation is not uniform across the *SC* layer, instead localizing in small patches of corneocytes within the imaged area. This example data set confirms that the method can be utilized to study the localization of both native and exogenous species within a single corneocyte layer, even within individual corneocyte cells. It should be noted that the primary ion dose applied for this analysis (even for a single image scan) exceeds the static SIMS regime and as such the data is not surface specific but actually represents the chemistry from both the surface and subsurface of these individual corneocytes. The extent of sample etching resulting from the total of 4 imaging scans acquired is demonstrated in the pre and post optical images (shown **SI Figure S2.1.2a** and **b** respectively) where a significant reduction in the visible corneocytes is observed post analysis within the analytical crater region.

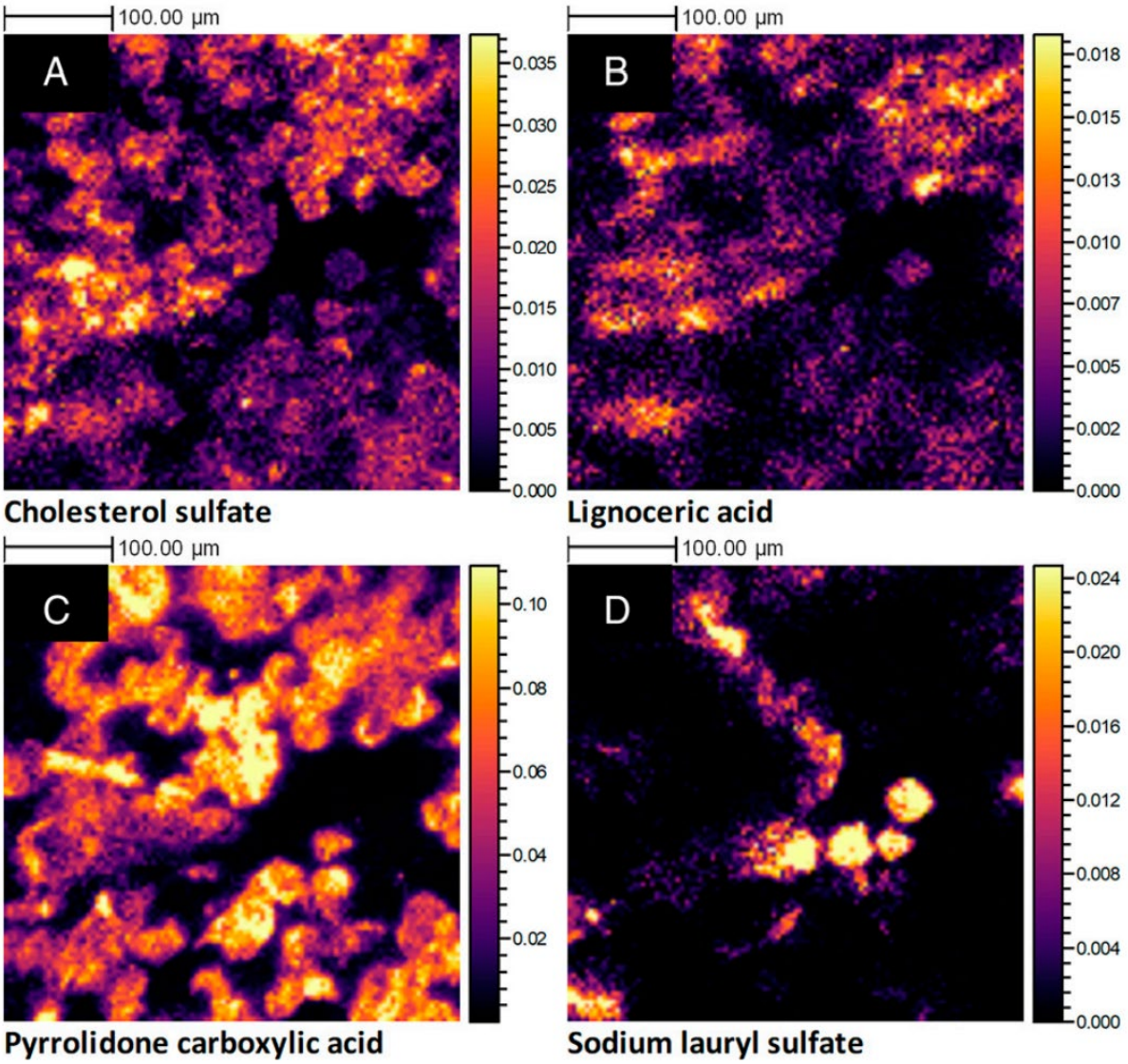


Figure 2.3. OrbiSIMS high resolution negative polarity ion images, produced from the analysis of an individual human corneocyte skin layer, collected *in vivo* using a tape stripping method. The primary ion beam was Ar_{1700}^{+}. The data shown is from tape strip 7, which represents the middle of the *stratum corneum*. The ion images illustrate the 2D spatial distribution for the following molecular ions **(a)** Cholesterol sulfate ($C_{27}H_{45}SO_4^-$) **(b)** Lignoceric acid ($C_{24}H_{47}O_2^-$) **(c)** Pyrrolidone carboxylic acid ($C_5H_6NO_3^-$) **(d)** Sodium lauryl sulfate ($C_{12}H_{25}SO_4^-$). All ion images have been normalized to the total ion image and their relative intensity scales set to 50 % of the maximum.

2.4.5 Peptide delivery through the *stratum corneum*.

In addition to the endogenous species discussed, we have demonstrated the ability to detect and identify exogenous molecules present in human skin following topical application of compounds.

Palmitoyl Tripeptide-1 (Pal-GHK) is a synthetic palmitoyl oligopeptide that is highly utilized in the anti-aging cosmetic market[244]. Commercial formulations containing the peptide have been shown to have clear anti-aging benefits[245,246], stimulating the deposition of fibrillin-1 microfibrils and reducing facial wrinkle clinical grade[245]. Using the 3D OrbiSIMS profiling method, we were able to track the permeation of this peptide through *ex vivo* human skin at commercially relevant levels, following the application of a commercial analogue formulation containing Pal-GHK at quantities <100 ppm (See SI for Franz cell method details). The data presented in **Figure 2.4a** demonstrates that the Pal-GHK molecular ion $[M+H]^+$ decreases in intensity with increasing skin depth, reaching a baseline level at the *SC* – epidermal boundary, hence showing delivery within the *SC* layer.

We were also able to monitor the permeation of this compound through individual layers of the *SC*, through analysis of tape strip samples collected from human volunteers *in vivo*, following the application of a commercial analogue formulation containing Pal-GHK (method details in the SI). This data, presented in **Figure 2.3b**, supports the findings from the *ex vivo* depth profile method, confirming that this Pal-GHK molecule is present at significant levels above the baseline level throughout the *SC*.

Kawashima *et al.* have recently demonstrated the analysis of a similar collagen tripeptide in skin using ToF-SIMS[212]. However, despite using a highly concentrated solution (10% by weight) their results state that the molecular ion peak of the tripeptide was “scarcely detected” in the second layer of the SC and multivariate analysis was needed to confirm its presence. Our analysis was conducted following

application of a complex formulation with the active compound at levels <100 ppm, so 1000 fold less. Yet despite its low concentration within the skin and its chemical similarity to native skin components, we were able to clearly identify the molecular [M+H$^+$] ion ($C_{30}H_{55}N_6O_5^+$) and assess its permeation as a function of skin depth from human *in vitro* and *in vivo* delivery.

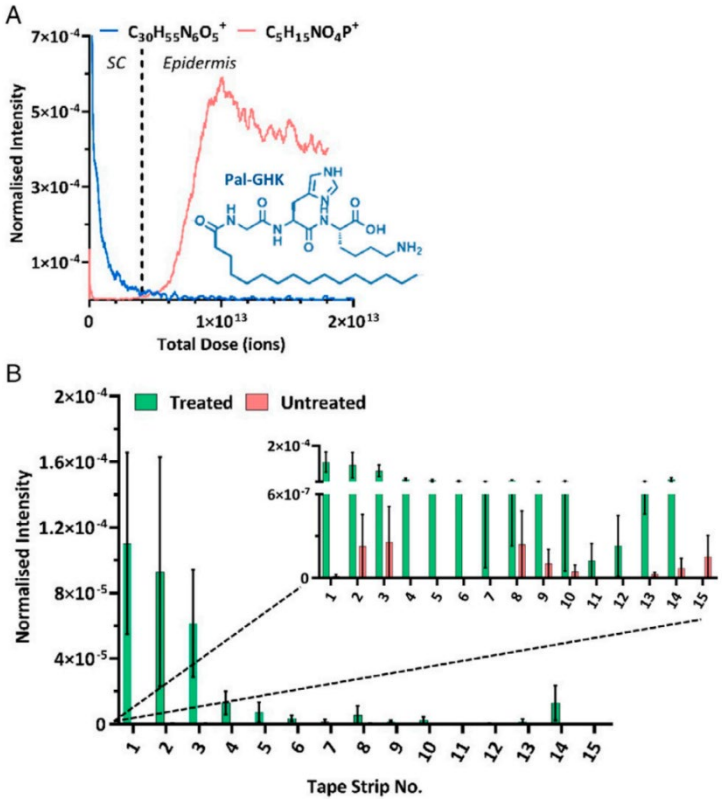


Figure 2.4. 3D OrbiSIMS data showing the ion intensity variation as function of skin depth for various different compounds, highlighting the subtle changes in skin chemistry that can be detected using this method. The primary ion beam was Ar_{3000}^+.The ion intensities have been normalized to the total ion count. **(a)** Data demonstrating the permeation of an exogenous compound, the palmitoyl oligopeptide Pal-GHK ($C_{30}H_{55}N_6O_5^+$), into the *stratum corneum* layer of *ex vivo* human skin tissue. The *stratum corneum* – epidermal boundary has been determined, and approximated with a dotted vertical line, based on the ion intensity variation of the intrinsic phosphocholine molecular ion ($C_5H_{15}NO_4P^+$). The profiles have been compressed using a running average method (100 data points) and the skin depth is represented by total ion dose. **(b)** Data showing the normalized intensity for the Pal-GHK molecular ion ($C_{30}H_{55}N_6O_5^+$) as a function of tape strip number, produced from OrbiSIMS analysis of human tape strips collected *in vivo* following application of a commercially relevant formulation. The graph contains data from 15 sequential tape strips collected from both treated and untreated sites and is represented as the average and standard error of three different volunteers (n=3).

2.5 Conclusions

Overall, our study has illustrated that the 3D OrbiSIMS technique, both single beam depth profiling and 2D high resolution imaging, can provide a detailed molecular characterization of the *stratum corneum*, by investigating the intricate distribution of both native and exogenous species within this tissue. The data presented has demonstrated the huge potential of this approach to provide molecular information for skin research, aiding the understanding of both fundamental biological processes and agricultural/pharmaceutical delivery.

Chapter 3. OrbiSIMS Profiling for Elucidating the Surface Chemistry of Wheat Leaves and Assessing Agrochemical Permeation

3.1 Abstract

The estimated size of the global agrochemicals market in 2022 amounted to USD 227.9 billion with a projected increase to USD 234.27 billion in 2023. At present there is limited knowledge of both chemical composition of leaves, namely the cuticle and epidermal layers, as well as the permeation mechanisms of pesticides. This significantly impacts the understanding of product function and hinders development. Our study uses the novel approach of OrbiSIMS depth profiling to elucidate the in situ molecular composition of these outermost layers of interest in wheat leaves. This investigation enables the precise localisation of endogenous species inherent in the leaf cuticle, for example, fatty acid species unique to the cutin and aldehydes associated with epicuticular waxes. Overall, <90 individually assigned species, across 7 compound classes were identified including their respective depth distributions. Following the application of a multi-component fungicide formulation in vivo to wheat leaves and to in vitro porcine skin, it was possible to identify and localise the active chemical ingredient (cyproconazole) as well as all other components. A range of concentrations reflecting typical application rates (<100 ppm) and potential exposure doses were analysed in leaves and skin and in all cases the relative distribution of all components could be

localised. We believe this methodology provides new insights into leaf chemistry and can be used as a highly effective tool to enable agrochemical product development.

Keywords: Agrochemicals, Wheat Leaves, Cuticle, 3D OrbiSIMS, Pesticides, Fungicides, Dermal Absorption, Skin, Stratum Corneum

3.2 Introduction

Plant leaves are composed of multiple layers, each serving specific functions in protecting and maintaining the health of the plant. These are defined as the cuticle, upper epidermis, palisade mesophyll, spongy mesophyll and lower epidermis[61]. The outermost layer, known as the cuticle, is a hydrophobic polymeric structure that acts as a primary defence barrier against environmental factors, for example biotics and xenobiotics[70], regulation of water and heat loss[71], providing a selective filter for absorption of UV[72] and resistance to mechanical stress.

Despite its seemingly simple structure (1 - 15 µm thickness), recent research[25,247] has revealed that the cuticle is a complex and dynamic system composed of various components including lipids, waxes, and cutin polyesters playing critical roles in plant physiology. Recent studies have highlighted the complex roles of individual molecular species involved in various metabolic pathways including fatty acid regulation of epidermal cell division[80] and cuticular polymeric signalling molecules involved in cell adhesion[76]. The molecular composition and functionality of individual cuticular compounds have been shown to have significant implications for the development of agrochemical formulations[27,28,29]. Agrochemicals, encompassing pesticides and fungicides are extensively employed to safeguard

crops and enhance agricultural output. Nevertheless, there is a lack of knowledge regarding their translocation through leaf tissues and the specific patterns of localization and distribution within the plant.

Numerous studies[73,74,75] have confirmed the composition of the cuticle, comprising of two major components firstly, cutin, a polyester of hydroxylated C_{16} and C_{18} fatty acids and glycerol and secondly, the epicuticular waxes consisting of a complex mixture of aliphatic hydrocarbons, alkanes, alcohols, ketones and aldehydes[76,77,78,79]. The molecular speciation of the cuticle consists of LC-MS quantification[87,88] resulting in the loss of spatial resolution due to extraction procedures. It is widely acknowledged that the cuticle matrix is predominately (<80%) composed of C_{16} and C_{18} fatty acids at approximately 1000 µg/cm^{-2}, [81] however, localisation of these individual species and others is not known. Waxes are a vital constituent of the leaf cuticle, serving a pivotal role in mitigating water loss and safeguarding against environmental stressors. Jefree *et al.*[89] demonstrated the homogenous dispersion of the epicuticular wax throughout the entire depth of the cuticle with a degree of embedding into the cutin layer, nevertheless, the precise composition, structure, and biosynthetic pathways governing leaf waxes have not been elucidated. Currently, there is limited knowledge regarding the exact distributions of wax constituents, including alkanes, aldehydes, alcohols, and esters. In addition to cuticular compounds, there are various species that are localised in the underlying epidermal layers of leaves. Flavonoids are diverse secondary metabolites in leaves, synthesized via the phenylpropanoid pathway[90]. Kaempferol and vitexin are two of the abundant flavonoids functioning as antioxidants, protect against oxidative stress, influence plant-microbe interactions,

and are regulated by environmental and physiological factors. Huang *et al.*[91] successfully quantified the presence of flavonoids within the leaf however, due to solvent-based extraction procedures spatially resolved data was not acquired. The resulting absence of the specific distributions of the key components is vital to understanding biological functions, stress responses and the effects of the absorption of pesticides.

Additional compounds associated with the deeper palisade and mesophyll layers encompass nucleic acids, vitamins, sugars and phospholipids, the depth distributions of which remain largely unexplored. As stated by Kerstiens[92], *in situ* analysis without prerequisite extraction would be crucial in understanding surface specific molecular information. Further research is required to unravel the complex and dynamic nature of leaf waxes and their contribution to the overall functionality of the leaf cuticle.

Current methodologies[87,248,249] for the characterisation of the plant cuticle necessitate laborious and time-consuming organic solvent extraction or mechanical stripping prior to analysis. Extraction procedures have some inherent issues for example the non-selectivity of the extractants including mesophilic contamination[250].

Time of flight secondary ion mass spectrometry (ToFSIMS) is a label free imaging technique offering the ability to provide *in situ* analysis with high chemical specificity and sensitivity. It allows simultaneous molecular speciation in addition to, tracking key molecular species both laterally and as a function of sample depth[200]. ToFSIMS has gained a lot of interest in the pharmaceutical[17,203] and

cosmetic industries[20,251] for tracking active ingredients in skin permeation studies. Converso *et al*[207] conducted an extensive study screening biocidal agrochemicals using ToFSIMS and attempting to visualise the permeation into biological samples. In total only 15 out of 44 compounds were reliably detected with the technique and only fludioxonil was observed in the biological sample. Although ToFSIMS offers several advantages including minimal sample preparation and label free analysis the technique suffers from limited chemical sensitivity and mass resolving power.

Many limitations of ToFSIMS are overcome by the recently developed OrbiSIMS technique[30]. Based on the ToFSIMS platform however, hybridised with an Orbitrap™ mass analyser, OrbiSIMS, can offer significant improvements with a mass resolving power of >240,000 at 200 *m/z*, permitting the detection of exogenous and endogenous species. The inclusion of gas cluster ion beams (GCIB) permits retention of intact molecules and large fragments. The present study exploits the improved capabilities of the OrbiSIMS to enable the observation of the molecular structure of wheat leaves specifically, exploring the chemical composition and distribution of key compounds present within the leaf cuticle.

Additionally, the surge of agrochemical usage has been increasingly linked to harmful health effects[252,253,254,255] in farmers from unintentional excessive dermal exposure. With the employment of the OrbiSIMS approach, the depth distribution of a model multi-component agrochemical fungicide formulation is also investigated with simultaneously observed skin and native leaf chemistry providing an *in-situ* context for localisation.

3.3 Materials and Methods

3.3.1 Reagents

HPLC grade methanol, acetonitrile, Teepol™ 610 S and phosphate buffered saline tablets were purchased from Sigma Aldrich, UK. An emulsifiable concentrate (EC) formulation of cyproconazole at a concentration of 50g/L containing a range of co-formulants (CCZ EC) were provided by Syngenta.

Cyproconazole, Synperonic™ L11, Solvesso™ 200 ND, Emulsogen EL 360, Atlox™ 4838B, Hallcomid® M-8-10 and the CCZ EC formulation were provided by Syngenta, UK (see **Table 3.1**).

Table 3.1: The composition of the CCZ EC formulation.

COMPONENT TRADE NAME	COMPONENT CHEMICAL DESCRIPTION	TYPICAL ROLE IN FORMULATION	COMPONENT CONCENTRATION IN FORMULATION (G/100ML)
CYPROCONAZOLE	2-(4-Chlorophenyl)-3-cyclopropyl-1-(1*H*-1,2,4-triazol-1-yl)-2-butanol	Hydrophobic active ingredient	5
EMULSOGEN EL360	Castor oil based ethoxylate, 36 mol EO	Non-ionic emulsifier	3
ATLOX™ 4838B	Calcium alkylaryl sulphonate in solvent (2-ethylhexan-1-ol)	Anionic emulsifier	3
SYNPERONIC™ L11	Polyoxyethylene (11) lauryl ether	Non-ionic emulsifier	3
HALLCOMID® M-8-10	Mixture of N, N-dimethyloctanamide and N, N- dimethyldecanamide	Partially water-soluble solvent	27
SOLVESSO™ 200ND	Aromatic solvent derived from crude oil	Water-immiscible solvent	27

3.3.2 OrbiSIMS Depth Profile Analysis of Wheat Leaves

Winter wheat plants of the Motown variety (3 weeks old) were cultivated and supplied by Syngenta, Jealott's Hill, UK. Using a vacuum oven at room temperature, the fully expanded leaves were dehydrated for 10 mins followed by analysis using the OrbiSIMS.

3.3.3 Leaf *in vivo* Permeation Study

The wheat leaves (still attached to the plant) were mounted between the donor and receptor chamber in a Franz-type static diffusion cell (PermeGear™, surface area 1.1 cm^2 and 3 ml receptor compartment) and 10 µL of the CCZ EC formulation was applied directly to the donor compartment. The leaves were exposed to the formulation for 2, 4 and 6 hours followed by dehydration at room temperature using a vacuum oven. The dehydrated leaves were then analysed using the OrbiSIMS.

3.3.4 Agrochemical Reference Preparation

Cyproconazole (active ingredient) and the co-formulants of the CCZ EC formulation including Emulsogen EL 360, Atlox™ 4838B, Synperonic™ L11 and Solvesso™ 200 ND were blotted onto individual silicon wafers and dehydrated in a vacuum oven for 4 hours at room temperature. The remaining residues on the silicon wafers were analysed using the OrbiSIMS.

3.3.5 Porcine Skin Preparation

The *ex vivo* full thickness skin samples were obtained from the flank regions of 4-6 month old pigs immediately after slaughter. Following storage for a maximum of 24 hours at 4°C, the skin was thoroughly washed with ultrapure water and the hair

was trimmed. Using a scalpel, any excess subcutaneous fat and cartilage was removed carefully without damaging the skin. Aluminium foil was used to wrap the skin and subsequently stored at -20^{o}C for a maximum of 3 months prior to use. 2 mm full thickness skin sections were used for skin permeation analysis.

3.3.6 Franz Cell Permeation Set-Up

Once defrosted, the *ex vivo* porcine skin was cut into 2 × 2 cm sections and mounted (dermal side up with the stratum corneum exposed to the donor solution) between the donor and receptor chamber in a Franz-type static diffusion cell with an exposed surface area of 1.1 cm^2 and a receptor compartment capacity of 3 ml. The agrochemical formulation, CCZ EC was applied (infinite dose, 0.5 ml) (1% v/v (1 part formulation and 99 parts water)) via the donor compartment and 3 ml of Phosphate Buffer Saline (pH 7.4) was placed in the receptor compartment. The skin was exposed to the formulation for 24 hours in a stirring water bath set to 37.5^{o}C. Following the allotted exposure time, the Franz cell was disassembled and the excess formulation was removed using a sponge soaked in Teepol solution (3% v/v). Using a vacuum oven, the skin was subsequently dehydrated at room temperature for 24 hrs before analysis with the OrbiSIMS.

3.3.7 OrbiSIMS Depth Profile Analysis of Skin and Leaves

Single beam depth analysis was performed with the employment of the OrbiSIMS using an Ar_{3000}^{+} cluster primary ion source operated at 20 keV and a GCIB current of 218 pA. For the acquisition of the depth profiles of the porcine skin, a 20 keV Ar3000+ ion beam was employed with a diameter of 20 µm. A random raster mode was utilised with a crater size of 280 x 280 µm with a total ion dose of 1.17 -

1.27×10^{17}ions/cm^2. To aid charge compensation argon gas flooding was in operation with a chamber pressure of 9 x 10^{-7} bar. The cycle time was set to 200 µs with the optimal target potential averaging at approximately -384.5 V. The depth profiles were collected in both positive and negative polarities with the mass resolution set at 240,000 at 200 *m/z* with a mass range of 75 - 1125 *m/z* and injection time of 500 ms. All data analysis was carried out using Surface Lab 7.1 (IONTOF GmbH) and molecular formula prediction (MFP)[240] was used to filter through the dataset.

3.3.8 Liquid Chromatography with Tandem Mass Spectrometry (LC-MS/MS) Analysis

LC-MS/MS quantification of active ingredient CCZ extracted from different Franz cell compartments (receptor fluid, skin wash, donor chamber wash, tape strips and remaining skin) was carried out using a QTRAP 6500 instrument, a hybrid triple quadrupole/linear ion trap (AB SCIEX). The QTRAP system was operated in the positive electrospray ionization (ESI) mode. An ACE 5 C18 Column, 160 X 4.6 was used, 5 µL of sample was injected. RP-LC separation was performed at a flow rate of 0.5 mL/min using solvent A (0.2 % v/v Formic Acid in Water) and solvent B (0.2 % v/v Formic Acid in Acetonitrile) in a gradient. The fragment ion transitions m/z 70 and m/z 125 of CCZ molecular ion m/z 292 had the highest peak intensities and were selected for quantification. LC-MS/MS data analysis was carried out using SCIEX Analyst® Software.

3.4 Results & Discussion

3.4.1 Determining the molecular composition of wheat leaves

A single ion beam (Ar_{3000}^+) OrbiSIMS depth profiling method was utilised to sputter through the wheat leaf from the cuticular surface. Secondary ion species were collected as a depth profile with the data yielding a range of species including both molecular species and fragment ions. The chemical profiling resulted in the detection of approximately 5000 ion species at an intensity of >1 x 10^5. The chemical filtering process[240] was employed due to the volume and complexity of the data obtained. The dataset was deconvoluted based on a combination of elemental composition (functionality) and double bond equivalents (DBE). With this approach, it was possible to assign approximately >90 different species across seven compound classes (namely fatty acids, aldehydes, amino acids, nucleic acids, phospholipids, vitamins and flavonoids). An example of each of these systems is assigned in the spectra and illustrated as a depth profile in **Figure 3.1a and b**, respectively. The assignments were then confirmed using a combination of previous literature and the LIPID MAPS® Structure Database[237].

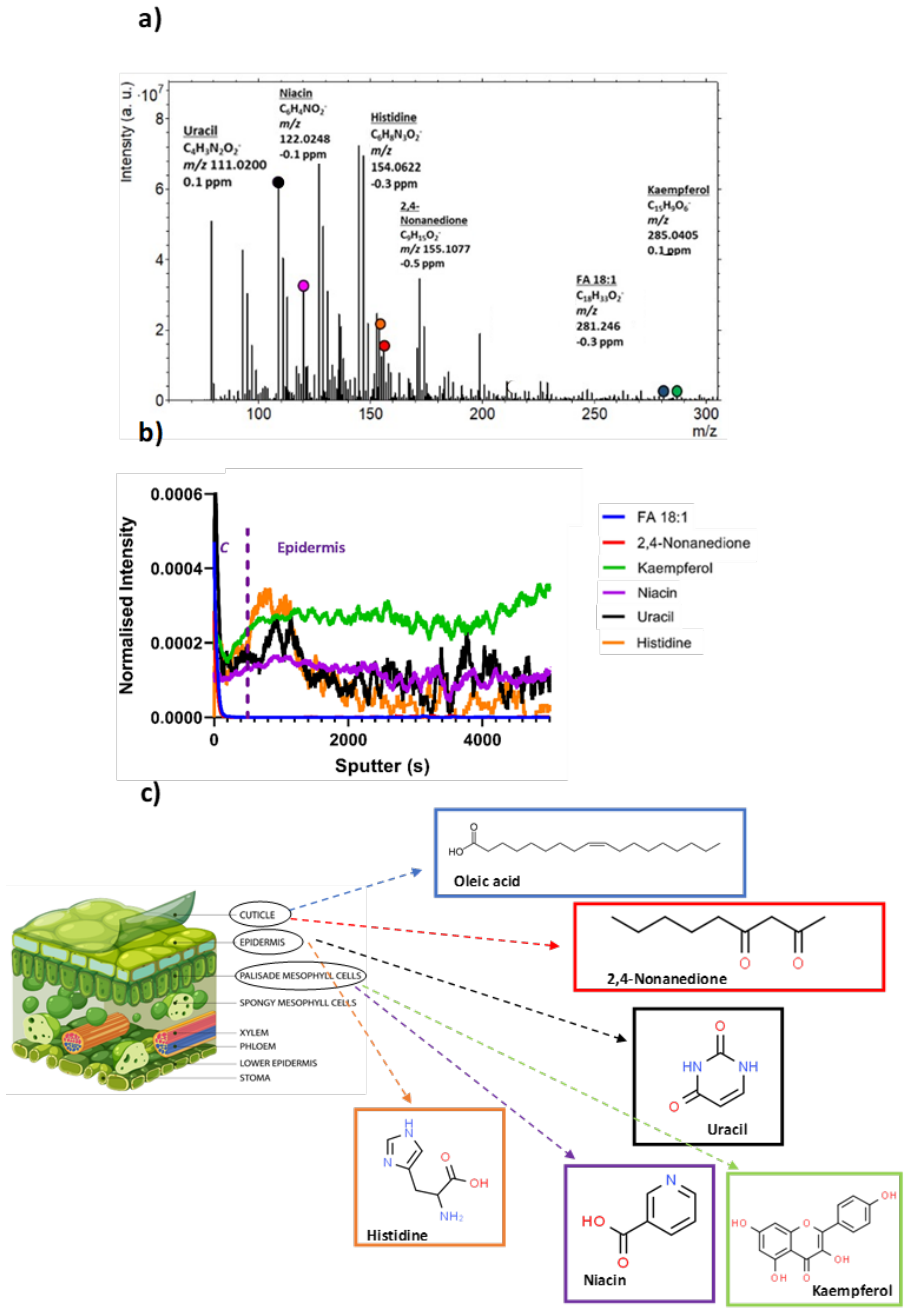


Figure 3.1. OrbiSIMS for label free imaging of *in situ* wheat leaf with mass resolving power of >240,000 and mass accuracy of <1 ppm. **(a)** A mass spectrum of negative polarity highlighting the molecular speciation of seven distinct compound classes (fatty acids, aldehydes, amino acids, nucleic acids, phospholipids, vitamins and flavonoids) employing the SIMS-MFP technique. **(b)** Overall localisation trends of example ions including: FA- Fatty acids (FA 18:1) ($C_{18}H_{33}O_2^-$) Ald- Aldehydes (2,4-Nonanedione) ($C_9H_{15}O_2^-$), AA- Amino acids (Histidine) ($C_6H_8N_3O_2^-$), Fla- Flavones (Kaempferol) ($C_{15}H_9O_6^-$), Vit- Vitamins (Niacin) ($C_6H_4NO_2^-$) and Nuc- Nucleic acids (Uracil) ($C_4H_3N_2O_2^-$). **(c)** Chemical structures of the key ions explored and localisation within the leaf structure.

The OrbiSIMS depth profiling method revealed that the seven compound classes displayed a variation in distribution trends within the wheat leaf as depicted in the example depth profile for each compound class in **Figure 3.1b**. The full molecular speciation and their respective depth profiles can be found in the supplementary information (**SI Figures S3.2-S3.8 and SI Tables S3.1-S3.7**). By etching a crater into the leaf and subsequently measuring the primary ion dose required to reach 10 µm, we were able to monitor the depth of the leaf cuticle, specifically, the transition from the leaf cuticle into the underlying epidermis. The cuticle-epidermal boundary was revealed to be at 500s in the OrbiSIMS depth profile, with the fatty acids and aldehydes abundant within the cuticle producing the cutin and epicuticular wax respectively. In contrast, the presence of amino acids for example histidine, and phospholipid fragments within the cuticle is minimal; however, their concentration significantly increases upon transition into the underlying epidermis.

Where previous studies have only demonstrated the quantification/presence of the lipid composition of the cuticle[256] and with no localisation information, using the OrbiSIMS a range of chemistries have been identified alongside their depth distribution. Fatty acids, a major constituent of the cuticle, responsible for a range of roles including antimicrobial agents[257,258], water homeostasis[259] and UV filtration[72] were identified including their respective depth distributions (**SI Figure S3.3**). The localisation of the most abundant fatty acid monomers of cutin[260], FA 18:1, is displayed in **Figure 3.1b**. FA 18:1 exhibits a rapid initial decrease in molecular ion intensity reaching a baseline as the cuticle-epidermal boundary is reached. The behaviour exhibited by the fatty acids observed in this analysis, are consistent with

previous studies[261] highlighting the localisation within the cuticle and concentrated at the cutin waxy layer exposed to the environment.

The leaf cuticle also consists of the epicuticular wax layer. Comprised of an array of hydrophobic organic compounds bound to the cutin, this layer plays multiple roles such as reducing water loss, providing protection against pathogens, and acting as a barrier against excessive UV radiation[262]. Among the major components of the epicuticular wax, we successfully identified and examined the depth distributions of monounsaturated aldehydes (**SI Figure S3.4**). The localisation trends of 2,4 nonanedione, is depicted in **Figure 3.1d**, where the intensity of the molecular ion rapidly decreases to baseline at the boundary between the cuticle and epidermis, confirming abundance in the cuticle. The distribution trends of fatty acids within the cuticle and aldehydes in the epicuticular wax layer exhibit minimal differences, indicating that the epicuticular waxes are integrated within the cutin polymer rather than being separate layers. Previous studies[263264] have emphasised the cohesive nature of the epicuticular waxes within the cutin structure however, our study (**Figure 3.1b**) extends to exposing the localisation of individual components within the entire structure.

Flavones are a prominent subclass of flavonoids, exhibiting diverse roles and functions in the physiology of leaves. They act as natural sunscreens, absorbing and filtering harmful UV-B and UV-A radiation to shield leaf tissues[265]. The antioxidant attributes of flavones facilitate the effective scavenging of reactive oxygen species (ROS)[266], while some flavones demonstrate allelopathic effects, inhibiting neighbouring plant growth[267]. The distribution pattern of kaempferol, involved in the inhibition of ROS-generating enzymes [268] is depicted in Figure 1b. The depth

distribution of kaempferol is characterised by negligible presence within the cuticle and a subsequent continual increase in intensity within the underlying epidermal region. Earlier investigations[269] proposed a complete absence of flavonoids within the cuticle. Nevertheless, our present study has successfully detected the small amounts of these compounds within the cuticular structure. This advancement enriches our comprehension of fundamental leaf chemistry, offering potential insights into refining agrochemical delivery methods.

Vitamins were also identified and their localisation patterns within the wheat leaf are presented in **Figure 3.1b**. These compounds play a pivotal role in the regulation of plant growth and development[270], encompassing vital functions in stress response mechanisms[271]. Niacin is recognized for its role in stress signal induction and protection against cell leakage and DNA damage exerting its influence by modulating the activity of transcription factors, pivotal regulators of gene transcription[272]. The ion intensity of niacin exhibits a progressive rise as it traverses the cuticle-epidermal boundary, succeeded by a gradual decline beyond 1000 sputter seconds within the epidermis. Prior investigations[273] provide evidence for the presence of niacin in the mesophyll layers, specifically within the cytosol, however, our study was able to identify negligible amounts of vitamins/derivatives, including niacin within the cuticle. Currently, it is unknown why there is a presence of vitamins within the cuticle as these are typically distributed within the cells of plant tissues where they are responsible for metabolic processes. A comprehensive list can be found in the **Figure S3.8**.

The label-free in situ imaging of wheat leaves without the need for prior sample preparation was successfully achieved. This enabled the molecular speciation

analysis of different leaf layers and the exploration of their depth distributions. Enhanced understanding of the molecular composition and localization patterns within the leaf, particularly the cuticle, is of utmost significance for the development of pesticide formulations with improved delivery and efficacy.

3.4.2 Agrochemical formulation delivery through wheat leaves

Cyproconazole is a widely employed broad-spectrum fungicide, extensively utilized for managing biotic stress, such as Septoria and powdery mildew prominent in cereal crops and fruit trees[274]. The CCZ EC comprises cyproconazole (50 g/L) as the active ingredient along with a range of co-formulants (see **Table 3.1**) with distinct roles, including ionic/anionic emulsifying agents and solvents. At present, liquid scintillation counting (LSC) represents the prevailing method for the quantification of pesticide foliar uptake, as demonstrated by Liu et al [275] in their study on pyraoxystrobin monitoring in cucumber plants. Additionally, LC-MS/MS is extensively utilized for the assessment of pesticide foliar permeation [276]. Nevertheless, these techniques are not without intrinsic limitations, such as their ability to quantify only the active ingredient, extraction procedures that compromise spatial resolution, and the requisite labelling or tagging for accuracy. No data is available regarding the *in-situ* permeation characteristics of cyproconazole or the constituents of the formulation which could be used to aid the understanding and development of crop protection systems.

Following the *in vivo* treatment of Motown wheat leaves (3 weeks old) with CCZ EC (1% v/v dilution), the OrbiSIMS depth profiling method was employed to investigate the permeation of the active ingredient and all co-formulants,

simultaneously. The OrbiSIMS depth profile data (**Figure 3.2**) shows the permeation of both the cyproconazole and each of the co-formulants can be evaluated within the leaf exhibiting varying behaviour for 2, 4 and 6 hrs. This information reveals an unprecedented level of detail in observing the complete agrochemical formulation *in-situ* from *in vivo* treated wheat leaves at application levels simulating real-life conditions (i.e. with the cyproconazole at <100 ppm applied dose).

The depth profiles depicted in **Figure 3.2**, highlight the distribution of the active ingredient and all the formulation constituents in *in vivo* wheat leaf across exposure time of 2, 4 and 6 hours. The presence of cyproconazole (**Figure 3.2a**) was observed using the chlorobenzyl molecular cation ($ClC_6H_4CH_2$+). The results revealed distinct temporal dynamics where after a 2-hour period, the molecular ion peak intensity was observed at the leaf surface, followed by a rapid decline to baseline levels. The 4 and 6 -hour exposure samples show the ion at relatively higher intensity within the upper surface of the cuticle. This ion intensity then reduces to negligible levels as it reaches the epidermal boundary, however, in both cases it then gradually increases to higher levels within the underlying epidermis suggesting significant permeation into the epidermal layer. Additionally, the 6 -hour time point exhibited a higher ion intensity compared to the 4-hour time point in the underlying epidermis. These findings reveal an increase in permeation with exposure time taking place between 2 and 6 hrs. Cyproconazole functions as a systemic fungicide, participating in the inhibition of ergosterol biosynthesis[277]. Our findings indicate that a minimum application period of 4 hours is necessary for cyproconazole to permeate into the leaf to execute its intended role.

The co-formulants incorporated into the emulsifiable concentrate undertake diverse functions. These encompass serving as stabilizing emulsifying agents (Emulsogen EL 360, Synperonic L11 SS CQ and Atlox^{TM} 4838B) for the formulation, serving as carrier solvents for the active ingredient (Hallcomid M-8-10), and functioning as water-immiscible solvents for maintaining emulsion stability in aqueous dilution (Solvesso^{TM} 200 ND). We achieved simultaneous detection of all formulation constituents from the analysis of the *in vivo* testing (**Figure 3.2**), eliminating the requirement for solvent extraction or the use of fluorescent markers. Hallcomid M-8-10, a carrier solvent for cyproconazole was monitored using the molecular ion ($C_9H_{18}NO$-). The ion intensity data (**Figure 3.2b**) revealed permeation characteristics similar to cyproconazole, whereby at the 2 -hour time point, localisation was predominant within the cuticle. However, with the progression of time, we observe a gradual permeation into the underlying epidermis, following a similar pattern to cyproconazole at 4 hours, and to a greater extent at 6 hours. Emulsogen EL 360 ($C_{11}H_{19}O_2$-), a non-ionic castor oil ethoxylate emulsifier, exhibited negligible permeation within the leaf during the initial 2 -hour exposure period, as indicated by the baseline ion intensity. However, at the 4 -hour point, the ion intensity remained at baseline within the cuticle but steadily increased in the underlying epidermis, suggesting localisation in the deeper tissues of the leaf. Remarkably, at the 6 -hour time point, the ion intensity for the molecular ion reached baseline levels throughout the leaf, indicating Emulsogen EL 360 may have potentially translocated through the leaf. The overall trend observed for the co-formulants implies they are predominantly localized at the leaf surface

with limited permeation into the leaf tissues, aligning with their intended role of formulation stabilisation as opposed to active permeation.

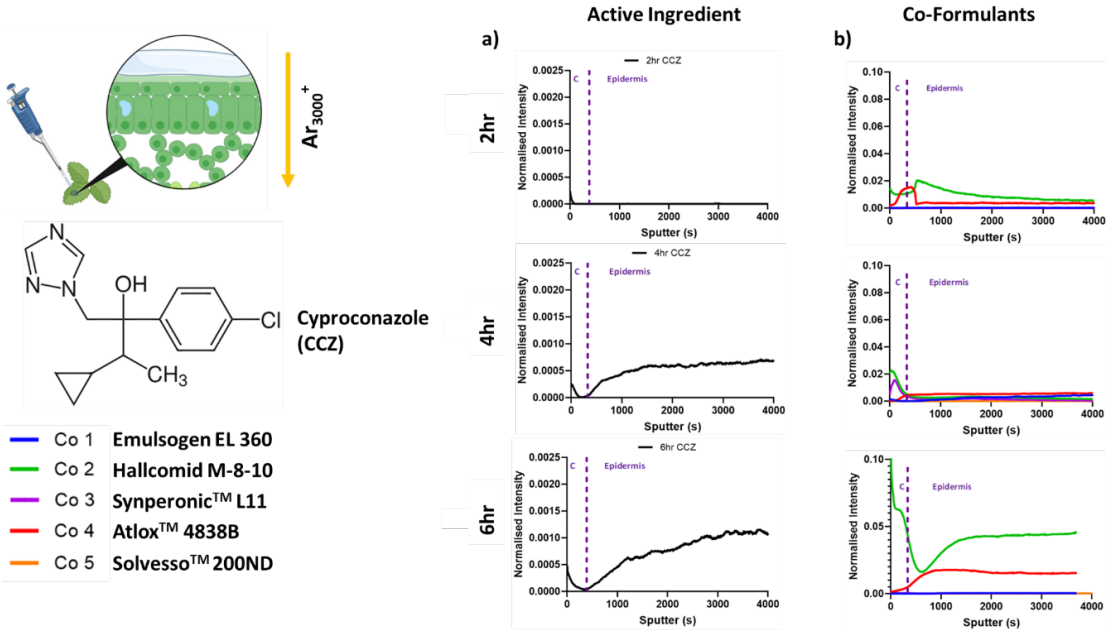


Figure 3.2. OrbiSIMS depth profile analysis of the fungicide, CCZ EC, through *in vivo* wheat leaf. **(a)** Localisation trends for the active ingredient CCZ- cyproconazole **($ClC_6H_4CH_2^+$) at 2, 4 and 6 hr exposure intervals. (b)** Depth distributions of five co-formulants (Emulsogen EL 360- non ionic emulsifier, Hallcomid M-8-10 AI carrier solvent, Synperonic™ L11 non-ionic emulsifier, Atlox™ 4838B- anionic emulsifier, Solvesso™ 200 ND- water immiscible solvent) through *in vivo* treated wheat leaves including ionic/anionic emulsifying agents and carrier solvents.

3.4.3 Assessing the dermal absorption of an agrochemical formulation

Previous studies by Starr *et al.*[278], have demonstrated the capability of the OrbiSIMS approach to monitor the transdermal penetration of exogenous compounds at very low concentrations, exemplified by the anti-aging peptide Pal-GHK. Considering the potential for unintentional skin exposure to agrochemical products at different concentrations during the process of mixing, loading, and application of the compound onto crops, initial experiments were conducted to examine the impact of dilution concentration (10%, 50% and 100% v/v) on the

transdermal absorption. Porcine tissue samples were tested *in vitro* using a Franz diffusion cell under infinite dose and subsequently the tissue was depth profiled using the OrbiSIMS approach to explore the dispersion of CCZ EC within ex vivo porcine skin (**Figure 3.3**). Infinite dose conditions were chosen to maximise the active permeation rate into skin as this should increase the concentration of active ingredient within the skin tissue and aid the detection with OrbiSIMS. Further studies have refined this method to include finite dose conditions that are closer to typical exposure scenarios. This data will be presented in separate publications at a later date.

Following 4 -hour exposure, this study successfully detected the presence of the cyproconazole molecular ion ($ClC_6H_4CH_2$+) at all pertinent concentrations within the porcine skin, as depicted in **Figure 3.3b**.

The OrbiSIMS profiling method allowed observation of permeation of the different concentrations of the agrochemical formulation through the porcine skin. A phosphocholine secondary molecular ion ($C_5H_{15}NO_4P^+$) was employed as an intrinsic marker to indicate the depth of the *stratum corneum*. Given the absence of phospholipids in the keratinized stratum corneum[216], an elevation in ion intensity signifies a transition into the underlying epidermis. Notably, at 4000 sputter seconds (**Figure 3.3c**), an increase in ion intensity of the phosphocholine marker was observed, indicating the boundary between the stratum corneum and the epidermis had been reached. The depth profile data for cyproconazole presented in **Figure 3.3d** clearly demonstrates that an elevation in the concentration of the fungicide correlates with an increase in its penetration into the skin after a 4 -hour period. The cyproconazole in the 10% v/v dilution of the

formulation exhibits negligible penetration into the skin, as indicated by the baseline ion intensity of the chlorobenzyl cation throughout the skin sample. At 50% there is a marginal increase in the observed ion intensity relative to the 10% concentration. Permeation follows as a steady state into the underlying epidermis, albeit at a relatively low ion intensity. In the case of the concentrated 100% undiluted formulation of cyproconazole, a significantly higher degree of permeation is observed, with the ion intensity increasing at the skin surface and reaching a maximum at the upper layers of the *stratum corneum*. Subsequently, there is a gradual decrease in ion intensity as the underlying epidermis is reached. The collected data indicates that higher concentrations of cyproconazole result in an intensified permeation process. This underscores the necessity for farmers to follow safe working practices including the use of the specified protective equipment while dealing with these systems especially, in the undiluted forms.

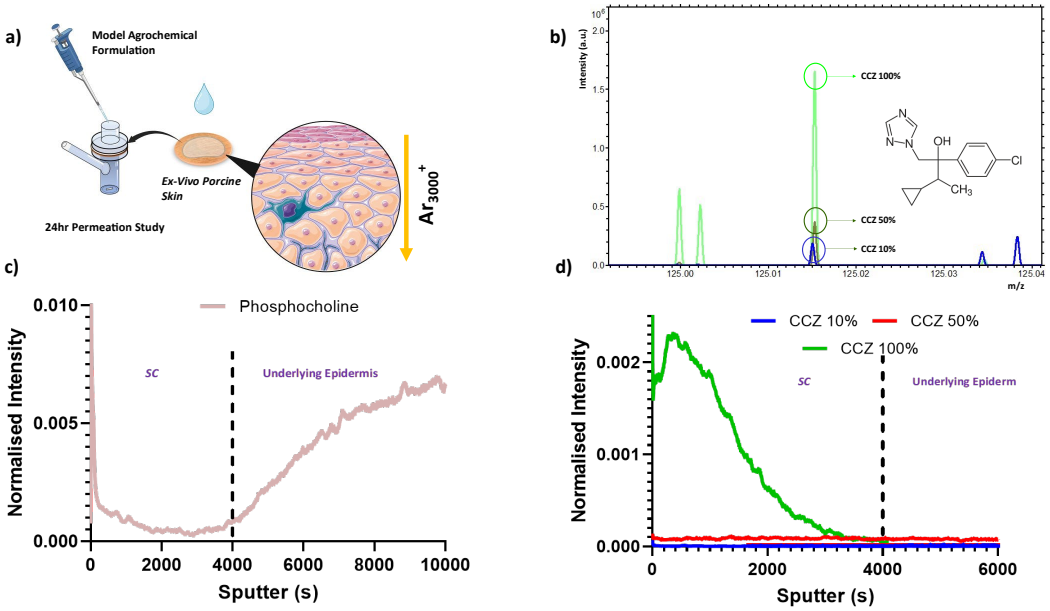


Figure 3.3. **(a)** Static Franz cell permeation study conducted under infinite dosing, assessing the dermal absorption of SAN 619 (EC) at 10%, 50% and 100% v/v dilutions. **(b)** OrbiSIMS mass spectra depicting the chlorobenzyl molecular ion for the overall depth profile at varying concentrations within *ex vivo* skin. **(c)** Data demonstrating the determination of the *stratum corneum*-epidermal boundary depicted by the phosphocholine biomarker ($C_5H_{15}NO_4P^+$). **(d)** *In situ* profiling of cyproconazole within porcine skin at 10%, 50% and 100% v/v dilution post 4 -hour exposure time.

Considering fungicide products are typically applied as a 1% v/v dilution for the treatment of cereal and vegetable crops, an important unintentional exposure scenario may involve this diluted form. The dermal absorption of the active ingredient in CCZ EC was examined using liquid chromatography-mass spectrometry (LC-MS/MS), to overcome the drawbacks relating to quantification using the OrbiSIMS.

As depicted in **Figure 3.4a** and Supplementary Information (**SI Table S3.8 and Figures S3.1.1-3.1.2**). **Figure 3.4a** illustrates the percentage recoveries obtained for the bulk analysis of tape strips relating to the *stratum corneum* and the remaining skin associated with the dermis. The analysis of tape strip quantification reveals a noticeable decline in recoveries on average, transitioning from 0.86% at the 4-hour exposure to 0.68% at the 7-hour exposure. This observation hints at a potential reduction of cyproconazole within the *stratum corneum*. However, this trend is reversed after a 24-hour exposure, with recoveries increasing to 2.27%, indicating an accumulation of the active ingredient over this time period. Conversely, the average recoveries for cyproconazole exhibit a gradual increase with extended exposure, measuring at 5.56% at 4 hrs, 9.14% at 7 hrs, and 13.16% at 24 hrs successively in the remaining skin. This pattern implies an accumulation of the compound within the underlying epidermal layers.

Despite the robustness of LC-MS/MS as a quantitative tool, it is not without limitations for quantifying skin permeation. The notable drawbacks are the loss of spatial resolution of the analyte caused by the bulk analysis of the *stratum corneum* via tape strips and the solvent-based extraction of the remaining skin required for the analysis of the dermis. The procedures for the sample preparation including the various washing procedures for the skin and extraction procedures are not highly accurate therefore the percentage recoveries are not precise and the ability to differentiate between samples is difficult. Additionally, the methodology suffered inherent issues with column carry over effects, affecting the accuracy of the quantitative analysis resulting in subpar total recoveries (<52%). LC-MS/MS of CCZ proved to be challenging highlighting the significant time investment required in order to develop a recovery and quantification method that results in an acceptable level of recovery and variability.

As depicted in **Figure 3.4b**, the permeation characteristics of cyproconazole from a 1% v/v dilution of CCZ EC in the *stratum corneum* were evaluated over different exposure times namely 4, 7 and 24 hrs. Following a 4-hour exposure, minimal permeation of cyproconazole in the *stratum corneum* was observed, with a gradual decrease in ion intensity from the skin surface to baseline. However, after a 7-hour exposure, a notable increase in ion intensity was observed at the surface of the *stratum corneum*, followed by a gradual decrease as the underlying epidermis was reached. Notably, after 24 hours, the ion intensity associated with the molecular ion of cyproconazole exhibits a diminished localisation within the stratum corneum and an elevated localisation within the underlying epidermis, signifying a deeper penetration into the skin. The relatively hydrophobic nature of the active

ingredient (LogP 2.9) suggests a rationale for its potential retention within the *stratum corneum*. According to Fick's law, the compound may diffuse slowly into the underlying epidermis when there is a significant concentration difference between these two regions, as previously reported by Sabri *et al* [18]. These findings provide insights into the kinetics of cyproconazole permeation and highlight the potential role of the *stratum corneum* as a reservoir for this hydrophobic compound. In comparison to the LC-MS/MS recoveries, the OrbiSIMS data suggests a notable increase in permeation of cyproconazole into the *stratum corneum* between 4 hr and 7 hrs however, the LC-MS/MS recoveries across the three replicates for the exposure times show a decrease from 0.86% to 0.68%. The difference is not statistically significant. In contrast, following 24 hrs of exposure we see a decrease in abundance of cyproconazole in the s*tratum corneum* according to the depth profile data however, the LC-MS/MS recoveries suggest an increase of 2.27%. The LC-MS/MS quantification is unclear due to the inherent flaws with carry over issues with this analyte thus affecting recoveries (<50%).

Interestingly, even at this relatively low applied concentration of 1% v/v, each of the co-formulants can also be observed throughout the series of experiments. After a 4 -hour exposure, minimal permeation of the formulation constituents into the skin was observed. The ion intensities of each co-formulant were notably high at the skin surface, followed by a rapid decrease to baseline within the mid regions of the *stratum corneum*. These findings suggest limited penetration of the co-formulants beyond the superficial layers of the skin, highlighting the role of the *stratum corneum* in acting as a barrier to their percutaneous uptake. Subsequently, following 7 -hours of exposure, a notable shift in the permeation behaviour of the

emulsifiers, Emulsogen EL 360 ($C_{11}H_{19}O_2^-$), Atlox^{TM} 4838B ($C_6H_5SO_3^-$) and solvent, Solvesso^{TM} 200 ND ($C_{14}H_{11}^+$) is observed. All three excipients exhibit an increase in ion intensity at the surface of the *stratum corneum*, followed by a relatively stable distribution within the underlying epidermis, indicating a uniform presence across the skin. After 24 -hours of exposure, distinct distribution patterns emerge among the emulsifiers. The ion intensity of Emulsogen EL 360 appears to be at baseline across the entire skin, implying potential complete translocation through the skin. The observed trend may stem from the Emulsogen EL 360 containing 'free' castor oil, known for its affinity for skin as an emollient thus allowing the permeation. In contrast, the ion intensities of Atlox^{TM} 4838B and Solvesso^{TM} 200 ND demonstrate an increase at the surface of the stratum corneum, peaking in the upper layers of the skin, and gradually decreasing as the underlying epidermis is reached. This distribution trend suggests Atlox^{TM} 4838B and Solvesso^{TM} 200 ND may have a higher degree of localization within the *stratum corneum* compared to the 7 -hour exposure period.

The utilization of the OrbiSIMS technique has facilitated the *in-situ* visualization of the distribution patterns of the complete CCZ EC formulation, eliminating the need for conventional solvent extraction methods, fluorescent labelling, or complicated sample preparation. The obtained skin permeation data, along with the analysis of wheat leaf uptake, offers crucial insights which can be utilised in the development of pesticide formulations with improved delivery within targeted species while minimising the risk of unintended percutaneous uptake for agricultural workers and spray operators.

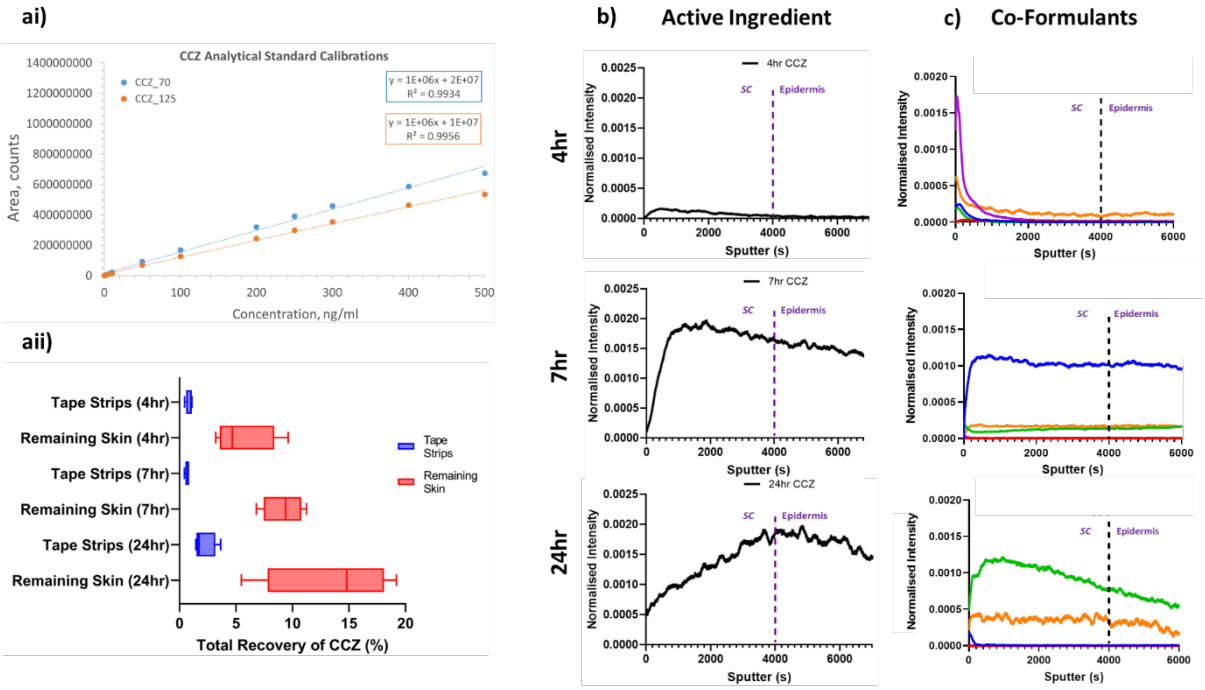


Figure 3.4. OrbiSIMS depth analysis of the fungicide, CCZ EC, through ex vivo porcine skin including the quantification of the dermal absorption of cyproconazole using LC-MS/MS. (ai) LC-MS/MS analytical standard calibrations.) (aii) Total recovery of cyproconazole in the tape strips and remaining skin post-Franz cell permeation after 4, 7 and 24 -hour exposure intervals. (b) Depth distributions of cyproconazole (ClC6H4CH2+) in ex vivo porcine skin at 4, 7, and 24 hours. (c) Distribution trends for the CCZ EC formulation excipients in ex vivo porcine skin after 4, 7 and 24 -hour exposure intervals.

3.5 Conclusions

The utilization of the OrbiSIMS depth profiling has provided the ability for label-free, in situ analysis of the molecular composition of wheat leaves. By employing the chemical filtering process, we successfully identified and assigned putative molecular species across seven distinct compound classes, including fatty acids, aldehydes, amino acids, nucleic acids, phospholipids, vitamins, and flavonoids. Notably, the absence of solvent-based extraction methods enabled us to precisely map the depth distribution of these molecular species within specific layers of the leaf. In particular, this analysis uncovered the presence of fatty acids associated with the cuticular cutin and aldehydes associated with epicuticular waxes, elucidating their abundance at the leaf surface and highlighting the intricate

interplay between these two layers. These findings offer valuable insights into the chemical architecture of wheat leaves and contribute to our understanding of the complex molecular landscape within plant tissues.

Furthermore, our study encompassed an additional analysis of exogenous compounds in addition to endogenous species within the leaf. The depth distribution of the CCZ EC fungicide formulation (active ingredient and all co-formulants) in both wheat leaves and porcine skin, considering different exposure durations. Notably, a complete formulation has been successfully tracked *in-situ*, obviating the necessity for solvent extraction or fluorescent labelling. This has been performed at relevant concentrations including the as applied, 1% v/v dilution (<100 ppm). The outcomes derived from this investigation establish a solid basis for advancing targeted pesticide delivery methods, thereby helping mitigate some of the recognized detrimental consequences associated with conventional approaches.

Chapter 4. OrbiSIMS Screening of Active Ingredients spanning Agrochemical, Pharmaceutical and Cosmetic Industries

4.1 Abstract

Franz cell diffusion stands as a frequently employed method for investigating the dermal absorption of various compounds utilised in pharmaceutical, cosmetic, and agrochemical applications. However, a primary limitation of this methodology arises when the test compound remains undetectable in the skin tissue following the procedure, resulting in inefficiencies and cost ineffectiveness. The OrbiSIMS is a relatively recent technique that can be employed for the label-free assessment of *in-situ* analyte absorption with sub-micron resolution. Here we report a high-throughput screening of 20 active ingredients relevant to the pharmaceutical, cosmetic and agrochemical fields within porcine skin homogenate to assess the sensitivity of the technique. Additionally, we effectively assessed the distribution patterns of a multi-component agrochemical formulation comprising three commonly used fungicidal active ingredients; cyproconazol, isopyrazam, and mefenoxam across *ex vivo* skin. The findings indicated, mefenoxam demonstrated minimal permeation across the entire membrane, however isopyrazam exhibited the highest penetration with cyproconazole displaying relatively low percutaneous absorption.

4.2 Introduction

The skin stands as the largest organ of the human body, forming a formidable primary physical and sensory barrier to the environment. Comprising three discrete layers, the epidermis establishes a formidable barrier against external biotic and abiotic stresses[279]. The dermis, functioning as a structural support[280] also plays a pivotal role in thermoregulation[281] and aids in sensation[282]. Meanwhile, the hypodermis serves as an energy reservoir[283] and provides attachment points connecting the skin to skeletal muscle and bone structures[284].

Recent research has highlighted the skin as an accessible and promising avenue for pharmaceutical[285] and cosmetic delivery[286]. This preference is attributed to several advantages, such as circumventing the first-pass metabolism[287], the skin acts as a reservoir for sustained drug delivery[288], and the presence of numerous dermal sites which contribute to minimizing toxicity and the potential for adverse systemic effects[289]. On the contrary, the skin, specifically the *stratum corneum*, is also a remarkable barrier to the topical absorption of compounds. Toxicologists routinely examine the percutaneous permeation kinetics of substances as an integral component of their standard investigative methodologies aimed at evaluating potential adverse health effects[149,290]. Agrochemicals represent a category of substances subject to regular scrutiny for dermal absorption[291,292,293,294], particularly concerning the possibility of excessive exposure among farmers during the application of these chemicals to crops.

Currently, Franz diffusion cells[156] are the 'gold' standard for the assessment of dermal penetration, enabling the application of test compounds to the skin and

facilitating the quantification of the permeation rate. These static diffusion cells replicate physiological skin conditions, providing a framework for 'realistic' absorption kinetics. However, a typical regulatory study involves radiolabelling the active ingredients in a formulation followed by liquid scintillation counting. Although this method provides accurate measures of the active ingredients within the skin, formulations containing more than one active ingredient require individual experiments with each radiolabelled active in turn. This therefore results in a relatively low throughput.

Additionally, the efficacy of Franz cell permeation studies can be compromised if the test compound remains undetectable at the target site, leading to inefficiencies and resource wastage. The OrbiSIMS[30] is a recent innovation in secondary ion mass spectrometry (SIMS) offering the ability to rapidly screen compounds *in-situ* at sub-micron levels.

Based on the ToF-SIMS platform, the OrbiSIMS is hybridised with an Orbitrap™ mass analyser, providing exceptional improvements in mass resolution (>240,000) and the incorporation of large cluster ion beams has significantly improved chemical sensitivity[295]. Due to the numerous advantages the technique offers, we have witnessed an increase in the implementation for biological sample analysis[296,214,213]. Passarelli[215] displayed the capability of the OrbiSIMS with the label-free detection of etoposide and olaparib in various sections of *ex vivo* brain at relatively low concentration levels. Starr *et al*[297] has demonstrated the penetration of the collagen synthesis promoting, Pal-GHK, within *ex vivo* skin, specifically the various layers of the *stratum corneum* at sub-micron levels.

Assessing the sensitivity of an analytical method is crucial to determine its capability to detect a wide spectrum of compounds with various chemistries. The capacity to detect these compounds within the skin is essential, considering that matrix effects can influence detection, and compounds inherent in the skin may overlap with the test compounds. In our prior investigation (**Chapter 3 Section 3.4.3**), we assessed the label-free dermal absorption of a comprehensive model agrochemical formulation, elucidating the localisation of each component within distinct layers of the *stratum corneum*. In this study, we present the percutaneous uptake of a model agrochemical formulation containing multiple active ingredients (cyproconazole, mefenoxam, and isopyrazam) at concentrations relevant to agricultural application. Additionally, we conduct a high-throughput screening of 20 compounds spanning the pharmaceutical, cosmetic, and agrochemical industries to assess the sensitivity of the OrbiSIMS across a spectrum of diverse chemistries.

4.3 Materials and Methods

4.3.1 Reagents

HPLC grade methanol, acetonitrile and phosphate buffered saline tablets were purchased from Sigma Aldrich, UK. Cyproconazole, Isopyrazam, Metalaxyl-M, Thiamethoxam, Trinexapac-ethyl, Glyphosate salt, Acibenzolar s-Methyl, Azoxystrobin and Cyantraniliprole were provided by Syngenta UK.

Cyproconazole, Isopyrazam, Mefenoxam, Synperonic™ L11, Solvesso™ 200 ND, Emulsogen EL 360, Atlox™ 4838B, Hallcomid® M-8-10 and an emulsifiable concentrate formulation containing Mefenoxam, Isopyrazam and Cyproconazole were provided by Syngenta, UK (see **Table 4.1**).

Table 4.1: The composition of the multi-AI formulation.

Component Trade name	***Component chemical description***	***Typical role in formulation***	***Concentration in formulation (g/100ml)***
Isopyrazam	3-(difluoromethyl)-1-methyl-N-(11-propan-2-yl-3-tricyclo[6.2.1.02,7]undeca-2(7),3,5-trienyl)pyrazole-4-carboxamide	Active ingredient (fungicide)	5
Mefenoxam	Alanine, N-(2,6-dimethylphenyl)-N-(2-methoxyacetyl)-, methyl ester	Active ingredient (fungicide)	5
Cyproconazole	2-(4-Chlorophenyl)-3-cyclopropyl-1-(1*H*-1,2,4-triazol-1-yl)-2-butanol	Active ingredient (fungicide)	5
Emulsogen EL360	Castor oil based ethoxylate, 36 mol EO	Nonionic emulsifier	3
Atlox™ 4838B	Calcium alkylaryl sulphonate in solvent (2-ethylhexan-1-ol)	Anionic emulsifier	3
Synperonic™ L11	Polyoxyethylene (11) lauryl ether	Nonionic emulsifier	3
Hallcomid® M-8-10	Mixture of N, N-dimethyloctanamide and N, N-dimethyldecanamide	Partially water-soluble solvent	24.5
Dowanol™ DPM	Dipropylene glycol monomethyl ether	Water-miscible solvent	24.5
Solvesso™ 200ND	Aromatic solvent derived from crude oil	Water-immiscible solvent	24.2

4.3.2 Porcine Skin Preparation

Ex vivo full-thickness porcine skin specimens were procured from the full thickness regions of 2 - 4week old pigs. Subsequent to a storage period of up to 24 hours at 4^{o}C, the skin underwent thorough cleansing with ultrapure water, and excess hair was meticulously trimmed. Employing a scalpel, any surplus subcutaneous fat and cartilage was delicately excised without compromising the skin. The prepared skin specimens were enveloped with aluminium foil and subsequently preserved at -

20°C for a maximum duration of 3 months before implementation. Sections of 2 mm full-thickness skin were utilized for the purpose of skin permeation analysis.

4.3.3 Franz Cell Permeation Set-Up for Multi-AI Formulation

The ex vivo porcine skin specimens were sectioned into 2 × 2 mm fragments and positioned (dermal side facing up) between the donor and receptor chambers of a Franz-type static diffusion cell. The cell featured an exposed surface area of 1.1 cm^2 and a receptor compartment capacity of 3 ml. An infinite dose of the multi-AI agrochemical formulation, constituting a 1% dilution, was administered through the donor compartment (0.5 ml), while 3 ml of Phosphate Buffer Saline (pH 7.5) was introduced into the receptor compartment. Sink conditions were diligently maintained throughout the experimental duration, during which the skin was exposed to the formulation for 24 hours within a stirring water bath set to 37.5°C.

4.3.4 Preparation of Porcine Skin Homogenates for AI Screening

Ex-vivo full-thickness porcine skin tissue was sectioned into small sections measuring 0.5 × 0.5 mm and weighing 50 mg. These sections were then placed in a homogenizer microtube, along with 2 beads of 6 mm in diameter and 1 ml of deionized (DI) water. The skin underwent homogenization using the BeadBug 3 instrument at 10,000 rpm for a duration of 180 seconds. Subsequent to homogenization, the skin was spiked with 100 µl of a 10 mg/ml active ingredient, followed by vortexing for 30 seconds. Specific details regarding the solvents employed in this process can be found in **Table 4.1**. The prepared skin was then situated on a microslide and subjected to dehydration using a vacuum oven for a period of 2 hours, rendering it ready for subsequent analysis.

4.3.5 OrbiSIMS Analysis of Skin with Multi-AI Formulation and AI Screening

Single-beam depth analysis was employed with the OrbiSIMS, utilizing an Ar_{3000}^{+} cluster primary ion source operating at 20 keV and a GCIB current of 218 pA. For the acquisition of depth profiles of porcine skin, a 20 keV Ar3000+ ion beam with a 20 µm diameter was employed in a random raster mode, featuring a crater size of 280 × 280 µm and a total ion dose ranging from 1.17 - 1.27×10^{17}ions/cm^2. Argon gas flooding was implemented for charge compensation, maintaining a chamber pressure of 9 × 10^{-7} bar. The cycle time was set at 200 µs, with the optimal target potential averaging approximately -384.5 V. Depth profiles were collected in both positive and negative polarities, with a mass resolution of 240,000 at 200 m/z, a mass range spanning 75 to 1125 m/z, and an injection time of 500 ms. The spiked skin homogenates were also analysed with the aforementioned parameters however, each sample was analysed for 250 scans. Data analysis was executed using Surface Lab 7.1 (IONTOF GmbH).

4.4 Results

4.4.1 Multiple-AI Agrochemical Formulation Delivery Through Skin

Previous studies, as detailed in Chapter 2 and 3, delved into the dermal absorption of an anti-aging active ingredient (Pal-GHK) and a multi-component agrochemical formulation at concentrations applicable to real-world conditions. Although this is useful for understanding permeation kinetics and enabling improved product development, the method has a relatively low throughput. As such, an investigation has been carried out to establish if multiple AIs could potentially be used in the same formulation simultaneously and therefore spatially resolved within the skin.

The positive polarity spectra, obtained through OrbiSIMS depth profiling in the range of 100 – 150, 150 – 200, 200 – 260 and 270 – 285 and 350 - 400 *m/z*, is illustrated in **Figure 4.1a-e** respectively, for treated porcine skin samples containing the multi-AI agrochemical formulation alongside control porcine skin. The molecular ion fragments specific to the active ingredients, including cyproconazole [$ClC_6H_4CH_2^+$], mefenoxam [$C_{15}H_{22}NO_4^+$] and isopyrazam [$C_{20}H_{24}F_2N_3O^+$], are exclusively detected in the spiked skin samples, with no presence in the control skin samples (**Figure 4.1a, d, e)**. This establishes them as effective diagnostic ions for monitoring permeation into the skin.

Notably, the endogenous species were also identified in both skin sample types, with **Figure 4.1b and c** depicting the molecular ions, $[M\text{-}H]^+$, of two example native compounds, phosphocholine [$C_5H_{15}NO_4P^+$] and palmitic acid [$C_{18}H_{33}O_2^+$]. The relative intensities exhibited by both of these endogenous compounds in both skin sample types are comparable. This would be beneficial for evaluating the impact of the dermal absorption of substances on the skin structure. Particularly, the distribution changes of key compounds present within the skin which allow the

determination of specific skin layers as function of analysis depth as shown in the native skin and leaf analysis (Chapters 3).

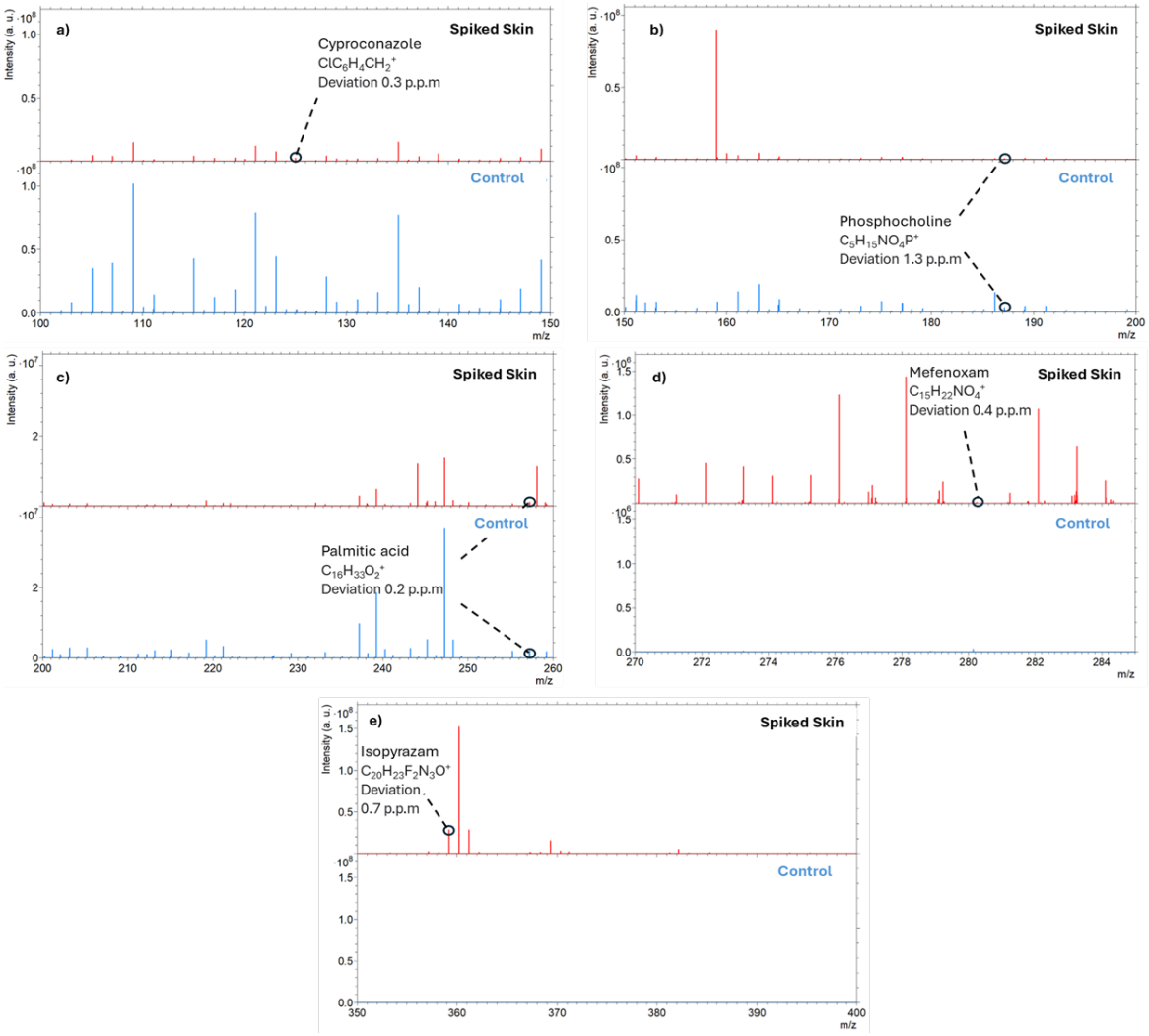


Figure 4.1. OrbiSIMS mass spectra showing the molecular ions identified for the active ingredients within the multi-AI formulation spiked into skin, including two endogenous chemical constituent examples of the skin, specifically **(a)** cyproconazole ([ClC6H4CH2+]) **(b)** phosphocholine fragment, [$C_5H_{15}NO_4P^+$], **(c)** palmitic acid, [$C_{18}H_{33}O_2^+$], **(d)** mefenoxam [$C_{15}H_{22}NO_4^+$] and **(e)** isopyrazam in spiked skin, [$C_{20}H_{24}F_2N_3O^+$].

Our earlier investigations using OrbiSIMS depth profiling, have successfully demonstrated the dermal absorption of a relatively low concentration (< 100 ppm) of an active ingredient (Pal-GHK) from an applied cosmetic formulation (**Chapter 2, Section 2.4.5**). Subsequent studies then demonstrated the same capability for a

model fungicide agrochemical formulation (**Chapter 3**). In this case, the method provided an *in situ* and label-free assessment of the active ingredient and all co-formulants at relatively low (applied) concentrations. Here the OrbiSIMS depth profiling approach has been extended to evaluate the *in situ* distribution of a model agrochemical formulation containing three active ingredients; cyproconazole, mefenoxam and isopyrazam at concentrations relevant to 'real life' conditions (1% v/v dilution), as displayed by the depth profiles in **Figure 4.2a**.

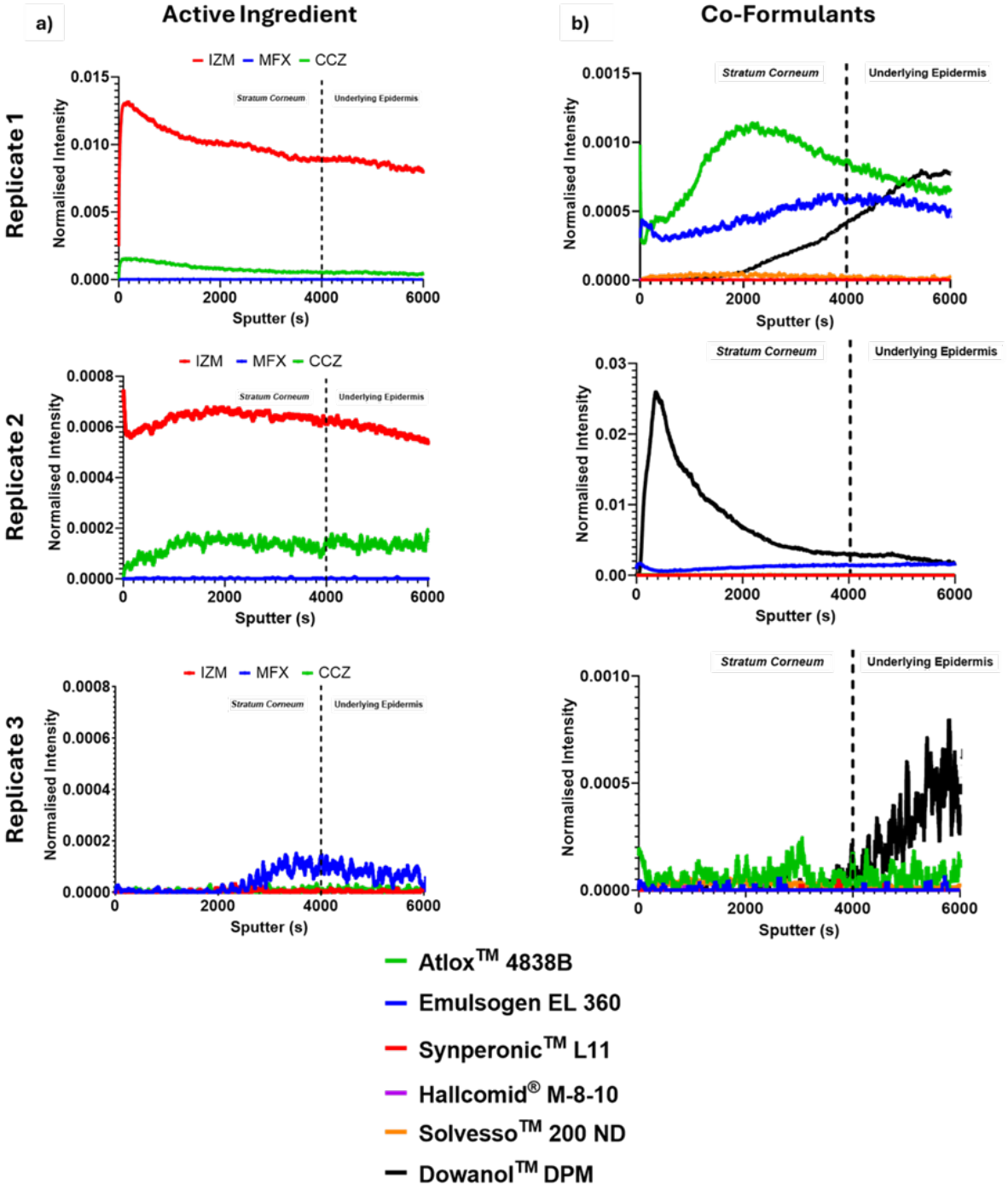


Figure 4.2. OrbiSIMS depth profiles of a multi-AI agrochemical formulation through *ex vivo* porcine skin showing **(a)** isopyrazam ($C_{20}H_{24}F_2N_3O^+$), mefenoxam ($C_{15}H_{22}NO_4^+$) and ($ClC_6H_4CH_2^+$) and **(b)** six co-formulants (Emulsogen EL 360- non-ionic emulsifier, Hallcomid M-8-10 AI carrier solvent, Synperonic™ L11 non-ionic emulsifier, Atlox™ 4838B- anionic emulsifier, Solvesso™ 200 ND- water immiscible solvent, Dowanol™ DPM water miscible solvent) through *ex vivo* treated porcine skin, including the replicate depth profiles.

Previously, the dermal depth distribution of cyproconazole in the CCZ EC formulation was revealed, as shown in **Chapter 3**, **Figure 3.4**. It is evident that the cyproconazole has penetrated deeper into the *stratum corneum* and into the epidermis. Cyproconazole ($ClC_6H_4CH_2^+$) demonstrates a similar behaviour with the multi-component formulation where the active ingredient is also localised in the underlying epidermis. However, there appears to be a steady distribution within the *stratum corneum* and epidermis possibly caused by the lower concentration of the carrier solvent, Hallcomid® M-8-10, used in the latter formulation causing reduced permeation.

The presence of isopyrazam was observed using the ion ($C_{20}H_{24}F_2N_3O^+$). After 24 hours of exposure, the ion intensity initiates at baseline, rapidly increases, reaching a maximum at the upper region of the *stratum corneum*, followed by a subsequent gradual decrease as the underlying epidermis is reached. Conversely, the ion intensity for mefenoxam ($C_{15}H_{22}NO_4^+$) remains consistently at the baseline throughout the skin. The illustrated trends imply isopyrazam permeates to a greater extent compared to cyproconazole, while mefenoxam exhibits no discernible absorption into the skin.

From the replicate depth profiles (**Figure 4.2 a,b,c**), it is apparent that Replicates 1 and 2 portray similar permeation kinetics for the active ingredients. Conversely, Replicate 3 displays minimal permeation of all active ingredients except mefenoxam, which has penetrated into the deeper regions of the *stratum corneum* and into the earlier portions of the epidermis. This variation is proposed to result from the use of biological material which can vary or may result from an as-yet unidentified issue in the third Franz cell experiment.

The permeation kinetics may be influenced by the lipophilicity of each of the active ingredients. Isopyrazam, with a quoted LogP of 4.25, exhibits higher lipophilicity compared to cyproconazole (2.91) and mefenoxam (1.71), indicating higher LogP values are correlated with enhanced permeability. Lee *et al*[298] further reinforced the relationship between lipophilicity and skin permeability, demonstrating the increase in skin penetration of drugs including lidocaine, ketoprofen and ibuprofen. The observed trends are likely solely due to the LogP values as opposed to the ion intensities of the compounds (will be discussed later). Molecular weight serves as another significant parameter commonly employed to anticipate skin permeation, wherein compounds below 500 Da typically demonstrate greater penetration. However, the distribution profiles reveal a departure from this norm for these active ingredients. Contrary to expectations, an escalation in molecular weight resulted in an increase in penetration. It can be deduced the increase in permeation can be attributed to the lipophilicity of the compound but also potentially the toxicity of the agrochemical. It is widely accepted that these compounds can adversely affect the chemistry and composition of the skin[299,300,301]. It is possible that in this case the increase in permeation may be attributed to the extent of the damage to the skin which in turn increases the penetration of the compound.

Significantly, as with previous work using single AIs (**Chapter 2, Section 2.4.5**) each individual component of the formulation is also identified within the skin at the 1% v/v concentration. Following 24 hours of exposure, a variety of different trends are evident for each co-formulant, portraying distinct localisations within the various skin layers. The ion intensities (**Figure 4.2b, Replicate 1**) for the emulsifying agent,

Synperonic™ L11 ($C_{12}H_{23}O^-$), and solvents, Hallcomid M-8-10 ($C_9H_{18}NO^-$) and Solvesso™ 200 ND ($C_{14}H_{11}^+$) consistently remain at baseline, indicating minimal to no dermal absorption. Notably, Hallcomid® M-8-10 exhibits little to no skin penetration despite serving as a carrier solvent for the active ingredients. The data suggests the *stratum corneum* serves as an effective barrier against these compounds, reducing the risk of exposure to agricultural workers. Conversely, the ion intensity for the anionic emulsifier, Atlox™ 4838B ($C_6H_5SO_3^-$), gradually increases reaching a maximum in the middle regions of the *stratum corneum* followed by a subsequent gradual decrease into the underlying epidermis. Similarly, the ion intensity for the castor oil based ethoxylate, Emulsogen EL360 ($C_{11}H_{19}O_2^-$), maintains a relatively stable distribution throughout the skin in contrast to Dowanol™ DPM, exhibiting a continued increase, reaching a peak in the surface layers of the epidermis. Since Emulsogen EL360 is an oil-based compound, it can readily traverse the barrier layer. As indicated by prior research[302,303,304], oils exhibit the capacity to markedly enhance the penetration of other compounds, and this phenomenon may be applicable in this context.

The replicate datasets (**Figure 4.2b**) reveal some variations in the co-formulant behaviour, showing differences in the distribution patterns within the skin. However, higher permeation of Emulsogen EL 360 and Dowanol™ DPM is consistently observed compared to the other constituents of the formulation. Emulsogen EL 360 demonstrates permeation into the underlying epidermis, while Dowanol™ DPM is localised in the outermost region of the *stratum corneum* in Replicate 2 and exhibits absorption into the epidermis in Replicate 3. The observed differences in the penetration of co-formulants and active ingredients may be

attributed to inherent variations in biological samples, leading to varied results. Specifically, for Replicate 3, potential issues with the Franz cell experiment are apparent, raising the likelihood of formulation loss and consequently reduced skin exposure.

The combination of Franz cell diffusion tests and the OrbiSIMS effectively facilitated the label-free, *in situ* identification and visualisation of the distribution of a complete formulation eliminating the need for complex sample preparation and solvent extraction procedures. Based on the preliminary experiments it could be possible to apply this methodology to systems with multiple AIs to accelerate the initial skin permeation evaluation phase. Evidently, the findings from this study portray, the dermal absorption of compounds can be predicted by their respective LogP values. Molecular weight is another parameter generally used for the prediction of skin permeation, with compounds below 500 Da exhibiting larger penetration.

Variability observed in the replicate Franz cell studies may stem from inherent differences in biological samples such as skin, as well as potential issues within the Franz cell experimental setup. A more comprehensive investigation is needed to delineate the underlying factors contributing to the observed variability in results. It is possible to control Franz cell variability by employing tritiated water[305] and possibly utilising reference samples for the validation of the technique[306].

4.4.2 Evaluation of the Sensitivity of the OrbiSIMS for Active Ingredients

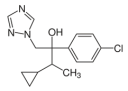
The Franz cell method is a regulatory requirement in the agrochemical industry, proving to be a relatively robust and reliable approach for the assessment of the dermal absorption of compounds. We have demonstrated the efficacy of the approach in tracking a single AI (Chapter 2), an AI with co-formulants (Chapter 3) and a formulation containing multiple AIs (Chapter 4). However, a notable limitation of the method is compounds can often go undetected, including the laborious and cost-ineffectiveness nature of the technique.

Dosing skin homogenates is routinely used in skin research[307,308,309] for the prediction and classification of the behaviour of compounds. A comparison of the ion intensities of namely, cyproconazole and Pal-GHK, to concentrations in spiked skin homogenates would provide essential insights into whether a compound can be detected in the skin and yield suitable permeation data.

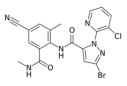
A small database comprising 20 frequently employed active ingredients across the agrochemical, pharmaceutical and cosmetic sectors were spiked in skin homogenates at a concentration of 10 mg/ml, these are outlined in the summary **Table 4.1**. Molecular ions, $[M\text{-}H^+]$ and $[M\text{-}H^-]$, of 12 compounds were identified in both positive and negative polarities, with four compounds detectable exclusively in one polarity and another four compounds detectable solely as fragments. Molecular ions are generally preferred, attributed to their ability to offer higher sensitivity and specificity when identifying a compound in a complex biological system. However, the detected fragment ions are of significant mass and representative of the compound structure, including their absence in the native skin chemistry.

Table 4.3. A breakdown of the active ingredients investigated in this study, encompassing their respective structures, structural formulas, molecular weights and molecular ions/fragments identified using the OrbiSIMS.

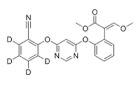
Agrochemicals



1) Cyproconazole
$C_{15}H_{18}ClN_3O$
MW: 291.1138
Molecular Ion/Fragments (*m/z*)
292.1208 (+ve)
290.1074 (-ve)



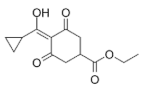
2) Cyantraniliprole
$C_{19}H_{14}BrClN_6O_2$
MW: 472.0050
Molecular Ion/Fragments (*m/z*)
473.0114 (+ve)
470.9986 (-ve)



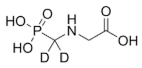
3) Azoxystrobin
$C_{19}H_{14}BrClN_6O_2$
MW: 403.1168
Molecular Ion/Fragments (*m/z*)
406.1403 (+ve)
404.1246 (-ve)



4) Metalaxyl
$C_{15}H_{21}NO_4$
MW: 279.1471
Molecular Ion/Fragments (*m/z*)
277.0051 (+ve)
274.8815 (-ve)



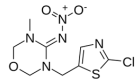
5) Trinexapol-ethyl
$C_{13}H_{16}O_5$
MW: 252.099775
Molecular Ion/Fragments (*m/z*)
x (+ve)
251.0926 (-ve)



6) Glyphosate
$C_3H_8NO_5P$
MW: 169.0140
Molecular Ion/Fragments (*m/z*)
x (+ve)
168.0071 (-ve)

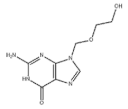


7) Acibenzolar-s-methyl
$C_8H_6N_2OS_2$
MW: 209.9922
Molecular Ion/Fragments (*m/z*)
159.0363 (+ve)
175.0331 (-ve)

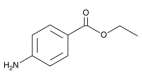


8) Thiamethoxam
$C_8H_{10}N_5ClO_3S$
MW: 291.0193
Molecular Ion/Fragments (*m/z*)
x (+ve)
243.0555 (-ve)

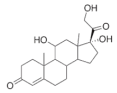
Pharmaceuticals



9) Acyclovir
$C_8H_{11}N_5O_3$
MW: 225.0862
Molecular Ion/Fragments (*m/z*)
226.0935 (+ve)
224.0785 (-ve)



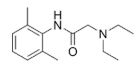
10) Benzocaine
$C_9H_{11}NO_2$
MW: 165.1891
Molecular Ion/Fragments (*m/z*)
166.0862 (+ve)
164.0712 (-ve)



11) Hydrocortisone
$C_{21}H_{30}O_5$
MW: 362.4599
Molecular Ion/Fragments (*m/z*)
363.2165 (+ve)
x (-ve)

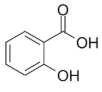


12) Imiquimod
$C_{14}H_{16}N_4$
MW: 240.3036
Molecular Ion/Fragments (*m/z*)
241.1449 (+ve)
239.1297 (-ve)

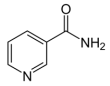


13) Lidocaine
$C_{14}H_{22}N_2O$
MW: 234.3373
Molecular Ion/Fragments (*m/z*)
x (+ve)
183.0119 (-ve)

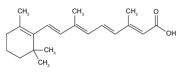
Cosmetics



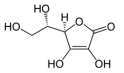
14) Salicylic acid
$C_7H_6O_3$
MW: 138.0317
Molecular Ion/Fragments (*m/z*)
x (+ve)
137.0238 (-ve)



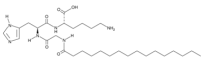
15) Niacinamide
$C_6H_6N_2O$
MW: 122.0480
Molecular Ion/Fragments (*m/z*)
123.0553 (+ve)
121.0403 (-ve)



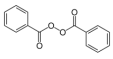
16) Trans-retinoic acid
$C_{20}H_{28}O_2$
MW: 300.2089
Molecular Ion/Fragments (*m/z*)
301.2162 (+ve)
299.1999 (-ve)



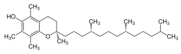
17) Vitamin C
$C_6H_8O_6$
MW: 176.0321
Molecular Ion/Fragments (*m/z*)
x (+ve)
175.0239 (-ve)



18) Pal-GHK
$C_{30}H_{54}N_6O_5$
MW: 578.4156
Molecular Ion/Fragments (*m/z*)
579.4231 (+ve)
577.4050 (-ve)



19) Benzoyl peroxide
$C_{14}H_{10}O_4$
MW: 242.0579
Molecular Ion/Fragments (*m/z*)
243.0652 (+ve)
241.0496 (-ve)



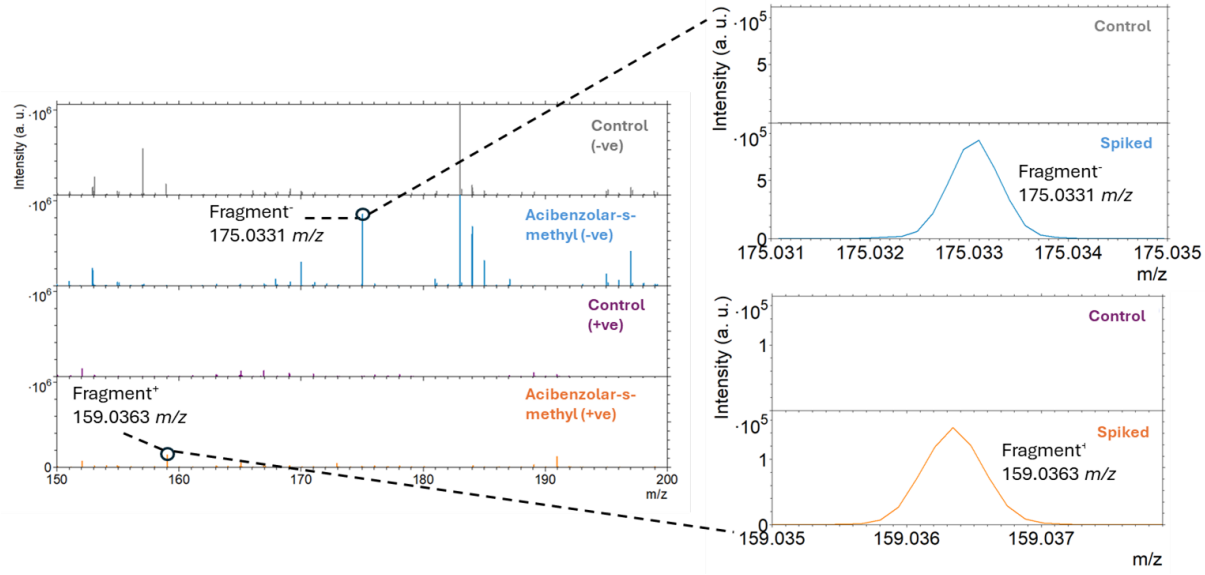
20) Vitamin E
$C_{29}H_{50}O_2$
MW: 430.3811
Molecular Ion/Fragments (*m/z*)
431.3836 (+ve)
429.3712 (-ve)

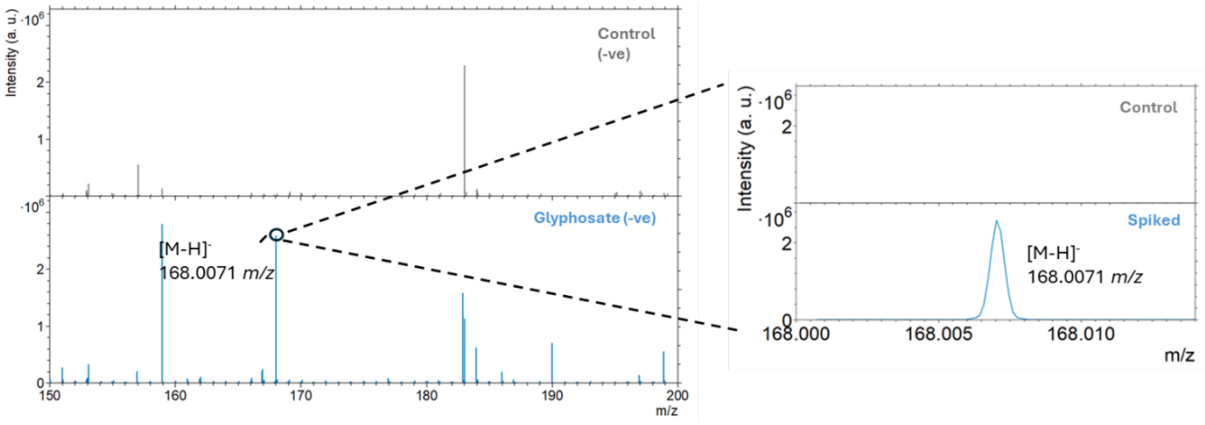
The OrbiSIMS depth profiling spectra in the range of 150 – 500 *m/z* for the agrochemical active ingredients are depicted in **Figure 4.3**. Evidently, the molecular ions, $[M-H]^-$ and $[M-H]^+$, of cyproconazole, azoxystrobin and cyantraniliprole are discernible in positive and negative polarities while the molecular ion for trinexapol-ethyl is exclusively present in the negative polarity.

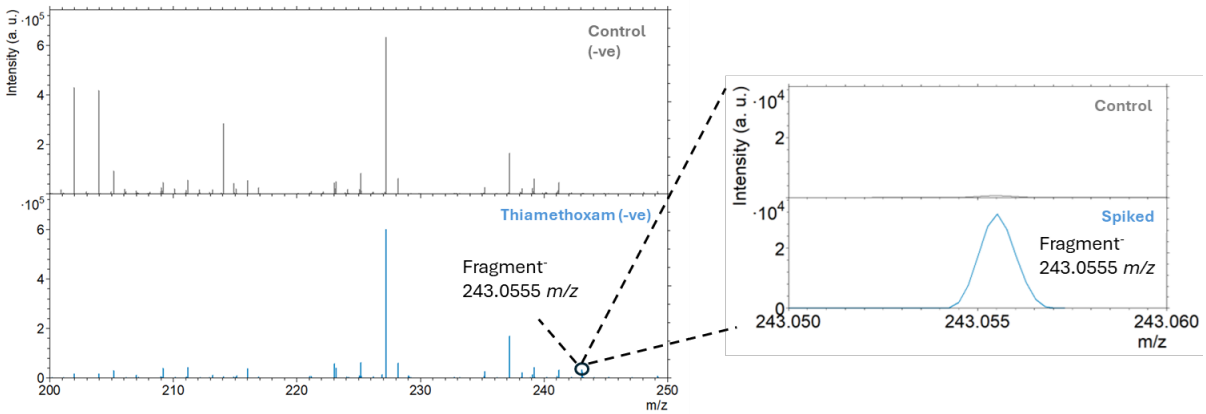
Acibenzolar-s-methyl and metalaxyl can be traced within the skin homogenates as fragments, present in both polarities, however, thiamethoxam can only be observed as a fragment in the negative polarity. Notably, all of the diagnostic peaks identified are completely resolved from the peaks present in the control skin homogenates, allowing for the tracking of these compounds in the skin tissue.

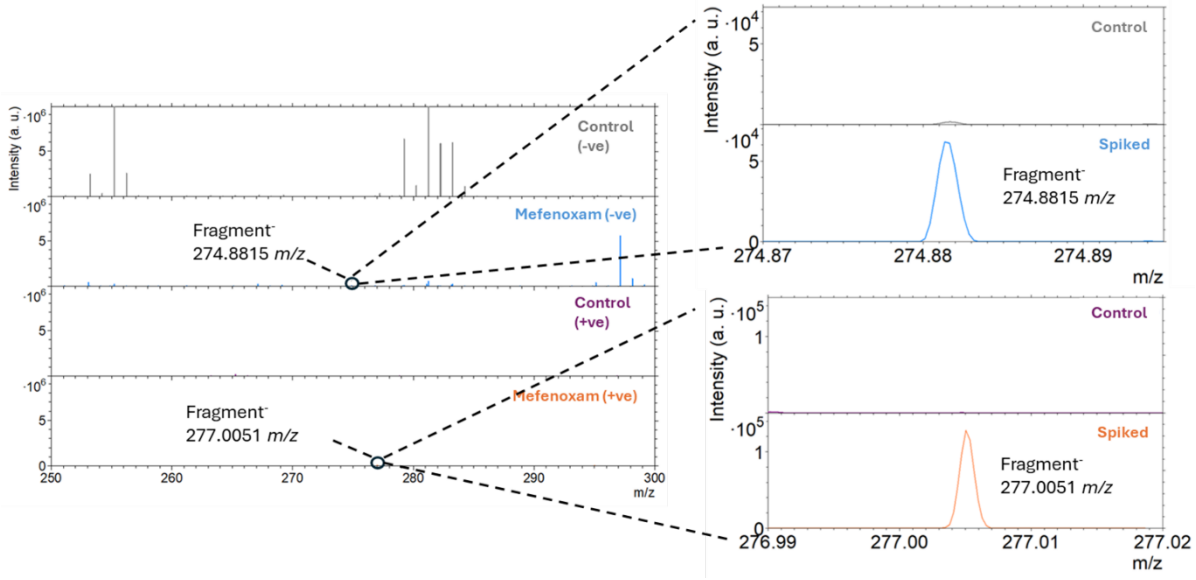
The species with higher molecular mass (>290 *m/z*) particularly, those containing more than one benzene group are identifiable as molecular ions. Polycyclic compounds such as cyproconazole, azoxystrobin and cyantraniliprole, contain various electron-donating groups, including methyl groups ($–CH_3$), ethyl groups ($–C_2H_5$), alkoxy groups (–OR), ethoxy ($–OC_2H_5$) and amino groups ($–NH_2$). These electron-donating groups contribute to increased electron density around the benzene ring, resulting in a stable structure undergoing reduced fragmentation by the Ar_{3000}^+ ion beam. Previous work by Dzepina *et al*[310] and Herring *et al*[311] provides additional support to the notion that these functional groups are responsible for the stabilisation of these structures. Their work demonstrates that the molecular ion was the predominant species identified for the 53 polycyclic compounds analysed using mass spectrometry. The combination of the Ar_{3000}^+ ion beam and Orbitrap™ has led to the detection of numerous molecular ions for

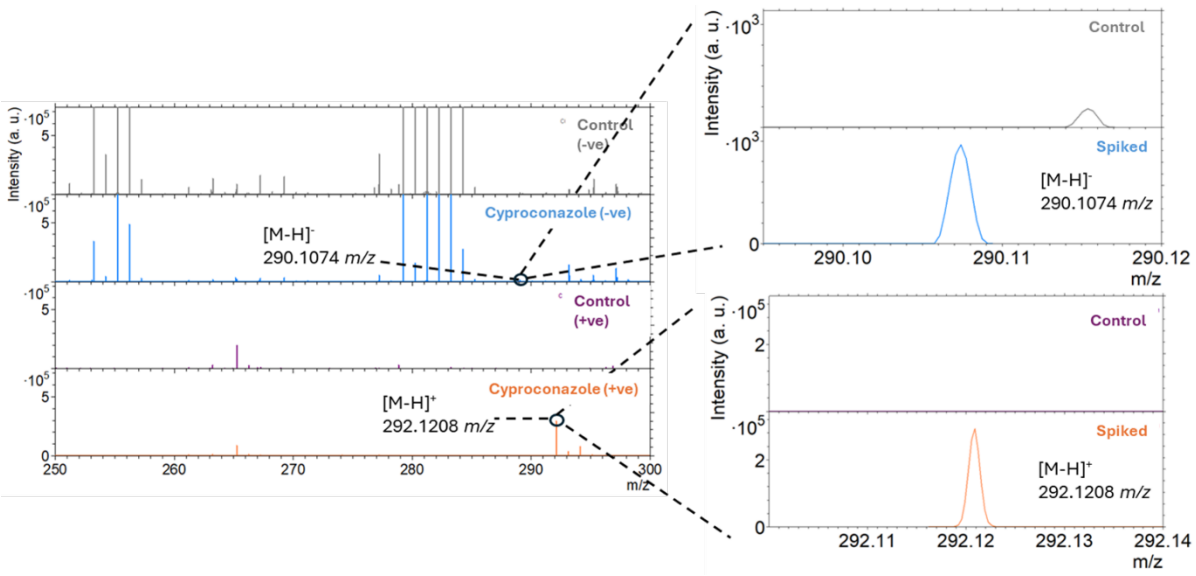
certain compounds in both positive and negative polarities, along with fragment ions of significant mass, representative of the overall compound structure.

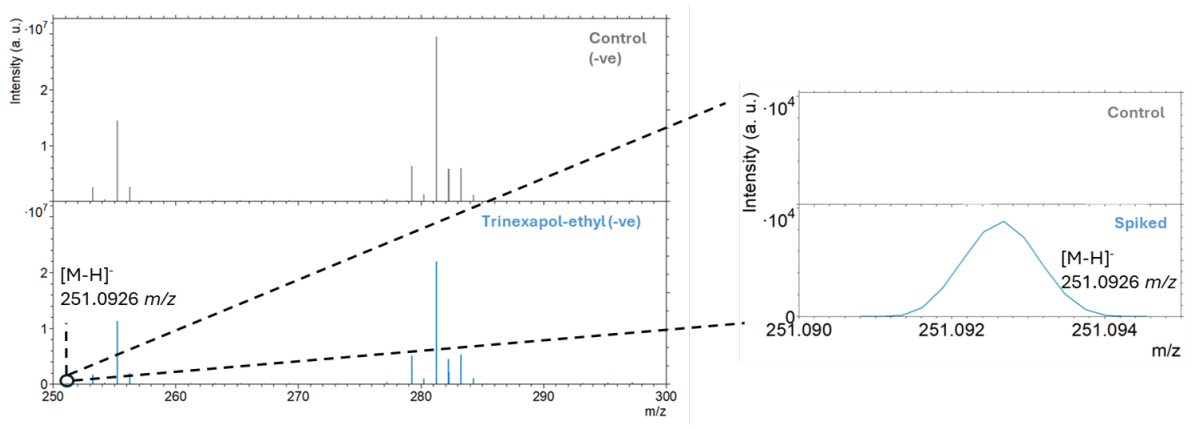







Control
(-ve)
Mefenoxam (-ve)
Fragment⁻
274.8815 m/z
Control
(+ve)
Mefenoxam (+ve)
Fragment⁻
277.0051 m/z
Intensity (a. u.)
m/z
Control
Spiked
Fragment⁻
274.8815 m/z
Fragment⁻
277.0051 m/z


Control
(-ve)
Cyproconazole (-ve)
[M-H]⁻
290.1074 m/z
Control
(+ve)
Cyproconazole (+ve)
[M-H]⁺
292.1208 m/z
Intensity (a. u.)
m/z
Control
Spiked
[M-H]⁻
290.1074 m/z
[M-H]⁺
292.1208 m/z


Control
(-ve)
Trinexapol-ethyl (-ve)
[M-H]⁻
251.0926 m/z
Intensity (a. u.)
m/z
Control
Spiked
[M-H]⁻
251.0926 m/z

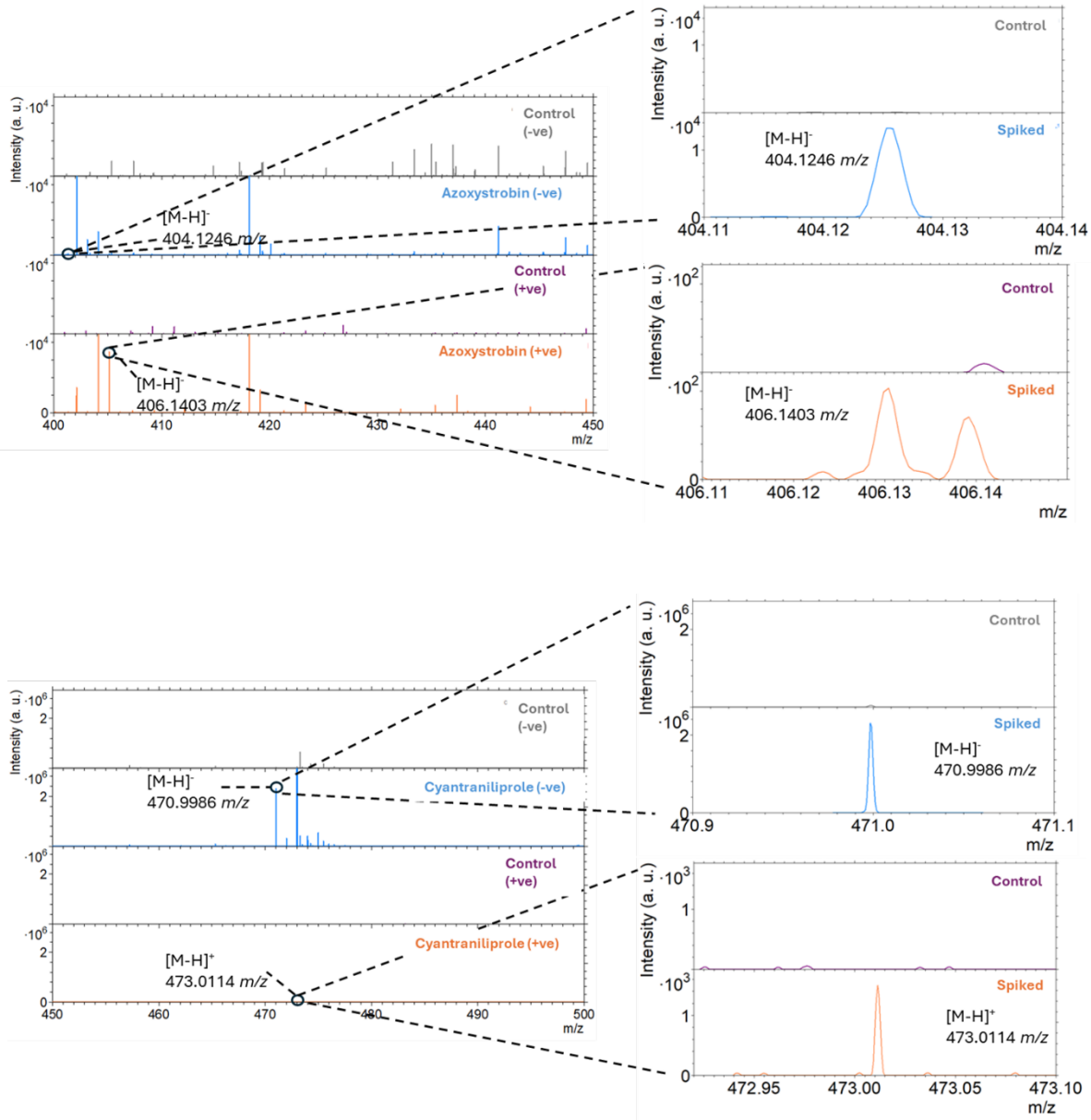
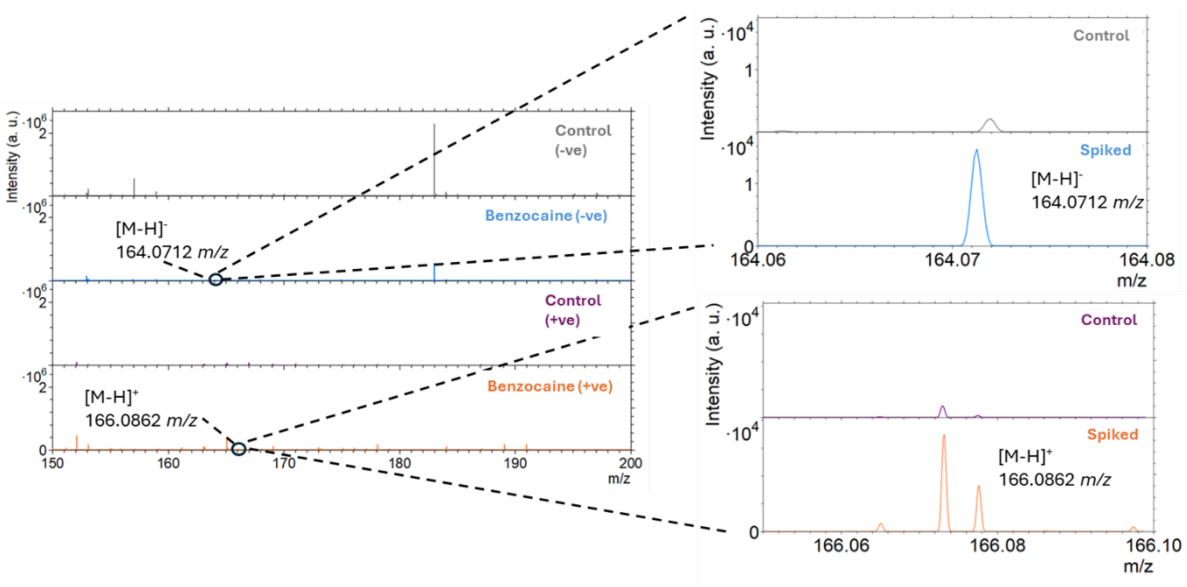
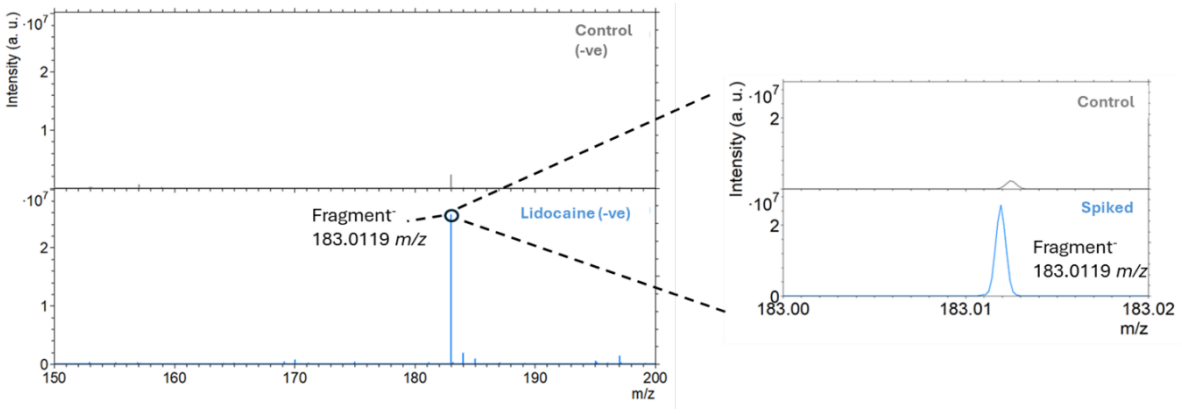


Figure 4.3. OrbiSIMS depth profiling mass spectra of the agrochemical active ingredients spiked in skin homogenates, illustrating the molecular ions and fragments detected within the spiked skin homogenates and their absence in the control skin homogenates.

The OrbiSIMS spectra for pharmaceutical active ingredients spiked into porcine skin homogenates, ranging from 160 to 370 *m/z* overlayed with control skin tissues is presented in **Figure 4.4**. The molecular ions of benzocaine (164.0712 *m/z* and 166.0862 *m/z*), acyclovir (224.0785 *m/z* and 226.0935 *m/z*), imiquimod (239.1297 *m/z* and 241.1449 *m/z*) are observed in positive and negative polarities, while hydrocortisone (363.2165 *m/z*) is identifiable as a $[M-H]^+$ ion in the positive

polarity. Lidocaine (183.0119 *m/z*) was the only compound from the pharmaceuticals to be detected as a fragment ion in the negative polarity with the potential loss of the ethylamine group ($C_2H_5NH_2^-$). Similarly, the diagnostic peaks for the active ingredients are absent in the control skin tissue, facilitating for the tracking of the skin permeation.





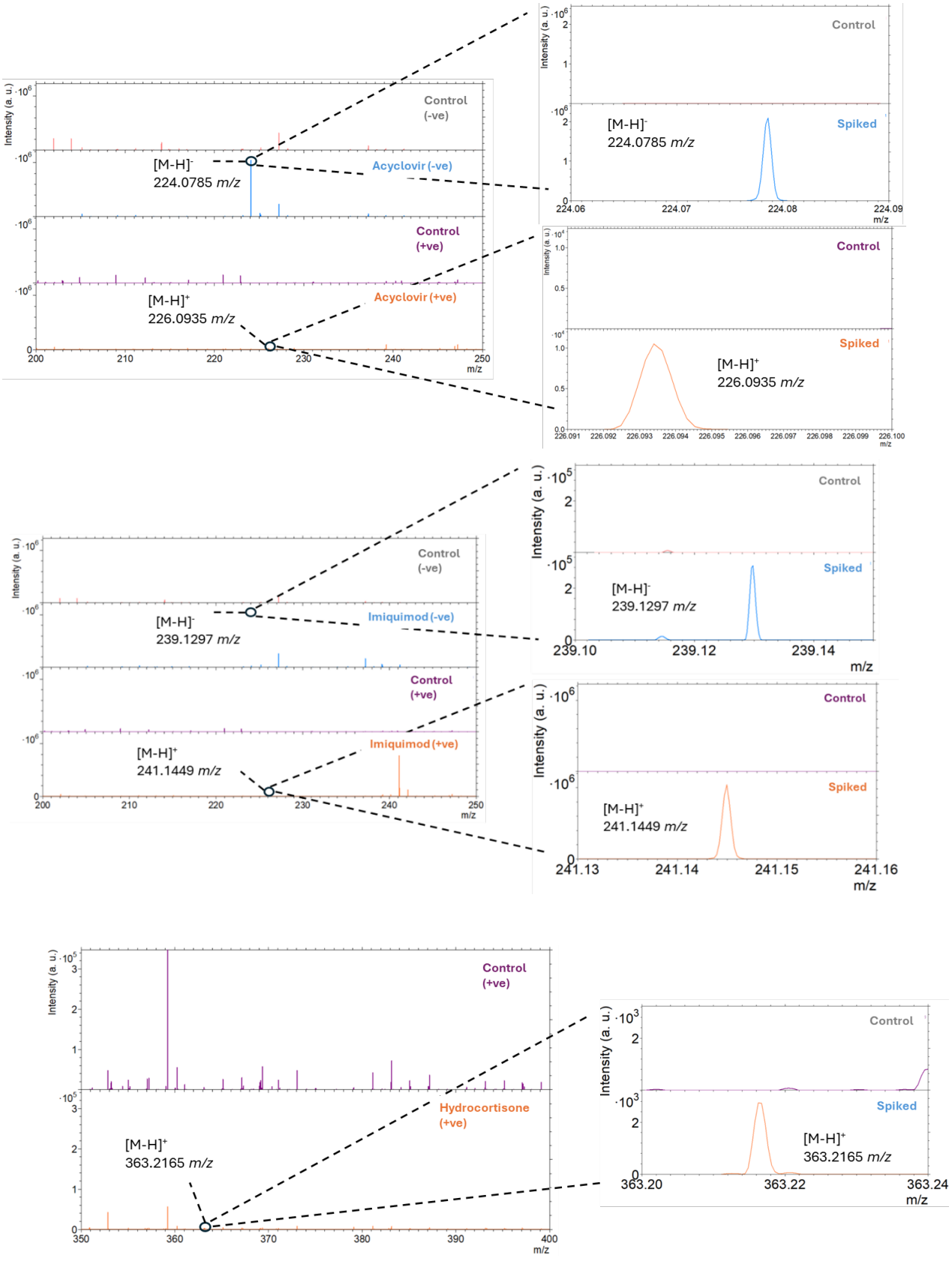
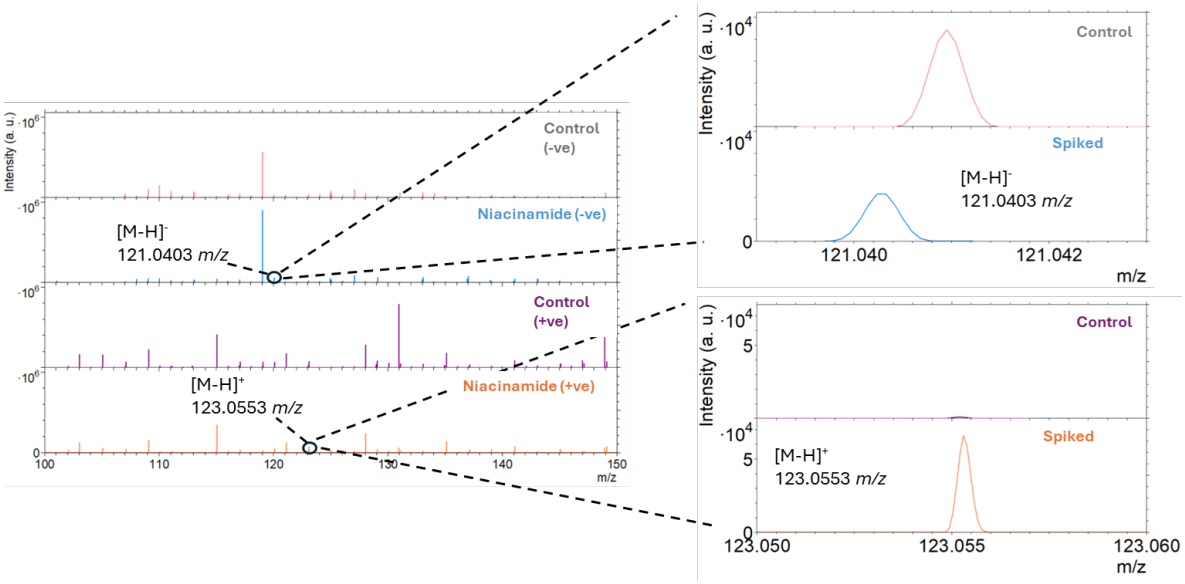
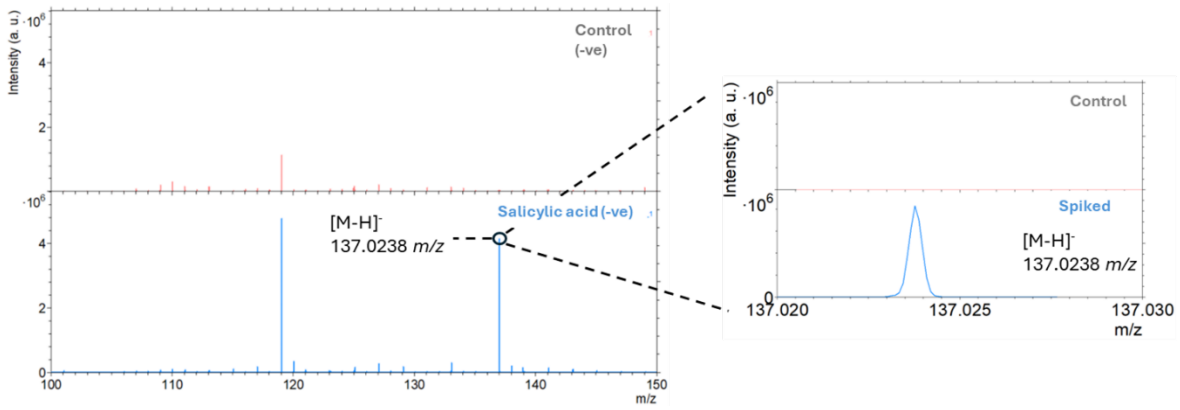


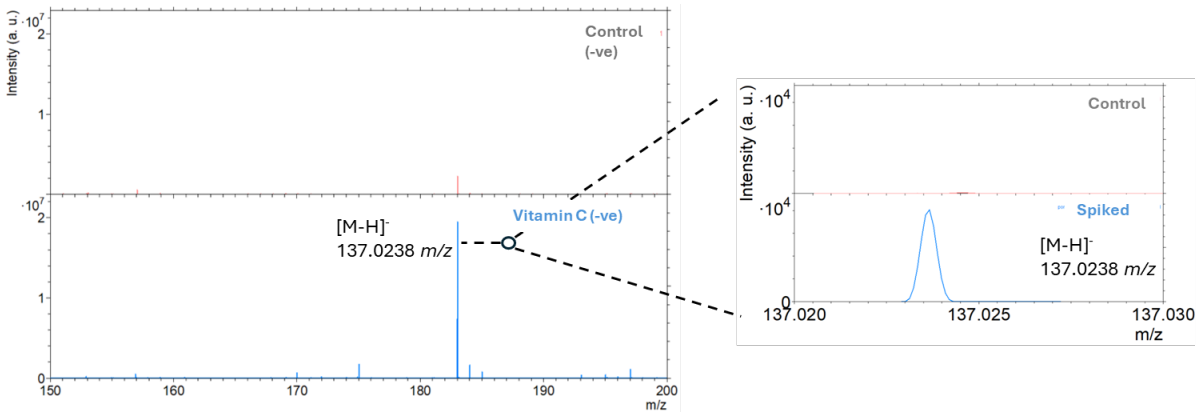
Figure 4.4. OrbiSIMS mass spectra of the pharmaceutical active ingredients spiked in skin homogenates, showing the molecular ions and fragments detected within the spiked skin homogenates.

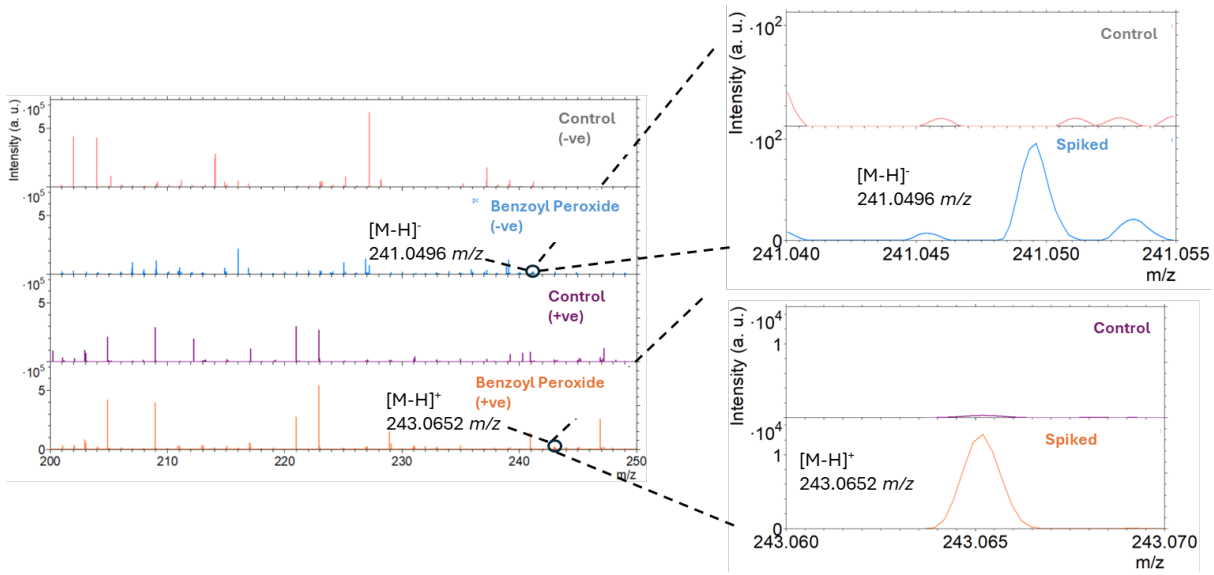
The cosmetic active ingredients were all identified in the skin homogenates as molecular ions in negative and positive polarities except for salicylic acid (137.0238 *m/z*) and niacinamide (175.0239 *m/z*), which were solely present in the negative polarity (**Figure 4.5**).

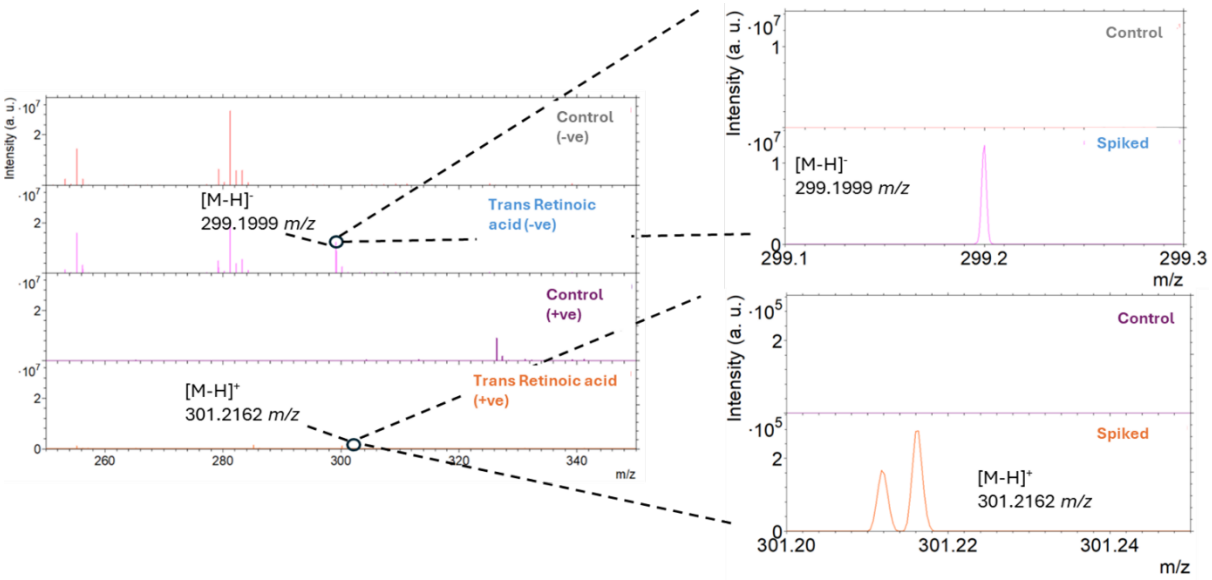
The highlighted ions in **Figures 4.3, 4.4 and 4.5**, are all completely resolved from the peaks present in the skin homogenates however, there is notable variability in the detection of the compounds. This variability in detecting the molecular ions or fragments of certain active ingredients can be attributed to the size of the compounds and functional groups. However, matrix effects exhibited by biological samples such as skin can lead to compound signal suppression including weak ionisation potentials for specific chemistries[312].

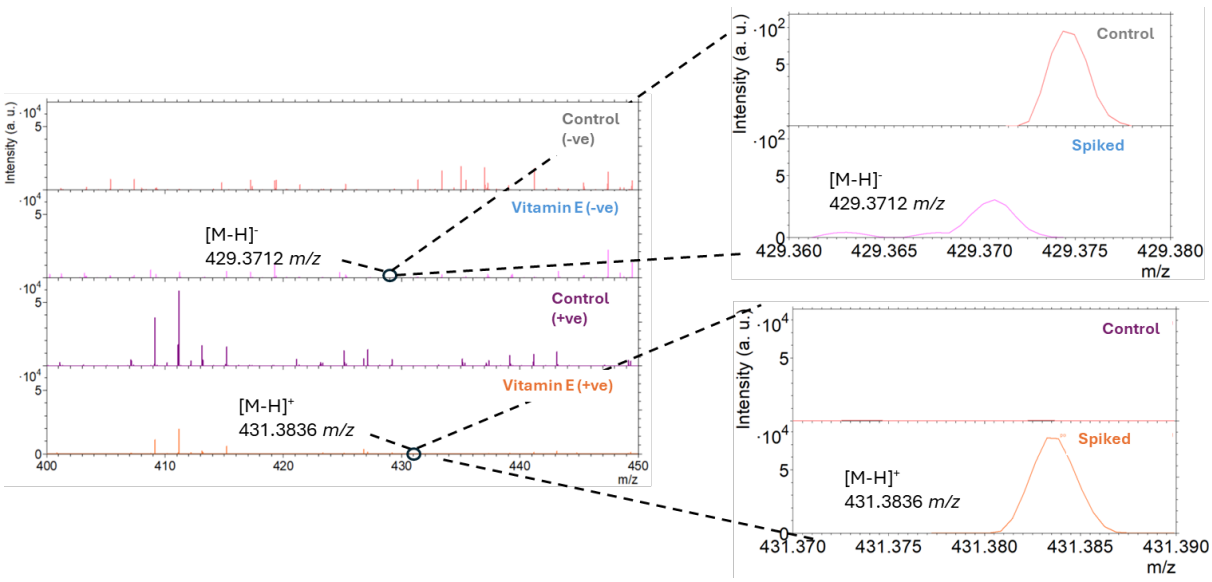



Control
(-ve)
Salicylic acid (-ve)
[M-H]-
137.0238 m/z
Intensity (a. u.)
m/z
Control
Spiked
[M-H]-
137.0238 m/z


Control
(-ve)
Vitamin C (-ve)
[M-H]-
137.0238 m/z
Intensity (a. u.)
m/z
Control
Spiked
[M-H]-
137.0238 m/z


Control
(-ve)
Benzoyl Peroxide
(-ve)
[M-H]-
241.0496 m/z
Control
(+ve)
Benzoyl Peroxide
(+ve)
[M-H]+
243.0652 m/z
Intensity (a. u.)
m/z
Control
Spiked
[M-H]-
241.0496 m/z
Control
Spiked
[M-H]+
243.0652 m/z


Control
(-ve)
[M-H]-
299.1999 m/z
Trans Retinoic
acid (-ve)
Control
(+ve)
[M-H]+
301.2162 m/z
Trans Retinoic acid
(+ve)
Intensity (a. u.)
m/z
Control
Spiked
[M-H]-
299.1999 m/z
[M-H]+
301.2162 m/z


Control
(-ve)
[M-H]-
429.3712 m/z
Vitamin E (-ve)
Control
(+ve)
[M-H]+
431.3836 m/z
Vitamin E (+ve)
Intensity (a. u.)
m/z
Control
Spiked
[M-H]-
429.3712 m/z
[M-H]+
431.3836 m/z

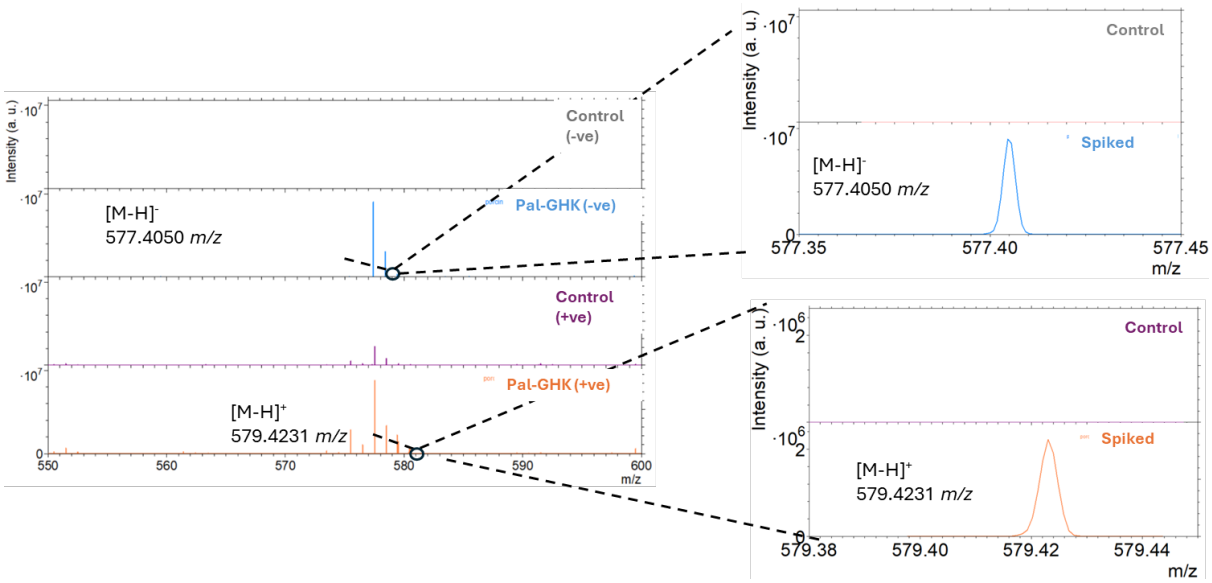

Control
(-ve)
[M-H]-
577.4050 m/z
Pal-GHK (-ve)
Control
(+ve)
[M-H]+
579.4231 m/z
Pal-GHK (+ve)
Intensity (a. u.)
m/z
Control
Spiked
[M-H]-
577.4050 m/z
[M-H]+
579.4231 m/z

Figure 4.5. OrbiSIMS mass spectra ranging from 100 to 600 *m/z* of the cosmetic active ingredients spiked in skin homogenates.

The analysis of skin homogenates treated with active ingredients proves to be a valuable approach for the rapid and efficient screening to determine the detectability of these compounds within the skin. The OrbiSIMS screening successfully identified 20 commonly used active ingredients across the agrochemical, pharmaceutical and cosmetic industries. Among these, 16 were detectable as molecular ions with 4 active ingredients being identified as large fragments representative of the chemical structures. The diagnostic ions were entirely resolved from the native skin chemistry, indicating their suitability for potentially observing the dermal absorption in skin.

4.4.3 Ion Intensity Comparison of the Active Ingredients

In Chapter 3 the dermal absorption of a 1% v/v concentration of an agrochemical formulation containing cyproconazole was detailed. The ion intensity for the compound proved adequate for tracking its distribution within the different layers of the skin. Consequently, the molecular ion of cyproconazole serves as a benchmark to provide insight into whether an agrochemical can be spatial resolved within skin.

To compare the signal intensity for the active ingredients the most intense molecular ion or fragment peaks were selected for each compound and plotted in order of most intense to least. The ordered ion intensities for the agrochemical active ingredients are presented in **Figure 4.6**. The glyphosate molecular ion exhibits the most intense signal (1.089×10^7) with thiamethoxam displaying the weakest (141015.8).

As shown in **Figure 4.6**, the cyproconazole molecular ion exhibits an ion intensity of 1.2473×10^6 which was successfully employed to track the dermal and foliar absorption demonstrated in **Chapter 3**. In comparison, the $[M-H]^-$ ions for glyphosate, cyantraniliprole and the fragment for acibenzolar-s-methyl display a greater extent in intensity in the negative polarity. The heightened signal would be advantageous for more accurate tracking of the compounds when evaluating percutaneous uptake. In contrast, thiamethoxam (217955) and metalaxyl (554960) show the weakest signal which may be difficult to detect at lower concentrations in the skin. The differences in the relative ion intensities for each compound are difficult to explain as they may be due to inherent ionisation potential of a given molecule. Similarly, the compounds may also experience potential matrix effects leading to signal suppression or enhancement. To better understand the variability in ion intensities further investigations are needed. Nevertheless, the reported method provides a relatively rapid and efficient way to assess whether a test compound is detectable within skin without necessitating Franz cell studies.

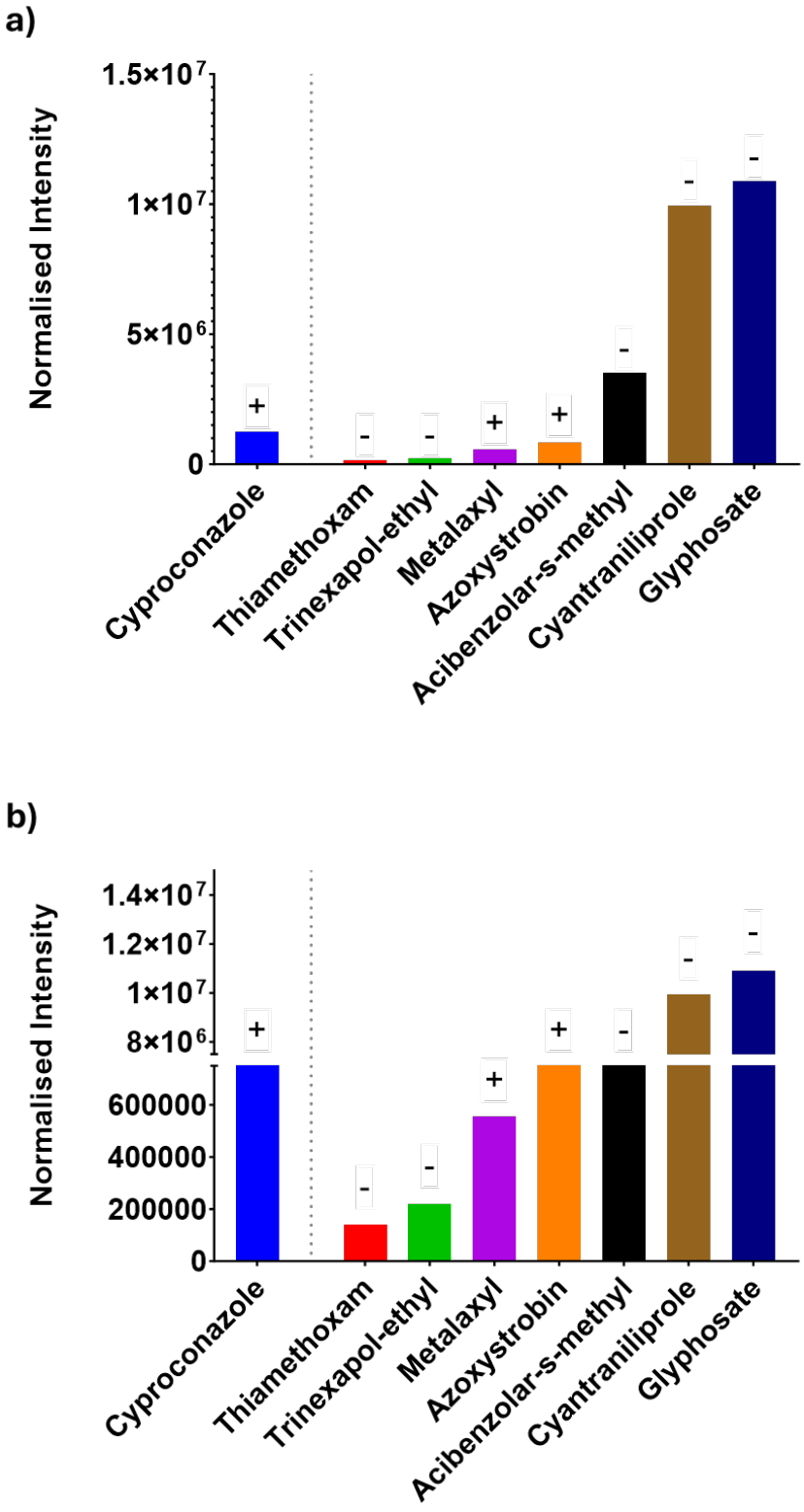


Figure 4.6. The highest ion intensities of the 8 agrochemicals detected in the skin homogenate samples, ordered from high to low, with '+' and '–' denoting the polarity in which the ion or fragment was observed. **(a)** The unadjusted scale for the normalised intensity. **(b)** A split y- axis bar chart illustrating the large range of values.

The drug compounds also demonstrate variability in the ion signal (**Figure 4.7**), with the lidocaine fragment exhibiting the highest intensity 1.4×10^8, while the hydrocortisone $[M\text{-}H]^+$ displayed the weakest signal. The molecular ions for imiquimod, acyclovir and benzocaine show very little differences in ion intensities compared to the other drug molecules.

Al-Mayahy *et al*[17] elucidated the permeation depth and lateral distribution characteristics of 5% w/v imiquimod into porcine skin using the ToF-SIMS equipped with a Bi_3^+ primary ion source. Despite achieving a relatively low ion intensity of approximately 2.0×10^6, the authors successfully localised the drug in the *stratum corneum*. Through the use of the Ar_{3000}^+ and Orbitrap™, a higher ion intensity of 2.13×10^8 was obtained for a lower concentration of the drug within the skin homogenates. Lidocaine emerges as a promising candidate for skin permeation, exhibiting the highest ion intensity, alongside acyclovir and benzocaine, which demonstrated a similar response to imiquimod. Hydrocortisone, with the lowest ion intensity (12329.1), due to possible matrix effects causing ion suppression, may provide inaccurate permeation data. The concentrations of active ingredients used for this analysis are relatively higher in comparison to commercially used products therefore, this increases the likelihood of detecting the analytes. Despite this, the method offers a rapid means to compare compound intensities and provides insights into their potential detectability within biological tissues.

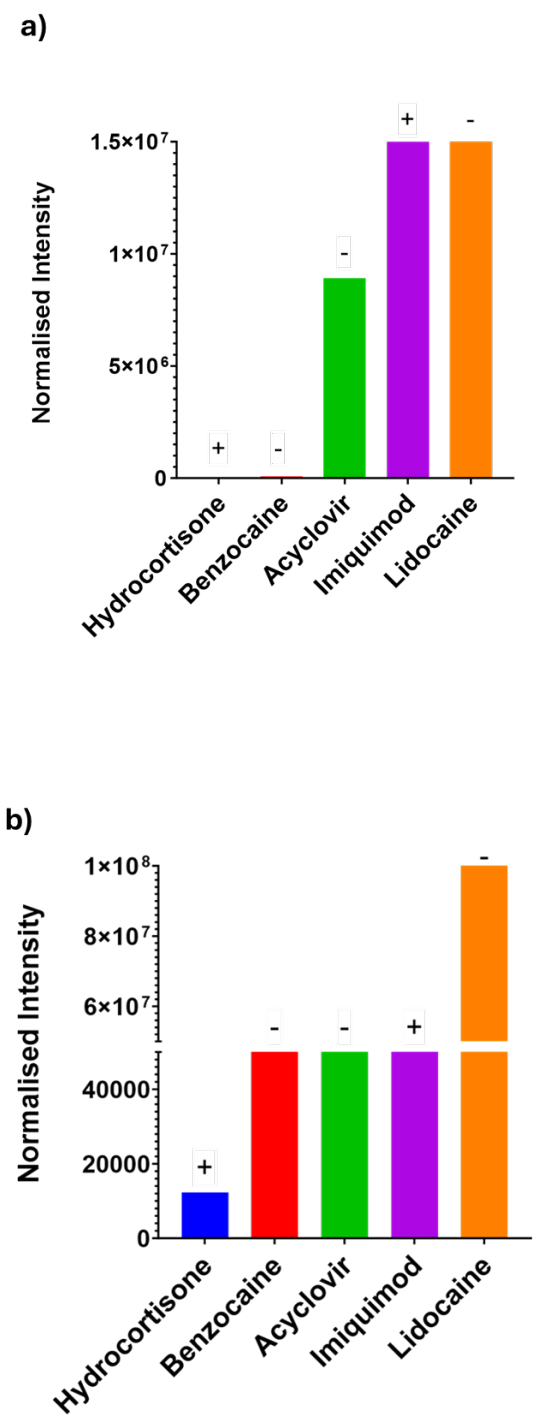


Figure 4.7. The highest ion intensities of the 5 pharmaceutical drugs detected in the skin homogenate samples, ordered from high to low, with '+' and '–' denoting the polarity in which the ion or fragment was observed. (a) The unadjusted scale for the normalised intensity. (b) A split y- axis bar chart illustrating the large range of values.

Chapter 2 highlights the investigation of the skin permeation of the anti-aging peptide, Pal-GHK, at relatively low, commercially relevant concentrations (<100 ppm), demonstrating the delivery into the *stratum corneum*. As shown in **Figure 4.8**, the peptide displays a relatively good ion intensity (3.91×10^7) allowing the detection of small amounts within the skin tissue. Similarly, trans-retinoic acid used in acne[313] and psoriasis[314] treatment is also good candidate for skin permeation studies, showing the highest ion intensity (5.17×10^7) for the molecular ion. Salicylic acid (1.69×10^7), vitamin E (364997), vitamin C (327883) and niacinamide (249496) have similar ion intensity outputs with benzoyl peroxide (59601.1) having the lowest ion intensity. Currently, the reason behind the variability in ion intensities for each of the compounds is unknown and further work is required.

Nonetheless, all the cosmetic active ingredients were effectively identified and completely resolved from the inherent skin chemistries. Additionally, we have treated the skin homogenates at relatively low concentrations in comparison to levels used in commercially available formulations. Starr *et al* was able to demonstrate the percutaneous uptake of 5% vitamin C with the utilisation of the ToFSIMS equipped with the Bi_3^+ primary ion beam. Here we employ lower concentrations of the active ingredients and still achieve favourable relative ion intensities.

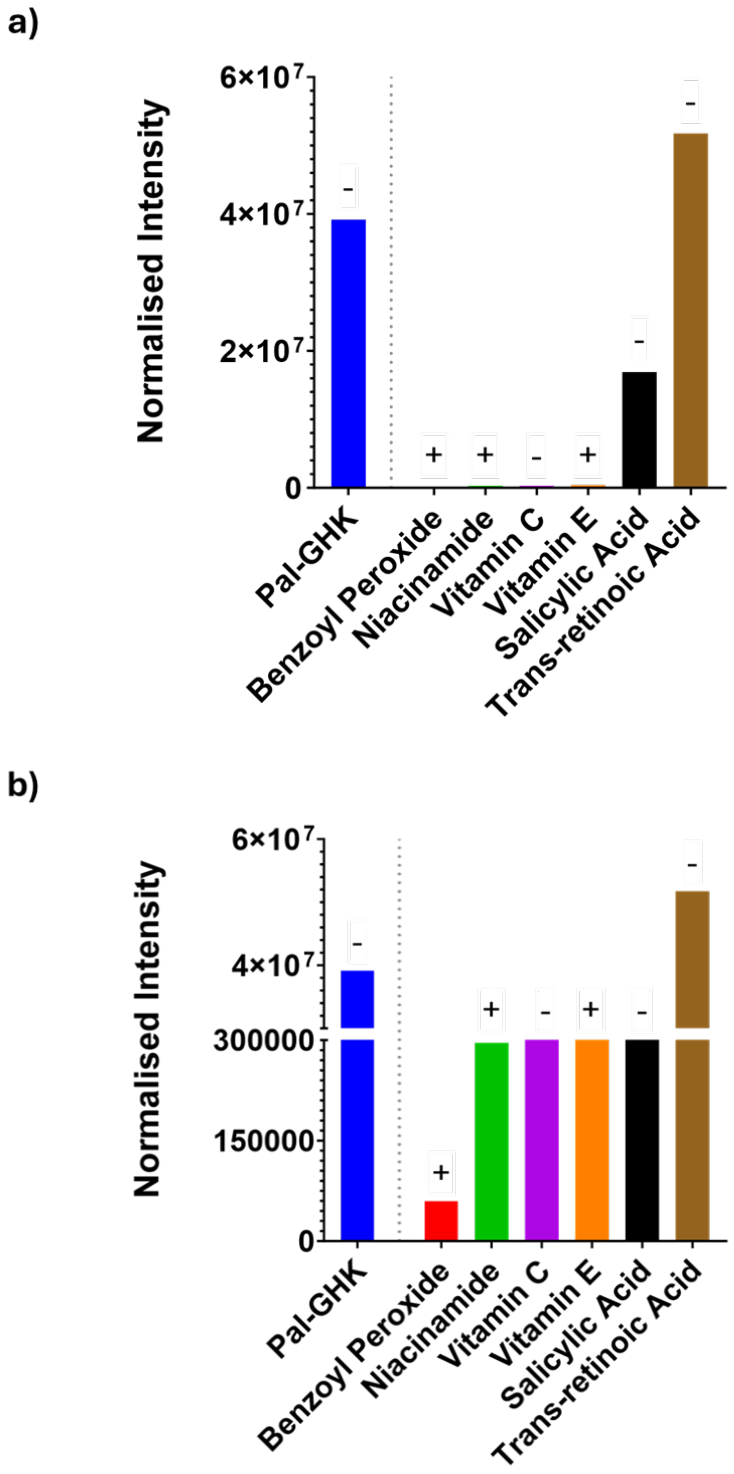


Figure 4.8. The highest ion intensities of the 7 cosmetic actives detected in the skin homogenate samples, ordered from high to low, with '+' and '–' denoting the polarity in which the ion or fragment was observed. **(a)** The unadjusted scale for the normalised intensity. **(b)** A split y- axis bar chart illustrating the large range of values.

Lipophilicity is an important parameter routinely used to predict the dermal penetration behaviour of compounds particularly, their transport across the *stratum corneum*[315,316,317]. The partition coefficient, LogP, is a measure of the lipophilicity or hydrophobicity of a given compound, represented by the ratio of its concentration in two immiscible solvents[318]. Generally, a larger LogP value signifies a greater degree of lipophilicity, suggesting a greater potential for skin permeation. Given the *stratum corneum* is predominantly lipid-based, a lipophilic compound experiences enhanced solubility in the lipids, facilitating its efficient traversal through the tissue[317,319,320,321].

The LogP value has previously been employed for the empirical prediction of the relative sensitivity for a given drug in doped liver tissue homogenates to the SIMS analytical technique [296]. The study revealed a positive correlation between the lipophilicity of the drug and SIMS sensitivity, indicating an increase in ion yield with an increase in the drugs lipophilicity. The linear correlation observed was hypothesised to be attributed to the relative solubility of the drug in the tissue or the potential reduction in ion suppression effects associated with the decreased salt concentration.

Similarly, the influence of the lipophilicity of the 20 active ingredients on the ion intensities obtained with the OrbiSIMS was examined. In **Figure 4.9**, we plot the ion intensities of all 20 active ingredients against their LogP to determine any potential trends. As illustrated, there was no discernible relationship observed between the lipophilicity of the active ingredients and the perceived ion intensity within the dosed skin homogenates. Presently, there is no apparent explanation for the absence of a trend, but it could be likely be attributed to matrix effects causing ion

signal suppression and weak ionisation for specific chemistries. Additionally, Vorng *et al*[296] inferred that the ion yield for drug compounds detected as negative ions where not dependant on the LogP values, and this effect was exacerbated with concentration of drugs above 1%. As such, it is possible there is an accumulation of all the aforementioned effects leading to the variability in ion intensities yielded. Further investigation is needed to fully understand the factors affecting the ion intensity yield however, the screening method proposed provides a relatively simple and cost-effective way to quickly assess whether a compound is detectable in skin tissue with necessitating Franz cell studies at the preliminary stage.

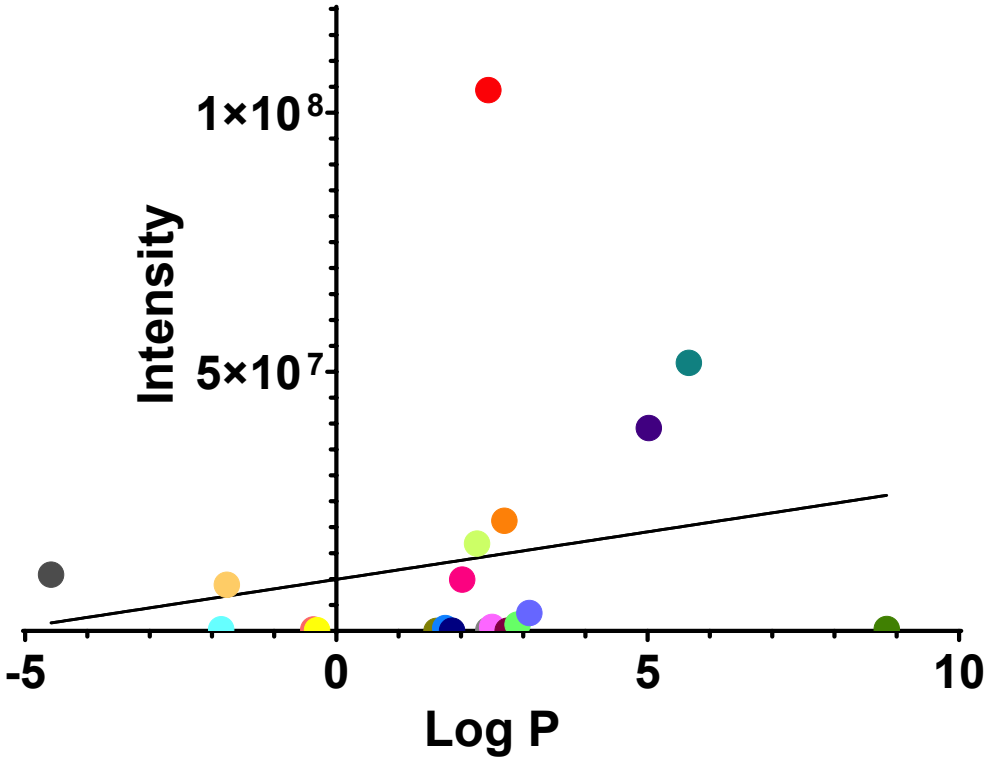


Figure 4.9. The impact of the LogP of an active ingredient on the ion intensity obtained by the OrbiSIMS in dosed skin homogenates.

4.4.4 Assessment of the Linearity of OrbiSIMS Intensity with Concentration

The linearity of a method refers to its capacity to yield results within a specified range that exhibit a proportional relationship to the concentration of the analyte[322]. This parameter is generally used to validate assays to establish the reliability/robustness of the methodology including determination of detection limits and revealing the concentration of unknown samples[323,324,325].

The active ingredients were spiked into the skin homogenates at a concentration range of 2.5 – 10 mg/ml, ensuring uniform distribution within the tissue. The linearity of cyproconazole, Pal-GHK and lidocaine was demonstrated, as shown in **Figure 4.9.1**. Following OrbiSIMS depth profiling, the three active ingredients provided satisfactory linear relationships, with R_2 values spanning from 0.82 to 0.98. Notably, the compounds are detectable at the lowest, 2.5 mg/ml concentration, suggesting the skin homogenates can possibly be dosed at a lower concentration and be calibrated to suitable levels for skin permeation studies.

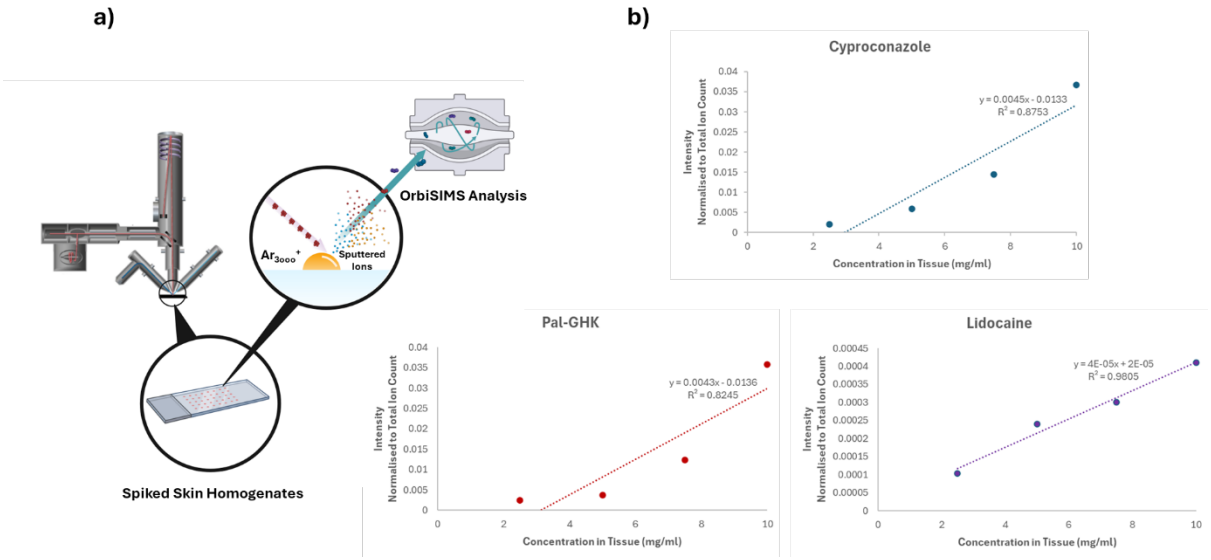


Figure 4.9.1. Assessment of the linearity of the OrbiSIMS approach for three actives ingredients; cyproconazole, Pal-GHK and lidocaine. **(a)** The principle of the skin homogenate analysis, utilising the Ar_{3000}^{+} primary ion beam for depth profiling. **(b)** Calibration curves for three active ingredients; cyproconazole, Pal-GHK and lidocaine, displaying a linear relationship.

4.5 Conclusion

In this work we have effectively employed the OrbiSIMS to demonstrate the percutaneous uptake of a multi-AI agrochemical formulation comprising cyproconazole, isopyrazam and mefenoxam at relevant 'real-life' concentrations (<100 ppm). Additionally, the investigation revealed the distribution patterns of all the constituents of the formulation, providing insights into their delivery into the various layers of the skin. These findings can contribute to high-throughput screening of multiple AI containing agrochemical formulations in addition to, the development of pesticides with multiple active ingredients and aid in minimising the risk to excessive exposure to agricultural workers.

Following on, 20 active ingredients most commonly utilised across the agrochemical, pharmaceutical and cosmetic industries were screened in skin

homogenates with the OrbiSIMS approach. All active ingredients were successfully identified in the skin homogenates, exhibiting varying ion intensities. The differences in ion signal cannot be explained currently, however, the molecular ion and fragment peaks depicted were completely resolved from the skin tissue, permitting potential skin permeation studies of these compounds. The linearity of the method was assessed at a concentration range of 2.5 – 10 mg/ml, demonstrating satisfactory linear relationships. The calibration curves not only offer insight into the robustness of the technique but also enable the calibration of appropriate concentrations for analysis and facilitate the potential elucidation of unknown compound concentrations in the skin tissue.

The OrbiSIMS screening approach shows promise for a reliable high-throughput method for the rapid and efficient assessment of compound sensitivity within the skin, bypassing the laborious Franz cell methodology at the preliminary stage.

5. Concluding Remarks and Future Perspectives

5.1 Conclusions

The primary objective of this thesis was to enhance the comprehension of the percutaneous uptake of agrochemicals with the employment of the advanced capabilities of the OrbiSIMS approach. Using the Ar_{3000}^{+} primary ion beam and the Orbitrap™ mass analyser, our investigation aimed to explore the *in situ* distributions and localisations of active pesticide ingredients, including the constituents of formulations across the various layers of the skin. As delineated in Chapter 1, current methodologies for the evaluation the skin permeation of compounds suffer notable limitations, particularly evident in liquid chromatography, necessitating the need for laborious solvent-based extraction procedures, leading to the loss of spatially resolved data for analytes. Similarly, fluorescence-based analytical techniques mandate the isotopic labelling of compounds, introducing potential adverse impacts on the dermal absorption of compounds.

Comprehending the chemical composition of the *stratum corneum* is imperative for gaining insights into fundamental biological processes and the percutaneous absorption of substances through this pivotal barrier. Chapter 2 provides an elucidation of the molecular architecture of the *stratum corneum*, encompassing the major key compounds that constitute the structure. The significant improvements in mass resolving power (>240,000 at 200 *m/z*) and mass accuracy (<0.1 ppm for biological samples) facilitated the identification and elucidation of the *in situ* localisation patterns of the endogenous species within the skin. Using a

chemical filtering software, a comprehensive breakdown of over 140 chemical species spanning five compound classes: amino acids, fatty acids, ceramides, phospholipids, and triglycerides were putatively assigned including their chemical gradients within the skin tissue.

The dermal absorption of a fungicidal agrochemical formulation containing the active ingredient, cyproconazole, was explored in Chapter 3. For the first time reported, we were able to demonstrate the percutaneous penetration of an entire pesticide formulation including all co-formulants at relevant real-life concentrations applied by agricultural workers. The localisation of each constituent was revealed including the effects of exposure time on the degree of permeation.

Currently, there is limited knowledge concerning the molecular composition of leaves specifically, the cuticle with scarce insight into the in-situ localisation of native compounds. This knowledge gap impedes advancements in crop management and the optimisation of product development. As such this chapter focused on the application of the OrbiSIMS coupled with the Ar_{3000}^+ primary ion beam for probing the endogenous species of leaf cuticles and the underlying epidermis. The investigation entailed OrbiSIMS depth profiling of *in vivo* Motown variety of wheat leaves, providing the assessment of the *in situ* distribution of the endogenous species. Particular focus on the leaf cuticle, yielded the chemical distributions of over 70 species encompassing, fatty acids and aldehydes in addition to, flavones, amino acids, nucleic acids and vitamins relating to the underlying epidermis. Similarly, the foliar absorption of the CCZ EC formulation was evaluated, resulting in the ability to track the entire formulation including effects of exposure times. The work highlighted was possible without the requirement of solvent-based

extraction procedures or isotopic labelling. The improvements in comprehending the molecular architecture of wheat leaves, encompassing permeation kinetics in both skin and wheat leaves, will prove advantageous in facilitating optimised crop management and product development.

Franz cell diffusion testing stands as the 'gold standard' for the assessment of the *in vitro* permeation of test compounds into various membranes, including the skin. Nevertheless, the inherent issue with this methodology is the frequent inability to detect the analyte of interest post-permeation study and the relative low output. Chapter 4 offers a relatively rapid and efficient screening method for 20 commonly used active ingredients spanning across the agrochemical, pharmaceutical and cosmetic industries. The approach facilitated the identification of all the compounds as either molecular ions or large fragment ions representative of the overall chemical structure. It was difficult to pinpoint the variability in ion intensities between each compound however, the method provided satisfactory linearity potentially allowing the deduction of unknown concentrations of compounds. Lastly, the dermal absorption of a multi-AI pesticide formulation was assessed, providing the label-free, *in situ* distributions of all of the constituents. The skin permeation of the active ingredients was potentially dependent upon the lipophilicity of the compound, with a higher LogP value indicating a greater extent of penetration into the deeper layers of the skin. The findings of the Chapter provide a relatively rapid and robust approach to gauge the sensitivity of compounds within skin tissue and a high-throughput Franz cell study approach, providing the ability to test multiple active compounds simultaneously.

5.2 Future Perspectives

The PhD project has provided unprecedented insight into the delivery of agrochemical formulations into the various layers of skin and wheat leaves. This is the first reporting of the *in situ*, label free visualisation of the depth distributions of a complete pesticide formulation at concentrations relevant to real-life conditions. Further work could extend this work by assessing the impact of these chemicals on the endogenous species of the skin and leaves. Such assessments are pivotal for ascertaining potential routes of exposure to agricultural workers and offer valuable perspectives on potential adverse effects. The comprehension of how agrochemicals influence the plant cuticle holds the promise of furnishing data for more precisely targeted delivery strategies. This avenue of research not only enhances our understanding of agrochemical interactions with plant surfaces but also carries implications for optimizing delivery methods and minimizing unintended ecological consequences.

Additionally, here we report the skin and foliar permeation of three fungicidal active ingredients. Subsequent experiments can expand upon these by exploring various categories of pesticide compounds including insecticides, herbicides and rodenticides. The distinct modes of action associated with different types of active ingredients likely contribute to varied penetration characteristics and interactions with both the skin and leaves.

Moreover, our present findings focus on an emulsifiable concentrate formulation. Subsequent studies may delve into alternative formulations such as suspension concentrates and wettable powders, each characterized by unique co-formulants.

These diverse formulations can elicit distinct behaviours when in contact with biological tissues, thereby warranting a comprehensive examination to better understand their respective impacts.

6. Supporting Information

6.1 Chapter 2 Supporting Information

Supplementary Information Text

Materials and Methods

Porcine skin acquisition. Porcine skin was obtained post-slaughter from pigs reared specifically for food, which ensured that removing the skin tissue was a secondary use of the animal. The ears were removed immediately after slaughter, prior to cleaning or hair removal in order to maintain skin integrity. The skin was stored for a maximum of 24 h at 4 °C, after which the tissue was washed with ultrapure water only and the hair trimmed with scissors. Using a scalpel, the outer-ear skin was detached from the underlying cartilage and any excess subcutaneous fat was removed. The skin was wrapped in aluminum foil and stored at −20 °C for a maximum of 3 months prior to use. Full thickness skin sections of approximately 2 mm were used for analysis.

***In vitro* Permeation Studies.** Once defrosted, circular *ex vivo* human skin was cut and mounted, dermal side down, between a donor and receptor chamber in a Franz-type static diffusion cell set-up (1) with an exposed surface area of 1.1 cm^2 and a receptor compartment volume of 3 mL. The receptor compartment was filled with Phosphate Buffered Saline (pH 7.5) and an infinite dose (200 mg) of a commercial analogue formulation containing Pal-GHK at <100 ppm was applied via the donor compartment. Sink conditions were maintained throughout the

experiments. The skin was exposed to the formulation for 4 h in a water bath set to 36.5 °C, which maintains a skin temperature of 32°C. After 4 h, the Franz cell was dismantled and the excess formulation was removed with a dry sponge. The skin was wiped with a sponge soaked in Teepol Solution (3 % v/v) and then dehydrated under vacuum at RT for 24 h before loading into the Hybrid-SIMS instrument for analysis. As the focus of the analysis was an exogenous peptide and not a native compound, for practical and time saving reasons we chose to prepare the samples under dehydrated conditions rather than frozen hydrated.

***In vivo* Permeation Studies.** Three Caucasian subjects (2 females, 1 male) aged between 30-55 were used for the study. All subjects gave informed consent to participate. The study was performed in a constant environment of 22 ± 2 °C and 50 ± 5 % humidity and subjects were acclimatized for 15 minutes prior to product application. A commercial analogue formulation containing Pal-GHK at <100 ppm was applied to one site on the volar forearm at 2 mg/cm^2 and one site was left untreated. Four hours post-application the sites were gently wiped with a tissue and 15 sequential tape strips were collected from each site using D-squame® strips (CuDerm). A D-squame® pressure instrument (CuDerm) was used to apply consistent pressure for 5 seconds before removing strips from the skin. Tape strips were then stored at 4°C until analysis.

Supplementary Information Figures

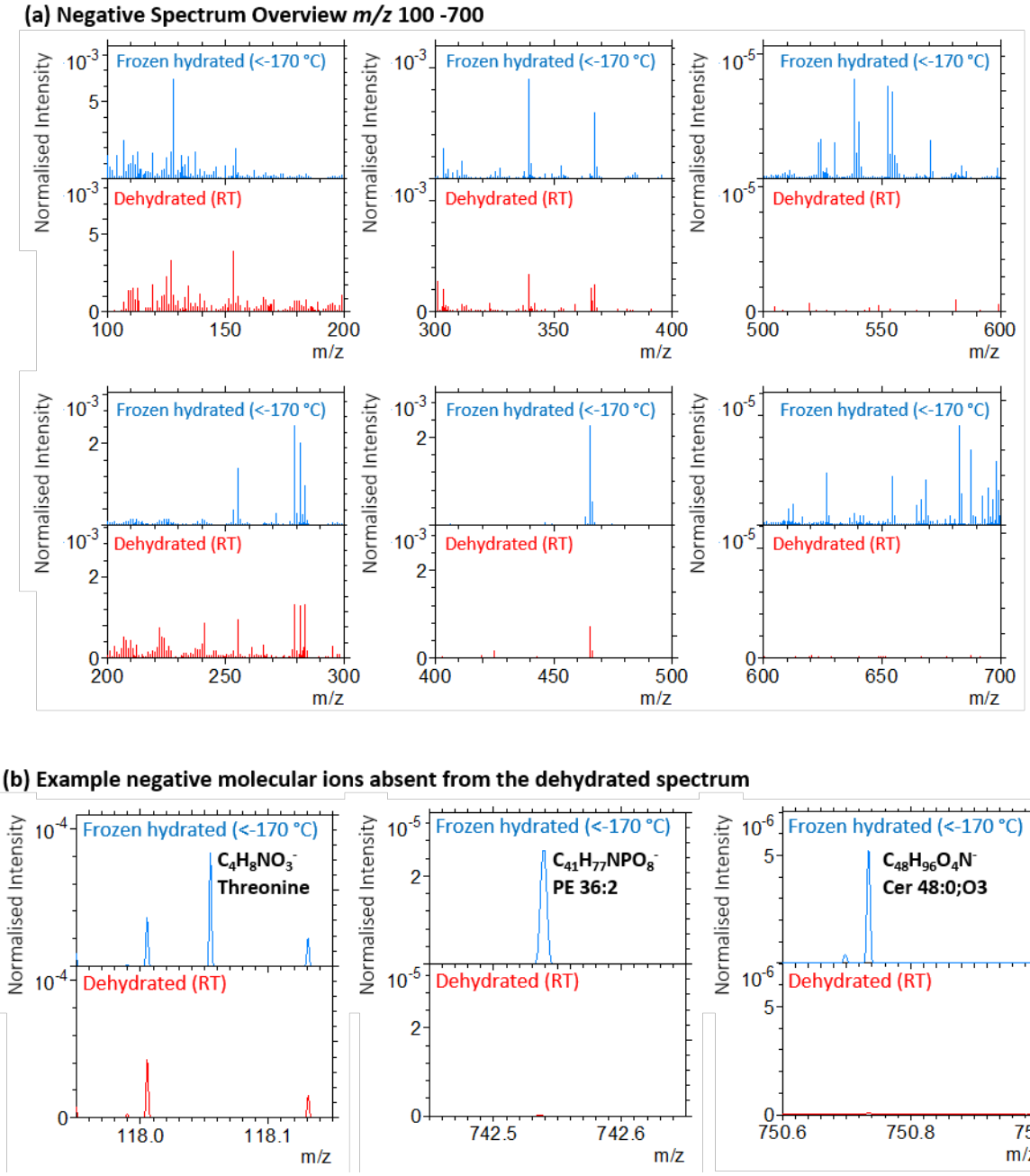


Figure S2.1. OrbiSIMS negative polarity spectral data, showing a comparison of the spectra for frozen hydrated (<-170 °C) vs. dehydrated (RT) *ex vivo* porcine skin tissue. The primary ion beam was Ar_{3000}^{+}. The total applied ion dose for the frozen hydrated and dehydrated sample was 1.8 x 10^{13} and 6.79 x 10^{13} respectively. **(a)** An overview of the spectrum from *m/z* 100 -700. The ion intensity has been

normalized to the total ion count. **(b)** Three example ion peaks that are absent from the dehydrated spectrum. Specifically, the putatively assigned molecular ions of amino acid threonine ($C_4H_8NO_3^-$), phospholipid PE 36:2 ($C_{41}H_{77}NPO_8^-$) and ceramide C48:0;O3 ($C_{48}H_{96}O_4N^-$).

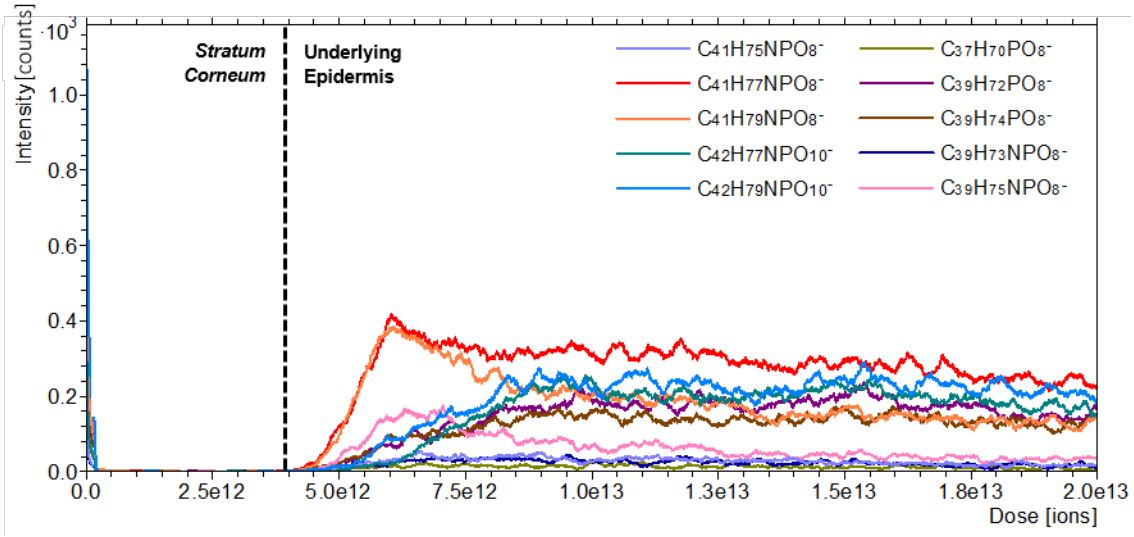


Figure S2.2. OrbiSIMS negative polarity depth profile data showing the ion intensity variation as function of ion dose/skin depth for the putatively assigned phospholipid species. The primary ion beam was Ar_{3000}^+. The 10 most intense ions are presented. These ions have been used to determine the *stratum corneum* – epidermal boundary, which is approximated with a dotted vertical line. The profile has been compressed using a running average method (100 data points).

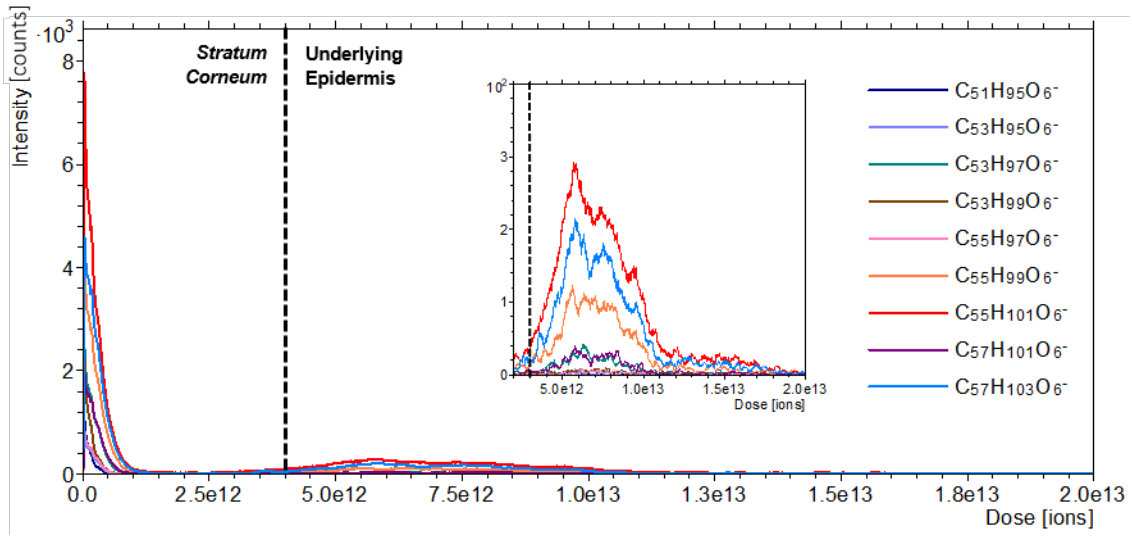


Figure S2.3. OrbiSIMS negative polarity depth profile data showing the ion intensity variation as function of ion dose/skin depth for the putatively assigned triglyceride species. The inset is a zoom in of the region between 2 x 10^{12} and 2 x 10^{13} ion dose. The primary ion beam was Ar_{3000}^{+}. The *stratum corneum* – epidermal boundary has been determined, and approximated with a dotted vertical line, based on the ion intensity variation of the phospholipid species (**Figure S2.2**). The profile has been compressed using a running average method (100 data points).

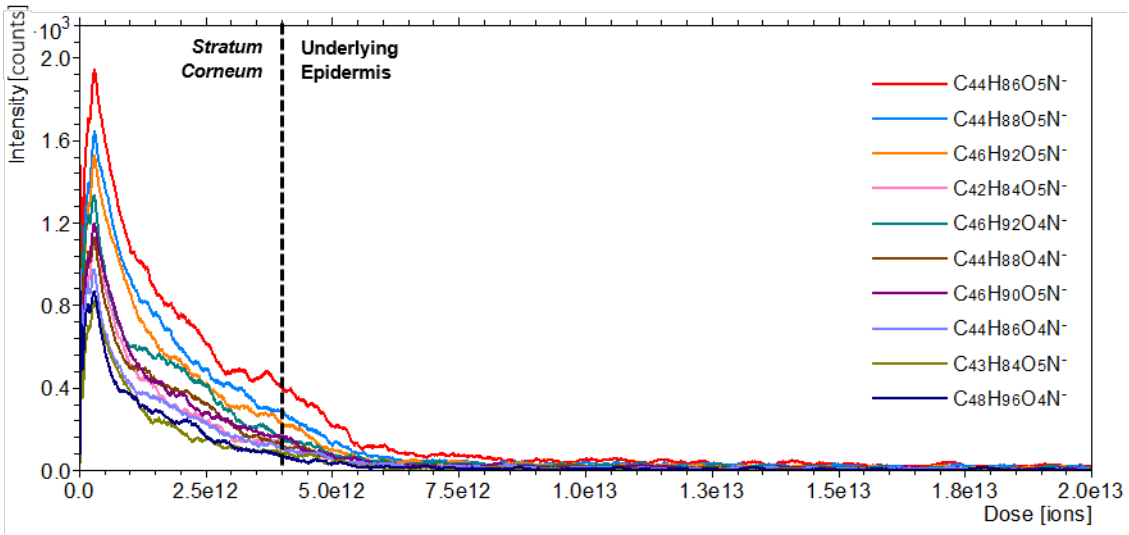


Figure S2.4. OrbiSIMS negative polarity depth profile data showing the ion intensity variation as function of ion dose/skin depth for the putatively assigned ceramide species. The primary ion beam was Ar_{3000}^{+}. The *stratum corneum* – epidermal boundary has been determined, and approximated with a dotted vertical line, based on the ion intensity variation of the phospholipid species (**Figure S2.2**). The profile has been compressed using a running average method (100 data points).

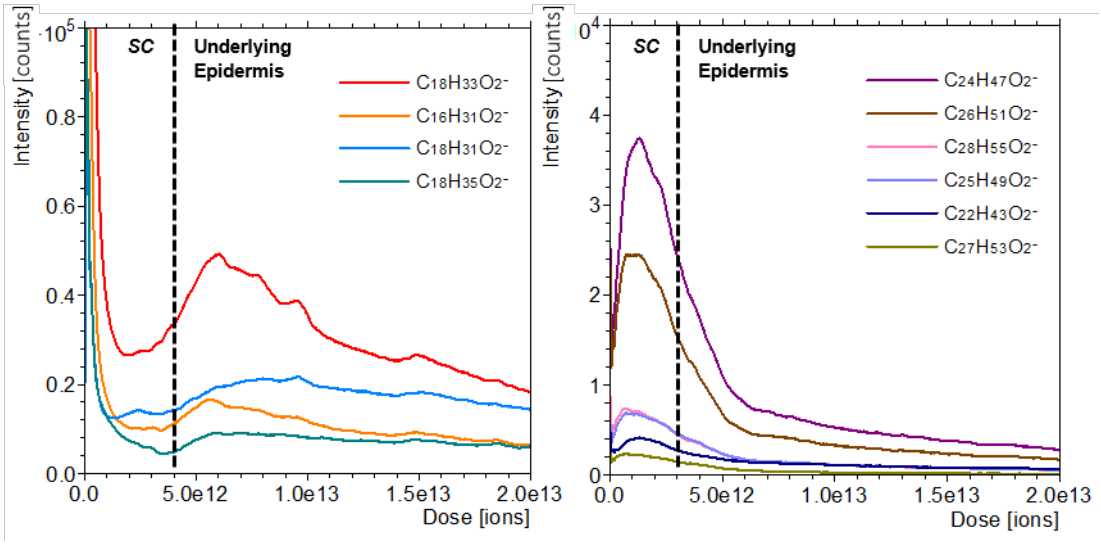


Figure S2.5. OrbiSIMS negative polarity depth profile data showing the ion intensity variation as function of ion dose/skin depth for the putatively assigned fatty acid species. This class of compounds presented two different trends with depth. The primary ion beam was Ar_{3000}^{+}. The *stratum corneum* – epidermal boundary has been determined, and approximated with a dotted vertical line, based on the ion intensity variation of the phospholipid species (**Figure S2.2**). The profile has been compressed using a running average method (100 data points).

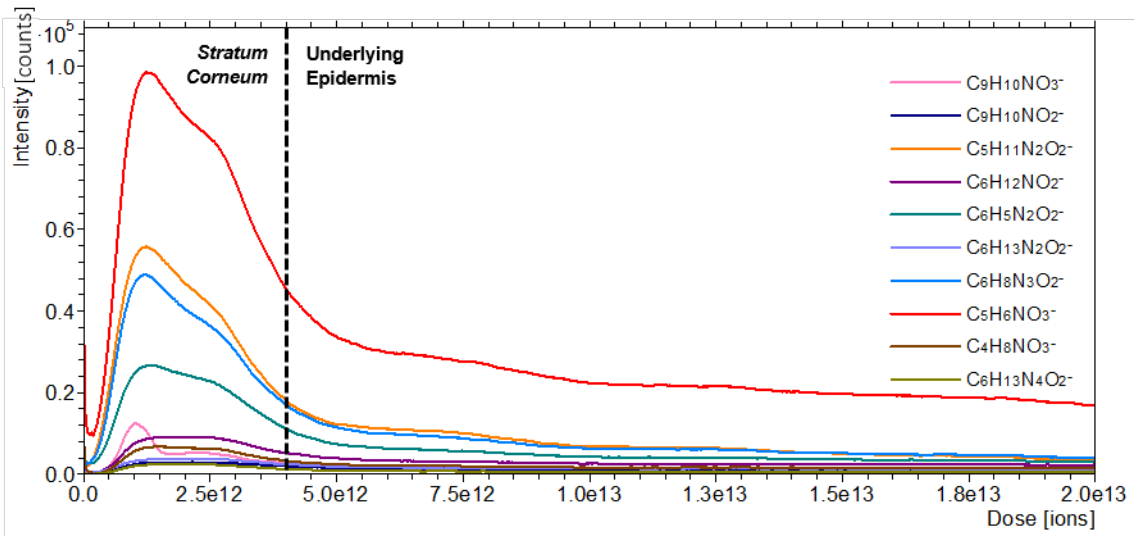
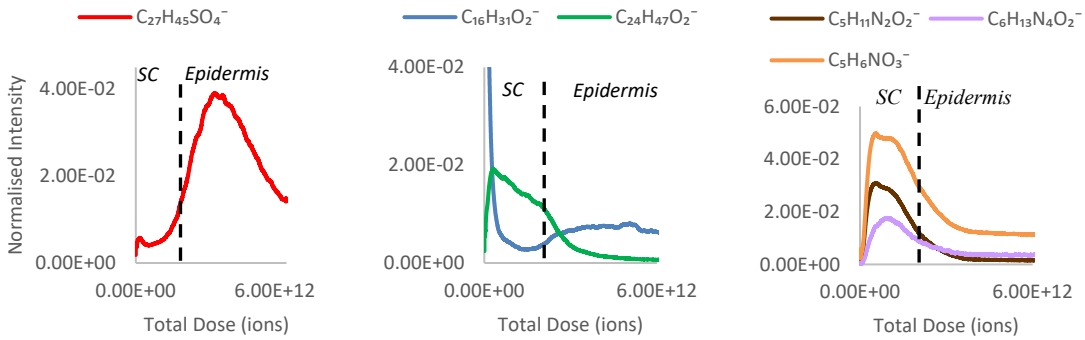
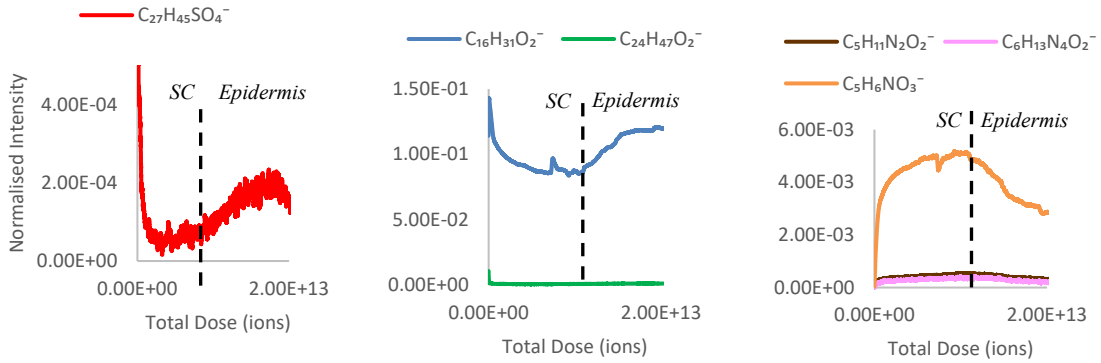


Figure S2.6. 3D OrbiSIMS negative polarity depth profile data showing the ion intensity variation as function of ion dose/skin depth for the putatively assigned amino acid species. The primary ion beam was Ar_{3000}^{+}. The *stratum corneum* – epidermal boundary has been determined, and approximated with a dotted vertical line, based on the ion intensity variation of the phospholipid species (**Figure S2.2**). The profile has been compressed using a running average method (100 data points).

a) Human skin sample 1



b) Human skin sample 2



c) Human skin sample 3

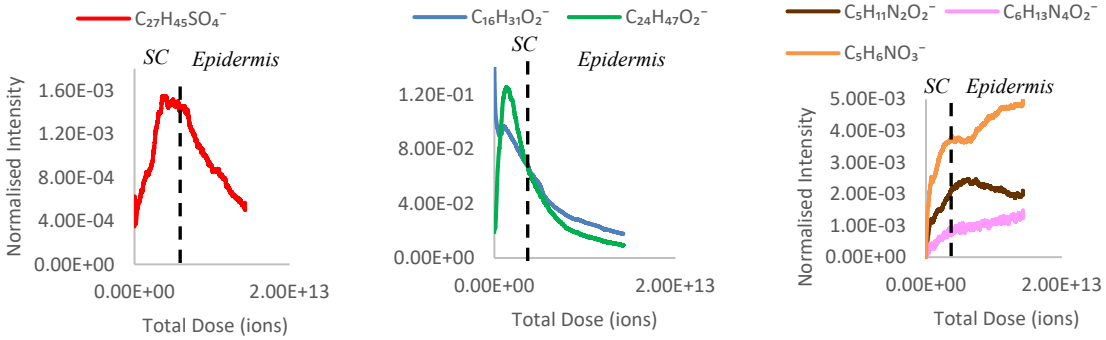


Figure S2.7: OrbiSIMS data showing the ion intensity variation as a function of skin depth for various native compounds in three different human skin samples (**SI Table S2.6**) with sample 1 analyzed in the cryo hydrated state and samples 2 and 3 analyzed in a dehydrated state. The ion intensities have been normalized to the

total ion count. The variation of depth distributions of the following compounds was assessed; cholesterol sulfate ($C_{27}H_{45}SO_4^-$), palmitic acid ($C_{16}H_{31}O_2^-$), lignoceric acid ($C_{24}H_{47}O_2^-$), arginine ($C_6H_{13}N_4O_2^-$), PCA ($C_5H_6NO_3^-$) and ornithine ($C_5H_{11}N_2O_2^-$).

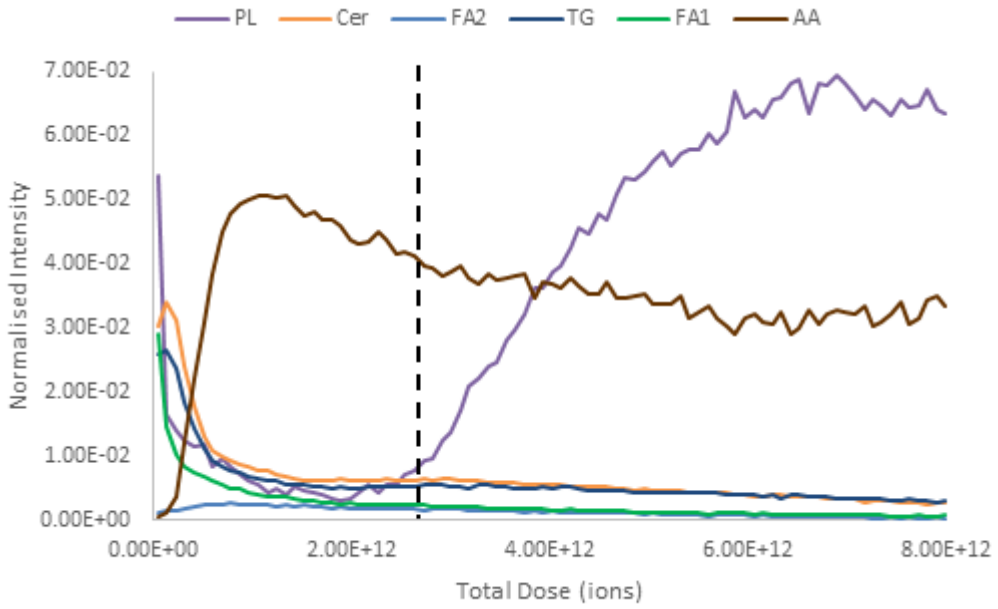


Figure S2.8: OrbiSIMS positive polarity depth profile data showing the ion intensity variation as function of ion dose/skin depth for various putatively assigned compounds. The primary ion beam was Ar_{3000}^+. The ion intensities have been normalized to the total ion count and the profiles have been compressed using a running average method (using a 100 data point average). The *stratum corneum* – epidermal boundary, approximated with a dotted vertical line, has been determined based on the ion intensity variation of the phospholipid species (**Figure S2.2**). Example ions from each identified compound class: PL – phospholipids ($C_5H_{15}NPO_4^+$), TG – triglycerides ($C_7H_{11}^+$), Cer – ceramides ($C_{39}H_{71}O_4^+$), FA1 and FA2 – fatty acids ($C_{18}H_{35}O_2^+$ and $C_{26}H_{56}NO_2^+$) and AA – amino acids ($C_6H_{15}N_4O_2^+$). The

normalized intensity for the phospholipid and amino acid ions have been multiplied by a factor of 10.

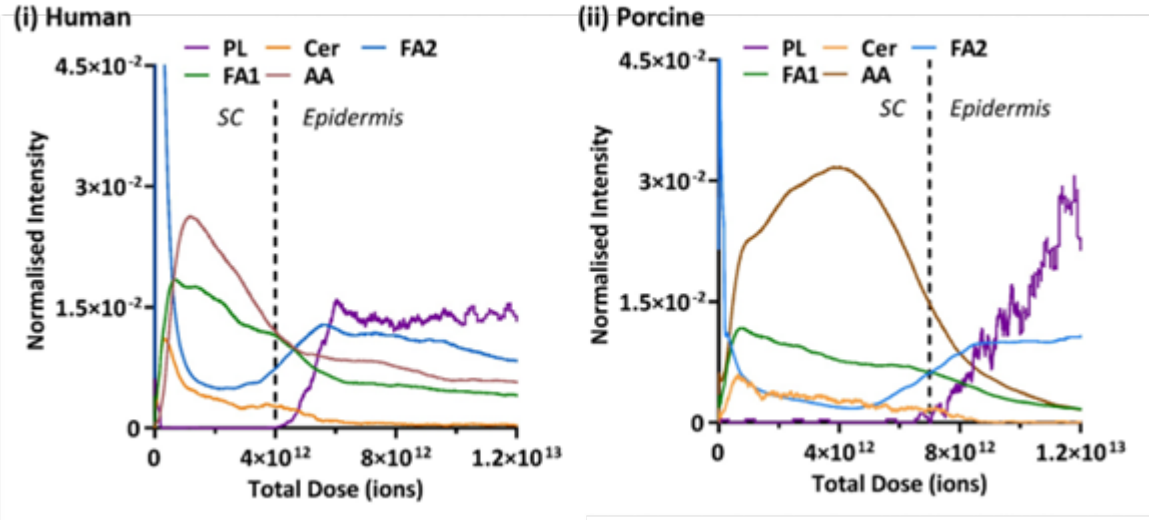


Figure S2.9. Data produced from 3D OrbiSIMS negative polarity depth profile analysis of frozen hydrated *ex vivo* skin, both human and porcine. The primary ion beam was Ar_{3000}^+. Depth profiles for both (i) human and (ii) porcine samples, showing the ion intensity variation as function of ion dose/skin depth for various putatively assigned compounds. The ion intensities have been normalized to the total ion count and the profiles have been compressed using a running average method (using a 100 data point average). The *stratum corneum* – epidermal boundary, approximated with a dotted vertical line, has been determined for each species based on the ion intensity variation of the phospholipid ion. Example ions from the following compound classes are shown: PL – phospholipids ($C_{41}H_{77}NPO_8^-$), Cer – ceramides ($C_{44}H_{86}NO_5^-$), FA1 and FA2 – fatty acids ($C_{27}H_{47}O_2^-$ and $C_{16}H_{31}O_2^-$), AA – amino acids ($C_5H_{11}N_2O_2^-$). The normalized intensity for the porcine ceramide and phospholipid ions has been multiplied by a factor of 100 and 1000 respectively.

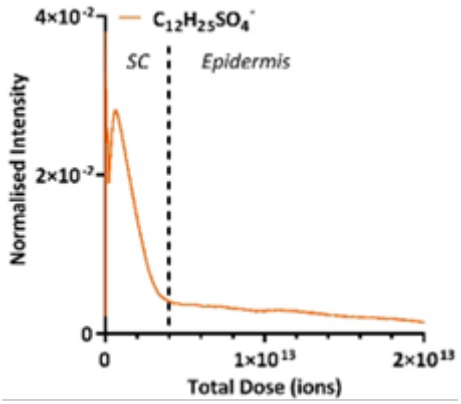
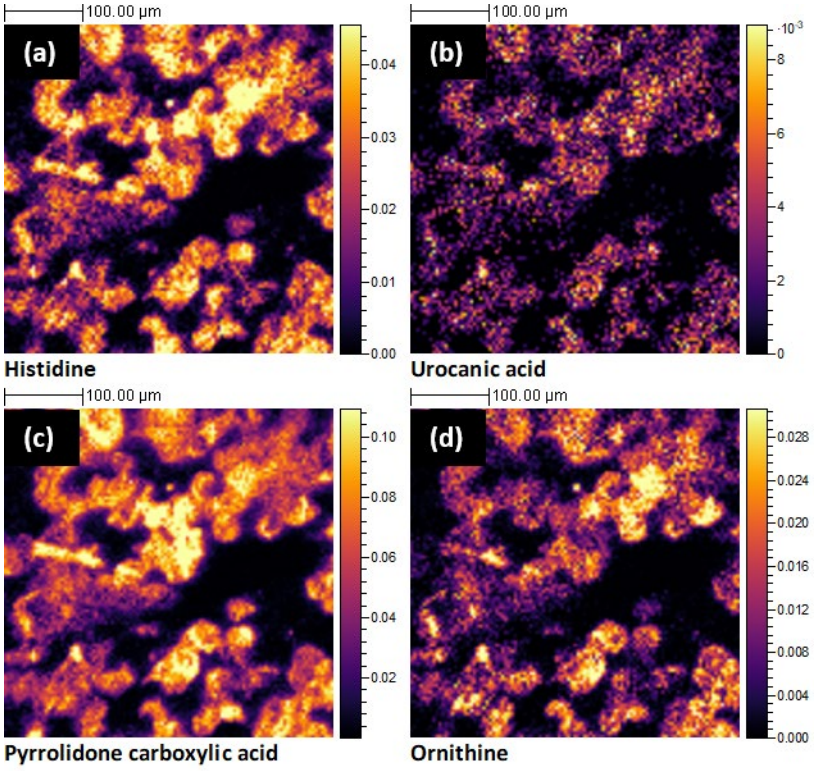


Figure S2.1.1. 3D OrbiSIMS negative polarity depth profile data showing the ion intensity variation as function of ion dose/skin depth for the putatively assigned exogenous compound sodium lauryl sulfate ($C_{12}H_{25}SO_4^-$). The primary ion beam was Ar_{3000}^+. The *stratum corneum* – epidermal boundary has been determined, and approximated with a dotted vertical line, based on the ion intensity variation of the phospholipid species (**Figure S2.2**). The ion intensity has been normalized to the total ion count and the profile has been compressed using a running average method (100 data points).



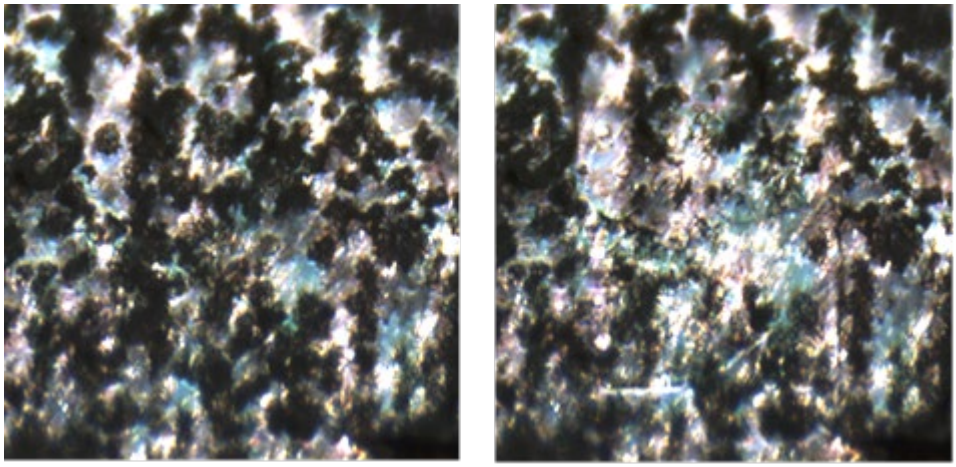


Figure S2.1.2. OrbiSIMS high resolution negative polarity ion images**,** produced from the analysis of an individual human corneocyte skin layer, collected *in vivo* using a tape stripping method. The data shown is from tape strip 7, which represents the middle of the *stratum corneum*. The ion images illustrate the 2D spatial distribution for the following molecular ions **(a)** Histidine ($C_6H_8N_3O_2^-$) **(b)** Urocanic acid ($C_6H_6N_2O_2^-$) **(c)** Pyrrolidone carboxylic acid ($C_5H_7NO_3^-$) **(d)** Ornithine

($C_5H_{12}N_2O_2^-$). All ion images have been normalized to the total ion image and their relative intensity scales set to 50 % of the maximum. Corresponding optical image taken pre and post analysis in (e) and (f) where white scale bar = 500 µm.

Supporting Information Tables

Table S2.1. Tabulated output from the SIMS-MFP software (2) showing the putative phospholipid assignments. The observed mass (*m/z*), chemical formula, molecular assignment and mass deviation are documented. All assignments were compared against the Lipid Maps Structural Database ® (3) and/or verified manually from previous literature.

Observed Mass (*m/z*)	Chemical Formula	Molecular Assignment	Mass Deviation
671.4656	$C_{37}H_{68}PO_8^-$	PA 34:2	0.7
673.4811	$C_{37}H_{70}PO_8^-$	PA 34:1	0.4
697.4811	$C_{39}H_{70}PO_8^-$	PA 36:3	0.4
699.4968	$C_{39}H_{72}PO_8^-$	PA 36:2	0.4
701.5125	$C_{39}H_{74}PO_8^-$	PA 36:1	-0.3
714.5076	$C_{39}H_{73}NPO_8^-$	PE 34:2	0.3
716.5234	$C_{39}H_{75}NPO_8^-$	PE 34:1	0.4
738.5076	$C_{41}H_{73}NPO_8^-$	PE 36:4	0.3
740.5234	$C_{41}H_{75}NPO_8^-$	PE 36:3	0.5
742.5391	$C_{41}H_{77}NPO_8^-$	PE 36:2	0.5

744.5548	$C_{41}H_{79}NPO_8^-$	PE 36:1	0.6
766.5390	$C_{43}H_{77}NPO_8^-$	PE 38:4	0.4
768.5543	$C_{43}H_{79}NPO_8^-$	PE 38:3	0.0
786.5287	$C_{42}H_{77}NPO_{10}^-$	PS 36:2	-0.4
788.5444	$C_{42}H_{79}NPO_{10}^-$	PS 36:1	0.4
812.5444	$C_{44}H_{79}NPO_{10}^-$	PS 38:3	0.3
835.5331	$C_{43}H_{80}PO_{13}^-$	PI 34:1	-0.7
861.5495	$C_{45}H_{82}PO_{13}^-$	PI 36:2	0.2
885.5499	$C_{47}H_{82}PO_{13}^-$	PI 38:4	0.7

Table S2.2. Tabulated output from the SIMS-MFP software (2) showing the putative triglyceride assignments. The observed mass (*m/z*), chemical formula, molecular assignment and mass deviation are documented. All assignments were compared against the Lipid Maps Structural Database ® (3) and/or verified manually from previous literature.

Observed Mass (*m/z*)	Chemical Formula	Molecular Assignment	Mass Deviation
803.7136	$C_{51}H_{95}O_6^-$	TG(16:0/14:0/18:1(9Z))	0.2
827.7136	$C_{53}H_{95}O_6^-$	TG(16:1(9Z)/16:1(9Z)/18:1(9Z))	0.2
829.7293	$C_{53}H_{97}O_6^-$	TG(16:1(9Z)/16:1(9Z)/18:0	0.0
831.7452	$C_{53}H_{99}O_6^-$	TG(16:0/16:1(9Z)/18:0)	0.2

853.7291	$C_{55}H_{97}O_6^-$	TG(18:2(9Z,12Z)/16:0/18:2	0.0
855.7449	$C_{55}H_{99}O_6^-$	TG(16:0/18:1(9Z)/18:2	-0.2
857.7606	$C_{55}H_{101}O_6^-$	TG(16:0/18:1/18:1)	-0.1
881.7605	$C_{57}H_{101}O_6^-$	TG(18:1/18:1/18:2)	-0.2
883.7762	$C_{57}H_{103}O_6^-$	TG(18:1(9E)/18:1(9E)/18:1	-0.1

Table S2.3. Tabulated output from the SIMS-MFP software (2) showing the putative ceramide assignments. The observed mass (*m/z*), chemical formula, molecular assignment and mass deviation are documented. All assignments were compared against the Lipid Maps Structural Database ® (3) and/or verified manually from previous literature.

Observed Mass (*m/z*)	Chemical Formula	Molecular Assignment	Mass Deviation
436.4160	$C_{28}H_{54}O_2N^-$	Cer 28:1;O	-0.5
438.4316	$C_{28}H_{56}O_2N^-$	Cer 28:0;O	-0.5
450.4317	$C_{29}H_{56}O_2N^-$	Cer 29:1;O	-0.7
452.4110	$C_{28}H_{54}O_3N^-$	Cer 28:1;O2	-0.1
454.4266	$C_{28}H_{56}O_3N^-$	Cer 28:0;O2	0
466.4265	$C_{29}H_{56}O_3N^-$	Cer 29:1;O2	-0.2
652.6253	$C_{41}H_{82}O_4N^-$	Cer 41:0;O3	0.2

654.6044	$C_{40}H_{80}O_5N^-$	Cer 40:0;O4	-0.1
666.6409	$C_{42}H_{84}O_4N^-$	Cer 42:0;O3	0.1
668.6202	$C_{41}H_{82}O_5N^-$	Cer 41:0;O4	0.2
678.6407	$C_{43}H_{84}O_4N^-$	Cer 43:1;O3	-0.2
680.6564	$C_{43}H_{86}O_4N^-$	Cer 43:0;O3	-0.2
680.6564	$C_{43}H_{86}O_5N^-$	Cer 43:0;O4	-0.1
682.6356	$C_{42}H_{84}O_5N^-$	Cer 42:0;O4	-0.2
692.6564	$C_{44}H_{86}O_4N^-$	ACer 44:0;O2 or Cer 44:1;O3*	-0.2
694.6357	$C_{43}H_{84}O_5N^-$	Cer 43:1;O4	-0.2
694.6721	$C_{44}H_{88}O_4N^-$	Cer 44:0;O3	-0.1
706.6721	$C_{45}H_{88}O_4N^-$	ACer 45:0;O2 or Cer 45:1;O3*	-0.1
708.6514	$C_{44}H_{86}O_5N^-$	ACer 44:0;O3 or Cer 44:1;O4*	-0.1
708.6877	$C_{45}H_{90}O_4N^-$	Cer 45:0;O3	-0.1
710.6671	$C_{44}H_{88}O_5N^-$	Cer 44:0;O4	-0.1
720.6878	$C_{46}H_{90}O_4N^-$	ACer 46:0;O2 or Cer 46:1;O3*	-0.1
722.6671	$C_{45}H_{88}O_5N^-$	ACer 45:0;O3 or Cer 45:1;O4*	-0.1
722.7035	$C_{46}H_{92}O_4N^-$	Cer 46:0;O3	0.0
724.6827	$C_{45}H_{90}O_5N^-$	Cer 45:0;O4	0.0
734.7034	$C_{47}H_{92}O_4N^-$	ACer 47:0;O2 or Cer 47:1;O3*	0.0
736.6827	$C_{46}H_{90}O_5N^-$	ACer 46:0;O3 or Cer 46:1;O4*	0.0
736.7192	$C_{47}H_{94}O_4N^-$	Cer 47:0;O3	0.0
738.6985	$C_{46}H_{92}O_5N^-$	Cer 46:0;O4	0.0
748.7189	$C_{48}H_{94}O_4N^-$	ACer 48:0;O2 or Cer 48:1;O3*	-0.4

750.6981	$C_{47}H_{92}O_5N^-$	ACer 47:0;O3 or Cer 47:1;O4*	0.0
750.7346	$C_{48}H_{96}O_4N^-$	Cer 48:0;O3	-0.3
752.7138	$C_{47}H_{94}O_5N^-$	Cer 47:0;O4	-0.3
764.7139	$C_{48}H_{94}O_5N^-$	ACer 48:0;O3 or Cer 48:1;O4*	0.0
764.7502	$C_{49}H_{98}O_4N^-$	Cer 49:0;O3	-0.1
766.7295	$C_{48}H_{96}O_5N^-$	Cer 48:0;O4	-0.2
778.7659	$C_{50}H_{100}O_4N^-$	Cer 50:0;O3	-0.1

* Without further investigation we were unable to distinguish whether the structure related to the ceramide or the acyl-ceramide.

Table S2.4. Tabulated output from the SIMS-MFP software (2) showing the putative fatty acid assignments. The observed mass (*m/z*), chemical formula, molecular assignment and mass deviation are documented. All assignments were compared against the Lipid Maps Structural Database ® (3) and/or verified manually from previous literature.

Observed Mass (*m/z*)	Chemical Formula	Molecular Assignment	Mass Deviation
235.1704	$C_{15}H_{23}O_{2-}$	FA 15:3	0
237.1861	$C_{15}H_{25}O_{2-}$	FA 15:2	0
239.2017	$C_{15}H_{29}O_{2-}$	FA 15:1	0.1
241.2174	$C_{15}H_{29}O_{2-}$	FA 15:0	0.1

249.1861	$C_{16}H_{25}O_{2-}$	FA 16:3	0.3
251.2018	$C_{16}H_{27}O_{2-}$	FA 16:2	0.3
255.2332	$C_{16}H_{31}O_{2-}$	FA 16:0	0.5
263.2019	$C_{17}H_{27}O_{2-}$	FA 17:3	0.5
265.2175	$C_{17}H_{29}O_{2-}$	FA 17:2	0.6
267.2332	$C_{17}H_{31}O_{2-}$	FA 17:1	0.6
269.2489	$C_{17}H_{33}O_{2-}$	FA 17:0	0.7
277.2174	$C_{18}H_{29}O_{2-}$	FA 18:3	0
279.2331	$C_{18}H_{31}O_{2-}$	FA 18:2	0.1
281.2488	$C_{18}H_{33}O_{2-}$	FA 18:1	0.2
283.2644	$C_{18}H_{35}O_{2-}$	FA 18:0	0.1
291.2332	$C_{19}H_{31}O_{2-}$	FA 19:3	0.4
293.2488	$C_{19}H_{33}O_{2-}$	FA 19:2	-0.5
295.2642	$C_{19}H_{35}O_{2-}$	FA 19:1	-0.5
297.2799	$C_{19}H_{37}O_{2-}$	FA 19:0	-0.4
303.233	$C_{20}H_{31}O_{2-}$	FA 20:4	-0.3
305.2487	$C_{20}H_{33}O_{2-}$	FA 20:3	-0.2
307.2643	$C_{20}H_{35}O_{2-}$	FA 20:2	-0.1
309.2799	$C_{20}H_{37}O_{2-}$	FA 20:1	-0.1
311.2957	$C_{20}H_{39}O_{2-}$	FA 20:0	0
319.2641	$C_{21}H_{35}O_{2-}$	FA 21:3	-0.8
321.2798	$C_{21}H_{37}O_{2-}$	FA 21:2	-0.7
323.2955	$C_{21}H_{39}O_{2-}$	FA 21:1	-0.2

325.3111	$C_{21}H_{41}O_{2-}$	FA 21:0	-0.6
331.2642	$C_{22}H_{35}O_{2-}$	FA 22:4	-0.4
333.2799	$C_{22}H_{37}O_{2-}$	FA 22:3	-0.2
335.2956	$C_{22}H_{39}O_{2-}$	FA 22:2	-0.2
337.3113	$C_{22}H_{41}O_{2-}$	FA 22:1	-0.2
339.3267	$C_{22}H_{43}O_{2-}$	FA 22:0	-0.9
349.3111	$C_{23}H_{41}O_{2-}$	FA 23:2	-0.5
351.3268	$C_{23}H_{43}O_{2-}$	FA 23:1	-0.5
353.3424	$C_{23}H_{45}O_{2-}$	FA 23:0	-0.5
365.3423	$C_{24}H_{45}O_{2-}$	FA 24:1	-0.9
367.3581	$C_{24}H_{47}O_{2-}$	FA 24:0	-0.8
377.3424	$C_{25}H_{45}O_{2-}$	FA 25:2	-0.5
379.3581	$C_{25}H_{47}O_{2-}$	FA 25:1	-0.5
381.3737	$C_{25}H_{49}O_{2-}$	FA 25:0	-0.6
391.3583	$C_{26}H_{47}O_{2-}$	FA 26:2	-0.1
393.3739	$C_{26}H_{49}O_{2-}$	FA 26:1	-0.1
395.3894	$C_{26}H_{51}O_{2-}$	FA 26:0	-0.8
405.3738	$C_{27}H_{49}O_{2-}$	FA 27:2	-0.4
407.3894	$C_{27}H_{51}O_{2-}$	FA 27:1	-0.4
409.4051	$C_{27}H_{53}O_{2-}$	FA 27:0	-0.5
419.3895	$C_{28}H_{51}O_{2-}$	FA 28:2	0
421.4052	$C_{28}H_{53}O_{2-}$	FA 28:1	-0.2
423.4208	$C_{28}H_{55}O_{2-}$	FA 28:0	-0.2

433.405	$C_{29}H_{53}O_{2-}$	FA 29:2	-0.3
435.4207	$C_{29}H_{55}O_{2-}$	FA 29:1	-0.5
437.4364	$C_{29}H_{57}O_{2-}$	FA 29:0	-0.5
447.4208	$C_{30}H_{55}O_{2-}$	FA 30:2	-0.1
449.4365	$C_{30}H_{57}O_{2-}$	FA 30:1	-0.3
451.4521	$C_{30}H_{59}O_{2-}$	FA 30:0	-0.3
463.4522	$C_{31}H_{59}O_{2-}$	FA 31:1	0
465.4676	$C_{31}H_{61}O_{2-}$	FA 31:0	-0.6
475.452	$C_{32}H_{59}O_{2-}$	FA 32:2	-0.6
477.4676	$C_{32}H_{61}O_{2-}$	FA 32:1	-0.5
479.4833	$C_{32}H_{63}O_{2-}$	FA 32:0	-0.5

Table S2.5. Tabulated output from the SIMS-MFP software (2) showing the putative amino acid assignments. The observed mass (*m/z*), chemical formula, molecular assignment and mass deviation are documented. All assignments were compared against the Lipid Maps Structural Database ® (3) and/or verified manually from previous literature.

Observed Mass (*m/z*)	Chemical Formula	Molecular Assignment	Mass Deviation
118.0509	$C_4H_8NO_3^-$	Threonine	-0.3
128.0353	$C_5H_6NO_3^-$	Pyroglutamic acid	-0.5

130.0872	$C_6H_{12}NO_2^-$	Leucine	-1.0
131.0825	$C_5H_{11}N_2O_2^-$	Ornithine	-0.8
137.0355	$C_6H_5N_2O_2^-$	Urocanic acid	-0.9
145.0981	$C_6H_{13}N_2O_2^-$	Lysine	-1.0
154.0621	$C_6H_8N_3O_2^-$	Histidine	-0.6
164.0716	$C_9H_{10}NO_2^-$	Phenylalanine	-0.6
173.1042	$C_6H_{13}N_4O_2^-$	Arginine	-1.0
180.0665	$C_9H_{10}NO_3^-$	Tyrosine	-0.6

Table S2.6. Tabulated output from the SIMS-MFP software (2) showing the putative ceramide assignments in positive mode. The observed mass (*m/z*), chemical formula, molecular assignment and mass deviation are documented. All assignments were compared against the Lipid Maps Structural Database ® (3) and/or verified manually from previous literature.

Observed Mass (*m/z*)	Chemical Formula	Molecular Assignment	Mass Deviation
578.5131	$C_{36}H_{68}O_4N_+$	Cer 36:3;O3	2.0
638.6079	$C_{40}H_{80}O_4N_+$	Cer 40:1;O3	-0.4
666.6390	$C_{42}H_{84}O_5N_+$	Cer 42:1;O4	-0.7

Table S2.7. Tabulated output from the SIMS-MFP software (2) showing the putative fatty acid assignments in positive mode. The observed mass (*m/z*), chemical formula, molecular assignment and mass deviation are documented. All assignments were compared against the Lipid Maps Structural Database ® (3) and/or verified manually from previous literature.

Observed Mass (*m/z*)	Chemical Formula	Molecular Assignment	Mass Deviation
101.0597	$C_5H_9O_{2+}$	FA 5:1	0.0
115.0752	$C_6H_{11}O_{2+}$	FA 6:1	1.5
115.0752	$C_6H_{11}O_{2+}$	FA 6:1	1.5
255.2316	$C_{16}H_{31}O_{2+}$	FA 16:1	-1.0
257.2473	$C_{16}H_{33}O_{2+}$	FA 16:0	-0.8
281.2473	$C_{18}H_{33}O_{2+}$	FA 18:2	-0.7
283.2630	$C_{18}H_{35}O_{2+}$	FA 18:1	-0.5
297.2786	$C_{19}H_{37}O_{2+}$	FA 19:1	0.6
307.2630	$C_{20}H_{35}O_{2+}$	FA 20:3	-0.5
309.2786	$C_{20}H_{37}O_{2+}$	FA 20:2	-0.6
311.2942	$C_{20}H_{39}O_{2+}$	FA 20:1	-0.8
323.2943	$C_{21}H_{39}O_{2+}$	FA 21:2	0.4

Table S2.8. Tabulated output from the SIMS-MFP software (2) showing the putative amino acid assignments in positive mode. The observed mass (*m/z*), chemical formula, molecular assignment and mass deviation are documented. All assignments were compared against the Lipid Maps Structural Database ® (3) and/or verified manually from previous literature.

Observed Mass (*m/z*)	Chemical Formula	Molecular Assignment	Mass Deviation
120.0654	$C_4H_{10}NO_{3+}$	Threonine	-1.0
130.0497	$C_5H_8NO_{3+}$	Pyroglutamic acid	-1.3
132.1017	$C_6H_{14}NO_{2+}$	Leucine	-1.6
133.0970	$C_5H_{13}N_2O_{2+}$	Ornithine	-1.2
139.0500	$C_6H_7N_2O_{2+}$	Urocanic acid	-1.2
147.1126	$C_6H_{15}N_2O_{2+}$	Lysine	-1.4
156.0765	$C_6H_{10}N_3O_{2+}$	Histidine	-1.6
166.0860	$C_9H_{12}NO_{2+}$	Phenylalanine	-1.5
175.1187	$C_6H_{15}N_4O_{2+}$	Arginine	-1.4
182.0810	$C_9H_{12}NO_{3+}$	Tyrosine	-0.9

Table S2.9. *Ex vivo* Human Skin Donor Information

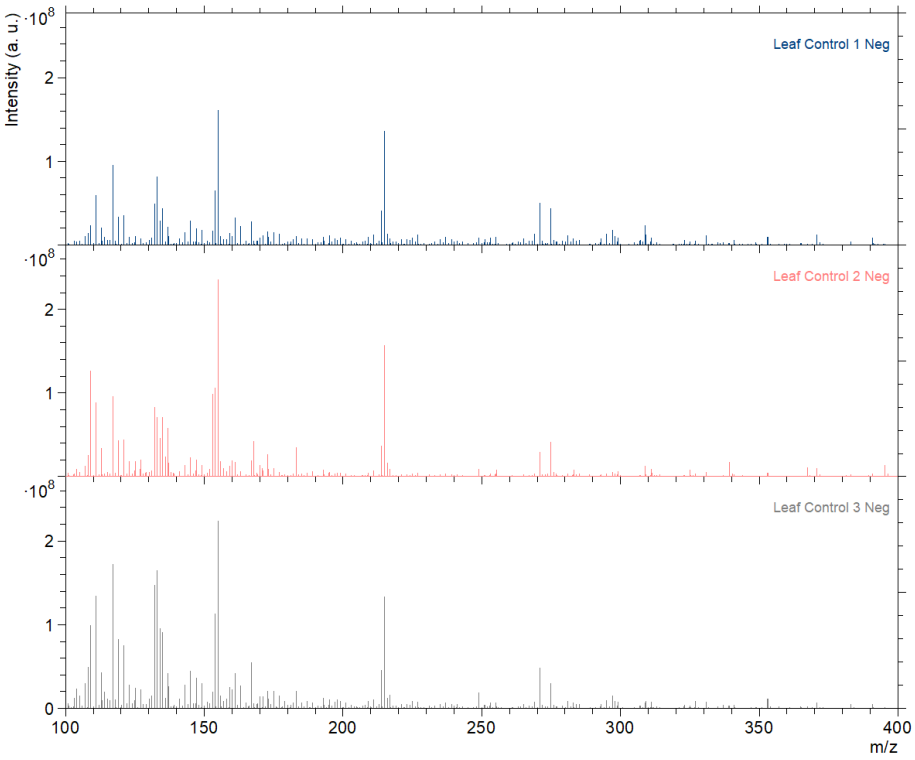
Donor #	Age	Location	Ethnicity
1	38	Abdomen	Caucasian
2	53	Arm	Caucasian
3	69	Abdomen	Caucasian

SI 6.1 References

1. Franz TJ (1975) Percutaneous absorption on the relevance of in vitro data. The Journal of investigative dermatology 64(3):190-195.
2. Sud M*, et al.* (2007) LMSD: LIPID MAPS structure database. *Nucleic acids research* 35(Database issue):D527-532
3. Edney MK, *et al.* (2021) Molecular Formula Prediction for Chemical Filtering of 3D OrbiSIMS Datasets. *Analytical Chemistry* https://doi.org/10.1021/acs.analchem.1c04898.

6.2 Chapter 3 Supporting Information

Supplementary Information Figures
Negative Polarity Spectrum of Wheat Leaf (100 - 800 *m/z*)



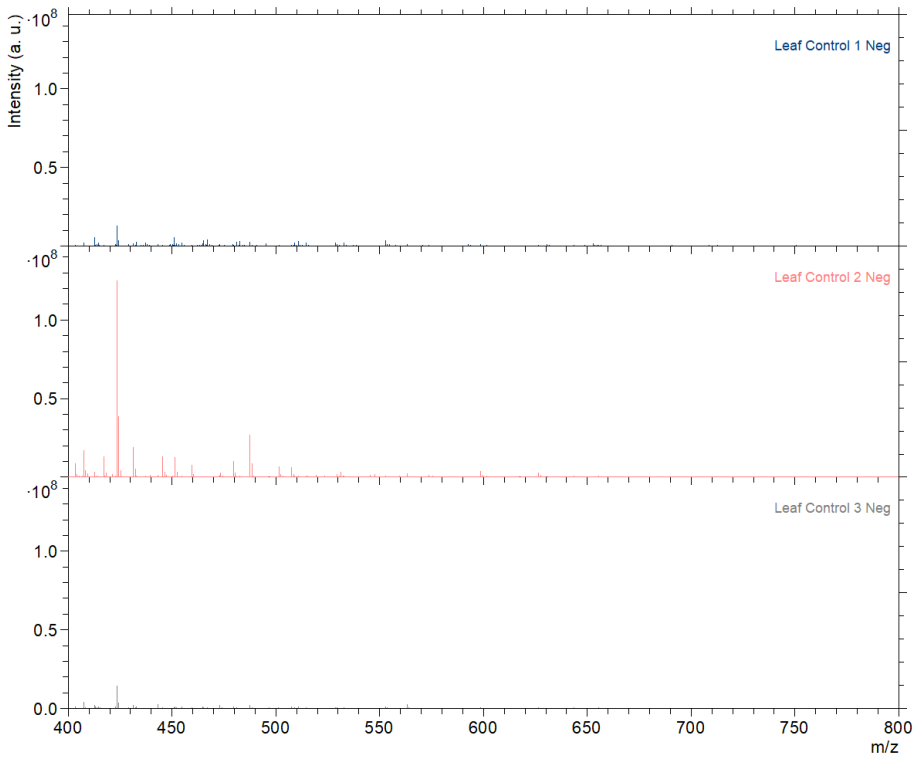


Figure S1. OrbiSIMS negative polarity mass spectral replicate data showing the differences between three separate Motown wheat leaves.

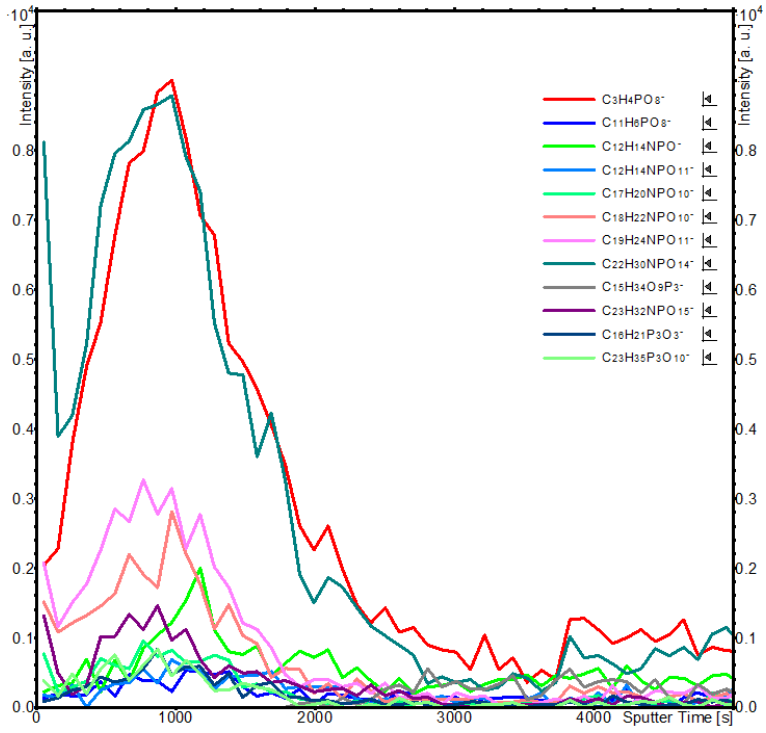


Figure S2. OrbiSIMS negative polarity depth profile data showing the ion intensity variation as function of ion dose/leaf depth for the putatively assigned phospholipid species present within Motown wheat leaves.

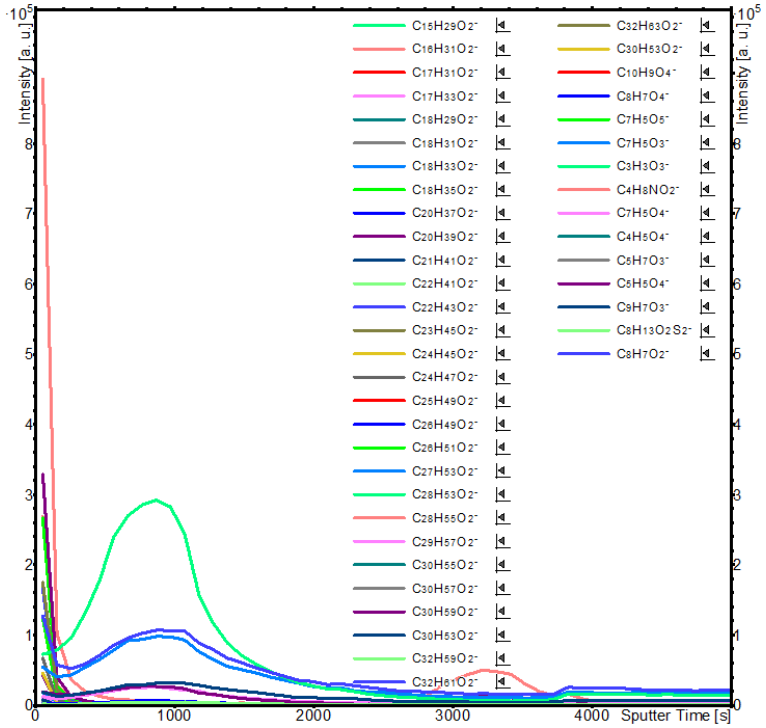


Figure S3. OrbiSIMS negative polarity depth profile data showing the ion intensity variation as function of ion dose/leaf depth for the putatively assigned fatty acid species present within Motown wheat leaves.

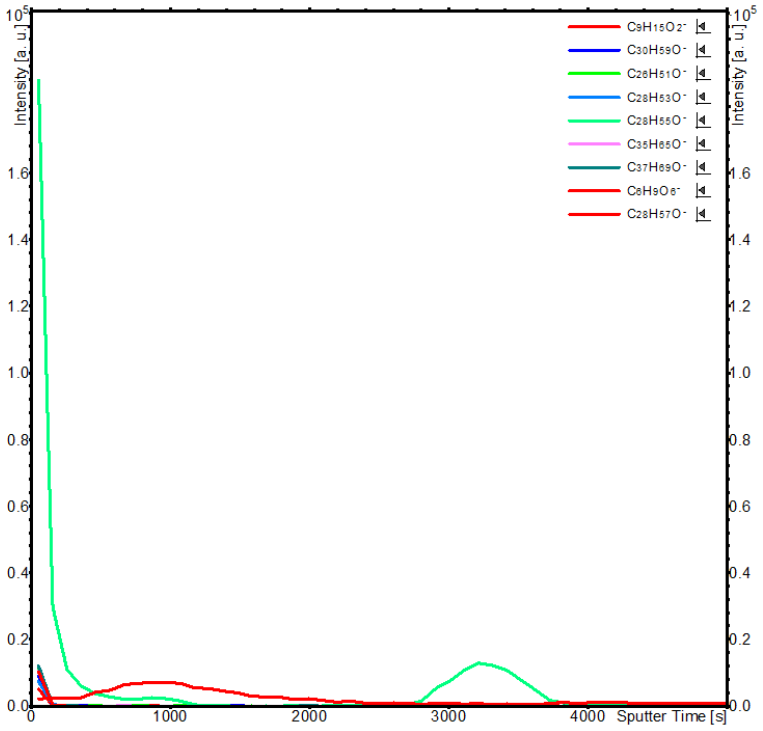


Figure S4. OrbiSIMS negative polarity depth profile data showing the ion intensity variation as function of ion dose/leaf depth for the putatively assigned aldehyde species present within Motown wheat leaves.

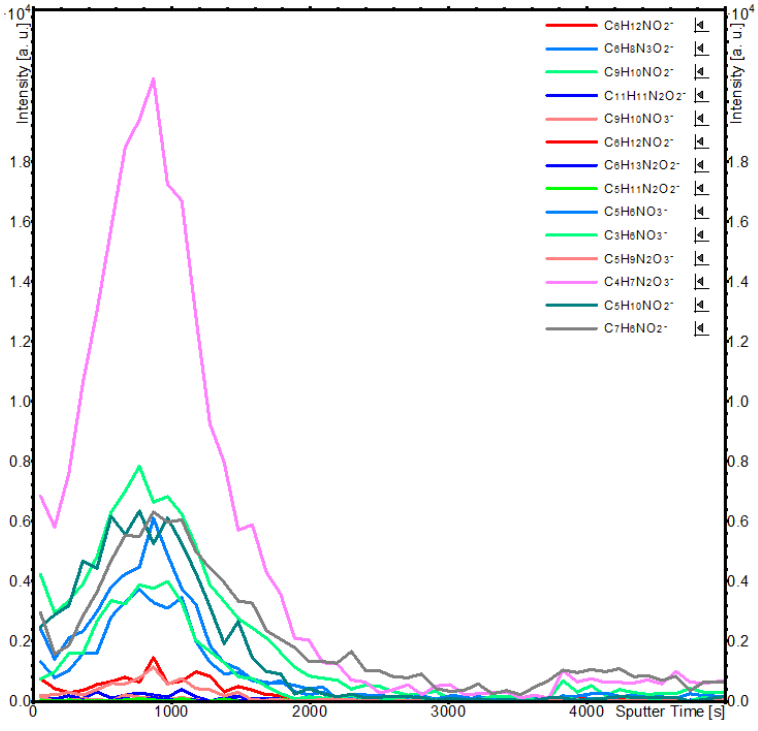


Figure S5. OrbiSIMS negative polarity depth profile data showing the ion intensity

variation as function of ion dose/leaf depth for the putatively assigned amino acid species present within Motown wheat leaves.

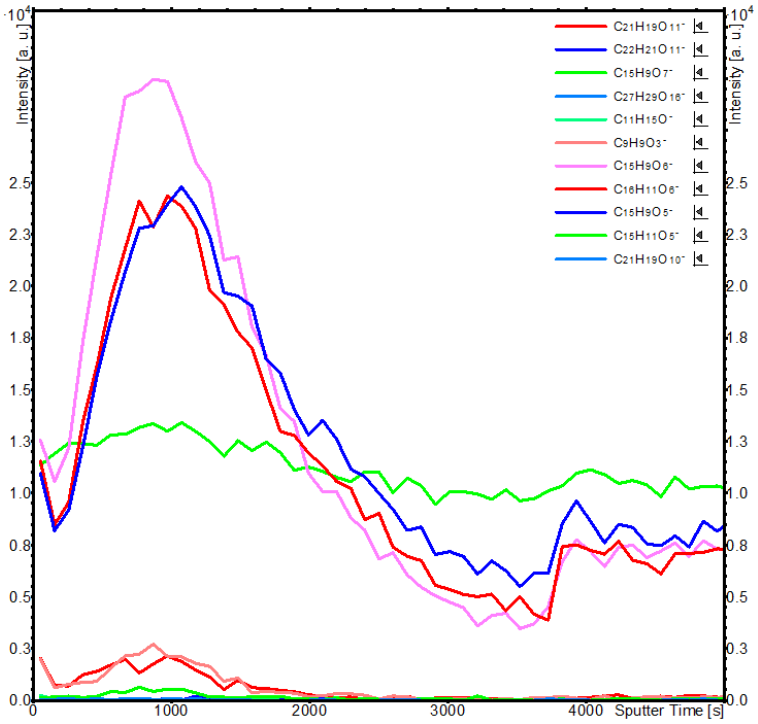


Figure S6. OrbiSIMS negative polarity depth profile data showing the ion intensity variation as function of ion dose/leaf depth for the putatively assigned flavone species present within Motown wheat leaves.

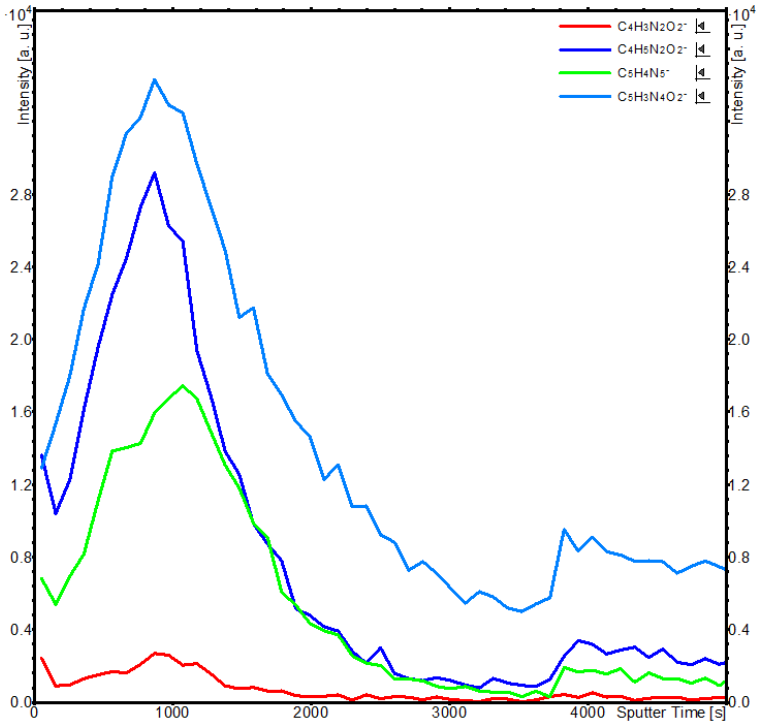


Figure S7. OrbiSIMS negative polarity depth profile data showing the ion intensity variation as function of ion dose/leaf depth for the putatively assigned nucleic acid species present within Motown wheat leaves.

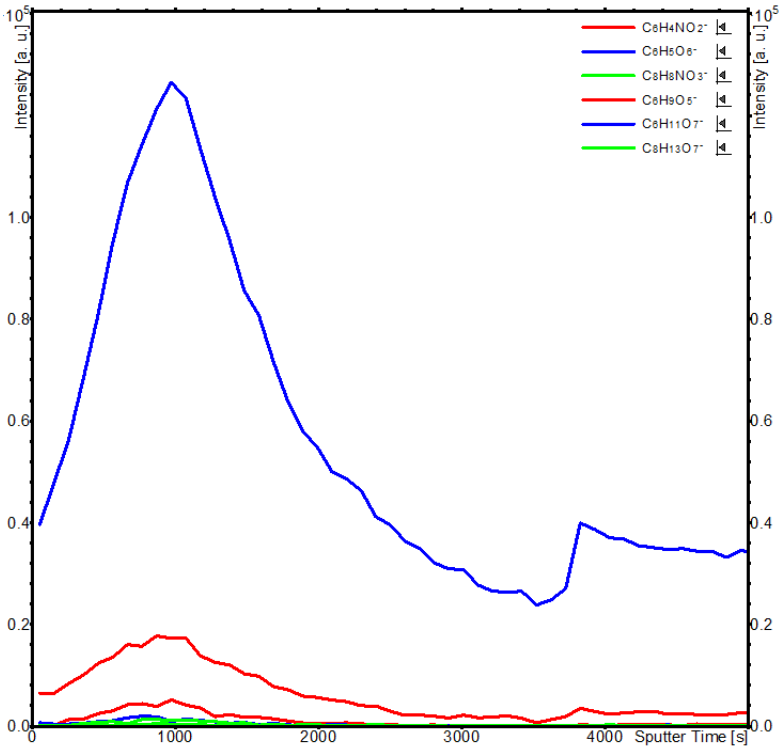
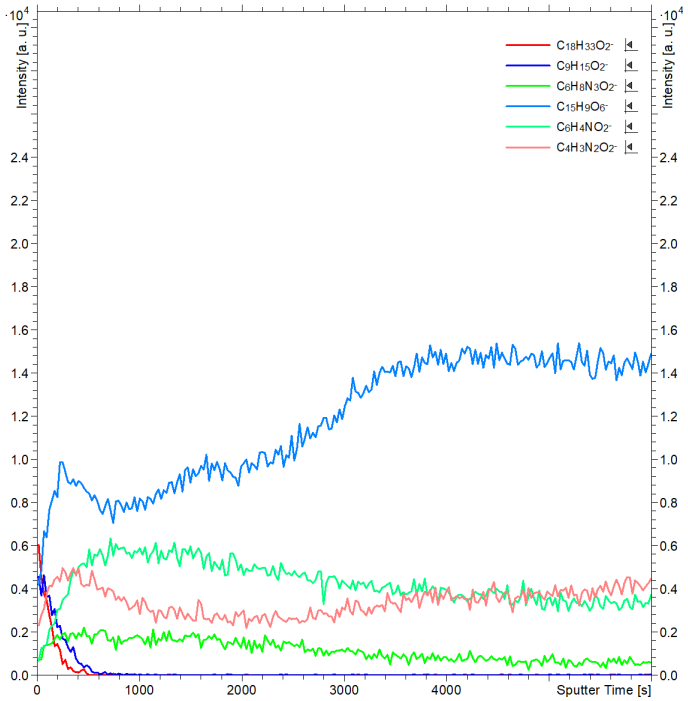
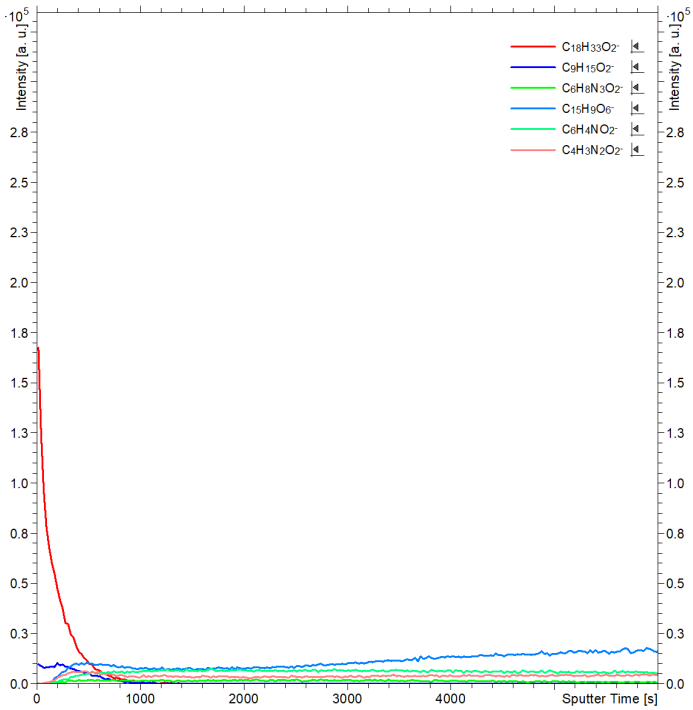


Figure S8. OrbiSIMS negative polarity depth profile data showing the ion intensity variation as function of ion dose/leaf depth for the vitamin/sugar species present within Motown wheat leaves.

(a)


Intensity [a. u.]
·10^4
Sputter Time [s]
C18H33O2-
C9H15O2-
C6H8N3O2-
C15H9O6-
C6H4NO2-
C4H3N2O2-

(b)


Intensity [a. u.]
·10^5
Sputter Time [s]
C18H33O2-
C9H15O2-
C6H8N3O2-
C15H9O6-
C6H4NO2-
C4H3N2O2-

(c)

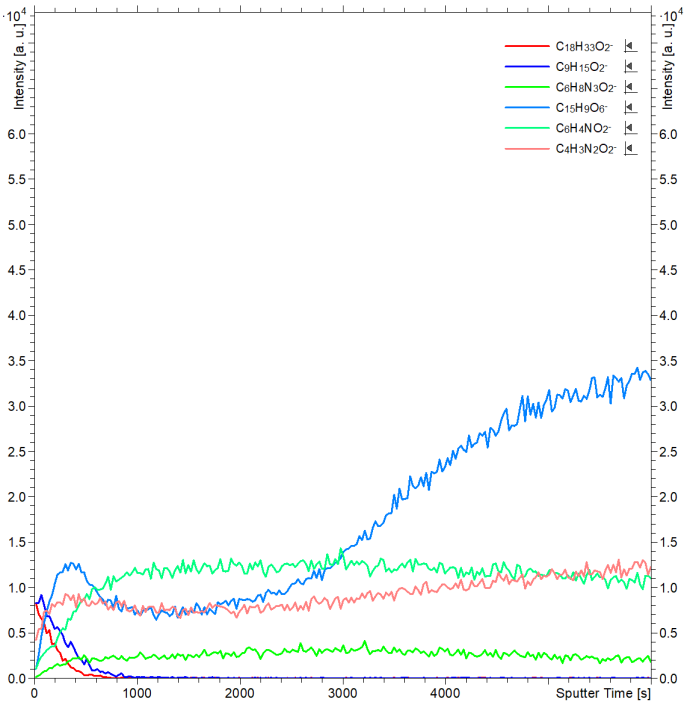


Figure S9. OrbiSIMS negative polarity depth profiles (**a, b** and **c**) replicated data demonstrating the variation in ion intensity as a function of ion dose/leaf depth for six compounds spanning six distinct compound classes. The compounds include FA 18:1 ($C_{18}H_{33}O_2$-), 2,4 nonanedione ($C_9H_{15}O_2$-), histidine ($C_6H_8N_3O_2$-), kaempferol ($C_{15}H_9O_6$-), niacin ($C_6H_4NO_2$-), and uracil ($C_4H_3N_2O_2$-).

Supplementary Information Tables

Table S3.1. Comprehensive data from SIMS-MFP software displaying the putatively assigned phospholipids. The dataset includes the observed mass (*m/z*), chemical formula, molecular assignments and mass deviations. Each assignment was cross-referenced against the Lipid Maps Structural Database and previous literature.

Observed Mass (*m/z*)	Chemical Formula	Mass Deviation
198.9654	$C_3H_4PO_8^-$	2.6
296.9808	$C_{11}H_6PO_8^-$	0.9
219.0816	$C_{12}H_{14}NPO^-$	-1.3
379.0310	$C_{12}H_{14}NPO_{11}^-$	0.1
429.0828	$C_{17}H_{20}NPO_{10}^-$	-0.5
443.0986	$C_{18}H_{22}NPO_{10}^-$	-0.2
473.1091	$C_{39}H_{75}NPO_8^-$	0.4
563.1409	$C_{22}H_{30}NPO_{14}^-$	-0.2
451.1416	$C_{15}H_{34}O_9P_3^-$	-1.1
593.1517	$C_{23}H_{32}NPO_{15}^-$	0.3
354.0701	$C_{16}H_{21}P_3O_3^-$	-2.3
564.1444	$C_{23}H_{35}P_3O_{10}^-$	-0.9

Table S3.2. Comprehensive data from SIMS-MFP software displaying the putatively assigned fatty acid species. The dataset includes the observed mass (*m/z*), chemical

formula, molecular assignments and mass deviations. Each assignment was cross-referenced against the Lipid Maps Structural Database and previous literature.

Observed Mass (*m/z*)	Chemical Formula	Molecular Assignment	Mass Deviation
241.2173	$C_{15}H_{29}O_2^-$	FA 15:0	0.1
255.2330	$C_{16}H_{31}O_{2-}$	FA 16:0	0.2
267.2330	$C_{17}H_{31}O_{2-}$	FA 17:1	0.0
269.2485	$C_{17}H_{33}O_{2-}$	FA 17:0	-0.2
277.2172	$C_{18}H_{29}O_{2-}$	FA 18:3	-0.4
279.2328	$C_{18}H_{31}O_{2-}$	FA 18:2	0.4
281.2485	$C_{18}H_{33}O_{2-}$	FA 18:1	0.3
283.2644	$C_{18}H_{35}O_{2-}$	FA 18:0	0.1
309.2799	$C_{20}H_{37}O_{2-}$	FA 20:1	0.3
311.2955	$C_{20}H_{39}O_{2-}$	FA 20:0	-0.1
353.3425	$C_{23}H_{45}O_{2-}$	FA 23:0	-0.1
365.3424	$C_{24}H_{45}O_{2-}$	FA 24:1	-0.1
367.3580	$C_{24}H_{47}O_{2-}$	FA 24:0	-0.2
381.3738	$C_{25}H_{49}O_{2-}$	FA 25:0	0.1
393.3739	$C_{26}H_{49}O_{2-}$	FA 26:1	0.3
395.3894	$C_{26}H_{51}O_{2-}$	FA 26:0	-0.2
409.4051	$C_{27}H_{53}O_{2-}$	FA 27:0	0.1
421.4053	$C_{28}H_{53}O_{2-}$	FA 28:1	0.4

423.4209	$C_{28}H_{55}O_{2-}$	FA 28:0	-0.4
437.4363	$C_{29}H_{57}O_{2-}$	FA 29:0	-0.2
447.4208	$C_{30}H_{55}O_{2-}$	FA 30:2	0.1
449.4365	$C_{30}H_{57}O_{2-}$	FA 30:1	0.2
451.4521	$C_{30}H_{59}O_{2-}$	FA 30:0	0.2
465.4676	$C_{31}H_{61}O_{2-}$	FA 31:0	0.4
475.4519	$C_{32}H_{59}O_{2-}$	FA 32:2	-0.3
477.4676	$C_{32}H_{61}O_{2-}$	FA 32:1	-0.0
479.4833	$C_{32}H_{63}O_{2-}$	FA 32:0	-0.0
445.4051	$C_{30}H_{63}O_{2-}$	FA 30:3	0.1
167.0350	$C_8H_7O_{4-}$	Vanillic acid	-0.3
169.0142	$C_7H_5O_{5-}$	Gallic acid	-0.1
137.0244	$C_7H_5O_{3-}$	Salicylic acid	-0.5
102.0560	$C_4H_8NO_{2-}$	Aminobutyric acid	0.2
153.0193	$C_7H_5O_{4-}$	Gentisic acid	-0.2
117.0194	$C_4H_5O_{4-}$	Succinic acid	0.3
115.0401	$C_5H_7O_{3-}$	alpha-Ketoisovaleric acid	0.1
129.0193	$C_5H_5O_{4-}$	Glutaconic acid	-0.1

163.0400	$C_9H_7O_{3-}$	Phenylpyruvic acid	0.1
205.0356	$C_8H_{13}O_2S_{2-}$	DL-a-Lipoic Acid	3.0
135.0451	$C_8H_7O_{2-}$	Phenylacetic acid	0.0

Table S3.3. Comprehensive data from SIMS-MFP software displaying the putatively assigned aldehyde species. The dataset includes the observed mass (*m/z*), chemical formula, molecular assignments and mass deviations. Each assignment was cross-referenced against the Lipid Maps Structural Database and previous literature.

Observed Mass (*m/z*)	Chemical Formula	Molecular Assignment	Mass Deviation
155.1076	$C_9H_{15}O_2^-$	Cis-6-nonenal	-0.5
435.4571	$C_{30}H_{59}O^-$	Triacontanal	-0.1
379.3945	$C_{26}H_{51}O^-$	Cyclohexane	-0.1
405.4102	$C_{28}H_{53}O^-$	Octacosadienol	0.1
407.4259	$C_{28}H_{55}O^-$	Hexacosanal	0.1

501.5041	$C_{35}H_{65}O^-$	(9E,26E)-pentatriaconta-9,26-dien-18-one	0.2
529.5355	$C_{37}H_{69}O^-$	28-Heptatriactontadien-2-one	0.2
177.0407	$C_6H_9O_6^-$	Gluconolactone	1.2
409.4415	$C_{28}H_{57}O^-$	Octacosanol	0.1

Table S3.4. Comprehensive data from SIMS-MFP software displaying the putatively assigned amino acid species. The dataset includes the observed mass (*m/z*), chemical formula, molecular assignments and mass deviations. Each assignment was cross-referenced against the Lipid Maps Structural Database and previous literature.

Observed Mass (*m/z*)	Chemical Formula	Molecular Assignment	Mass Deviation
130.0873	$C_6H_{12}NO_2^-$	Leucine	-0.6
154.0622	$C_6H_8N_3O_2^-$	Histidine	0.3
164.0717	$C_9H_{10}NO_2^-$	Phenylalanine	-0.0
203.0827	$C_{11}H_{11}N_2O_2^-$	Tryptophan	0.2
180.0665	$C_9H_{10}NO_3^-$	Tyrosine	-0.6

130.0873	$C_6H_{12}NO_2^-$	L-isoleucine	-0.6
145.0982	$C_6H_{13}N_2O_2^-$	Lysine	-0.3
131.0825	$C_5H_{11}N_2O_2^-$	Ornithine	0.5
128.0353	$C_5H_6NO_3^-$	Pyroglutamic acid	0.1
104.0353	$C_3H_6NO_3^-$	Serine	0.0
145.0609	$C_5H_9N_2O_3^-$	Glutamine	0.6
131.0461	$C_4H_7N_2O_3^-$	Asparagine	0.5
116.0718	$C_5H_{10}NO_2^-$	Valine	0.1
136.0403	$C_7H_6NO_2^-$	Salicylamide	-0.5

Table S3.5. Comprehensive data from SIMS-MFP software displaying the putatively assigned flavones species. The dataset includes the observed mass (*m/z*), chemical formula, molecular assignments and mass deviations. Each assignment was cross-referenced against the Lipid Maps Structural Database and previous literature.

Observed Mass (*m/z*)	Chemical Formula	Molecular Assignment	Mass Deviation
447.0936	$C_{21}H_{19}O_{11}^-$	Cynaroside	0.6
461.1086	$C_{22}H_{21}O_{11}^-$	Peonidin-3-O-glucoside	-0.7
301.1269	$C_{15}H_9O_7^-$	Quercetin	-0.0
609.1467	$C_{27}H_{29}O_{16}^-$	Rutin	0.9
163.1128	$C_{11}H_{15}O^-$	Jasmone	-0.1

165.0557	$C_9H_9O_3^-$	Caffeyl-alcohol	-0.4
285.0404	$C_{15}H_9O_6^-$	Kaempferol	0.1
299.0561	$C_{16}H_{11}O_6^-$	Pratensin	-0.1
269.0456	$C_{15}H_9O_5^-$	Apigenin	0.2
271.0613	$C_{15}H_{11}O_5^-$	Naringenin	0.5
431.0987	$C_{21}H_{19}O_{10}^-$	Vitexin	0.8

Table S3.6. Comprehensive data from SIMS-MFP software displaying the putatively assigned nucleic acids species. The dataset includes the observed mass (*m/z*), chemical formula, molecular assignments and mass deviations. Each assignment was cross-referenced against the Lipid Maps Structural Database and previous literature.

Observed Mass (*m/z*)	Chemical Formula	Molecular Assignment	Mass Deviation
111.0200	$C_4H_3N_2O_2^-$	Uracil	0.1
113.0357	$C_4H_5N_2O_2^-$	Hydrouracil	0.3
134.0472	$C_5H_4N_5^-$	Adenine	-0.1
151.0250	$C_5H_3N_4O_2^-$	Xanthine	-0.2

Table S3.7. Comprehensive data from SIMS-MFP software displaying the putatively assigned vitamin/sugar species. The dataset includes the observed mass (*m/z*), chemical formula, molecular assignments and mass deviations. Each assignment was cross-referenced against the Lipid Maps Structural Database and previous literature.

Observed Mass (*m/z*)	Chemical Formula	Molecular Assignment	Mass Deviation
122.0247	$C_6H_4NO_2^-$	Niacin	-0.1
173.0093	$C_6H_5O_6^-$	Dehydroascorbic acid	1.2
166.0509	$C_8H_8NO_3^-$	Pyridoxal	-0.3
161.0455	$C_6H_9O_5^-$	Levoglucosan	-0.2
195.0511	$C_6H_{11}O_7^-$	Gluconic acid	0.7
221.0667	$C_8H_{13}O_7^-$	6-Acetyl-D-glucose	0.2

Supplementary Information- LC-MS

Table S3.8. Comprehensive data from LC-MS full recovery, displaying the total recoveries (%) of cyproconazole (CCZ) in the donor compartment, skin wash, tape strips, remaining skin and receptor fluid.

	Total Recovery (%)				
Replicates	**Donor Compartment**	**Skin Wash**	**Tape Strip**	**Remaining Skin**	**Receptor Fluid**
4hr R1	5.96	2.84	0.45	3.21	8.60
4hr R2	3.82	18.50	1.03	4.67	0.33
4hr R3	3.81	13.55	1.09	9.62	0.62
7hr R1	3.31	4.67	0.43	11.23	0.43
7hr R2	6.15	4.31	0.82	9.39	0.87
7hr R3	4.36	13.94	0.80	6.81	1.29
24hr R1	17.45	5.61	1.44	14.80	1.05
24hr R2	21.11	5.71	1.73	19.21	2.72
24hr R3	8.56	14.79	3.65	5.47	0.11

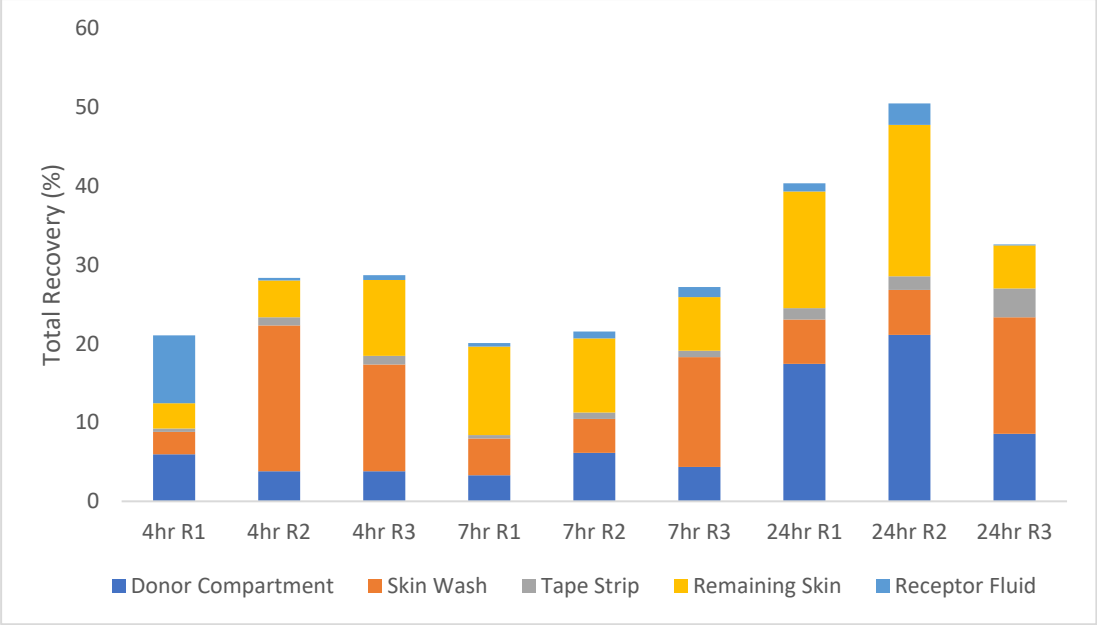


Figure S3.1.1. Comprehensive data from LC-MS full recovery, displaying the total recoveries (%) of cyproconazole (CCZ) in the donor compartment, skin wash, tape strips, remaining skin and receptor fluid.

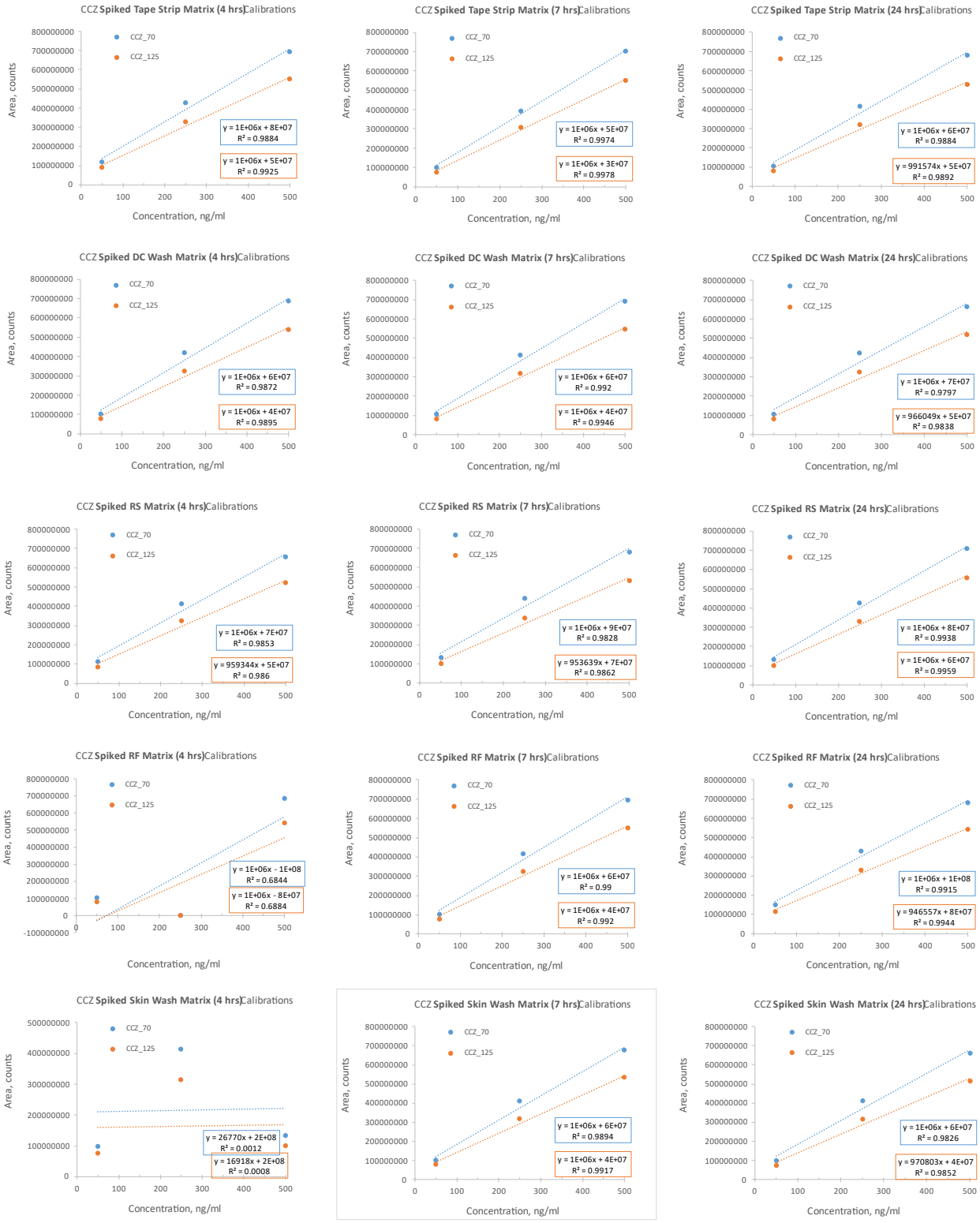


Figure S3.1.2. Comprehensive data from LC-MS full recovery, displaying the matrix matched calibrations for cyproconazole (CCZ) in the donor compartment, skin wash, tape strips, remaining skin and receptor fluid.

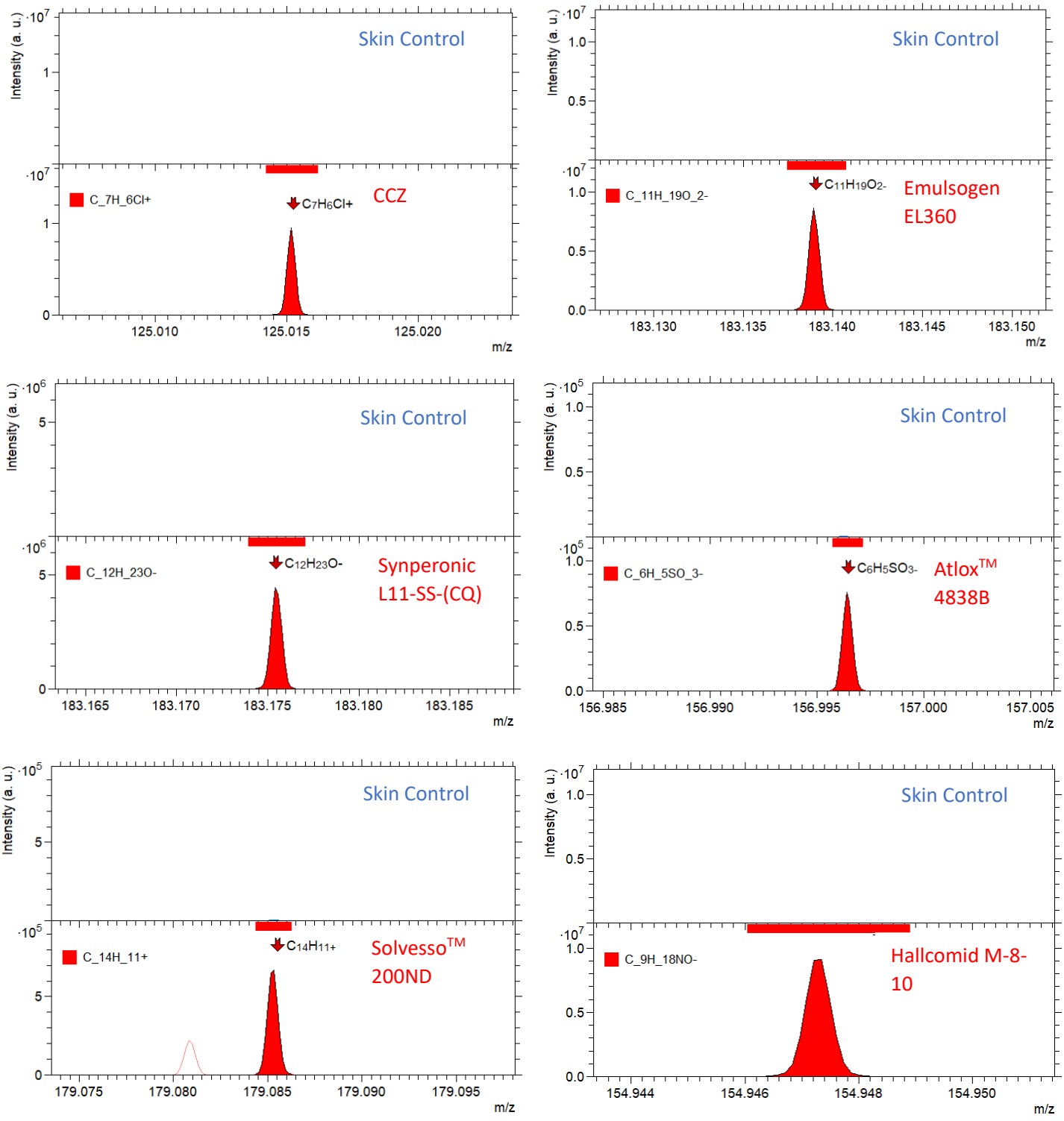


Figure S3.1.3. OrbiSIMS negative polarity mass spectral data showing the diagnostic ions for the model agrochemical formulation used for the depth profiling in porcine skin.

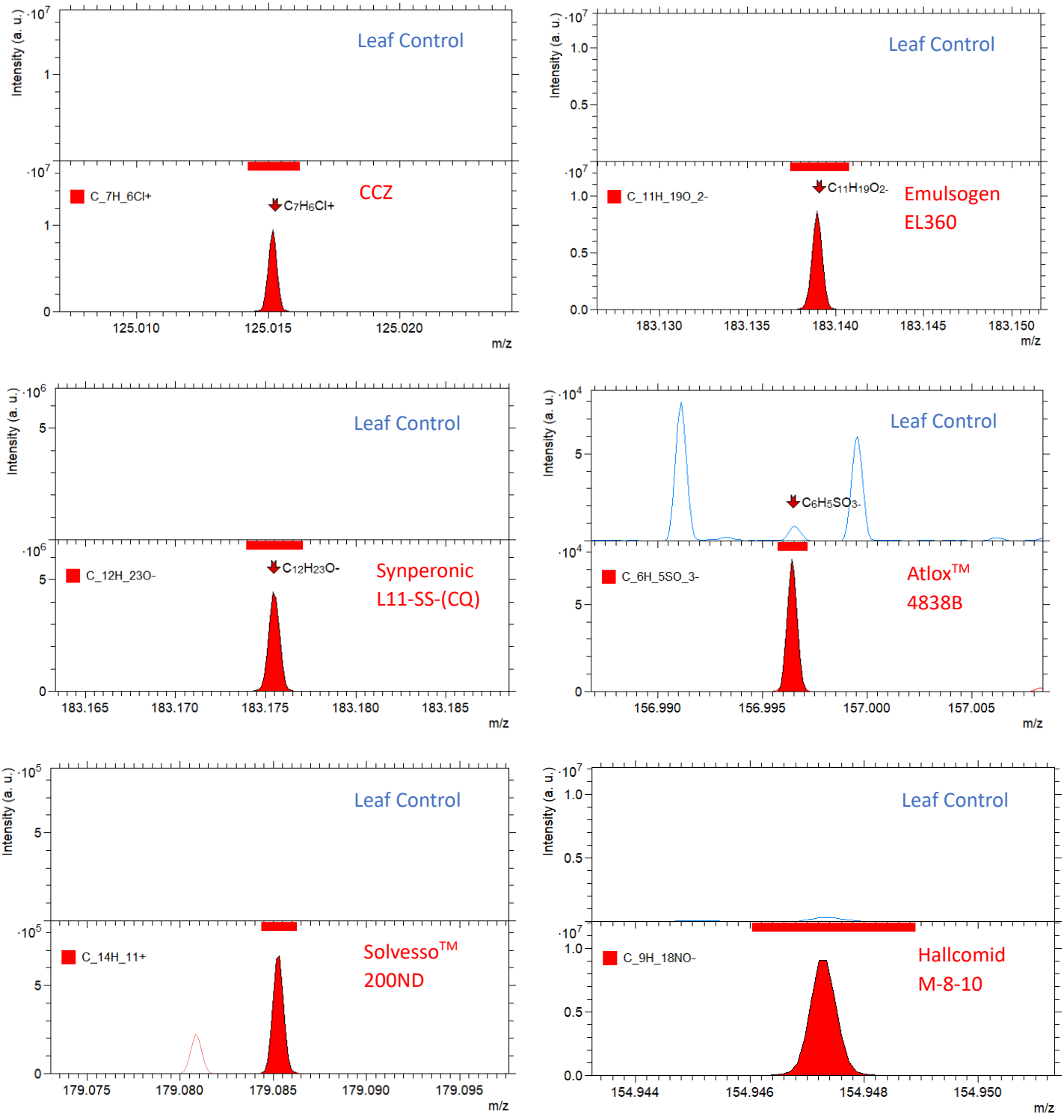


Figure S3.1.4. OrbiSIMS negative polarity mass spectral data showing the diagnostic ions for the model agrochemical formulation used for the depth profiling in Motown leaves.

7. References

1. Kawana M, Miyamoto M, Ohno Y, Kihara A. Comparative profiling and comprehensive quantification of stratum corneum ceramides in humans and mice by LC/MS/MS. J Lipid Res. 2020 Jun 1;61(6):884–95.

2. Van Smeden J, Hoppel L, Van Der Heijden R, Hankemeier T, Vreeken RJ, Bouwstra JA. LC/MS analysis of stratum corneum lipids: ceramide profiling and discovery. J Lipid Res. 2011;52(6):1221.

3. Van Smeden J, Boiten WA, Hankemeier T, Rissmann R, Bouwstra JA, Vreeken RJ. Combined LC/MS-platform for analysis of all major stratum corneum lipids, and the profiling of skin substitutes. Biochimica et Biophysica Acta (BBA) - Molecular and Cell Biology of Lipids. 2014 Jan 1;1841(1):70–9.

4. Lerche CM, Olsen P, Nissen CV, Philipsen PA, Wulf HC. A novel LC-MS/MS method to quantify eumelanin and pheomelanin and their relation to UVR sensitivity - A study on human skin biopsies. Pigment Cell Melanoma Res. 2019 Nov 1;32(6):809–16.

5. Cajka T, Fiehn O. Comprehensive analysis of lipids in biological systems by liquid chromatography-mass spectrometry. Trends Analyt Chem. 2014 Oct 10;61:206.

6. Rudan MV, Mishra A, Klose C, Eggert US, Watt FM. Human epidermal stem cell differentiation is modulated by specific lipid subspecies. Proc Natl Acad Sci U S A. 2020 Sep 8;117(36):22173–82.

7. Kao J, Patterson FK, Hall J. Skin penetration and metabolism of topically applied chemicals in six mammalian species, including man: An in vitro study with benzo[a]pyrene and testosterone. Toxicol Appl Pharmacol. 1985;81(3):502–16.

8. Jiménez-Rodríguez A, Guardado-Félix D, Antunes-Ricardo M. Challenges and Strategies for Topical and Transdermal Delivery of Bioactive Peptides. Crit Rev Ther Drug Carrier Syst. 2022;39(1).

9. Tariq MI, Afzal S, Hussain I, Sultana N. Pesticides exposure in Pakistan: A review. Environ Int. 2007 Nov 1;33(8):1107–22.

10. Ye M, Beach J, Martin JW, Senthilselvan A. Occupational Pesticide Exposures and Respiratory Health. Int J Environ Res Public Health [Internet]. 2013 Nov 28 [cited 2023 Dec 7];10(12):6471. Available from: /pmc/articles/PMC3881124/

11. Ye M, Beach J, Martin JW, Senthilselvan A. Pesticide exposures and respiratory health in general populations. Journal of Environmental Sciences. 2017 Jan 1;51:361–70.

12. Mnif W, Hassine AIH, Bouaziz A, Bartegi A, Thomas O, Roig B. Effect of Endocrine Disruptor Pesticides: A Review. Int J Environ Res Public Health. 2011;8(6):2303.

13. McKinlay R, Plant JA, Bell JNB, Voulvoulis N. Endocrine disrupting pesticides: Implications for risk assessment. Environ Int. 2008 Feb 1;34(2):168–83.

14. Frazier LM. Reproductive disorders associated with pesticide exposure. J Agromedicine [Internet]. 2007 [cited 2023 Dec 7];12(1):27–37. Available from: https://pubmed.ncbi.nlm.nih.gov/18032334/

15. Bretveld RW, Thomas CMG, Scheepers PTJ, Zielhuis GA, Roeleveld N. Pesticide exposure: the hormonal function of the female reproductive system disrupted? Reproductive Biology and Endocrinology [Internet]. 2006 May 31 [cited 2023 Dec 7];4:45. Available from: /pmc/articles/PMC1524969/

16. Damalas CA, Koutroubas SD. Farmers' exposure to pesticides: Toxicity types and ways of prevention. Toxics. 2016 Jan 8;4(1).

17. Al-Mayahy MH, Sabri AH, Rutland CS, Holmes A, McKenna J, Marlow M, et al. Insight into imiquimod skin permeation and increased delivery using microneedle pre-treatment. European Journal of Pharmaceutics and Biopharmaceutics. 2019 Jun 1;139:33–43.

18. Sabri A, Ogilvie J, McKenna J, Segal J, Scurr D, Marlow M. Intradermal delivery of an immunomodulator for basal cell carcinoma; expanding the mechanistic insight in solid microneedle enhanced delivery of hydrophobic molecules. Mol Pharm [Internet]. 2020 Jun 8 [cited 2020 Jul 27]; Available from: https://pubs.acs.org/doi/abs/10.1021/acs.molpharmaceut.0c00347

19. Okamoto M, Tanji N, Katayama Y, Okada J. TOF-SIMS investigation of the distribution of a cosmetic ingredient in the epidermis of the skin. Appl Surf Sci [Internet]. 2006 Jul 30 [cited 2022 Aug 22];252(19):6805–8. Available from: https://www.researchgate.net/publication/248193517_TOF-SIMS_investigation_of_the_distribution_of_a_cosmetic_ingredient_in_the_epidermis_of_the_skin

20. Starr NJ, Abdul Hamid K, Wibawa J, Marlow I, Bell M, Pérez-García L, et al. Enhanced vitamin C skin permeation from supramolecular hydrogels, illustrated using in situ ToF-SIMS 3D chemical profiling. Int J Pharm. 2019 May 30;563(1):21–9.

21. Turner R, Wevrett SR, Edmunds S, Brown M, Atkinson R, Shea T. Validation of an analytical method to quantify the permeation and penetration of flurbiprofen into human pharynx tissue. Biomedical Chromatography. 2019 Aug 1;33(8):44–99.

22. Katakam LNR, Katari NK. Development of in-vitro release testing method for permethrin cream formulation using Franz Vertical Diffusion Cell apparatus by HPLC. Talanta Open. 2021 Dec 1;4.

23. Sil BC, Moore DJ, Lane ME. Use of LC-MS analysis to elucidate by-products of niacinamide transformation following in vitro skin permeation studies. Int J Cosmet Sci. 2018 Oct 1;40(5):525–9.

24. Hemathilake DMKS, Gunathilake DMCC. Agricultural productivity and food supply to meet increased demands. Future Foods: Global Trends, Opportunities, and Sustainability Challenges. 2022 Jan 1;539–53.

25. Reynoud N, Petit J, Bres C, Lahaye M, Rothan C, Marion D, et al. The Complex Architecture of Plant Cuticles and Its Relation to Multiple Biological Functions. Front Plant Sci. 2021 Dec 10;12(1):773–82.

26. Dominguez E, Heredia-Guerrero JA, Heredia A. The biophysical design of plant cuticles: an overview. New Phytologist [Internet]. 2011 Mar 1 [cited 2023 Aug 9];189(4):938–49. Available from: https://onlinelibrary.wiley.com/doi/full/10.1111/j.1469-8137.2010.03553.x

27. Schreiber L. Polar Paths of Diffusion across Plant Cuticles: New Evidence for an Old Hypothesis. Ann Bot [Internet]. 2005 [cited 2023 Oct 10];95(7):1073. Available from: /pmc/articles/PMC4246894/

28. Staiger S, Seufert P, Arand K, Burghardt M, Popp C, Riederer M. The permeation barrier of plant cuticles: uptake of active ingredients is limited by very long-chain aliphatic rather than cyclic wax compounds. Pest Manag Sci [Internet]. 2019 Dec 1 [cited 2023 Oct 10];75(12):3405–12. Available from: https://onlinelibrary.wiley.com/doi/full/10.1002/ps.5589

29. Coret JM, Chamel AR. Influence of some nonionic surfactants on water sorption by isolated tomato fruit cuticles in relation to cuticular penetration of glyphosate. Pestic Sci. 1993;38(1):27–32.

30. Passarelli MK, Pirkl A, Moellers R, Grinfeld D, Kollmer F, Havelund R, et al. The 3D OrbiSIMS - Label-free metabolic imaging with subcellular lateral resolution and high mass-resolving power. Nat Methods. 2017 Dec 1;14(12):1175–83.

31. Coates M, Blanchard S, MacLeod AS. Innate antimicrobial immunity in the skin: A protective barrier against bacteria, viruses, and fungi. PLoS Pathog [Internet]. 2018 Dec 1 [cited 2023 Dec 7];14(12). Available from: /pmc/articles/PMC6283644/

32. Mifsud T, Modestini C, Mizzi A, Falzon O, Cassar K, Mizzi S. The Effects of Skin Temperature Changes on the Integrity of Skin Tissue: A Systematic Review. Adv Skin Wound Care. 2022 Oct 1;35(10):565.

33. Dréno B. Anatomy and physiology of skin and cutaneous annexes. Ann Dermatol Venereol. 2009;136(SUPPL. 10).

34. Voegeli D. Prevention and management of moisture-associated skin damage. Nurs Stand [Internet]. 2019 Jan 25 [cited 2023 Dec 7];34(2):77–82. Available from: https://pubmed.ncbi.nlm.nih.gov/31468844/

35. Gilaberte Y, Prieto-Torres L, Pastushenko I, Juarranz Á. Anatomy and Function of the Skin. Nanoscience in Dermatology. 2016 Aug 25;1–14.

36. Lopez-Ojeda W, Pandey A, Alhajj M, Oakley AM. Anatomy, Skin (Integument). StatPearls. 2022 Oct 17;

37. Hofmann E, Schwarz A, Fink J, Kamolz LP, Kotzbeck P. Modelling the Complexity of Human Skin In Vitro. Biomedicines [Internet]. 2023 Mar 1 [cited 2023 Dec 9];11(3):794. Available from: /pmc/articles/PMC10045055/

38. Eckert RL, Rorke EA. Molecular biology of keratinocyte differentiation. Environ Health Perspect. 1989;80:109–16.

39. Cichorek M, Wachulska M, Stasiewicz A, Tymińska A. Skin melanocytes: biology and development. Advances in Dermatology and Allergology/Postępy Dermatologii I Alergologii. 2013;30(1):41.

40. Jaitley S, Saraswathi TR. Pathophysiology of Langerhans cells. J Oral Maxillofac Pathol. 2012 May;16(2):244.

41. Farage MA, Miller KW, Elsner P, Maibach HI. Structural characteristics of the aging skin: a review. Cutan Ocul Toxicol. 2007 Oct;26(4):343–57.

42. Elias PM. The skin barrier as an innate immune element. Semin Immunopathol. 2007 Apr;29(1):3–14.

43. Harding CR. The stratum corneum: structure and function in health and disease. Dermatol Ther. 2004;17 Suppl 1(1):6–15.

44. Ishida-Yamamoto A, Igawa S. The biology and regulation of corneodesmosomes. Cell Tissue Res. 2015 Jun 4;360(3):477–82.

45. Del Rosso JQ, Levin J. The Clinical Relevance of Maintaining the Functional Integrity of the Stratum Corneum in both Healthy and Disease-affected Skin. J Clin Aesthet Dermatol. 2011 Sep;4(9):42.

46. Riethmüller C. Assessing the skin barrier via corneocyte morphometry. Exp Dermatol. 2018 Aug 1;27(8):923–30.

47. Hogan MB, Peele K, Wilson NW. Skin Barrier Function and Its Importance at the Start of the Atopic March. J Allergy (Cairo). 2012 May 7;2012:1–7.

48. Bragulla HH, Homberger DG. Structure and functions of keratin proteins in simple, stratified, keratinized and cornified epithelia. J Anat. 2009;214(4):559.

49. Abd E, Yousef SA, Pastore MN, Telaprolu K, Mohammed YH, Namjoshi S, et al. Skin models for the testing of transdermal drugs. Clin Pharmacol. 2016 Oct 19;8:176.

50. Agarwal S, Krishnamurthy K. Histology, Skin. StatPearls. 2023 May 1;

51. Van Smeden J, Hoppel L, Van Der Heijden R, Hankemeier T, Vreeken RJ, Bouwstra JA. LC/MS analysis of stratum corneum lipids: ceramide profiling and discovery. J Lipid Res. 2011;52(6):1221.

52. Laffet GP, Genette A, Gamboa B, Auroy V, Voegel JJ. Determination of fatty acid and sphingoid base composition of eleven ceramide subclasses in stratum corneum by UHPLC/scheduled-MRM. Metabolomics. 2018 May 1;14(5).

53. Norlén L, Nicander I, Lundsjö A, Cronholm T, Forslind B. A new HPLC-based method for the quantitative analysis of inner stratum corneum lipids with special reference to the free fatty acid fraction. Arch Dermatol Res. 1998;290(9):508–16.

54. van Smeden J, Janssens M, Gooris GS, Bouwstra JA. The important role of stratum corneum lipids for the cutaneous barrier function. Biochimica et Biophysica Acta (BBA) - Molecular and Cell Biology of Lipids. 2014 Mar 1;1841(3):295–313.

55. Rawlings A V., Matts PJ. Stratum Corneum Moisturization at the Molecular Level: An Update in Relation to the Dry Skin Cycle. Journal of Investigative Dermatology. 2005 Jun 1;124(6):1099–110.

56. Camera E, Ludovici M, Galante M, Sinagra JL, Picardo M. Comprehensive analysis of the major lipid classes in sebum by rapid resolution high-performance liquid

chromatography and electrospray mass spectrometry. J Lipid Res. 2010 Nov 1;51(11):3377–88.

57. Borecka O, Rhodes LE, Webb AR, Dutton JJ, Fraser WD. A newly developed and validated LC–MS/MS method for measuring 7-dehydrocholesterol (7DHC) concentration in human skin: a tool for vitamin D photobiology research. Photochemical and Photobiological Sciences. 2022 Nov 1;21(11):2001–9.

58. Norlén L, Nicander I, Lundsjö A, Cronholm T, Forslind B. A new HPLC-based method for the quantitative analysis of inner stratum corneum lipids with special reference to the free fatty acid fraction. Arch Dermatol Res. 1998;290(9):508–16.

59. Chen SH, Chuang YJ. Analysis of fatty acids by column liquid chromatography. Anal Chim Acta. 2002 Aug 16;465(1–2):145–55.

60. Sjövall P, Skedung L, Gregoire S, Biganska O, Clément F, Luengo GS. Imaging the distribution of skin lipids and topically applied compounds in human skin using mass spectrometry. Sci Rep. 2018 Dec 1;8(1):1–14.

61. Hu Y, Yang L, Gao C, Liao D, Long L, Qiu J, et al. A comparative study on the leaf anatomical structure of Camellia oleifera in a low-hot valley area in Guizhou Province, China. PLoS One [Internet]. 2022 Jan 1 [cited 2023 Oct 10];17(1). Available from: /pmc/articles/PMC8775352/

62. Bielczynski LW, Łączki MK, Hoefnagels I, Gambin A, Croce R. Leaf and Plant Age Affects Photosynthetic Performance and Photoprotective Capacity. Plant Physiol. 2017 Dec 1;175(4):1648.

63. Valladares F, Hernández LG, Dobarro I, García-Pérez C, Sanz R, Pugnaire FI. The Ratio of Leaf to Total Photosynthetic Area Influences Shade Survival and Plastic Response to Light of Green-stemmed Leguminous Shrub Seedlings. Ann Bot. 2003 Apr 1;91(5):584.

64. Adnew GA, Pons TL, Koren G, Peters W, Röckmann T. Leaf-scale quantification of the effect of photosynthetic gas exchange on δ17O of atmospheric CO2. Biogeosciences. 2020 Jul 31;17(14):3903–22.

65. Canvin DT, Berry JA, Badger MR, Fock H, Osmond CB. Oxygen Exchange in Leaves in the Light. Plant Physiol. 1980 Aug 1;66(2):307.

66. Clum HH. The Effect of Transpiration and Environmental Factors on Leaf Temperatures II. Light Intensity and the Relation of Transpiration to the Thermal Death Point. Am J Bot. 1926 Apr;13(4):230.

67. Nilson SE, Assmann SM. The Control of Transpiration. Insights from Arabidopsis. Plant Physiol. 2007;143(1):27.

68. Patel D, Franklin KA. Temperature-regulation of plant architecture. Plant Signal Behav. 2009 Jul;4(7):579.

69. Levin A, Nackley L. Principles and Practices of Plant-based Irrigation Management. Horttechnology. 2021 Dec 1;31(6):650–60.

70. Arya GC, Sarkar S, Manasherova E, Aharoni A, Cohen H. The Plant Cuticle: An Ancient Guardian Barrier Set Against Long-Standing Rivals. Front Plant Sci. 2021 Jun 25;12(1).

71. Kerstiens G. Water transport in plant cuticles: an update. J Exp Bot [Internet]. 2006 Aug 1 [cited 2023 Aug 9];57(11):2493–9. Available from: https://dx.doi.org/10.1093/jxb/erl017

72. Solovchenko A, Merzlyak M. Optical properties and contribution of cuticle to UV protection in plants: Experiments with apple fruit. Photochemical and Photobiological Sciences. 2003;2(8):861–6.

73. Jenkin S, Molina I. Isolation and Compositional Analysis of Plant Cuticle Lipid Polyester Monomers. J Vis Exp [Internet]. 2015 Nov 22 [cited 2023 Oct 10];2015(105). Available from: /pmc/articles/PMC4692744/

74. Saladin S, D'Aronco S, Ingram G, Giorio C. Direct surface analysis mass spectrometry uncovers the vertical distribution of cuticle-associated metabolites in plants. RSC Adv [Internet]. 2023 Mar 3 [cited 2023 Oct 10];13(13):8495. Available from: /pmc/articles/PMC10012332/

75. Baker EA, Parsons E. Scanning electron microscopy of plant cuticles. J Microsc [Internet]. 1971 Aug 1 [cited 2023 Oct 10];94(1):39–49. Available from: https://onlinelibrary.wiley.com/doi/full/10.1111/j.1365-2818.1971.tb02359.x

76. Daher FB, Braybrook SA. How to let go: pectin and plant cell adhesion. Front Plant Sci. 2015 Jul 14;6(JULY).

77. Jetter R, Kunst L, Samuels AL. Composition of Plant Cuticular Waxes. Annual Plant Reviews online. 2018 Apr 19;145–81.

78. Tulloch AP. Chemistry of waxes of higher plants. Chemistry and Biochemistry of Natural Waxes. 1976;1(1):235–87.

79. Riederer M, Schreiber L. Protecting against water loss: analysis of the barrier properties of plant cuticles. J Exp Bot. 2001;52(363):2023–32.

80. Lolle SJ, Cheung AY, Sussex IM. Fiddlehead: An Arabidopsis mutant constitutively expressing an organ fusion program that involves interactions between epidermal cells. Dev Biol. 1992;152(2):383–92.

81. Suh MC, Samuels AL, Jetter R, Kunst L, Pollard M, Ohlrogge J, et al. Cuticular Lipid Composition, Surface Structure, and Gene Expression in Arabidopsis Stem Epidermis. Plant Physiol [Internet]. 2005 [cited 2022 Aug 22];139(4):1655. Available from: /pmc/articles/PMC1310549/

82. Ananthapadmanabhan KP, Mukherjee S, Chandar P. Stratum corneum fatty acids: their critical role in preserving barrier integrity during cleansing. Int J Cosmet Sci. 2013 Aug;35(4):337–45.

83. Karabourniotis G, Liakopoulos G, Bresta P, Nikolopoulos D. The Optical Properties of Leaf Structural Elements and Their Contribution to Photosynthetic Performance and Photoprotection. Plants. 2021 Jul 1;10(7):1455.

84. Fricke W, Pritchard J, Leigh RA, Tomos AD. Cells of the Upper and Lower Epidermis of Barley (Hordeum vulgare L.) Leaves Exhibit Distinct Patterns of Vacuolar Solutes. Plant Physiol. 1994;104(4):1201–8.

85. Gotoh E, Suetsugu N, Higa T, Matsushita T, Tsukaya H, Wada M. Palisade cell shape affects the light-induced chloroplast movements and leaf photosynthesis. Scientific Reports 2018 8:1. 2018 Jan 24;8(1):1–9.

86. Borsuk AM, Roddy AB, Théroux-Rancourt G, Brodersen CR. Structural organization of the spongy mesophyll. New Phytologist. 2022 May 1;234(3):946–60.

87. Jenkin S, Molina I. Isolation and Compositional Analysis of Plant Cuticle Lipid Polyester Monomers. JoVE (Journal of Visualized Experiments). 2015 Nov 22;2015(105):533–86.

88. Thiombiano B, Gontier E, Molinié R, Marcelo P, Mesnard F, Dauwe R. An untargeted liquid chromatography–mass spectrometry-based workflow for the structural characterization of plant polyesters. The Plant Journal [Internet]. 2020 Jun 1 [cited 2023 Aug 9];102(6):1323–39. Available from: https://onlinelibrary.wiley.com/doi/full/10.1111/tpj.14686

89. Jeffree CE. The Fine Structure of the Plant Cuticle. Annual Plant Reviews. 2007 Nov 12;23(2):11–125.

90. Falcone Ferreyra ML, Rius SP, Casati P. Flavonoids: Biosynthesis, biological functions, and biotechnological applications. Front Plant Sci. 2012 Sep 28;3(SEP):343–53.

91. Huang M, Zhang Y, Xu S, Xu W, Chu K, Xu W, et al. Identification and quantification of phenolic compounds in Vitex negundo L. var. cannabifolia (Siebold et Zucc.) Hand.-Mazz. using liquid chromatography combined with quadrupole time-of-flight and triple quadrupole mass spectrometers. J Pharm Biomed Anal [Internet]. 2015 Apr 1 [cited 2023 Oct 10];108(10):11–20. Available from: https://pubmed.ncbi.nlm.nih.gov/25703235/

92. Kerstiens G. Cuticular water permeability and its physiological significance. J Exp Bot. 1996;47(305):1813–32.

93. Pimentel D. Environmental and economic costs of the application of pesticides primarily in the United States. Integrated Pest Management. 2009;1:89–111.

94. Alout H, Roche B, Dabiré RK, Cohuet A. Consequences of insecticide resistance on malaria transmission. PLoS Pathog. 2017 Sep 1;13(9):e1006499.

95. Erhirhie EO, Ihekwereme CP, Ilodigwe EE. Advances in acute toxicity testing: strengths, weaknesses and regulatory acceptance. Interdiscip Toxicol. 2018;11(1):12.

96. World Health Organisation. Public health impact of pesticides used in agriculture. Geneva; 1990 Jan.

97. Wongta A, Sawarng N, Tongchai P, Sutan K, Kerdnoi T, Prapamontol T, et al. The Pesticide Exposure of People Living in Agricultural Community, Northern Thailand. J Toxicol. 2018;2018.

98. Thundiyil JG, Stober J, Besbelli N, Pronczuk J. Acute pesticide poisoning: a proposed classification tool. Bull World Health Organ. 2008 Mar 1;86(3):209.

99. Zarn JA, Hänggi E, Kuchen A, Schlatter JR. The significance of the subchronic toxicity in the dietary risk assessment of pesticides. Regul Toxicol Pharmacol. 2010 Oct;58(1):72–8.

100. Banerjee BD. Sub-chronic effect of DDT on humoral immune response to a thymus-independent antigen (bacterial lipopolysaccharide) in mice. Bull Environ Contam Toxicol. 1987 Nov;39(5):822–6.

101. Lee JY, Park H, Lim W, Song G. Developmental toxicity of chlorpropham induces pathological changes and vascular irregularities in zebrafish embryos. Comparative Biochemistry and Physiology Part C: Toxicology & Pharmacology. 2020 Oct 1;236:108802.

102. Clofenotane | C14H9Cl5 | CID 3036 - PubChem [Internet]. [cited 2023 Dec 9]. Available from: https://pubchem.ncbi.nlm.nih.gov/compound/Clofenotane

103. Luo XW, Ong HY, Tan C, Foo SC, Ong CN. Environmental and biological monitoring of organochlorine residues after the plague epidemic in Surat, India - A preliminary study. Environ Monit Assess. 1997;44(1–3):369–74.

104. Van Den Berg H. Global Status of DDT and Its Alternatives for Use in Vector Control to Prevent Disease. Environ Health Perspect. 2009 Nov;117(11):1663.

105. Dong K. Insect sodium channels and insecticide resistance. Invert Neurosci. 2007 Mar;7(1):30.

106. Mitra J, Raghu K. Effects of DDT on the growth of crop plants. Environ Pollut. 1989;61(2):157–70.

107. Turusov V, Rakitsky V, Tomatis L. Dichlorodiphenyltrichloroethane (DDT): ubiquity, persistence, and risks. Environ Health Perspect. 2002;110(2):125–8.

108. Longnecker MP, Rogan WJ, Lucier G. The human health effects of DDT (dichlorodiphenyltrichloroethane) and PCBS (polychlorinated biphenyls) and an overview of organochlorines in public health. Annu Rev Public Health. 1997;18:211–44.

109. Diamanti-Kandarakis E, Bourguignon JP, Giudice LC, Hauser R, Prins GS, Soto AM, et al. Endocrine-Disrupting Chemicals: An Endocrine Society Scientific Statement. Endocr Rev. 2009 Jun;30(4):342.

110. Soto AM, Sonnenschein C. Endocrine disruptors: DDT, endocrine disruption and breast cancer. Vol. 11, Nature Reviews Endocrinology. Nature Publishing Group; 2015. p. 507–8.

111. Barthel E. Increased risk of lung cancer in pesticide-exposed male agricultural workers. J Toxicol Environ Health. 1981;8(5–6):1040.

112. VoPham T, Bertrand KA, Hart JE, Laden F, Brooks MM, Yuan JM, et al. Pesticide exposure and liver cancer: a review. Cancer Causes Control. 2017 Mar 1;28(3):190.

113. Baris D, Zahm SH, Cantor KP, Blair A. Agricultural use of DDT and risk of non-Hodgkin's lymphoma: pooled analysis of three case-control studies in the United States. Occup Environ Med. 1998;55(8):522–7.

114. Zabalza A, Orcaray L, Fernández-Escalada M, Zulet-González A, Royuela M. The pattern of shikimate pathway and phenylpropanoids after inhibition by glyphosate or quinate feeding in pea roots. Pestic Biochem Physiol. 2017 Sep 1;141:96–102.

115. Gasnier C, Dumont C, Benachour N, Clair E, Chagnon MC, Séralini GE. Glyphosate-based herbicides are toxic and endocrine disruptors in human cell lines. Toxicology. 2009 Aug 21;262(3):184–91.

116. Jaga K, Dharmani C. Sources of exposure to and public health implications of organophosphate pesticides. Rev Panam Salud Publica. 2003;14(3):171–85.

117. Colovic MB, Krstic DZ, Lazarevic-Pasti TD, Bondzic AM, Vasic VM. Acetylcholinesterase Inhibitors: Pharmacology and Toxicology. Curr Neuropharmacol. 2013 Apr 25;11(3):335.

118. Tizhe E, Ibrahim N, Fatihu M, Ambali S, Igbokwe I, Tizhe U. Pancreatic function and histoarchitecture in Wistar rats following chronic exposure to Bushfire®: the mitigating role of zinc. J Int Med Res. 2018 Aug 1;46(8):3296–305.

119. Peixoto F. Comparative effects of the Roundup and glyphosate on mitochondrial oxidative phosphorylation. Chemosphere. 2005;61(8):1115–22.

120. Keillor G. Pesticides: Carbofuran under Review. Environ Health Perspect. 2008 Oct;116(10):A425.

121. Jada MY, Gungula DT, Jacob I, Al-Khatib K. Efficacy of Carbofuran in Controlling Root-Knot Nematode (*Meloidogyne javanica* Whitehead, 1949) on Cultivars of Bambara Groundnut (*Vigna subterranea* (L.) Verdc.) in Yola, Nigeria. International Journal of Agronomy. 2011;2011:1–5.

122. IUPAC. Carbofuran (Ref: OMS 864) [Internet]. [cited 2023 Dec 9]. Available from: https://sitem.herts.ac.uk/aeru/iupac/Reports/118.htm

123. Mnif W, Hassine AIH, Bouaziz A, Bartegi A, Thomas O, Roig B. Effect of Endocrine Disruptor Pesticides: A Review. Int J Environ Res Public Health. 2011;8(6):2303.

124. Lin JN, Lin CL, Lin MC, Lai CH, Lin HH, Yang CH, et al. Increased Risk of Dementia in Patients With Acute Organophosphate and Carbamate Poisoning: A Nationwide Population-Based Cohort Study. Medicine. 2015 Jul 1;94(29):e1187.

125. Matošević A, Radman Kastelic A, Mikelić A, Zandona A, Katalinić M, Primožič I, et al. Quinuclidine-Based Carbamates as Potential CNS Active Compounds. Pharmaceutics. 2021 Mar 1;13(3):420.

126. Mitchell CA, Donaldson M, Francese S, Clench MR. MALDI MSI analysis of lipid changes in living skin equivalents in response to emollient creams containing palmitoylethanolamide. Methods. 2016 Jul 15;104:93–100.

127. Fearn S. Characterisation of biological material with ToF-SIMS: A review. Materials Science and Technology (United Kingdom). 2015 Jan 1;31(2):148–61.

128. Paudel KS, Milewski M, Swadley CL, Brogden NK, Ghosh P, Stinchcomb AL. Challenges and opportunities in dermal/transdermal delivery. Ther Deliv. 2010;1(1):131.

129. Anderson SE, Wells JR, Fedorowicz A, Butterworth LF, Meade BJ, Munson AE. Evaluation of the contact and respiratory sensitization potential of volatile organic compounds generated by simulated indoor air chemistry. Toxicol Sci. 2007 Jun;97(2):355–63.

130. Bos JD, Meinardi MMHM. The 500 Dalton rule for the skin penetration of chemical compounds and drugs. Exp Dermatol. 2000 Jun;9(3):165–9.

131. Chen SS, Taylor JS, Mulford LA, Norris CD. Influences of molecular weight, molecular size, flux, and recovery for aromatic pesticide removal by nanofiltration membranes. Desalination [Internet]. 2004 Jan 15 [cited 2023 Dec 9];160(2):103–11. Available from: https://ntut.elsevierpure.com/en/publications/influences-of-molecular-weight-molecular-size-flux-and-recovery-f

132. Feldmann RJ, Maibach HI. Regional variation in percutaneous penetration of 14C cortisol in man. J Invest Dermatol. 1967;48(2):181–3.

133. Akomeah FK, Martin GP, Muddle AG, Brown MB. Effect of abrasion induced by a rotating brush on the skin permeation of solutes with varying physicochemical properties. Eur J Pharm Biopharm. 2008 Mar;68(3):724–34.

134. Hafeez F, Maibach H. Occlusion effect on in vivo percutaneous penetration of chemicals in man and monkey: partition coefficient effects. Skin Pharmacol Physiol [Internet]. 2013 Apr [cited 2023 Dec 9];26(2):85–91. Available from: https://pubmed.ncbi.nlm.nih.gov/23327987/

135. Thredgold L, Gaskin S, Quy C, Pisaniello D. Exposure of Agriculture Workers to Pesticides: The Effect of Heat on Protective Glove Performance and Skin Exposure to Dichlorvos. Int J Environ Res Public Health [Internet]. 2019 Dec 1 [cited 2023 Dec 9];16(23):4798. Available from: /pmc/articles/PMC6926567/

136. Zhai H, Ebel JP, Chatterjee R, Stone KJ, Gartstein V, Juhlin KD, et al. Hydration vs. skin permeability to nicotinates in man. Skin Res Technol. 2002;8(1):13–8.

137. Williams AC, Barry BW. Penetration enhancers. Adv Drug Deliv Rev [Internet]. 2004 Mar 27 [cited 2023 Dec 9];56(5):603–18. Available from: https://pubmed.ncbi.nlm.nih.gov/15019749/

138. Brand RM, Spalding M, Mueller C. Sunscreens can increase dermal penetration of 2,4-dichlorophenoxyacetic acid. J Toxicol Clin Toxicol. 2002;40(7):827–32.

139. Schmook FP, Meingassner JG, Billich A. Comparison of human skin or epidermis models with human and animal skin in in-vitro percutaneous absorption. Int J Pharm. 2001 Mar 14;215(1–2):51–6.

140. van Ravenzwaay B, Leibold E. A comparison between in vitro rat and human and in vivo rat skin absorption studies. Hum Exp Toxicol. 2004 Sep;23(9):421–30.

141. Barbero AM, Frasch HF. Pig and guinea pig skin as surrogates for human in vitro penetration studies: A quantitative review. Toxicology in Vitro. 2009 Feb 21;23(1):1–13.

142. Hueber-Becker F, Nohynek GJ, Dufour EK, Meuling WJA, de Bie ATHJ, Toutain H, et al. Occupational exposure of hairdressers to [14C]-para-phenylenediamine-containing oxidative hair dyes: A mass balance study. Food and Chemical Toxicology. 2007 Jan 1;45(1):160–9.

143. Lademann J, Jacobi U, Surber C, Weigmann HJ, Fluhr JW. The tape stripping procedure - evaluation of some critical parameters. European Journal of Pharmaceutics and Biopharmaceutics. 2009 Jun 1;72(2):317–23.

144. Carley S, Hogg K. Towards evidence based emergency medicine: best BETs from the Manchester Royal Infirmary. Tape stripping the stratum corneum and the effectiveness of EMLA. Emerg Med J. 2002;19(4):327.

145. Nylander-French LA. A tape-stripping method for measuring dermal exposure to multifunctional acrylates. Ann Occup Hyg. 2000 Dec 1;44(8):645–51.

146. Zsikó S, Cutcher K, Kovács A, Budai-Szűcs M, Gácsi A, Baki G, et al. Nanostructured Lipid Carrier Gel for the Dermal Application of Lidocaine: Comparison of Skin Penetration Testing Methods. Pharmaceutics 2019, Vol 11, Page 310. 2019 Jul 2;11(7):328.

147. Pulsoni I, Lubda M, Aiello M, Fedi A, Marzagalli M, Hagen J von, et al. Comparison Between Franz Diffusion Cell and a novel Micro-physiological System for In Vitro Penetration Assay Using Different Skin Models. SLAS Technol. 2022 Jun 1;27(3):161–71.

148. Misík J, Pavlíková R, Cabal J, Novotný L, Kuča K. METHOD OF STATIC DIFFUSION CELLS FOR ASSESSMENT OF PESTICIDES SKIN PERMEATION. Military Medical Science Letters. 2011 Jun 10;80(2):46–51.

149. Morais RP, Hochheim S, de Oliveira CC, Riegel-Vidotti IC, Marino CEB. Skin interaction, permeation, and toxicity of silica nanoparticles: Challenges and recent therapeutic and cosmetic advances. Int J Pharm. 2022 Feb 25;614:121–439.

150. Seo JE, Kim S, Kim BH. In vitro skin absorption tests of three types of parabens using a Franz diffusion cell. Journal of Exposure Science & Environmental Epidemiology 2017 27:3. 2016 Jul 20;27(3):320–5.

151. Ng SF, Rouse J, Sanderson D, Eccleston G. A Comparative Study of Transmembrane Diffusion and Permeation of Ibuprofen across Synthetic Membranes Using Franz Diffusion Cells. Pharmaceutics. 2010 Jun;2(2):209–23.

152. Rajitha P, Biswas R, Sabitha M, Jayakumar R. Methotrexate in the Treatment of Psoriasis and Rheumatoid Arthritis: Mechanistic Insights, Current Issues and Novel Delivery Approaches. Curr Pharm Des. 2017 Jun 2;23(24):3550–66.

153. Ameen D, Michniak-Kohn B. Development and in vitro evaluation of pressure sensitive adhesive patch for the transdermal delivery of galantamine: Effect of penetration enhancers and crystallization inhibition. European Journal of Pharmaceutics and Biopharmaceutics. 2019 Jun 1;139(1):262–71.

154. Addicks WJ, Flynn GL, Weiner N. Validation of a Flow-Through Diffusion Cell for Use in Transdermal Research. Pharmaceutical Research: An Official Journal of the American Association of Pharmaceutical Scientists. 1987 Aug 4;4(4):337–41.

155. Bronaugh RL, Stewart RF. Methods for in vitro percutaneous absorption studies IV: The flow-through diffusion cell. J Pharm Sci. 1985 Jan 21;74(1):64–7.

156. Franz TJ. Percutaneous absorption on the relevance of in vitro data. J Invest Dermatol [Internet]. 1975 [cited 2023 Nov 3];64(3):190–5. Available from: https://pubmed.ncbi.nlm.nih.gov/123263/

157. Clowes HM, Scott RC, Heylings JR. Skin absorption: Flow-through or static diffusion cells. Toxicology in Vitro. 1994 Aug 1;8(4):827–30.

158. Walters KA, Watkinson AC, Brain KR. In vitro skin permeation evaluation: the only realistic option. Int J Cosmet Sci. 1998;20(5):307–16.

159. SES Analyses. Equipment that measures permeati [Internet]. [cited 2023 Dec 10]. Available from: https://www.ses-analysesysteme.de/PG_SES-Franz_Cell_inline_uk.htm

160. Yao C, Myung K, Wang N, Johnson A. Spray retention of crop protection agrochemicals on the plant surface. ACS Symposium Series. 2014;1171:1–22.

161. Wu C, CropScience B, Parkway CW, Louis S, Varanasi V, Perez-Jones A. A nondestructive leaf-disk assay for rapid diagnosis of weed resistance to multiple herbicides. Weed Sci. 2021 May 1;69(3):274–83.

162. L'Haridon F, Besson-Bard A, Binda M, Serrano M, Abou-Mansour E, Balet F, et al. A Permeable Cuticle Is Associated with the Release of Reactive Oxygen Species and Induction of Innate Immunity. PLoS Pathog. 2011 Jul;7(7):e1002148.

163. Chiu YC, Chen BJ, Su YS, Huang WD, Chen CC. A Leaf Disc Assay for Evaluating the Response of Tea (Camellia sinensis) to PEG-Induced Osmotic Stress and Protective Effects of Azoxystrobin against Drought. Plants. 2021 Mar 1;10(3):1–19.

164. Kasote DM, Jayaprakasha GK, Patil BS. Leaf Disc Assays for Rapid Measurement of Antioxidant Activity. Scientific Reports 2019 9:1. 2019 Feb 13;9(1):1–10.

165. Pedon de Araujo Cardoso T, Viturino da Silva JW, Kishishita J, Galindo Bedor CN, Galindo Bedor DC, Pereira de Santana D, et al. Pesticide dermal absorption: Case study x in vitro study. Environ Toxicol Pharmacol. 2020 Apr 1;75:103313.

166. Vittal LVM, Rookes J, Boyd B, Cahill D. Analysis of plant cuticles and their interactions with agrochemical surfactants using a 3D printed diffusion chamber. Plant Methods [Internet]. 2023 Dec 1 [cited 2023 Dec 14];19(1):1–14. Available from: https://plantmethods.biomedcentral.com/articles/10.1186/s13007-023-00999-y

167. Freund DM, Sammons KA, Makunga NP, Cohen JD, Hegeman AD. Leaf Spray Mass Spectrometry: A Rapid Ambient Ionization Technique to Directly Assess Metabolites from Plant Tissues. J Vis Exp. 2018 Jun 21;2018(136):57949.

168. Woottisin N, Sukprasert S, Kulsirirat T, Tharavanij T, Sathirakul K. Evaluation of the Intestinal Permeability of Rosmarinic Acid from Thunbergia laurifolia Leaf Water

Extract in a Caco-2 Cell Model. Molecules 2022, Vol 27, Page 3884. 2022 Jun 17;27(12):3884.

169. Lv G, Du C, Ma F, Shen Y, Zhou J. Rapid and Nondestructive Detection of Pesticide Residues by Depth-Profiling Fourier Transform Infrared Photoacoustic Spectroscopy. ACS Omega. 2018 Mar 31;3(3):3548–53.

170. Xiao G, Dong D, Liao T, Li Y, Zheng L, Zhang D, et al. Detection of Pesticide (Chlorpyrifos) Residues on Fruit Peels Through Spectra of Volatiles by FTIR. Food Anal Methods. 2015 Apr 10;8(5):1341–6.

171. Räsch A, Hunsche M, Mail M, Burkhardt J, Noga G, Pariyar S. Agricultural adjuvants may impair leaf transpiration and photosynthetic activity. Plant Physiology and Biochemistry. 2018 Nov 1;132:229–37.

172. Jiang L, Gu K, Liu R, Jin S, Wang H, Pan C. Rapid detection of pesticide residues in fruits by surface-enhanced Raman scattering based on modified QuEChERS pretreatment method with portable Raman instrument. SN Appl Sci. 2019 Jun 1;1(6):1–9.

173. Yang T, Qu Y, Hickey M, Wang W, Zhao B, Bi S, et al. Mapping of Pesticide Transmission on Biological Tissues by Surface Enhanced Raman Microscopy with a Gold Nanoparticle Mirror. ACS Appl Mater Interfaces. 2019 Nov 27;11(47):44894–904.

174. Tognaccini L, Ricci M, Gellini C, Feis A, Smulevich G, Becucci M. Surface Enhanced Raman Spectroscopy for In-Field Detection of Pesticides: A Test on Dimethoate Residues in Water and on Olive Leaves. Molecules 2019, Vol 24, Page 292. 2019 Jan 15;24(2):292.

175. Malgorzata Baranska, Maciej Roman, Jan Cz. Dobrowolski, Hartwig Schulz, Rafal Baranski. Recent Advances in Raman Analysis of Plants: Alkaloids, Carotenoids, and Polyacetylenes. Curr Anal Chem. 2013 Feb 15;9(1):108–27.

176. Schubert F, Kallmeyer J. Liquid scintillation counting at the limit of detection in biogeosciences. Front Microbiol. 2023;14:1194848.

177. Schubert F, Kallmeyer J. Liquid scintillation counting at the limit of detection in biogeosciences. Front Microbiol. 2023;14.

178. Man F, Gawne PJ, T.M. de Rosales R. Nuclear imaging of liposomal drug delivery systems: A critical review of radiolabelling methods and applications in nanomedicine. Adv Drug Deliv Rev. 2019 Mar 15;143:134–60.

179. Peng CT. Quenching correction in liquid scintillation counting. Adv Tracer Methodol. 1966;3:81–94.

180. Del Río-Sancho S, Merino V, López-Castellano A, Kalia YN. A UHPLC-UV Method to Quantify Skin Deposition and Transdermal Permeation of Tizanidine Hydrochloride. J Chromatogr Sci. 2016;54(5):790–5.

181. Praça FSG, Bentley MVLB, Lara MG, Pierre MBR. Celecoxib determination in different layers of skin by a newly developed and validated HPLC-UV method. Biomed Chromatogr. 2011;25(11):1237–44.

182. Klimeš J, Sochor J, Doležal P, Körner J. HPLC evaluation of diclofenac in transdermal therapeutic preparations. Int J Pharm. 2001 Apr 17;217(1–2):153–60.

183. Zillich O V., Schweiggert-Weisz U, Hasenkopf K, Eisner P, Kerscher M. Release and in vitro skin permeation of polyphenols from cosmetic emulsions. Int J Cosmet Sci. 2013 Oct;35(5):491–501.

184. Pedersen S, Marra F, Nicoli S, Santi P. In vitro skin permeation and retention of parabens from cosmetic formulations. Int J Cosmet Sci. 2007 Oct;29(5):361–7.

185. Angelo T, Pires FQ, Gelfuso GM, da Silva JKR, Gratieri T, Cunha-Filho MSS. Development and validation of a selective HPLC-UV method for thymol determination in skin permeation experiments. J Chromatogr B Analyt Technol Biomed Life Sci. 2016 Jun 1;1022:81–6.

186. Wang JCT, Willia RR, Wang L, Loder J. In vitro skin permeation and bioassay of chlorhexidine phosphanilate, a new antimicrobial agent. Pharm Res. 1990;7(10):995–1002.

187. Belsey NA, Cordery SF, Bunge AL, Guy RH. Assessment of dermal exposure to pesticide residues during re-entry. Environ Sci Technol. 2011 May 15;45(10):4609–15.

188. Nielsen J, Nielsen F, Sorensen J. In Vitro Percutaneous Penetration of Five Pesticides--Effects of Molecular Weight and Solubility Characteristics - PubMed. Ann Occup Hyg [Internet]. 2004 Oct 27 [cited 2020 Jun 15];8(1):697–705. Available from: https://pubmed.ncbi.nlm.nih.gov/15509631/

189. Hanson KM, Behne MJ, Barry NP, Mauro TM, Gratton E, Clegg RM. Two-photon fluorescence lifetime imaging of the skin stratum corneum pH gradient. Biophys J. 2002 Sep 1;83(3):1682–90.

190. Umino Y, Ipponjima S, Denda M. Modulation of lipid fluidity likely contributes to the fructose/xylitol-induced acceleration of epidermal permeability barrier recovery. Arch Dermatol Res. 2019 May 6;311(4):317–24.

191. Discenza DJ, Lynch J, Miller J, Verderame M, Levine M. Detection of Organochlorine Pesticides in Contaminated Marine Environments via Cyclodextrin-Promoted Fluorescence Modulation. ACS Omega. 2017 Dec 31;2(12):8591–9.

192. Ahn J, Kim KH, Choe K, Lim JH, Lee SK, Kim YS, et al. Quantitative two-photon microscopy imaging analysis of human skin to evaluate enhanced transdermal delivery by hybrid-type multi-lamellar nanostructure: retraction. Biomed Opt Express. 2020 Oct 10;11(10):5871.

193. Bakonyi M, Gácsi A, Kovács A, Szűcs MB, Berkó S, Csányi E. Following-up skin penetration of lidocaine from different vehicles by Raman spectroscopic mapping. J Pharm Biomed Anal. 2018 May 30;154:1–6.

194. Kang Y, Zhang F. Image of the distribution profile of targets in skin by Raman spectroscopy-based multivariate analysis. Skin Research and Technology. 2022 May 1;28(3):402–9.

195. Saar BG, Contreras-Rojas LR, Xie XS, Guy RH. Imaging drug delivery to skin with stimulated Raman scattering microscopy. Mol Pharm. 2011 Jun 6;8(3):969–75.

196. Tippavajhala VK, de Oliveira Mendes T, Martin AA. In Vivo Human Skin Penetration Study of Sunscreens by Confocal Raman Spectroscopy. AAPS PharmSciTech. 2018 Feb 1;19(2):753–60.

197. Wang BG, König K, Halbhuber KJ. Two-photon microscopy of deep intravital tissues and its merits in clinical research. J Microsc. 2010;238(1):1–20.

198. Kijima S, Todo H, Matsumoto Y, Masaki R, Kadhum WR, Sugibayashi K. A useful technique using imaging mass spectrometry for detecting the skin distribution of topically applied lidocaine. J Drug Deliv Sci Technol. 2016 Jun 1;33(1):157–63.

199. Bonnel D, Legouffe R, Eriksson AH, Mortensen RW, Pamelard F, Stauber J, et al. MALDI imaging facilitates new topical drug development process by determining quantitative skin distribution profiles. Anal Bioanal Chem. 2018 Apr 1;410(11):2815–28.

200. Massonnet P, Heeren RMA. A concise tutorial review of TOF-SIMS based molecular and cellular imaging. J Anal At Spectrom [Internet]. 2019 Oct 30 [cited 2023 Sep 24];34(11):2217–28. Available from: https://pubs.rsc.org/en/content/articlehtml/2019/ja/c9ja00164f

201. Mazel V, Richardin P. ToF-SIMS Study of Organic Materials in Cultural Heritage: Identification and Chemical Imaging. Organic Mass Spectrometry in Art and Archaeology. 2009 Jan 1;433–57.

202. Aoki D, Saito K, Matsushita Y, Fukushima K. Distribution of Cell Wall Components by TOF-SIMS. Secondary Xylem Biology: Origins, Functions, and Applications. 2016;363–79.

203. Judd AM, Scurr DJ, Heylings JR, Wan KW, Moss GP. Distribution and visualisation of chlorhexidine within the skin using ToF-SIMS: A potential platform for the design of more efficacious skin antiseptic formulations. Pharm Res. 2013 Jul 1;30(7):1896–905.

204. Cersoy S, Richardin P, Walter P, Brunelle A. Cluster TOF-SIMS imaging of human skin remains: analysis of a South-Andean mummy sample. J Mass Spectrom. 2012 Mar;47(3):338–46.

205. Delvaux X, Noël C, Poumay Y, Houssiau L. Probing the human epidermis by combining ToF-SIMS and multivariate analysis. Biointerphases. 2023 Jan 1;18(1).

206. Starr NJ, Johnson DJ, Wibawa J, Marlow I, Bell M, Barrett DA, et al. Age-Related Changes to Human Stratum Corneum Lipids Detected Using Time-of-Flight Secondary Ion Mass Spectrometry Following in Vivo Sampling. Anal Chem. 2016 May 3;88(8):4400–8.

207. Converso V, Fearn S, Ware E, McPhail DS, Flemming AJ, Bundy JG. Analysis and imaging of biocidal agrochemicals using ToF-SIMS. Sci Rep. 2017 Dec 1;7(1):1–10.

208. Cliff B, Weibel DE, Lockyer NP, Jungnickel H, Stephens G, Vickerman JC. Detection of chlorinated pesticides on the surface of fungus using ToF-SIMS. Appl Surf Sci. 2003 Jan 15;203(204):710–3.

209. Perkins MC, Bell G, Briggs D, Davies MC, Friedman A, Hart CA, et al. The application of ToF-SIMS to the analysis of herbicide formulation penetration into and through leaf cuticles. Colloids Surf B Biointerfaces. 2008 Nov 15;67(1):1–13.

210. Holmes AM, Scurr DJ, Heylings JR, Wan KW, Moss GP. Dendrimer pre-treatment enhances the skin permeation of chlorhexidine digluconate: Characterisation by in vitro percutaneous absorption studies and Time-of-Flight Secondary Ion Mass Spectrometry. European Journal of Pharmaceutical Sciences. 2017 Jun 15;104(1):90–101.

211. Dreisewerd K, Yew JY. Mass spectrometry imaging goes three dimensional. Nat Methods. 2017 Dec 1;14(12):1139–40.

212. Aoyagi S, Kodama Y, Passarelli MK, Vorng JL, Kawashima T, Yoshikiyo K, et al. OrbiSIMS Imaging Identifies Molecular Constituents of the Perialgal Vacuole Membrane of Paramecium bursaria with Symbiotic Chlorella variabilis. Anal Chem. 2019 Oct 17;91(22):14545–51.

213. Zhang J, Brown J, Scurr D, Bullen A, MacLellan-Gibson K, Williams P, et al. Cryo-OrbiSIMS for 3D molecular imaging of a bacterial biofilm in its native state. bioRxiv. 2019 Nov 30;1(1):1–17.

214. Kotowska AM, Trindade GF, Mendes PM, Williams PM, Aylott JW, Shard AG, et al. Protein identification by 3D OrbiSIMS to facilitate in situ imaging and depth profiling. Nature Communications 2020 11:1. 2020 Nov 17;11(1):1–8.

215. Passarelli MK, Newman CF, Marshall PS, West A, Gilmore IS, Bunch J, et al. Single-cell analysis: visualizing pharmaceutical and metabolite uptake in cells with label-free 3D mass. Anal Chem. 2015 Jul 7;87(13):6696–702.

216. Menon GK, Cleary GW, Lane ME. The structure and function of the stratum corneum. Int J Pharm [Internet]. 2012 Oct 1 [cited 2023 Jun 13];435(1):3–9. Available from: https://pubmed.ncbi.nlm.nih.gov/22705878/

217. Mojumdar EH, Bouwstra JA. Stratum Corneum Lipid Composition and Organization. Cosmetic Formulation. 2019 Apr 5;47–60.

218. HORII I, NAKAYAMA Y, OBATA M, TAGAMI H. Stratum corneum hydration and amino acid content in xerotic skin. Br J Dermatol. 1989;121(5):587–92.

219. Ramasastry P, Downing DT, Pochi PE, Strauss JS. Chemical composition of human skin surface lipids from birth to puberty. J Invest Dermatol. 1970;54(2):139–44.

220. Shetage SS, Traynor MJ, Brown MB, Raji M, Graham-Kalio D, Chilcott RP. Effect of ethnicity, gender and age on the amount and composition of residual skin surface components derived from sebum, sweat and epidermal lipids. Skin Res Technol. 2014 Feb;20(1):97–107.

221. Sandilands A, Sutherland C, Irvine AD, McLean WHI. Filaggrin in the frontline: role in skin barrier function and disease. J Cell Sci. 2009 May 1;122(Pt 9):1285–94.

222. Rogers J, Harding C, Mayo A, Banks J, Rawlings A. Stratum corneum lipids: the effect of ageing and the seasons. Arch Dermatol Res. 1996;288(12):765–70.

223. Boireau-Adamezyk E, Baillet-Guffroy A, Stamatas GN. Age-dependent changes in stratum corneum barrier function. Skin Res Technol. 2014 Nov 1;20(4):409–15.

224. Bak H, Hong S phil, Jeong SK, Choi EH, Lee SE, Lee SH, et al. Altered epidermal lipid layers induced by long-term exposure to suberythemal-dose ultraviolet. Int J Dermatol. 2011 Jul;50(7):832–7.

225. Biniek K, Levi K, Dauskardt RH. Solar UV radiation reduces the barrier function of human skin. Proc Natl Acad Sci U S A. 2012 Oct 16;109(42):17111–6.

226. Ishikawa J, Narita H, Kondo N, Hotta M, Takagi Y, Masukawa Y, et al. Changes in the ceramide profile of atopic dermatitis patients. J Invest Dermatol. 2010;130(10):2511–4.

227. Yamamoto H, Hattori M, Chamulitrat W, Ohno Y, Kihara A. Skin permeability barrier formation by the ichthyosis-causative gene FATP4 through formation of the barrier lipid ω- O-acylceramide. Proc Natl Acad Sci U S A. 2020 Feb 11;117(6):2914–22.

228. Jamin EL, Jacques C, Jourdes L, Tabet JC, Borotra N, Bessou-Touya S, et al. Identification of lipids of the stratum corneum by high performance thin layer chromatography and mass spectrometry. Eur J Mass Spectrom (Chichester). 2019 Jun 1;25(3):278–90.

229. Kubo A, Ishizaki I, Kubo A, Kawasaki H, Nagao K, Ohashi Y, et al. The stratum corneum comprises three layers with distinct metal-ion barrier properties. Scientific Reports 2013 3:1. 2013 Apr 25;3(1):1–11.

230. Sjövall P, Gregoire S, Wargniez W, Skedung L, Luengo GS. 3D Molecular Imaging of Stratum Corneum by Mass Spectrometry Suggests Distinct Distribution of Cholesteryl Esters Compared to Other Skin Lipids. Int J Mol Sci. 2022 Nov 1;23(22).

231. Čižinauskas V, Elie N, Brunelle A, Briedis V. Fatty acids penetration into human skin ex vivo: A TOF-SIMS analysis approach. Biointerphases. 2017 Mar 1;12(1).

232. Cox P, Squier CA. Variations in lipids in different layers of porcine epidermis. J Invest Dermatol. 1986;87(6):741–4.

233. Bommannan D, Potts RO, Guy RH. Examination of stratum corneum barrier function in vivo by infrared spectroscopy. J Invest Dermatol. 1990;95(4):403–8.

234. Bonté F, Saunois A, Pinguet P, Meybeck A. Existence of a lipid gradient in the upper stratum corneum and its possible biological significance. Arch Dermatol Res. 1997;289(2):78–82.

235. Newell CL, Vorng JL, MacRae JI, Gilmore IS, Gould AP. Cryogenic OrbiSIMS Localizes Semi-Volatile Molecules in Biological Tissues. Angew Chem Int Ed Engl. 2020 Oct 5;59(41):18194–200.

236. Kind T, Fiehn O. Seven Golden Rules for heuristic filtering of molecular formulas obtained by accurate mass spectrometry. BMC Bioinformatics. 2007 Mar 27;8(1):1–20.

237. Sud M, Fahy E, Cotter D, Brown A, Dennis EA, Glass CK, et al. LMSD: LIPID MAPS structure database. Nucleic Acids Res [Internet]. 2007 Jan [cited 2022 Aug 22];35(Database issue). Available from: https://pubmed.ncbi.nlm.nih.gov/17098933/

238. Malm J, Giannaras D, Riehle MO, Gadegaard N, Sjövall P. Fixation and drying protocols for the preparation of cell samples for time-of-flight secondary ion mass spectrometry analysis. Anal Chem. 2009 Sep 1;81(17):7197–205.

239. Van Nuffel S, Parmenter C, Scurr DJ, Russell NA, Zelzer M. Multivariate analysis of 3D ToF-SIMS images: method validation and application to cultured neuronal networks. Analyst. 2015 Dec 14;141(1):90–5.

240. Edney MK, Kotowska AM, Spanu M, Trindade GF, Wilmot E, Reid J, et al. Molecular Formula Prediction for Chemical Filtering of 3D OrbiSIMS Datasets. Anal Chem [Internet]. 2022 Mar 22 [cited 2022 Aug 22];94(11):4703–11. Available from: https://pubs.acs.org/doi/full/10.1021/acs.analchem.1c04898

241. Haratake A, Komiya A, Horikoshi T, Uchiwa H, Watanabe S. Acceleration of de novo cholesterol synthesis in the epidermis influences desquamation of the stratum corneum in aged mice. Skin Pharmacol Physiol. 2006 Aug;19(5):275–82.

242. Epstein EH, Williams ML, Elias PM. The epidermal cholesterol sulfate cycle. J Am Acad Dermatol. 1984;10(5 Pt 1):866–8.

243. Gray GM, Yardley HJ. Lipid compositions of cells isolated from pig, human, and rat epidermis. J Lipid Res. 1975 Nov 1;16(6):434–40.

244. Ferreira MS, Almeida IF, Magalhães MC, Sousa-Lobo JM. Trending anti-aging peptides. Cosmetics. 2020 Dec 1;7(4):1–15.

245. Watson REB, Ogden S, Cotterell LF, Bowden JJ, Bastrilles JY, Long SP, et al. Effects of a cosmetic “anti-ageing” product improves photoaged skin [corrected]. Br J Dermatol. 2009;161(2):419–26.

246. Lintner K, Peschard O. Biologically active peptides: from a laboratory bench curiosity to a functional skin care product. Int J Cosmet Sci. 2000;22(3):207–18.

247. Dominguez E, Heredia-Guerrero JA, Heredia A. The biophysical design of plant cuticles: an overview. New Phytologist. 2011 Mar 1;189(4):938–49.

248. Holloway PJ. Plant Cuticles: Physicochemical Characteristics and Biosynthesis. Air Pollutants and the Leaf Cuticle. 1994;1(1):1–13.

249. Ensikat HJ, Neinhuis C, Barthlott W. Direct access to plant epicuticular wax crystals by a new mechanical isolation method. Int J Plant Sci. 2000;161(1):143–8.

250. Skoss JD. Structure and Composition of Plant Cuticle in Relation to Environmental Factors and Permeability. https://doi.org/101086/335891. 2015 Oct 19;117(1):55–72.

251. Okamoto M, Tanji N, Katayama Y, Okada J. TOF-SIMS investigation of the distribution of a cosmetic ingredient in the epidermis of the skin. Appl Surf Sci. 2006 Jul 30;252(19):6805–8.

252. Parks CG, Walitt BT, Pettinger M, Chen JC, De Roos AJ, Hunt J, et al. Insecticide use and risk of rheumatoid arthritis and systemic lupus erythematosus in the women's health initiative observational study. Arthritis Care Res (Hoboken). 2011 Feb;63(2):184–94.

253. Holsapple MP. Autoimmunity by pesticides: A critical review of the state of the science. Toxicol Lett. 2002 Feb 28;127(1–3):101–9.

254. Hoppin JA, Umbach DM, Long S, London SJ, Henneberger PK, Blair A, et al. Pesticides are Associated with Allergic and Non-Allergic Wheeze among Male Farmers. Environ Health Perspect. 2017 Apr 1;125(4):535–43.

255. Bassil KL, Vakil C, Sanborn M, Cole DC, Kaur JS, Kerr KJ. Cancer health effects of pesticides: Systematic review. G. Balint, Antala B, Carty C, Mabieme JMA, Amar IB, Kaplanova A, editors. Canadian Family Physician. 2007;53(10):1705–11.

256. Bourgault R, Matschi S, Vasquez M, Qiao P, Sonntag A, Charlebois C, et al. Constructing functional cuticles: analysis of relationships between cuticle lipid composition, ultrastructure and water barrier function in developing adult maize leaves. Ann Bot [Internet]. 2020 Jan 8 [cited 2023 Aug 14];125(1):79–91. Available from: https://dx.doi.org/10.1093/aob/mcz143

257. Manandhar JB, Hartman GL. Anthracnose development on pepper fruits inoculated with Colletotrichum gloeosporioides. Plant Dis. 1995 Jan 1;79(4):380–3.

258. Nabatanzi A, Nkadimeng SM, Lall N, Kabasa JD, McGaw LJ. Antioxidant and Anti-Inflammatory Activities of Kigelia africana (Lam.) Benth. Evid Based Complement Alternat Med. 2020;2020.

259. Schuster AC, Burghardt M, Alfarhan A, Bueno A, Hedrich R, Leide J, et al. Effectiveness of cuticular transpiration barriers in a desert plant at controlling water loss at high temperatures. AoB Plants. 2016 Jan 1;8(1):1–27.

260. Nawrath C. The Biopolymers Cutin and Suberin. https://doi.org/101199/tab0021. 2002 Apr 4;2002(1):1–21.

261. Arrieta-Baez D, Cruz-Carrillo M, Gómez-Patiño MB, Zepeda-Vallejo LG. Derivatives of 10,16-Dihydroxyhexadecanoic Acid Isolated from Tomato (Solanum lycopersicum) as Potential Material for Aliphatic Polyesters. Molecules 2011, Vol 16, Pages 4923-4936. 2011 Jun 15;16(6):4923–36.

262. Eglinton G, Hamilton RJ. Leaf Epicuticular Waxes. Science (1979). 1967 Jun 9;156(3780):1322–35.

263. Buschhaus C, Jetter R. Composition differences between epicuticular and intracuticular wax substructures: How do plants seal their epidermal surfaces? J Exp Bot. 2011 Jan;62(3):841–53.

264. BARTHLOTT W, NEINHUIS C, CUTLER D, DITSCH F, MEUSEL I, THEISEN I, et al. Classification and terminology of plant epicuticular waxes. Botanical Journal of the Linnean Society. 1998 Mar;126(3):237–60.

265. Ferreyra MLF, Serra P, Casati P. Recent advances on the roles of flavonoids as plant protective molecules after UV and high light exposure. Physiol Plant [Internet]. 2021

Nov 1 [cited 2023 May 12];173(3):736–49. Available from: https://onlinelibrary.wiley.com/doi/full/10.1111/ppl.13543

266. Fini A, Brunetti C, Ferdinando M Di, Ferrini F, Tattini M. Stress-induced flavonoid biosynthesis and the antioxidant machinery of plants. https://doi.org/104161/psb6515069 [Internet]. 2011 May [cited 2023 May 12];6(5):709–11. Available from: https://www.tandfonline.com/doi/abs/10.4161/psb.6.5.15069

267. Mitchell MJ, Keogh DP, Crooks JR, Smith SL. Effects of plant flavonoids and other allelochemicals on insect cytochrome P-450 dependent steroid hydroxylase activity. Insect Biochem Mol Biol. 1993 Jan 1;23(1):65–71.

268. Hofer S, Geisler S, Lisandrelli R, Ngoc HN, Ganzera M, Schennach H, et al. Pharmacological Targets of Kaempferol Within Inflammatory Pathways—A Hint Towards the Central Role of Tryptophan Metabolism. Antioxidants 2020, Vol 9, Page 180 [Internet]. 2020 Feb 21 [cited 2023 May 12];9(2):180. Available from: https://www.mdpi.com/2076-3921/9/2/180/htm

269. Gorton HL, Vogelmann TC. Effects of Epidermal Cell Shape and Pigmentation on Optical Properties of Antirrhinum Petals at Visible and Ultraviolet Wavelengths. Plant Physiol [Internet]. 1996 [cited 2023 May 12];112(3):879–88. Available from: https://pubmed.ncbi.nlm.nih.gov/12226425/

270. Tambasco-Studart M, Titiz O, Raschle T, Forster G, Amrhein N, Fitzpatrick TB. Vitamin B6 biosynthesis in higher plants. Proc Natl Acad Sci U S A [Internet]. 2005 Sep 20 [cited 2023 May 12];102(38):13687–92. Available from: https://www.pnas.org/doi/abs/10.1073/pnas.0506228102

271. Pastori GM, Kiddle G, Antoniw J, Bernard S, Veljovic-Jovanovic S, Verrier PJ, et al. Leaf Vitamin C Contents Modulate Plant Defense Transcripts and Regulate Genes That Control Development through Hormone Signaling. Plant Cell [Internet]. 2003 Apr 1 [cited 2023 May 12];15(4):951. Available from: /pmc/articles/PMC152340/

272. Berglund T, Wallström A, Nguyen T Van, Laurell C, Ohlsson AB. Nicotinamide; antioxidative and DNA hypomethylation effects in plant cells. Plant Physiology and Biochemistry. 2017 Sep 1;118:551–60.

273. Roje S. Vitamin B biosynthesis in plants. Phytochemistry. 2007 Jul 1;68(14):1904–21.

274. Gisi U, Schaub F, Wiedmer H, Ummel E. SAN 619 F, a new triazole fungicide. 1986 British Crop Protection Conference Pests and Diseases Vol 1. 1986;33–40.

275. Liu X, Chen X, Ding X, Wu H. Uptake and distribution characteristics of the novel fungicide pyraoxystrobin in cucumber plants. RSC Adv [Internet]. 2018 Jul 30 [cited 2023 Oct 12];8(48):27152–6. Available from: https://pubs.rsc.org/en/content/articlehtml/2018/ra/c8ra05140b

276. Liu Q, Liu Y, Dong F, Sallach JB, Wu X, Liu X, et al. Uptake kinetics and accumulation of pesticides in wheat (Triticum aestivum L.): Impact of chemical and plant properties. Environmental Pollution. 2021 Apr 15;275:116637.

277. Machera K. Developmental toxicity of cyproconazole, an inhibitor of fungal ergosterol biosynthesis, in the rat. Bull Environ Contam Toxicol [Internet]. 1995 Mar

[cited 2023 Aug 15];54(3):363–9. Available from: https://pubmed.ncbi.nlm.nih.gov/7749267/

278. Starr NJ, Khan MH, Edney MK, Trindade GF, Kern S, Pirkl A, et al. Elucidating the molecular landscape of the stratum corneum. Proc Natl Acad Sci U S A [Internet]. 2022 Mar 22 [cited 2022 Aug 22];119(12). Available from: https://www.pnas.org/doi/abs/10.1073/pnas.2114380119

279. Wickett RR, Visscher MO. Structure and function of the epidermal barrier. Am J Infect Control. 2006 Dec 1;34(10):S98–110.

280. Hashmi S, Marinkovich MP. Molecular organization of the basement membrane zone. Clin Dermatol [Internet]. 2011 [cited 2023 Nov 16];29(4):398–411. Available from: https://pubmed.ncbi.nlm.nih.gov/21679867/

281. Romanovsky AA. Skin temperature: its role in thermoregulation. Acta Physiol (Oxf) [Internet]. 2014 Mar [cited 2023 Nov 16];210(3):507. Available from: /pmc/articles/PMC4159593/

282. Glatte P, Buchmann SJ, Hijazi MM, Illigens BMW, Siepmann T. Architecture of the Cutaneous Autonomic Nervous System. Front Neurol. 2019 Sep 10;10:469–534.

283. Mittal B. Subcutaneous adipose tissue & visceral adipose tissue. Indian J Med Res [Internet]. 2019 May 1 [cited 2023 Nov 16];149(5):573. Available from: /pmc/articles/PMC6702693/

284. May CA, Bramke S. In the human, true myocutaneous junctions of skeletal muscle fibers are limited to the face. J Anat. 2021 Aug 1;239(2):450.

285. Prausnitz MR, Mitragotri S, Langer R. Current status and future potential of transdermal drug delivery. Nat Rev Drug Discov. 2004;3(2):115–24.

286. Kim B, Cho HE, Moon SH, Ahn HJ, Bae S, Cho HD, et al. Transdermal delivery systems in cosmetics. Biomedical Dermatology. 2020 Dec;4(1).

287. Kao J, Patterson FK, Hall J. Skin penetration and metabolism of topically applied chemicals in six mammalian species, including man: An in vitro study with benzo[a]pyrene and testosterone. Toxicol Appl Pharmacol. 1985;81:502–16.

288. Cao Y, Kakar P, Hossen MN, Wu MX, Chen X. Sustained epidermal powder drug delivery via skin microchannels. J Control Release. 2017 Mar 3;249:102.

289. Gandhi J, Suthar D, Patel H, Shelat P, Parejiya P. Development and characterization of microemulsion based topical gel of essential oil of clove (Syzygium aromaticum) for superficial fungal infections. Advances in Traditional Medicine. 2021 Sep 1;21(3):519–34.

290. Matsuo K, Hirobe S, Okada N, Nakagawa S. Analysis of Skin Permeability and Toxicological Properties of Amorphous Silica Particles. Biol Pharm Bull. 2016;39(7):1201–5.

291. Clarke JF, Cordery SF, Morgan NA, Knowles PK, Guy RH. Dermal Absorption of Pesticide Residues. Chem Res Toxicol. 2018 Dec 17;31(12):1356–63.

292. Kim SH, Jang JB, Park KH, Paik MK, Jeong SH. Evaluation of Dermal Absorption Rate of Pesticide Chlorpyrifos Using In Vitro Rat Dermal Tissue Model and Its Health Risk Assessment. Biomedical Science Letters. 2016 Dec 31;22(4):140–9.

293. Hughes MF, Edwards BC. In vitro dermal absorption of pyrethroid pesticides in human and rat skin. Toxicol Appl Pharmacol. 2010 Jul 1;246(1–2):29–37.

294. Aggarwal M, Fisher P, Kluxen FM, Maas W, Morgan N, Parr-Dobrzanski R, et al. Assessing in vitro dermal absorption of dry residues of agrochemical sprays using human skin within OECD TG 428. Regulatory Toxicology and Pharmacology. 2019 Aug 1;106:55–67.

295. Seah MP, Havelund R, Gilmore IS. Systematic Temperature Effects in the Argon Cluster Ion Sputter Depth Profiling of Organic Materials Using Secondary Ion Mass Spectrometry. J Am Soc Mass Spectrom. 2016 Aug 1;27(8):1411–8.

296. Vorng JL, Kotowska AM, Passarelli MK, West A, Marshall PS, Havelund R, et al. Semiempirical rules to determine drug sensitivity and ionization efficiency in secondary ion mass spectrometry using a model tissue sample. Anal Chem. 2016 Nov 15;88(22):11028–36.

297. Starr NJ, Khan MH, Edney MK, Trindade GF, Kern S, Pirkl A, et al. Elucidating the molecular landscape of the stratum corneum. Proc Natl Acad Sci U S A. 2022 Mar 22;119(12).

298. Kim NS, Uchida T, Kitagawa K, Yagi A, Goto S. Relationship between lipophilicity and skin permeability of various drugs from an ethanol/water/lauric acid system. Biol Pharm Bull. 1994;17(10):1421–4.

299. Febriana SA, Khalidah M, Huda FN, Sutarni S, Mahayana I, Indrastuti N, et al. Prevalence of pesticide related occupational diseases among Indonesian vegetable farmers – A collaborative work. Toxicol Rep. 2023 Jan 1;10:571–9.

300. Macfarlane E, Carey R, Keegel T, El-Zaemay S, Fritschi L. Dermal Exposure Associated with Occupational End Use of Pesticides and the Role of Protective Measures. Saf Health Work. 2013 Sep;4(3):141.

301. O'Malley M. The Regulatory Evaluation of the Skin Effects of Pesticides. Hayes' Handbook of Pesticide Toxicology, Third Edition: Volume 1. 2010 Jan 1;1:701–87.

302. Rajan R, Vasudevan DT. Effect of permeation enhancers on the penetration mechanism of transfersomal gel of ketoconazole. J Adv Pharm Technol Res. 2012;3(2):116.

303. Caliskan* UK, Karakus MM. Essential Oils as Skin Permeation Boosters and Their Predicted Effect Mechanisms. Journal of Dermatology and Skin Science. 2020;2(3):24–30.

304. Jiang Q, Wu Y, Zhang H, Liu P, Yao J, Yao P, et al. Development of essential oils as skin permeation enhancers: penetration enhancement effect and mechanism of action. Pharm Biol. 2017;55(1):1600.

305. Lawrence JN. Electrical resistance and tritiated water permeability as indicators of barrier integrity of in vitro human skin. Toxicology in Vitro. 1997 Jun 1;11(3):241–9.

306. Ng SF, Rouse JJ, Sanderson FD, Meidan V, Eccleston GM. Validation of a Static Franz Diffusion Cell System for In Vitro Permeation Studies. AAPS PharmSciTech. 2010 Sep;11(3):1441.

307. Pawar KR, Mulabagal V, Smith F, Kolli CS, Rangari VK, Babu RJ. Stability-indicating HPLC assay for lysine-proline-valine (KPV) in aqueous solutions and skin homogenates. Biomedical Chromatography. 2015 May 1;29(5):716–21.

308. Traberg A, Pinto FE, Hansen ACN, Haedersdal M, Lerche CM, Janfelt C. Quantitative Mass Spectrometry Imaging of Bleomycin in Skin Using a Mimetic Tissue Model for Calibration. Pharmaceuticals (Basel). 2022 Dec 1;15(12):ph15121583.

309. Roseboom IC, Rosing H, Beijnen JH, Dorlo TPC. Skin tissue sample collection, sample homogenization, and analyte extraction strategies for liquid chromatographic mass spectrometry quantification of pharmaceutical compounds. J Pharm Biomed Anal. 2020 Nov 30;191:113590.

310. Dzepina K, Arey J, Marr LC, Worsnop DR, Salcedo D, Zhang Q, et al. Detection of particle-phase polycyclic aromatic hydrocarbons in Mexico City using an aerosol mass spectrometer. Int J Mass Spectrom. 2007 Jun 1;263(2–3):152–70.

311. Herring CL, Faiola CL, Massoli P, Sueper D, Erickson MH, McDonald JD, et al. New Methodology for Quantifying Polycyclic Aromatic Hydrocarbons (PAHs) Using High-Resolution Aerosol Mass Spectrometry. Aerosol Science and Technology. 2015 Nov 2;49(11):1131–48.

312. Zhou W, Yang S, Wang PG. Matrix effects and application of matrix effect factor. https://doi.org/104155/bio-2017-0214. 2017 Nov 24;9(23):1839–44.

313. Schmidt N, Gans EH. Tretinoin: A Review of Its Anti-inflammatory Properties in the Treatment of Acne. J Clin Aesthet Dermatol. 2011 Nov;4(11):29.

314. Zhao Y, Wang C, Zou B, Fu L, Ren S, Zhang X. Design and Evaluation of Tretinoin Fatty Acid Vesicles for the Topical Treatment of Psoriasis. Molecules. 2023 Dec 1;28(23):7868.

315. Lee CK, Uchida T, Kitagawa K, Yagi A, Kim N -S, Goto S. Skin permeability of various drugs with different lipophilicity. J Pharm Sci. 1994;83(4):562–5.

316. Kim NS, Uchida T, Kitagawa K, Yagi A, Goto S. Relationship between lipophilicity and skin permeability of various drugs from an ethanol/water/lauric acid system. Biol Pharm Bull. 1994;17(10):1421–4.

317. Chen CP, Chen CC, Huang CW, Chang YC. Evaluating Molecular Properties Involved in Transport of Small Molecules in Stratum Corneum: A Quantitative Structure-Activity Relationship for Skin Permeability. Molecules : A Journal of Synthetic Chemistry and Natural Product Chemistry. 2018;23(4):911.

318. Bergazin TD, Tielker N, Zhang Y, Mao J, Gunner MR, Francisco K, et al. Evaluation of log P, pK a, and log D predictions from the SAMPL7 blind challenge. J Comput Aided Mol Des. 2021 Jul 1;35(7):771–802.

319. Cross SE, Magnusson BM, Winckle G, Anissimov Y, Roberts MS. Determination of the effect of lipophilicity on the in vitro permeability and tissue reservoir

characteristics of topically applied solutes in human skin layers. J Invest Dermatol. 2003 May 1;120(5):759–64.

320. Surber C, Wilhelm KP, Hori M, Maibach HI, Guy RH. Optimization of Topical Therapy: Partitioning of Drugs into Stratum Corneum. Pharmaceutical Research: An Official Journal of the American Association of Pharmaceutical Scientists. 1990;7(12):1320–4.

321. Rougier A, Rallis M, Krien P, Lotte C. In vivo percutaneous absorption: a key role for stratum corneum/vehicle partitioning. Arch Dermatol Res. 1990 Dec;282(8):498–505.

322. Moosavi SM, Ghassabian S, Moosavi SM, Ghassabian S. Linearity of Calibration Curves for Analytical Methods: A Review of Criteria for Assessment of Method Reliability. Calibration and Validation of Analytical Methods - A Sampling of Current Approaches. 2018 Feb 9;

323. Moosavi SM, Ghassabian S, Moosavi SM, Ghassabian S. Linearity of Calibration Curves for Analytical Methods: A Review of Criteria for Assessment of Method Reliability. Calibration and Validation of Analytical Methods - A Sampling of Current Approaches. 2018 Feb 9;

324. Kowalska M, Woźniak M, Kijek M, Mitrosz P, Szakiel J, Turek P. Management of validation of HPLC method for determination of acetylsalicylic acid impurities in a new pharmaceutical product. Scientific Reports 2022 . 2022 Jan 6;12(1):1–9.

325. Jurado JM, Alcázar A, Muñiz-Valencia R, Ceballos-Magaña SG, Raposo F. Some practical considerations for linearity assessment of calibration curves as function of concentration levels according to the fitness-for-purpose approach. Talanta. 2017 Sep 1;172:221–9.